Polyoxometalate-Stabilized Ruthenium Nanoparticles: The Polyoxometalate-Metal Interface in Multifunctional Catalysis

Lan Feng

A thesis submitted in partial fulfilment of the requirements for the award of

Doctor of Philosophy

School of Natural and Environmental Sciences
(Chemistry)
Newcastle University,
Newcastle upon Tyne, UK

September 2018

Dedication

To my beloved parents, Lianwang and Aixin

Abstract

Polyoxometalates (POMs) are metal-oxide polynuclear anions. The interface between a metal (often in the form of nanoparticles) and a metal oxide is important in heterogeneous catalysis and has been the subject of intense research over years. The stabilization of metal nanoparticles (such as Pd, Pt, Ag, Au, Ir, Rh, Ru) by polyoxometalates has been studied by Weinstock, Papaconstintinou and Kortz. This represents a new type of catalytic material where molecules (e.g. H_2) may be activated at the metal nanoparticles while the POM provides redox and Brønsted acid functionality. Metal nanoparticles and POM molecular metal oxides have each been applied in chemical synthesis, electrochemistry and photocatalysis, but by exploiting the interface between metal nanoparticles and POMs, this project aimed to design new nanoscale catalysts that incorporate the features associated with each component. A convenient method of reduction by hydrogen was used to synthesize POM-stabilized ruthenium nanoparticles, which were subsequently incorporated into immobilized systems as catalysts. The catalysts were then tested for a range of transformations.

The brief history of the development of POMs, the classification and structure of POMs and the function and application of POMs is discussed in Chapter 1. The use of polymer-immobilised ionic liquid phase (PIILP) and graphite-like carbon nitride (C_3N_4) as supports is introduced based on previous research.

In Chapter 2, the preparation of a series of POM stabilized ruthenium nanoparticles in aqueous solution is discussed, wherein the different kinds of POMs ($H_3PW_{12}O_{40}$, $H_3PMo_{12}O_{40}$, $H_4SiW_{12}O_{40}$, $K_6[P_2W_{18}O_{62}]\cdot 19H_2O$ and $K_{10}[P_2W_{17}O_{61}]\cdot 20H_2O$) were used to prepare Ru^0@POM in solution. The result of these showed that the POM anions were adsorbed onto the surface of metal

nanoparticles due to the POM anions being able to afford negative charges to metal nanoparticles. The performance of the resulting nanoclusters for a range of reactions was assessed. In Fischer-Tropsch synthesis, the hydrogenation of CO to produce hydrocarbons occurred at 150 ^{o}C over 18 hrs. According to the results of electrochemical CO_2 reduction in acid aqueous solution, Ru^0@POM nanoclusters also improved reaction performance compared with pure Ru^0 nanoparticles.

Ru^0 nanoparticles and POMs have been shown to act in tandem for (i) activation of H_2 and (ii) creation of strong Brønsted acidity, but these POM-stabilised Ru^0 nanoparticles are difficult to recover and recycle. The high solubility of POMs in aqueous solution has limited the application of Ru^0@POM nanoclusters; and in Chapter 3 describes attempts to address this problem through the use of water-tolerant polymer-immobilised ionic liquid phase (PIILP) supports upon which to immobilize Ru^0/POM nanoparticles, to give Ru^0@POM/PIILP bifunctional catalysts for the hydrogenation of trans-cinnamaldehyde, 5-hydroxymethylfurfural and furfural. Ru^0@POM/PIILP exhibited excellent catalytic performance in terms of both conversion and selectivity.

In Chapter 4, catalysts prepared by adsorbing polyoxometalate-stabilized ruthenium nanoparticles onto carbon nitride are described. The g-C_3N_4 is a semiconductor with a high surface area and is an attractive support for POM-stabilized ruthenium nanoparticles. This Ru^0@POM/C_3N_4 material is a potential redox and photocatalyst for hydrogenolysis of cellobiose to sorbitol, selective hydrogenation of levulinic acid and water splitting. The H_2 production efficiency of Ru^0@$H_3PW_{12}O_{40}$/C_3N_4 was 6.44 times higher than that of g-C_3N_4. The Ru^0@$H_3PW_{12}O_{40}$/C_3N_4 catalyst gave a high sorbitol yield (85%) for hydrogenolysis of cellobiose and was highly selectivite for GVL (almost 100%) in the hydrogenation of levulinic acid.

The catalysts described in Chapters 2-4 were characterized by a combination of techniques including NMR, UV-vis, XRD, FT-IR, UV-DRS, TGA, SEM, TEM and XPS analysis.

The results obtained in this thesis emphasize the potential of polyoxometalate-stabilized ruthenium nanoparticles in new functional composites for catalysis. In the future, more extensive research will expand their use for conversion of biomass and platform chemicals as well as for green electrocatalytic reduction and photocatalysis.

Acknowledgements

I arrived in Newcastle, England in 2014 with a determination to work to the best of my ability, with aspirations to become the best I could be in my chosen field. Many people have helped and guided me during the years of my study.

I would like to thank my supervisor, Dr R. John Errington for his constant support, his serious work ethic, rigorous scientific research attitude and his committed and patient guidance of my project.

Thanks to Dr Simon Doherty for his provision of experimental instruments and his pertinent guidance which has greatly benefited me when carrying out my experiments.

I wish to acknowledge the support of Professor Pawel J Kulesza and his electrochemistry team at the University of Warsaw, Poland for their wonderful help of CO_2 electroreduction.

A very big thank you to Professor Ye Wang, Dr Welping Deng and their group at the University of Xiamin, China for their awesome support of Fisher-Tropsch synthesis, hydrogenolysis of cellobiose and water splitting.

My thanks also go to my group members, Thompson Izuagie, Kate Phipps, Daniel Lebbie, Einas Abood and Tom Backhouse of the Dr Simon Doherty Group, for their friendship and support. It was a privilege to work alongside them.

I am also deeply grateful to my parents for their love, care and support during all my studies. Throughout my life they have always encouraged me to pursue my dreams and have been my greatest inspiration.

A new chapter in my life is beginning but I will always remember those mentioned above who have set me the highest of standards to follow.

Abbreviations

AC	Activated carbon
AIBN	Azodiisobutyronitrile
ATRP	Atom transfer radical polymerization
BET	Brunauer, Emmett and Teller
CAL	Cinnamaldehyde
CNTs	Carbon nanotubes
COL	Cinnamyl alcohol
DHMF	2,5-dihydroxymethyl furan
DHTMF	2,5-dihydroxymethyltetrahydrofuran
DMF	2,5-dimethylfuran
EDS	Energy dispersive spectrometer
EPR	Electron spectrum
FA	Furfuryl alcohol
FFA	Furfural
FMO	Frontier-molecular Orbital
F-T synthesis	Fischer-Tropsch synthesis
FT-IR	Fourier transform infrared spectroscopy
GC	Gas chromatography
GC-MS	Gas chromatography-mass spectrometer
g-C_3N_4	Graphitic carbon nitride
GVL	γ-Valerolactone
HCAL	Hydrocinnamic aldehyde
HCOL	Hydrocinnamic alcohol
HMF	5-hydroxymethylfurfural
HOMO	Highest occupied molecular orbital
HPA	Heteropolyacid
HPLC	High performance liquid chromatography

LA	Levulinic acid
LUMO	Lowest unoccupied molecular orbital
MF	5-methyl furfural
MFA	5-methyl furfuryl alcohol
MTHFA	5-methyltetrahydrofurfuryl alcohol
NHE	Normal hydrogen electrode
NMR	Nuclear magnetic resonance spectroscopy
OMC	Ordered mesoporous carbon
POMs	Polyoxometalates
PVP	Polyvinyl pyrrolidone
PIILP	Polymer immobilised ionic liquid phases
Ru^0	Ruthenium nanoparticles
Ru^0@POM/PIILP	PIILP containing POM stabilized Ru^0
Ru^0@POM	POM stabilized ruthenium nanoparticles
Ru^0@$H_3PW_{12}O_{40}/C_3N_4$	POM stabilized Ru^0 adsorbed onto C_3N_4
Ru^0/PIILP	PIILP stabilized ruthenium nanoparticles
RAFT	Reversible addition-fragmentation chaintransfer
RDE	Rotating disk electrode
ROMP	Ring-opening metathesis polymerization
SEM	Scanning electron microscope
TEM	Transmission electron microscopy
TGA	Thermal gravimetric analysis
THF	Tetrahydrofuran
THFA	Tetrahydrofurfuryl alcohol
UV-DRS	UV diffuse reflectance spectrum
UV-Vis	Ultraviolet–visible spectroscopy
XAFS	X-ray absorption fine structure
XPS	X-ray photoelectron spectroscopy
XRD	Powder X-ray diffraction

Table of Contents

List of Figures

Chapter 1. Background

Chapter 3. Polymer immobilized ionic liquids containing polyoxometalate-stabilized ruthenium nanoparticles

List of Tables

List of Schemes

Chapter 1

Background

Chapter 1. Background

1.1 Polyoxometalates

1.1.1 A brief background to polyoxometalates chemistry

Polyoxometalates (POMs) have been studied for more than one hundred years, and represent an important research field in inorganic chemistry and catalytic chemistry. The polyanions are formed by the condensation of oxyanions, such as:

$$7MO_4^{2-} + 8H^+ \longrightarrow M_7O_{24}^{6-} + 4H_2O \ (M = Mo, W)$$

The heteropolyanions are formed by the incorporation of other elements, such as:

$$12WO_4^{2-} + PO_4^{3-} + 24H^+ \longrightarrow PW_{12}O_{40}^{3-} + 12H_2O$$

The corresponding acid salt is called a heteropoly acid, i.e. $H_3PW_{12}O_{40}$, which is the classical heteropoly acid, 12-phosphotungstic acid.

As early as 1826, Berzelius described the yellow precipitate produced by adding ammonium molybdate to phosphoric acid, which is known as 12-phosphomolybdic acid. At that time, the question of its composition and structure was not discussed. It was not until 1862 that Marignac discovered tungstosilicic acid and its salts and accurately determined the composition of these heteropoly compounds, and truly opened the era of POM research. In 1872, Scheibler synthesized 12-phosphotungstic acid. Miolati and Rosenheim measured and synthesized phosphomolybdic acid [$H_7P(Mo_2O_7)_6$] by conductometric titration and ether extraction, respectively. In 1929, Pauling proposed a three-dimensional model of 12 series of POM structures, that is, the "basket" structure of heteropoly acids, thus making the development of heteropoly acid chemistry enter a new period.[1] According to Pauling's model,

12-silicotungstic acid and 12-phosphotungstic acid can be written as: $H_4[SiO_4W_{12}O_{18}(OH)_{36}]$ and $H_3[PO_4W_{12}O_{18}(OH)_{36}]$. Although the idea was incorrect, it represented a new way of thinking, and laid a foundation for the later development of heteropoly acids. In 1934, J.F. Keggin of the Bragg research group prepared $H_3PW_{12}O_{40}\cdot 5H_2O$ by drying 12-phosphotungstic acid containing about 30 H_2O using P_2O_5. The XRD of $H_3PW_{12}O_{40}\cdot 5H_2O$ powder showed 32 sharp diffraction lines, which were compared with the calculated results and a structural model was proposed.[2] The structure of the 2:18 heteropoly compound $K_6[P_2W_{18}O_{62}]_{14}\cdot H_2O$ was determined by Dawson in 1953.[3] Therefore, the 2:18 heteropoly compounds are the Dawson structure. In 1974, the 1:6 heteropoly compounds conjectured by Anderson in 1937 were finally identified as the Anderson structure[4], such as $[TeMo_6O_{24}]^{6-}$. The above three structures together with Waugh[4,5], Silverton[6] and Lindqvist structures are the six basic structures of heteropoly compounds. Since the 1980s, POM research has become more active than ever, with a great expansion in applied resarch.

In recent years, due to the overlap of various disciplines, new methods have been introduced into POM chemistry. In addition to conventional solution synthesis under conventional conditions, hydrothermal / solvothermal synthesis, high-temperature solid-phase synthesis and other synthesis methods are now used extensively.

1.1.2 Structure and characterization of polyoxometalates

1.1.2.1 Structure of polyoxometalates

Polyoxometalates can be classified into:[7]

(1) A 1:12 series of heteropoly anions with tetrahedral coordination. The structure of this kind of POM is also called Keggin structure (Figure 1.1). Typical representatives are $[PW_{12}O_{40}]^{3-}$, $[PMo_{12}O_{40}]^{3-}$, $[SiW_{12}O_{40}]^{3-}$ and $[SiMo_{12}O_{40}]^{3-}$, etc.

(2) A 2:18 series of heteropoly anions with tetrahedral coordination. This kind of POM is called Dawson structure. The typical representative is $[P_2W_{18}O_{62}]^{6-}$, $[As_2W_{18}O_{62}]^{6-}$ and $[As_2Mo_{18}O_{62}]^{3-}$ ect. The structure of these heteropoly anions is shown in Figure 1.1. It consists of two identical half-cells that are connected by a plane of symmetry perpendicular to the triple axis of rotation. Each half cell is a central XO_4 (X = P, As, etc.) tetrahedron surrounded by nine MO_6 (M = W, Mo, etc.) octahedra, which are connected together by edges. Among them, the half-cells also share a common side with the center XO_4 tetrahedron.

(3) A 1:6 series of heteropoly anions with octahedral coordination. This kind of POM is called Anderson structure, typical representative is $[Te^{VI}Mo_6O_{24}]^{6-}$ and $[X^{III}Mo_6O_{24}]^{9-}$ (X = Al, Ga, Cr, Fe, Co, Rh, etc.). The structure of these heteropoly anions is shown in Figure 1.1. It consists of seven octahedra in a plane, and six MoO_6 octahedra forming a ring around the central TeO_6 octahedron.

(4) A 1:12 series of heteropoly anions with icosahedral coordination. This kind of POM, called Silverton structure, is typically represented by $[X^{n+}Mo_{12}O_{42}]^{(12-n)-}$ (X = Ce^{IV}, Zr^{IV}, Th^{IV}).The heteropoly anion structure is shown in Figure 1.1. It is composed of 12 MoO_6 octahedra, with a central icosahedral Ce with a coordination number of 12. It contains 42 oxygen atoms, which is different from the tetrahedral coordination $[PMo_{12}O_{40}]^{3-}$ and $[PW_{12}O_{40}]^{3-}$, and belongs to the 1: 12B series where the central atom is 12 coordinated.

(5) A 1:9 series of heteropoly anions with octahedral coordination. The structure of the POM is also called Waugh structure, which is represented by

$[X^{n+}Mo_9O_{24}]^{(10-n)-}$ (X = Mn^{IV}, Ni^{IV})and so on. This heteropoly anion structure is shown in Figure 1.1, Mn with octahedral coordination is partially surrounded by MoO_6 octahedra.

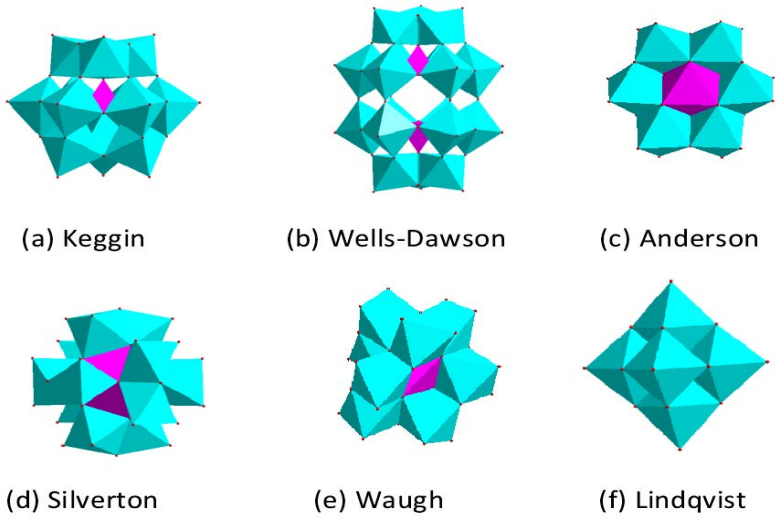

Figure 1.1 (a) Keggin, (b) Dawson, (c) Anderson, (d) Silverton, (e) Waugh and (f) Lindqvist structures of polyoxometalates

In addition to the above five types, there are 1:11 and 2:17 series of heteropoly compounds. Among the above kinds of POM, the most commonly encountered is the 1:12 series with tetrahedral coordination, that is, the POM with Keggin structure.

1.1.2.2 Characterization

The methods to characterize the structure of POM include: vibrational spectroscopy, electron paramagnetic resonance (EPR), nuclear magnetic resonance spectroscopy (NMR), X-ray single crystal and powder diffraction (XRD) and X-ray absorption fine structure (XAFS).

(1) Vibrational spectroscopy includes infrared and Raman spectroscopy. Infrared spectroscopy (IR) is the most commonly used method in heteropoly

anion chemistry. It can be used to identify heteropolyanions, mainly for the determination of solid POM. In POMs with the Keggin structure, the vibrational stretching frequency of each bond is as follows:

$X\text{-}O_a$: W 1079 cm^{-1}, Mo 1064 cm^{-1}

$M{=}O_d$: W 983 cm^{-1}, Mo is 964 cm^{-1}

$M\text{-}O_b\text{-}M$: 890-850 cm^{-1}

$M\text{-}O_c\text{-}M$: 800-760 cm^{-1}

The IR results show that the skeleton vibration characteristics of Keggin structures are almost the same between 600 and 1200 cm^{-1} when the number of crystal water and the counter-cations are different.[8] Therefore, the primary structure of POM is reflected by IR spectra, and it is quite stable.

To confirm the target POM, reference IR spectra are used as controls. IR spectra of the heteropoly anion in the solution and the crystal are similar, and results show that the structure of solute anion is consistent with that observed in crystal. The IR structural determination of POMs is used extensively for the molecular recognition and molecular structure resolution, in catalytic reactions and redox reactions of POM.

Raman spectroscopy can provide useful information for the identification of chemical species in solid samples and aqueous solution. It is an important method for the study of POMs. For example, Mioc et al. have studied the Raman spectra of POM, which are used to recognize H_3O^+, H_2O and the interaction between, $OH\cdots H_2O$, $H_3O^+\cdots H_2O$ and $H_2O\cdots H_2O$.

(2) Electronic spectroscopy (ultraviolet-visible spectroscopy). POMs generally have two absorption bands at 200 and 260 nm, and the absorption bands belongs to the electron transition.

(3) Nuclear magnetic resonance (NMR). NMR can not only provide information about the structure and solution equilibria involving heteropoly anions, but also can be used to identify heteropoly anion.

(4) X-ray powder diffraction (XRD) and X-ray absorption fine structure (XAFS). XRD is an important method to study the structure and properties of solids. Two points should be paid attention to in the application of this method: (a) If the sample is amorphous or vitreous, there is a broad peak, which can not be identified; (b) The same POM with Keggin structure have different positions of diffraction peaks. This is because the XRD characterizes the secondary or tertiary structure of the POM. The diffraction peaks of the POM are different when the counterious or the crystal water are different. The position of the diffraction peak determines the lattice structure of the crystal and the diffraction intensity depends on the position of atoms in the crystal cell. The experimental results show that the secondary or tertiary structures of POM are easy to change.

X-ray absorption fine structure (XAFS) is the general name of XAFS and XANES. It includes atomic valence, electron state, coordination symmetry and local structure information around the atoms absorbing X-rays.

1.1.2.2.1 Acidity and characterization of POMs

POMs exhibit stronger acidity than traditional inorganic oxyacids (sulfuric acid, phosphoric acid, etc.). Acidic POMs are completely dissociated in aqueous solution and gradually dissociated in organic solvents.[9] The order of acidity of conventional POM is: $H_3PW_{12}O_{40}$ > $H_4PW_{11}VO_{40}$ > $H_3PMo_{12}O_{40}$ ~ $H_4SiW_{12}O_{40}$ > $PMo_{11}VO_{40}$ ~ $H_3SiMo_{12}O_{40}$ >> HCl, HNO_3.[10]

As a solid acid catalyst, the most important property of POM lies in their unique acidity. It is a protic acid and its acidity is stronger than that of SiO_2-Al_2O_3.

H_3PO_4/SiO_2, molecular sieve and other solid acids.[11] The acid strength of POM mainly depends on the elements and counter-cations, so the acid catalysts with certain acid strength can be designed and synthesized by changing the composition elements and counter-cations. At present, there are five main methods to adjust the acid strength of POM catalysts: (1) proper selection of anionic; (2) partial neutralization to form acid salts; (3) salt forming with different metal ions; (4) salt formation with different organic bases; (5) dispersion on a support.

The results show that the acidity of heteropolyacid salts may include the following five mechanisms: (1) protons in acid salts; (2) weak acidic protons due to partial hydrolysis of heteropolyanions during preparation; (3) protons produced by acid dissociation of water molecules coordinated with metal ions; (4) Lewis acidity of metal ions; (5) protons produced by hydrogen reduction of metal ions.[7]

Both in solution and solid, POMs have strong Brønsted acidity, and their salts have both Brønsted acid sites and Lewis acid sites. Its acidity is characterized by the type of acid center, the strength of acid center and the concentration of acid center.

Table 1.1 IR bands of pyridine in 1400-1700cm^{-1} region on solid acids

Pyridine hydrogen bonding	Pyridine coordination bond	Pyridine cations
1400-1447(vs)	1447-1460(vs)	1485-1500(vs)
1485-1490(w)	1485-1500(vs)	1540(s)
1580-1600(s)	1488-1503(v)	1620(s)
	1580(v)	1640(s)
	1600-1633(s)	

The adsorption of ammonia and pyridine on the surface of solid acid can distinguish the type of solid surface acid, that is, the type B-acid and L-acid. Basila and Kantne have indicated that ammonia has three adsorption forms on SiO_2-Al_2O_3: the physical adsorption ammonia, the coordination bond and the ionic form NH_4^+, each adsorption state can be detected with a corresponding absorption band.[12] Similarly, the band of coordination bond formed between pyridine and surface is different from that of pyridine ion, as shown in Table 1.1.[13] When adsorbed on a strong B-acid site, it exists in the form of a pyridine cation ($C_5H_5NH^+$), and when adsorbed on the L-acid center, it exists in the form of a coordination compound containing an acceptor bond. In other words, 1540 cm^{-1} is the characteristic absorption band of pyridine adsorbed on the B-acid center, and 1450 cm^{-1} is the characteristic absorption band of pyridine adsorbed on the L-acid center.

For example, Yue et al. used in situ TPD-FTIR technique to characterize the surface acid type of $H_3PMo_{11}VO_{40}\cdot 12H_2O$, $H_3AsMo_{11}VO_{40}\cdot 8H_2O$ catalyst. It was found that only L-acid sites existed on the surface when the purification temperature was below 120 ^oC. When higher than 120 ^oC, B-acid and L-acid exist simultaneously.

The commonly used methods for the determination of acid strength and acid content of POM and their salts are Hammett indicator method, n-butylamine potentiometric titration method and NH_3-TPD method.[14-17]

1.1.2.2.2 Redox characterization

Redox properties of POMs are another important characteristic of POMs for catalysis. The redox ability also depends on the central heteroatom, the addenda atom and the counter-cations. When the skeleton metal atom is fixed, the oxidation ability of the POM increases with the increase of electronegativity

of the central atoms, which is consistent with the experimental results in the order of oxidation: $SMo_{12}O_{40}^{2-}$ > $AsW_{12}VO_{40}^{3-}$ > $PMo_{12}O_{40}^{3-}$ > $GeMo_{12}O_{40}^{4-}$ > $SiMo_{12}O_{40}^{4-}$ > $AlMo_{12}O_{40}$. [5-18] It also accords with the results of quantum chemistry calculation.

The redox properties of POM can be characterized by polarography and voltammetry.[19] This is because its redox potential can well reflect its redox ability. In addition to characterizing its redox properties, the polarographic method has historically been used to distinguish isomers, identify heteropoly anions and study the structural transformation between reductive states.

1.1.3 Polyoxometalate-stabilized with metal nanomaterials

Up to now, there are a variety of methods and stabilizers used to synthesize metal nanoparticles.[20-27] Nanoparticle synthesis using POMs is different from other methods using various reductions and “stabilizers”. The synthetic method is simple, the reaction conditions are mild. Different from other stabilizers, POM, as a stabilizer, can enhance the properties of metal nanoparticles because of its electrocatalysis, photocatalysis, and redox, ect.[28] In particular, the catalytic activity of POM stabilized with gold nanoparticles metal is very significant.[29-32]

POMs can be used as a reducing agent, stabilizer and photocatalyst to synthesize nanoparticles with many advantages, such as: (1) the method of synthesis is simple and has fewer steps; (2) can exist stably in a large pH range; (3) can be used as reducing agent, stabilizer and photocatalyst at the same time[33,34] (4) the nanoparticles can be modified, coordinated and bonded with other functional molecules to obtain new functional materials.

Therefore, using POM to synthesize new functional nanoparticles and study their applications has gradually become of great interest.

1.1.4.1 Synthesis of nanoparticles coated with Keggin type polyoxometalate

As early as 1956, Chalkley had used a photochemical method to prepare elemental silver by using the one-electron reduced Keggin anion $[PW_{12}O_{40}]^{4-}$ as a reducing agent.[35] The principle of the reaction is as follows:

$$PW_{12}O_{40}^{4-} + Ag^{+} \longrightarrow PW_{12}O_{40}^{3-} + Ag^{0}$$

Chemical reduction is the most common method for the synthesis of silver nanoparticles. In general, in chemical reduction, the most common reductants are hydrogen, citrate, ascorbic acid, borohydride, etc.[36-40] The use of POM can be attributed to one method, because POM can be used as photocatalysts, as well as reductants (recent work by Laurent Ruhlmann suggests that POMs serve to generate radicals in solution by photochemical reaction with RCH_2OH and the radicals act as reducing agents for M^{n+}) and stabilizers.[33,41,42]

The reduced POMs have two most basic applications: (1) reducing precious or toxic metal, and degradation of organic pollutants in the system at the same time; (2) can provide a simple and effective method to synthesize metal nanoparticles. Reduced POM is a very effective reductant. It can be easily oxidized by many chemical reagents, including metal ions, such as: Ag^{+}, Cu^{2+}, Pd^{2+}, Au^{3+}, Hg^{2+}, Cr^{6+}, and so on.[42,43]

Troupis et al. proposed that the reduction of metal ions to zero valence single substance requires that organic substrates act as electron donors and POM be used as photocatalysts in photocatalytic cycles, and that the following reactions occur:[43]

$$POM + S \xrightarrow{hv} POM(e^{-}) + S_{ox}$$

$$POM(e^{-}) + M^{n+} \longrightarrow POM(e^{-}) + M^{0}$$

By adjusting the appropriate reaction conditions, in a low ionic strength environment, nanoparticles such as Ag, Au, Pd, Pt with a narrow size range can be obtained by this method. Using the Keggin type heteropoly anions $[SiW_{12}O_{40}]^{5-}$ and $[PW_{12}O_{40}]^{4-}$ as photocatalytic reductants, four noble metal nanoparticles (Ag^0, Au^0, Pd^0, Pt^0) were successfully synthesized by this method.[34, 44]

Compared with other ligands, the size of heteropoly anions is large and the negative charge is high, it can prevent metal nanoparticles from aggregating. For example, $[SiW_{12}O_{40}]^{4-}$ is spherical, with four negative charges and a diameter of about 1.2 nm, and is not protonated even at pH = 1.[34]

The choice of POM with appropriate redox potential can control the size of silver nanoparticles. The more negative the reduction potential of POM, the faster the reduction rate of Ag, for example, $H_2W_{12}O_{40}^{7-}$ > $SiW_{12}O_{40}^{5-}$ >$P_2W_{18}O_{62}^{8-}$ > $P_2W_{18}O_{62}^{7-}$ > $P_2Mo_{18}O_{62}^{10-}$ > $P_2Mo_{18}O_{62}^{8-}$.[41] In addition, increasing the concentration of POM reductants will lead to the gradual formation of small nanoparticles, and the concentration of silver ions will also affect the size of the particles, and the increase in the amount of silver ions will lead to a larger size of the silver ion.[45]

Gordeev presented the ability of POMs to act as catalytic reducing reagents and stabilizers upon radiolysis of aqueous solutions of metal ions for the formation of Ag, Cu, Cd, Ti, Pd, Co, and Ni nanoparticles.

Gordeev et al indicated that radiolysis reduced $[PW_{12}O_{40}]^{3-}$ to $[PW_{12}O_{40}]^{4-}$ and then transfer electrons to Ag^+ to form a stable Ag^0 nanoparticles.[42] Inspired by this, Papaconstantinou et al found that in the deoxygenated POM/S/M^{n+} (POM: PW_{12} or SiW_{12}, S: isopropanol or 2,4-dichlorophenol, M^{n+}: Ag^+, Pd^{2+}, Cu^{2+}) solution, metal precipitates or nanosol were prepared by adjusting the ionic strength of the solution, and POM were excited by ultraviolet light. Heteropoly blue is obtained from isopropanol (as an electron donor), and then the electron

is transferred from heteropoly blue to Ag^{+} to form Ag^{0}, thus forming a photocatalytic process. In the process, the POM acts as photocatalyst, reductant and stabilizer.

Shanmugam et al described a one-step chemical method in which gold and silver particles were implanted into the complex.[43] They proved that $[SiW_{12}O_{40}]^{5-}$ are helpful in promoting the reduction of metal nanoparticles on the composite film. The average size of silver particles was 16 nm, which can be controlled by controlling the immersion time and the concentration of metal ion solution. The size distribution of silver particles can be changed by changing the concentration of $[SiW_{12}O_{40}]^{5-}$ in the composite film.[46,47] The preparation method is shown in Figure 1.2. First, the composite membrane is synthesized by sol-gel method and spin-coated on the glass; then the composite film is immersed in $AgNO_3$ solution and irradiated in sunlight, and the blue composite film gradually turns yellow within a few minutes due to the formation of silver particles on the composite film.

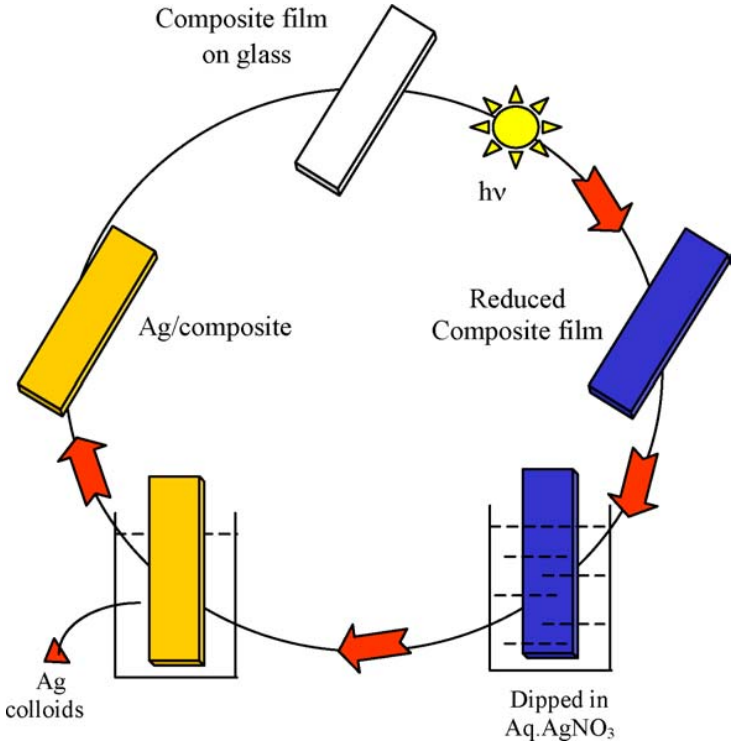

Figure 1.2 Preparation of Ag NPs embedded composite film

In 2003, Mandal et al reported that gold nanoparticles stabilized by photochemically active $[PW_{12}O_{40}]^{4-}$ can reduce Ag ions at their surface to give Au-Ag core-shell bimetallic nanoparticles under UV irradiation.[48] This method is unique in that the reaction takes only a few seconds at room temperature and the reduction of POM is mild (Figure 1.3).

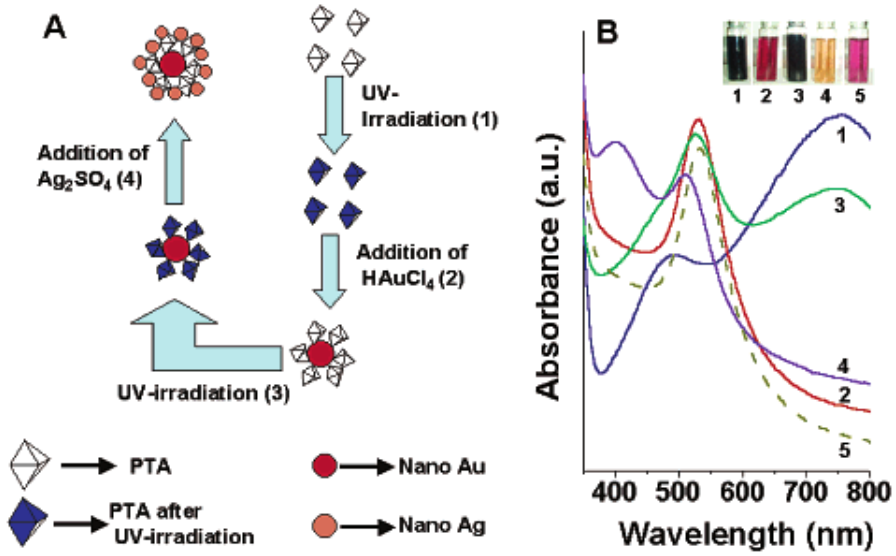

Figure 1.3 (A) Scheme of synthesis of Au core Ag shell NPs by the Keggin ion-mediated. (B) UV-vis spectra of (1) PTA solution after UV irradiation; (2) addition of $HAuCl_4$ solution to PTA solution and then UV irradiation; (3) solution 2 after further UV irradiation; (4) addition of Ag_2SO_4 solution to solution 3; and (5) addition of Ag_2SO_4 solution to solution 2.

In 2008, Nadjo et al used $K_9[H_4PV^{IV}W_{17}O_{62}]$ (HPV^{IV}) as a reducing agent and stabilizer to reduce the Pd^{2+} in acid solution to obtain about HPV-capped palladium nanoparticles nanoparticles (6 nm).[49] Moreover, HPV-capped the small size palladium nanoparticles can further self-assemble into a stable supramolecular hollow structure (blackberry structure) with a diameter of 60~100 nm (Figure 1.4). The blackberry structure nanoparticles have a much better hydrogen storage capacity than ordinary isolated palladium nanoparticles.

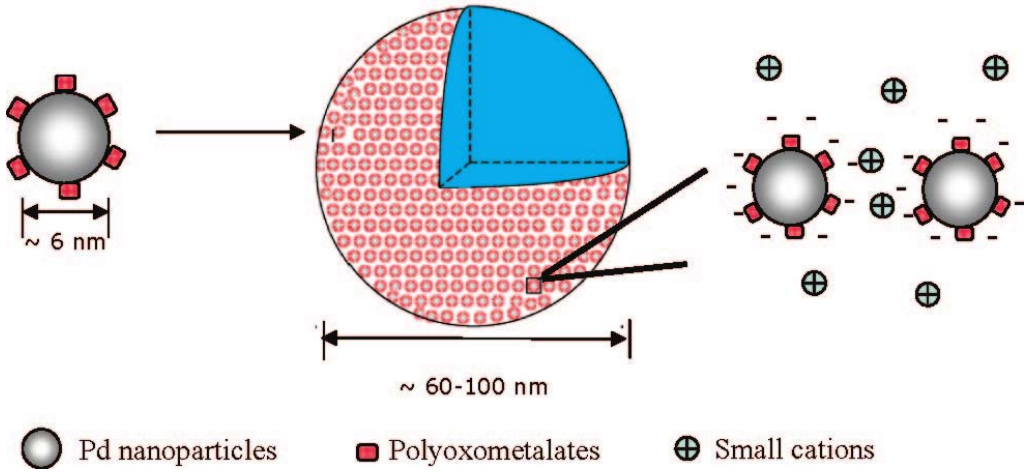

Figure 1.4 The 3 nm radius Pd NPs with a layer of HPV on the surface self-organize into aggregates.

1.1.4 Application of Keggin type polyoxometalate

POMs are a widely used species, which can play a powerful role in the selective oxidation of organic molecules as well as in treating various viruses. As an important branch of metal-oxo cluster, POM has become the new functional materials, the research of POM compounds has been involved in almost all fields, including the field of functional materials, catalysis and biomedicine.[50-66] The application of POM has the advantages: (1) In solvents, the structure of the basic POM skeleton remains the same as that of the original solid state. (2) There are many kinds of POM, and POM of different charges, sizes and shapes provide a solid basis for molecular design and assembly, making it possible to synthesize target molecular aggregates and target functional materials as electron receptors. (3) POM can be used as an electron acceptor, reduced to mixed valence heteropoly blue and combined with the organic π electron donor to form an inorganic-organic hybrid cluster.

The early study of POM was devoted mainly to the synthesis and characterization of new POM species. Until the 1960s, people gradually became interested in the properties and applications of POM, thus began a new

era. Since then, POMs have been widely used in various fields because of their excellent properties, especially the multifunctional, modifiable and adjustable Keggin heteropoly anions. The skeleton of this kind of heteropolyanion is composed of M^{VI} atoms with d^0, which are coordinated to oxygen (O^{2-}) ligand atoms. Therefore, this kind of POM may behave as an oxidizing agent and can be used in various homogeneous and heterogeneous catalytic systems.[59]

1.1.4.1 Catalysis with Keggin type heteropolytungstate

Hill and Khenkin were the first to use Keggin type heteropolytungstate as a catalyst.[67] They found that tetra-substituted Keggin type POM $[Fe^{II}_4(H_2O)_2(PW_9O_{34})_2]^{10-}$ had high selectivity to epoxidation of alkene, which was not found in other iron-containing POM. In the same reaction system, three different $[Fe^{II}PW_{11}O_{39}]$, $[(Fe^{III})(SiW_9O_{37})]^{7-}$ and $[Fe^{II}_4(H_2O)_2(PW_9O_{34})_2]^{10-}$ were used as catalysts, respectively. Their selectivity for the epoxidation of hexene is 79% and 90%, respectively. Therefore, the POM with a multi-iron sandwich have stronger catalytic selectivity to the reaction. Subsequently, Neumann and Gara used $[WZnMn_2^{II}(ZnW_9O_{34})_2]^{12-}$ as catalysts for epoxidation of olefins by H_2O_2 oxidation. It shows that the high charge of POM is also helpful for catalysis. Therefore, the highly charged Keggin type sandwich structure POM has become a hot topic in the field of catalysis, and this class of POM is considered to be the most promising catalyst. They exhibit many advantages over other compounds in the catalytic process, for example, (1) their pH stability ranges from 6 to 10; (2) the substitution points in sandwich structure can be replaced by many other transition metals, such as Mn^{2+}, Mn^{3+}, Fe^{2+}, Fe^{3+}, Co^{2+}, Ni^{2+}, Cu^{2+}, Zn^{2+}, Pd^{2+} and Pt^{2+}, which provides an opportunity for the design of new, better and more efficient catalysts; (3), their elemental composition can be modified, solubility can be adjusted, redox reversible, size, charge density, morphology and so on are all adjustable, and thus can meet the requirements

of various reactions on these aspects of the catalyst properties; (4) their selectivity, reaction rate and catalytic activity in redox of organics are very high, and can be recycled for hundreds or even thousands of times.

Hybrid catalytic materials prepared by ionic liquids and POM are important for the development of POM catalysts. Wang et al. used imidazole, pyridine and quaternary ammonium salts modified with propane sulfonic acid as cations of ionic liquids to form a new solid organic heteropoly salt with Keggin POM anion (Figure 1.5), which exhibited high activity for various esterification reactions. The catalyst was solid and insoluble in water at room temperature, and when the reaction temperature was raised to 110 ^{o}C, the catalyst is soluble in polycarboxylic acid or polyol as reactants. After the reaction temperature decreases and the catalyst changes to a solid precipitation which is easy to separate and reused.

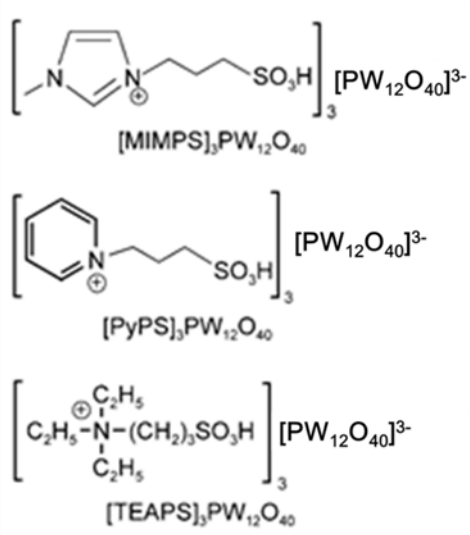

Figure 1.5 POM modified ionic liquids catalyst

Yan et al. synthesized a series of heteropolyacid salt/ionic liquid catalysts by reaction of POM with ionic liquids, which were used in transesterification of trimethylolpropane to synthesize self-degradabl] lubricating oils.[68]

$[PyBS]_3[PW_{12}O_{40}]$showed the best activity, and had the characteristics of easy separation and high yield compared with the traditional catalyst.

1.1.4.2 Electrocatalytic performance

(1) Homogeneous electrocatalytic reduction: after the reduction of many POMs on an electrode, a series of reduced polyanions called "heteropoly blue" are formed. These heteropoly blue anions often have electrocatalytic activity and can be used for catalytic reduction in some reactions. For example, α-$[SiW_{12}O_{40}^{4-}]$ in acidic aqueous solution is easily reduced to [*α*-$SiW_{12}O_{40}^{5-}$] and [α-$H_2SiW_{12}O_{40}^{6-}$] on the cathode. Both of them exhibit high electrocatalytic activity for nitrite ion reduction and hydrogen evolution.[69]

(2) Homogeneous electrocatalytic oxidation: because the central atom and the coordination atom in the heteropoly anions are in the highest valence state, it is difficult to reoxidize on the anode. Therefore, it is necessary to replace one or more coordination atoms with some transition metal ions or lanthanide ions with a variable valence before they can be used as electrocatalytic oxidants. For example, ruthenium substituted $[PW_{11}O_{39}Ru^{III}(H_2O)]^{4-}$ easily loses two electrons on the anode, oxidizes to $[PW_{11}O_{39}Ru^{V}O]^{4-}$ and then catalyzes the oxidation of organic compounds such as dimethyl sulfoxide, alcohols, etc.[70,71]

(3) Heterogeneous electrocatalysis: in addition to homogeneous electrocatalysis, heteropolyanions can also be used to modify electrode surfaces, e.g. in conducting polymers for heterogeneous electrocatalysis. For example, $[SiW_{12}O_{40}^{4-}]$, $[PMo_{12}O_{40}^{3-}]$ and $[P_2W_{18}O_{62}^{6-}]$ can be incorporated into an electrode of poly (4-vinylpyridine-12-dibromodecane). These modified electrodes maintain the electrocatalytic properties of heteropoly anions in solution, and some of them have a better catalytic effect.[72-74]

The electrochemistry and electrocatalysis of substituted POMs are less studied. Studies by Toth and Anson, focused on the electrochemistry of Fe substituted

Keggin POM and their electrocatalytic reduction of H_2O_2, NO_2^- and NO^-. In the process of catalytic reduction, Fe is not only the catalytically active site but also the inner electron transfer channel between the catalyst and the substrate.[75]

1.1.4.3 Photocatalytic application

The photochemical reduction of α-Keggin structure $H_3PW_{12}O_{40}$ to heteropoly blue was noticed 80 years ago, and this phenomenon has been applied to the colorimetric test for elements, such as P, Si, As, Ge and the identification of uric acid, sugar and other biological compounds. In 1978, Isobe M of Tokyo University of Technology, Japan, noticed the photochromic effect of ammonium molybdate salt, and has done a lot of work in this field.[76] The study of POM photochemistry has been paid more and more attention. Hill and Foxon in the USA and Papaconstantinon in Greece have done a great deal of pioneering work on the photochemical principle, photocatalytic reaction and photochemical synthesis with POMs, which has laid a foundation for the further development of POM photochemistry.[33,63,77-72]

Since 1980, researchers have begun to study the photocatalytic properties of POM. Since the special structures of POM and their salts are similar to semiconductor metal (oxide atoms with 2*p* electron configurations and transition metal atoms with d^0 electron configurations). Therefore, polyoxometalates can be used for photocatalytic experiments. The reaction mechanism of POM (HPA) photocatalysis can be summarized as follows: the electrons in the oxygen atom 2*p* orbit are excited into the transition metal empty 5*d* orbit. This is an O-M charge transfer transition, i.e. OMCT. Based on the analysis of the molecular orbital theory, it can be seen that when the HPA molecule is illuminated, the energy absorbed by HPA is excited from the highest occupied orbit (HOMO orbital) to the lowest unoccupied molecular orbital

(LUMO orbital), an excited HPA* is formed, which has a strong oxidation capacity. This gives them the ability to oxidize other substances while being themselves reduced to heteropoly blue.

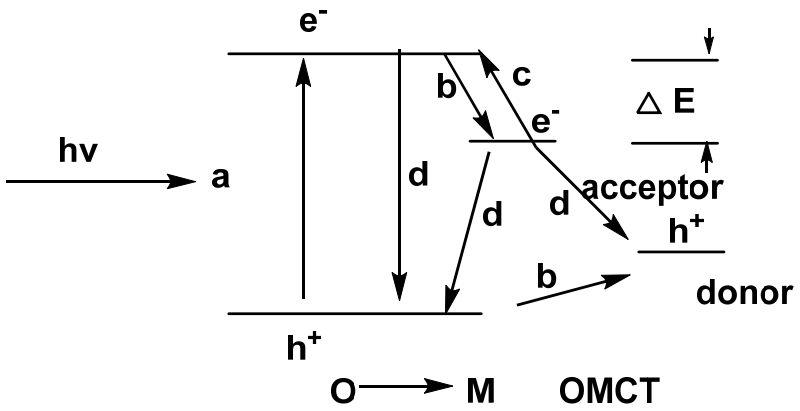

Figure 1.6 POM electron transfer model

Fig. 1.6 can be explained as follows: (a) electron transition produces "electron hole"; (b) hole and electron are captured by electron donor and acceptor respectively, oxidant is reduced and reductant is oxidized; (c) HPA was reduced to get HPA^-, then HPA^- was oxidized again and released electrons; (d) electron hole recombination, which has no effect on photocatalytic reaction, should be avoided as far as possible.

The mechanism of photocatalytic degradation of organic compounds by POM presented by Papaconstantinou et al can be explained by the following method:[33,80,83]

HPA + hv → HPA* (photoactive)

HPA* + S → HPA(e^-) + S(+) (redox reaction)

HPA* + H_2O → HPA(e^-) +··OH + H (·OH radical formation)

HPA(e^-) + H^+ + O_2 → HPA + H_2O (regeneration of catalyst)

The difference of LUMO and HOMO energy of POM is equivalent to that between the conduction band and valence band of TiO_2. The excited states

formed by photoexcitation have similar redox properties. For example, the redox potential of excited Keggin type POM is 2.63 eV, while that of excited state of TiO_2 is 2.53 eV. Both of them have strong oxidation ability. Therefore, many organic reactions have thermodynamically difficult which only be carried out under harsh conditions can be successfully completed under mild experimental conditions through the photocatalytic action of POMs or TiO_2.

At present, there are many reports on the application of POM photocatalytic properties in organic chemical reactions, typical of which are (1) photocatalytic dehydrogenation of alkanes, alcohols, amines and oxygenated acids. Dehydrogenation of alkanes is an important reaction in the petroleum industry. (2) the activation of unsaturated hydrocarbon bonds remote from functional groups (carbonyl) in naphthenic ketones.[84] (3) the functionalization of alkanes; If POM as a highly selective photoinitiator, the functionalization of alkanes can be successfully completed at room temperature and atmospheric pressure, and the resulting products are of practical value. (4) degradation and mineralization of organic pollutants; Such reactions are of particular importance in the field of environmental catalysis.

At present, POM photocatalytic degradation of organic pollutants such as organic sulphide, halogenated hydrocarbon, halogenated aromatics and halogenphenol in homogeneous system is mainly reported, and their mineralization into CO_2 and simple inorganic compounds. Photoactivated POM has a catalytic activity similar to that of TiO_2 for these organic pollutants which are difficult to degrade by other methods. In addition, Papaconstantinon et al studied the photocatalytic properties and mechanism of Keggin species H_3PW_{12}, H_4SiW_{12} and other compounds, and studied the degradation of organic pollutants in homogeneous system and the application of POM was extended

to the recovery of heavy metal ions and the synthesis of nanoparticles.[42,63,78,83,85-89]

1.1.4.4 Pharmaceutical chemistry

The application of POMs in pharmacology began in 1971. The first discovered POMs with in vivo and in vitro antiviral activity were Keggin type $[SiW_2O_{40}]^{4-}$ and $[BW_{12}O_{40}]^{5-}$. In the mid-1980s, heteropoly antimonates $(NH_4)_{17}Na[NaSb_9W_{21}O_{86}]$ (HPA-23) were found to inhibit HIV reverse transcriptase and were used as anti-AIDS drugs. Then it was found that the Keggin type POM $[(VO)_3(SbW_9O_{33})_2]^{12-}$ had a strong inhibitory effect on HIV-1.[90,91] In addition, many other Keggin polyoxometalates exhibited anticancer, antiviral and antitumor activities.[92] Up to now, there have been hundreds of kinds of POMs with various anticancer, antiviral and anti-tumor activities, which have the characteristics of low toxicity, high stability and high activity in pharmacology. It has aroused great interest from researchers of various disciplines, including chemistry, biology and medicine. Since then, POM drug chemistry has developed rapidly.

1.2 Polymer immobilised ionic liquid phases (PIILPs)

1.2.1 Ionic liquids (ILs)

Since the discovery of the first room temperature ionic liquids in 1951, with the further understanding of the physical and chemical properties of ionic liquids, the kinds and applications of ionic liquids have been continuously developed.[93] In recent years, ionic liquids, as green solvents and catalysts, have been widely used in biomass research.

1.2.1.1 Concept and classification of ionic liquids

(1) Ionic liquids are only composed of ions and are liquid at low temperature (usually less than 100 °C). Conventional molten salts consisting of smaller ions have a higher melting point. For example, the melting point of NaCl is about 800 °C. If a salt has one or two large volume ions, the diffusion and charge distribution are asymmetric, and the interaction between ions weakens, leading to a significant decrease in melting point, even a liquid at room temperature.[94] Ionic liquids are generally composed of organic cations and inorganic anions, and are divided into imidazoles, pyridines and pyrrolidines according to cations (Figure 1.7), while the anions are mainly Cl^-, Br^-, I^-, BF_4^-, CH_3COO^-, NO_3^-, HSO_4^-, and so on. According to the solubility of ionic liquids in water, they can be divided into hydrophilic ionic liquids and hydrophobic ionic liquids. For example, most of the ionic liquids such as BmimCl, BmimAc and $BmimBF_4$ are hydrophilic, while $BmimPF_6$ and $BPyPF_6$ are hydrophobic ionic liquids. In addition, according to the acidity and basicity of ionic liquids, they can also be divided into acidic ionic liquids, basic ionic liquids and neutral ionic liquids. The acidic ionic liquids include Lewis acidic ionic liquids and Brønsted acidic ionic liquids.

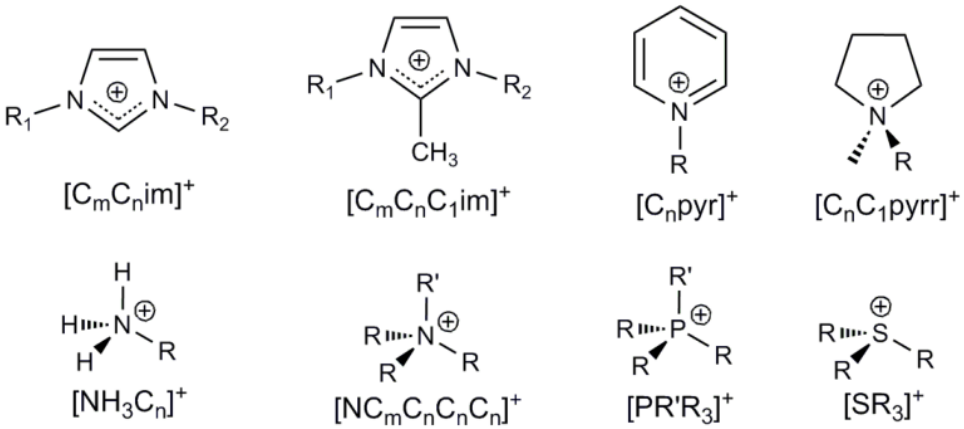

Figure 1.7 A series of cations for ionic liquids (ILs)

Due to the strong tuneability electronic and structures of ionic liquids, different structures of ionic liquids can be obtained by changing different combinations of anions and cations. The synthetic methods of ionic liquids include direct synthesis and two-step synthesis. The main results are as follows:

(a) Direct synthesis. Bonhôte and Souza et al synthesized ionic liquids by one-step reaction of alkyl imidazole with trifluoromethane sulfonate and ethyl trifluoroacetate with high yield. However, the raw materials used are expensive.[95,96] (b) Two-step synthesis method. Firstly, alkylation of chlorinated alkanes with alkyl imidazole was carried out to obtain the target cation halide. As the reaction is a nucleophilic substitution reaction, it is a highly exothermic process. Therefore, in order to avoid impurities in the synthesis process, it is necessary to carry out the reaction in dry and inert atmosphere and at a lower temperature. [97,98] After purification by extraction, drying and recrystallization, halogen ions were replaced with metal salts, ammonium salts or conjugated acids containing target anions, and then purified. For example, hydrophilic ionic liquids usually use water as the reaction medium. After the reaction, the ionic liquids are extracted by dichloromethane, the solvent is removed, and the target ionic liquids are obtained after vacuum drying (Figure 1.8).

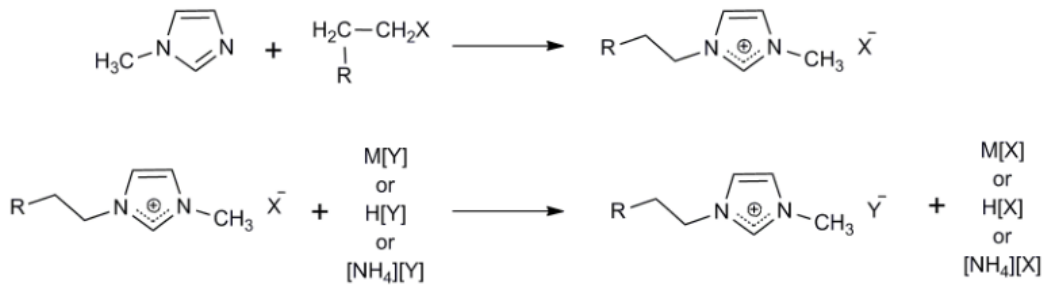

Figure 1.8 Two-step synthesis method for ionic liquid

Compared with conventional molten salts and conventional organic solvents, ionic liquids have the following characteristics: (1) wide liquid range; (2) low

saturated vapor pressure; (3) the designable structures; (4) high solubility; (5) chemical and thermal stability.[99] (2) Task specific ionic liquids are a kind of ionic liquid which is synthesized for special application and feature one or more functional groups in the anion or cations.[100] At present, more studies have been done on the introduction of functional groups, such as –OH, -SH, -NH_2, -SO_3H, including acid-base ionic liquids, chiral ionic liquids, POM ionic liquids, chelate ionic liquids, and so on, on the side chains of cations, which have been widely used in hydroformylation, asymmetric hydrogenation, carbon-carbon coupling, oxidation and other catalysis, organic synthesis solvents, extractants and so on, with enhanced reaction selectivity, conversion, stability and easy recovery.[101]

1.2.2 Polymer immobilised ionic liquid phases (PIILPs)

Polymer immobilised ionic liquid phases (PIILPs) refers to a class of ionic liquid polymers which are formed by ionic liquid monomer polymerization and have anion and cationic groups on the repeating unit, and have the excellent properties of both ionic liquids and polymers.[102] According to the chemical structure, PIILPs can be divided into the following categories (Figure 1.9): (1) polycationic ionic liquids, which are linked to the main chain of polymers by covalent bonds; (2) polyanionic ionic liquids, which are covalently bonded with each other. (3) Amphoteric polyionic liquids, cations and anions are connected to the polymer main chains by covalent bonds.[103] Because PIILPs have the combined advantages of ionic liquids and polymers, and overcome the fluidity of ionic liquids, PIILPs have attracted much interest in the field of polymer science in recent years.[104-107]

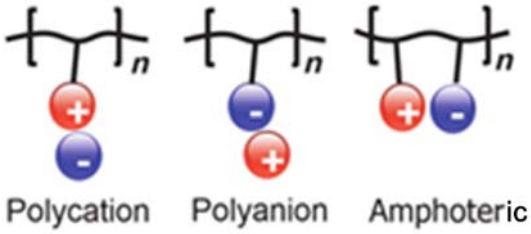

Figure 1.9 General structures of PIILPs

1.2.2 Synthesis of PIILPs

The synthesis of PIILPs can be achieved by free radical polymerization of ionic liquid monomers. Similar to the properties of ionic liquids, many kinds of PIILPs with different structures and functions can be synthesized by designing and combining the anions or cations of PIILPs. At present, the preparation of PIILPs by cationic monomer polymerization of imidazolium salt has been studied. It can be functionalized by anion exchange before polymerization (monomer) or after polymerization (polymer) (Figure 1.10). For example, Mecerreyes et al prepared and polymerized 1-vinyl-3-butylimidazole chloride and bromide, and regulated the hydrophobicity of the polymer by plasma exchange with PF_6^-, BF_4^-, $(CF_3SO_2)_2N^-$, $CF_3SO_3^-$. Polyionic liquid gel was prepared by microemulsion polymerization by Texter et al, solvent-responsive porous polymer materials (gels) were prepared by anion exchange.[105]

In recent years, controlled-active atom transfer radical polymerization (ATRP) and reversible addition-fragmentation chain transfer (RAFT) polymerization, ring-opening metathesis polymerization (ROMP), *in-situ* polymerization, cyclopolymerization, dehydrogenative coupling polymerization, etc. Modern polymerization methods have also been initially introduced for the synthesis of PIILPs.[102,105,108,109]

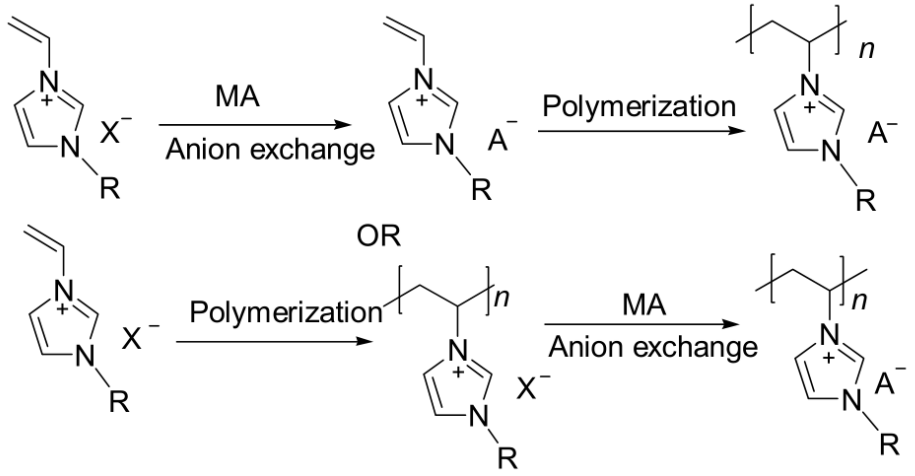

Figure 1.10 General synthetic routes of PIILPs

1.2.3 Ionic liquid-based organic-inorganic POM catalysts

Organic-inorganic hybrid materials have the characteristics of both organic and inorganic materials. POMs have good thermal stability, and the addenda atoms generally exist in the highest oxidation state. They are a kind of bifunctional catalysts with both oxidation and acidity, and because of the high designability of ionic liquids, many researchers first combine the functionalized ionic liquids suitable for a particular reaction system with the corresponding POM to prepare solid catalysts, which have a good application in many organic reactions such as oxidation reaction, esterification and redox reaction.

Kakati et al. modified the anions and synthesized a catalyst $[(C_6H_5CH_2)(CH_3)_3N]_3[H_3V_{10}O_{28}]_3 \cdot H_2O$ with vanadium as the active center.[110] It was used in the selective oxidation of benzyl alcohol to benzophenone, and the conversion reached 98% in one minute at room temperature. Sun et al synthesized a tungsten ionic liquid $[(CH_3)N(n\text{-}C_8H_{17})_3]_2[W_2O_{11}]$. The catalyst was used to catalyze cyclohexanol to cyclohexanone without solvent, no byproducts were generated. The best oxidation effect was obtained under the conditions: oxygen source hydrogen peroxide 15 mmol, reaction temperature

65 °C, cyclohexanol 5 mmol, catalyst amount 50 mmol refluxing for 8 h. The yield of cyclohexanone was over 99%. The catalyst can be recycled for 4 times after simple recovery.

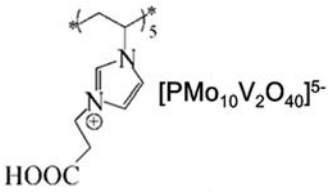

Figure 1.11 Polymeric acid ionic liquid-POM catalyst

Leng et al exchanged carboxylic acid functionalized ionic liquids with Keggin type V-containing POM to obtain an ionic liquid-POM catalyst (Figure 1.11), which was used in the hydroxylation of benzene.[111] The catalytic performance of H_2O_2 as oxidant and acetonitrile as solvent was investigated. The results showed that the polymer had high heterogeneous catalytic performance, the yield of phenol reached 26.9%, selectivity reached 100%, and the yield of phenol was still 17.8% after 4 cycles. A novel organometallic polyoxometalate hybrid (Figure 1.12) was prepared to catalyze the hydroxylation of benzene with ionic liquid supported Schiff base as cationic ion and phosphorus molybdenum vanadate ion as anions.[112] A compound with two V catalytic centers was formed. The catalyst showed excellent catalytic activity in the heterogeneous reaction of benzene hydroxylation, with a yield of 19.6% and selectivity of 100%. The catalyst was reused by simple filtration and recovery, and the structure of the catalyst remained unchanged after being used 4 times. In the same year, they also loaded the polymeric ionic liquid-POM catalyst into magnetic material and synthesized a kind of ionic polymer magnetic composite catalyst Fe_3O_4@PIL-PMoV based on POM, which realized the efficient and rapid recovery of the catalyst.

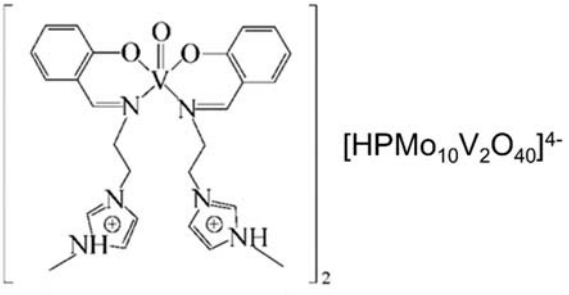

Figure 1.12 Schiff base -POM catalyst supported by ionic liquid

Concentrated sulfuric acid is commonly used as catalyst for esterification reaction in industry. The concentrated sulfuric acid is cheap, has good catalytic activity and absorbency, and can effectively promote the reaction to the direction of ester formation, thus increasing the conversion rate of the reaction. Therefore, it is the most widely used. But the concentrated sulfuric acid corrodes the equipment very seriously, accompanied by the serious environmental pollution, and the product selectivity is low. Therefore using a hybrid catalyst instead of concentrated sulfuric acid not only overcomes the above disadvantages but also improves the recovery efficiency of catalyst. Leng et al. designed and synthesized a POM sulfonic acid functionalized ionic liquid catalyst (the synthesis route is shown in Figure 1.13), and used it to catalyze a variety of esterification reactions without a solvent.[113] The results showed that the catalyst had a high catalytic effect and selectivity, and the catalyst was easy to be recovered and reused.

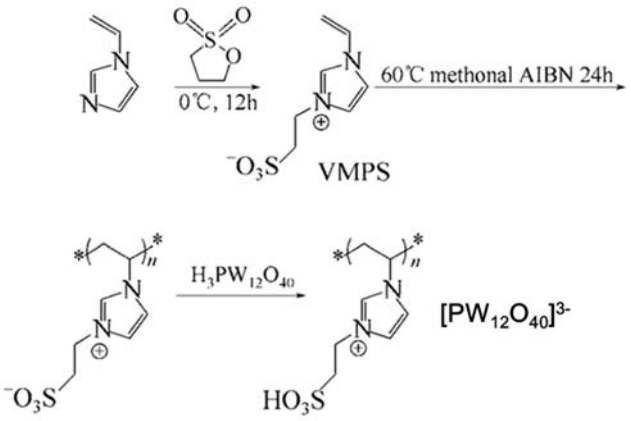

Figure 1.13 Synthesis of POM sulfonic acid functionalized polymerized ionic liquids

Epoxides are very important organic raw materials and chemical intermediates, which are widely used in fine chemical, petrochemical and organic synthesis. At present, the traditional methods of epoxidation are mainly chlorohydrination method and common oxidation method. The chlorohydrin process can be divided into three processes: chloroalcoholization, saponification and purification. The common oxidation method is a method of catalyzing carbon-carbon unsaturated double bond epoxidation with organic peroxide under the condition of peroxycarboxylic acid. Epoxides were prepared using proton acid (sulfuric acid or phosphoric acid) as catalyst. These two methods have many disadvantages, such as high production cost, serious environmental pollution, complex technology and many by-products. With the development of research, more and more green and environmental protection catalysts have been developed. At present, many kinds of highly efficient epoxidation catalysts, such as metal compounds, molecular sieves, hydrotalcite, POM and ionic liquids, have been studied. However, organic and inorganic hybrid materials based on ionic liquids have been widely studied in catalytic epoxidation because of their advantages of being green, clean and effective, and recyclable.[114, 115]

Raisa et al. have prepared three kinds of phosphotungstic acid with tetrabutylammonium salts and 1-ethyl-3-methyl imidazole salts: $[(n\text{-}C_4H_9)_4N]_3\{PO_4[WO(O_2)_2]_4\}$, $[(n\text{-}C_4H_9)_4N]_5Na_{0.6}H_{1.4}[PW_{11}O_{39}]$ and $[(C_2H_5)(CH_3)C_3H_3N_2]_5NaH[PW_{11}O_{39}]$.[116,117] Using 34% hydrogen peroxide as oxidant and acetonitrile as solvent, the epoxidation of butadiene was carried out. It was found that the conversion rate of 1,3-butadiene to 3,4-epoxy-1-butene could reach 97%, and the utilization ratio of hydrogen peroxide almost reached 100%. $[(C_2H_5)(CH_3)C_3H_3N_2]_5NaH[PW_{11}O_{39}]$ showed the best catalytic activity.

Wang et al synthesized a mesoporous dihydroxyl functionalized POM ionic liquid catalyst (Figure 1.14) and catalyzed cyclooctene epoxidation with H_2O_2 as an oxygen source in a heterogeneous system.[118] The results show that the catalytic effect of the catalyst is 4 times that of the homogeneous catalyst and 14 times that of the non-porous catalyst.

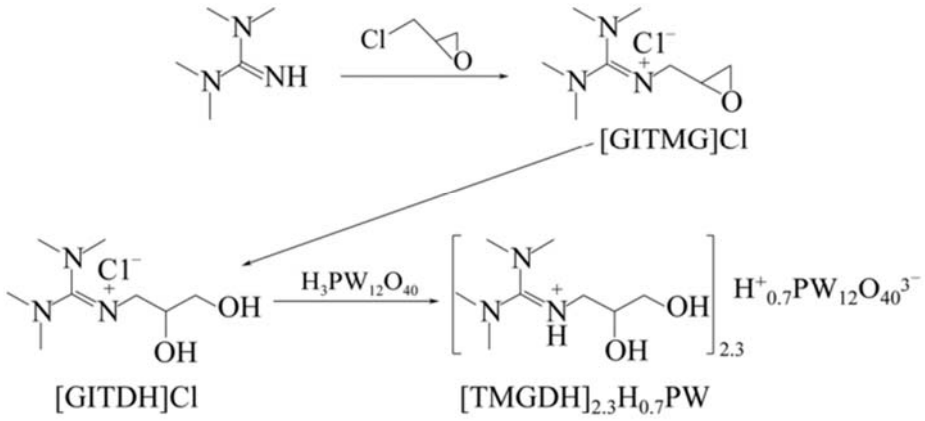

Figure 1.14 Synthesis of dihydroxy-functionalized POM ionic liquids

A kind of binuclear long-chain alkylimidazole cationic Venturello complex catalyst $[D_nmim]_{1.5}PW_4O_{24}$ (Figure 1.15) was synthesized by Wu et al.[119] The catalytic activity of the catalyst in the epoxidation of olefins with hydrogen peroxide as an oxygen source was investigated. The results show that this kind

of catalyst exhibits phase transfer catalysis and has a high catalytic activity and selectivity. The conversion of cyclohexene and selectivity of cyclohexane over binuclear dodecyl imidazole POM catalyst reached 97.7% and 96.3% respectively. The cyclohexene conversion and the selectivity of cyclohexane can still reach 72.4% and 96.3% after repeated use for 4 times. At the same time, they used this kind of catalyst to catalyze the epoxidation of soybean oil. The influence of the length of organic cationic carbon chain on the epoxidation reaction, the reuse of catalyst and the reaction conditions were investigated under the condition of no solvent and hydrogen peroxide as the oxygen source. The results show that this kind of catalyst had good catalytic activity and reusability.

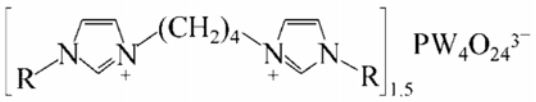

Figure 1.15 Dinuclear imidazole peroxophosphate tungstate catalyst

In general, ionic liquids as solvents and catalysts take part in chemical reactions, most of which are homogeneous processes. The homogeneous reaction can increase the contact between reactants and obtain a good catalytic effect. Based on the flexible and adjustable denaturation of ionic liquids, they can be made into amphiphilic heterogeneous catalysts by changing the hydrophilic and oil-lipophilic properties of anions and cations. High efficiency of phase transfer catalysis is realized. On this basis, it can also be made into polymers or various porous materials to increase the contact surface between the active center and the reactant and to improve the catalytic activity. Therefore, ionic liquids have a wider application prospect in heterogeneous catalysis.

1.3 Graphitic carbon nitride

The new carbon-nitrogen materials formed by the combination of the two elements have attracted much attention after their discovery, and in recent years, it has been found that the materials have various new functions and have been paid more attention by many researchers in recent years. It is worth mentioning that the functional properties of new carbon-nitrogen materials as catalysts and catalyst carriers in recent years have attracted wide attention, and it is a potential material for the development of new technologies for sustainable development.

1.3.1 Structure of graphitic carbon nitride

In the 1980s, A.Y. Liu and M. L. Cohen of the University of Berkeley in the United States replaced the Si atoms in β-Si_3N_4 with C atoms based on the first pseudopotential energy band theory under the condition of local density of state approximation.[120] The existence of β-C_3N_4, which does not exist in nature, is predicted. Shortly afterwards, Teter and Hemley of the Carnegie Institute in Washington calculated five possible phases of C_3N_4, namely α phase (α-C_3N_4), β phase (β-C_3N_4), cubic phase (c-C_3N_4), pseudocubicy phase (p-C_3N_4) and graphite phase (g-C_3N_4). Because of their most stable chemical properties, moderate band gap, environmentally sound and low cost of raw materials, C_3N_4 have been favored by researchers for a long time.[121] In 2009, Wang's research group prepared mesoporous g-C_3N_4.[122] It was found that mesoporous g-C_3N_4 has good catalytic properties for photodegradation of water to produce hydrogen under visible light, which initiated a wave of research on g-C_3N_4, which makes g-C_3N_4 come to prominence in the field of photocatalysis in the future. It is called graphitic carbon nitride, because g-C_3N_4 has a lot of

similarities to graphite, especially in the microstructure of g-C_3N_4, which has a layered structure similar to graphite, and it is made up of a single layer of g-C_3N_4. Therefore, the force between layers is van der Waals force, and the distance between layers is about 0.326 nm, which is slightly smaller than that of graphite.

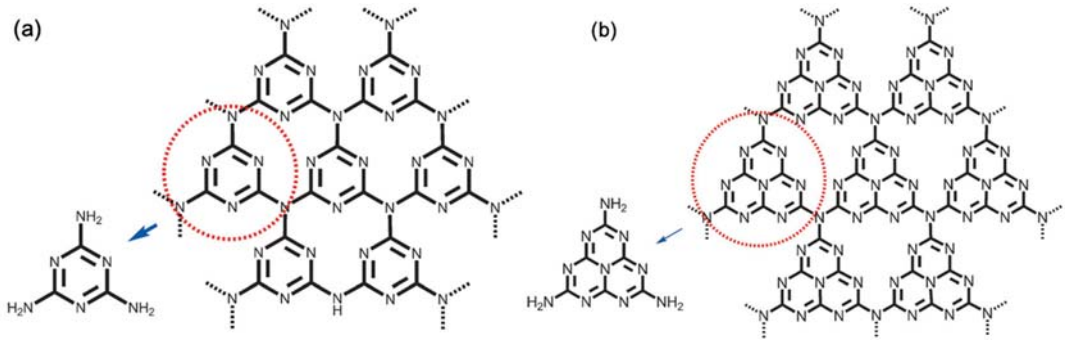

Figure 1.16 The g-C_3N_4 consisting of (a) 1,3-*s*-triazines (C_3N_3) and (b) *tris*-*s*-triazines (C_6N_7)

As shown in Figure 1.16, there may be two structural formulae for graphitic carbon nitride: the net structure formed by the outer end N atoms of the basic structural units of the 1,3-*s*-triazines (C_3N_3) and *tri*s-*s*-triazines (C_6N_7), which belong to the space groups of *R3m* and *P6m2*, respectively.[123] The elements of C and N are connected by *δ* bond between C and N in sp^2 hybrid mode, in which the solitary pair electrons in the P_z orbital are coupled to form a conjugated electron delocalization system similar to aromatic benzene ring.

1.3.2 Preparation of g-C_3N_4

1.3.2.1 Solid state reaction method

The solid state reaction method usually uses the compound containing 1,3-*s*-triazines structure as precursor to prepare g-C_3N_4, such as melamine and cyanuric chloride. This is because the triazine structure can reduce the reaction energy barrier of nitrogen and carbon bonding in solid phase synthesis process,

which is more favorable to ensure the uniform growth of the crystal structure. Guo et al. by using cyanuric chloride in solid state reaction with $NaNH_2$, NaN_3 or K at a certain temperature, respectively, showed that the g-C_3N_4 produced by this method, the N content can be adjusted, and molar ratios of C/N of 0.8, 1.04 and 4 respectively, were obtained.[124]

1.3.2.2 Electrochemical deposition technology

Electrochemical deposition technology not only requires simple equipment, but it is also easy to operate, and can effectively reduce the reaction energy barrier and reaction system temperature. Fu et al. used acetonitrile as electrolyte to prepare carbon nitride film under 80 ^oC, which are characterized by FTIR and XRD.[125] It is known that the synthesized products contain C-N and C=N bonds, and g-C_3N_4 crystals exist.

1.3.2.3 Pyrolysis organics

The process of thermal condensation is not easy to control for pyrolytic organics. The reaction process is shown in Figure 1.17 below. A series of products with different structures were obtained by controlling the final temperature of pyrolysis. XRD analysis showed that the structure of the products changed from melem to graphite phase gradually with the increase of pyrolysis temperature in a certain temperature range. The results of FTIR and XPS showed that the products were mainly composed of C-N double bond with sp^2 and C-N single bond with sp^3. TEM photos showed that the product had multilayer structure. In addition, the researchers introduced the template agent into the preparation process of thermal decomposition. After treatment of precursor and template, the products of specific morphology were obtained. Wang et al summarized that

some surfactants were used as templates to prepare highly ordered nano-porous carbon nitride.[126]

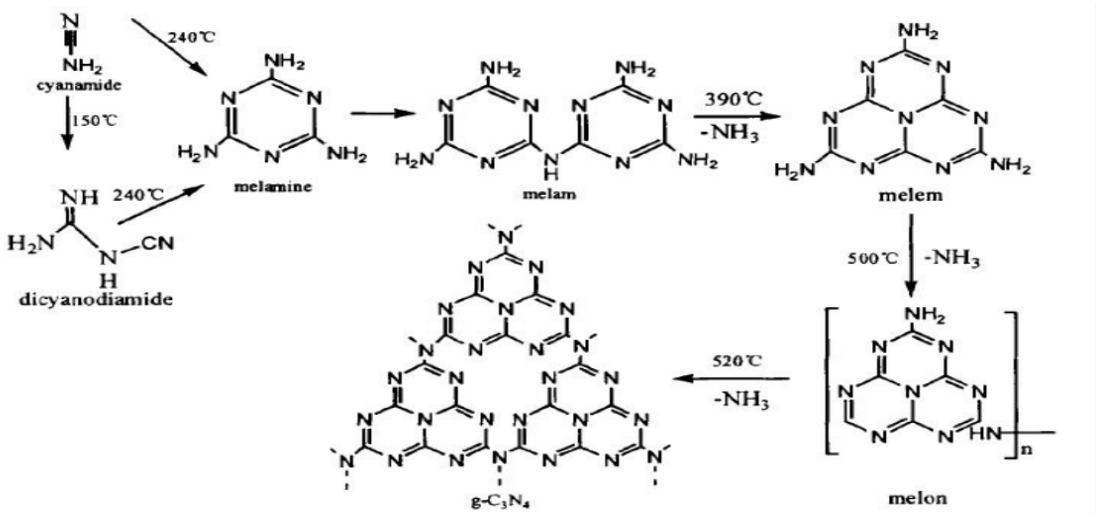

Figure 1.17 Schematic diagram of preparation of g-C_3N_4 by pyrolytic organic matter

1.3.2.4 Solvothermal synthesis

Solvothermal synthesis is usually used to prepare powder materials with small particle size. This method has the advantages of low synthesis temperature, short reaction time, similar final product morphology and uniform size. In addition, by adjusting the reaction conditions, the self-assembly process of reactants can be affected, and to prepare g-C_3N_4 nanostructures with special morphology. By the solvothermal reaction of CN_3Cl_3 with NaN_3 at 220 ^oC, the high quality g-C_3N_4 carbon nanotubes with an inner diameter of 50-100 nm and a wall thickness of 20-50 nm were obtained by Guo et al..[127]

1.3.3 Functional application of graphitic carbon nitride

The g-C_3N_4 has many advantages such as low price, good thermal and chemical stability, and can easily be modified chemically, so it has gained unprecedented research interest in recent years. Because of its unique

graphite-like stacking structure and sp^2 hybrid π-conjugate electron band structure, it has a promising future in catalysis, electronics, optics, materials and fuel cells.

1.3.3.1 As the organic reaction catalyst

Selective catalysis in organic reactions is of much interest. Carbon nitride has strong nucleophilic ability on its surface and forms hydrogen bond, Brønsted base site and Lewis acid site easily. It can be used in traditional catalytic reactions.

Carbon nitride and its modified materials have been found to be good catalysts for selective catalytic oxidation and hydrogenation.

Goettmann et al showed that the mesoporous g-C_3N_4 was a good Lewis base catalyst, which could facilitate the Friedel-Crafts acylation of benzene and acetyl chloride.[128,129] In addition, chlorine free electron nucleophilic reagents such as ethanol and formic acid can react with benzene with Friedel-Crafts acylation under the catalysis of g-C_3N_4.[130] The application of g-C_3N_4 in green chemical synthesis was expanded. Since then, various catalytic applications have been developed, such as the cyclization of various nitriles and acetylene compounds, the activation of various alcohols to obtain ketoacid esters, and the Knoevenagel condensation of benzyl alcohol with malonitrile.[131-133] After unsaturated carbon compounds were obtained with high selectivity, activated saturated C-H bond was successfully converted from toluene and dimethyl methane to benzaldehyde or benzophenone.[134]

1.3.3.2 Photocatalytic mechanism of g-C_3N_4 and its application in the field of photocatalysis

1.3.3.2.1 Photocatalytic mechanism of g-C_3N_4

The band gap of g-C_3N_4 is 2.7 eV (Figure 1.18) and it has a visible light response, so it is known that g-C_3N_4 is a typical polymer semiconductor, in which the C and N atoms in the structure are hybridized by sp^2 to form a highly delocalized π conjugate system.[135,136] In addition, (the photocatalytic reaction mechanism of g-C_3N_4 is shown in Figure 1.19), when the light absorption of g-C_3N_4 is equal to or greater than its band gap energy, the electrons from valence band transmit to conduction band, and then excited to bind to the oxygen molecules adsorbed on the surface to form superoxide ion free radicals, which can react further with the surrounding water to form superhydroxyl radicals and hydrogen peroxide. The valence band excited the transition of electrons to form an electron hole which reacts with the surrounding water or hydroxyl ions to form strongly oxidized hydroxyl radicals. The organic dyes, such as methylene blue, can be oxidized to water and carbon dioxide by the formation of perhydroxyl radical and hydrogen peroxide.

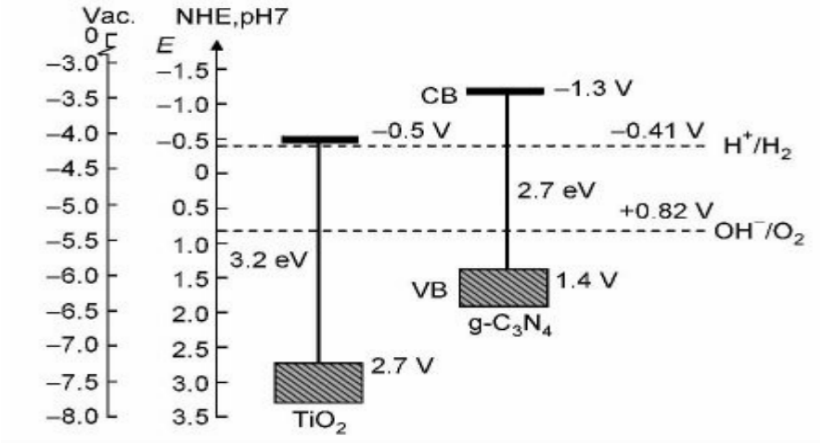

Figure 1.18 The g-C_3N_4 semiconductor band structure diagram

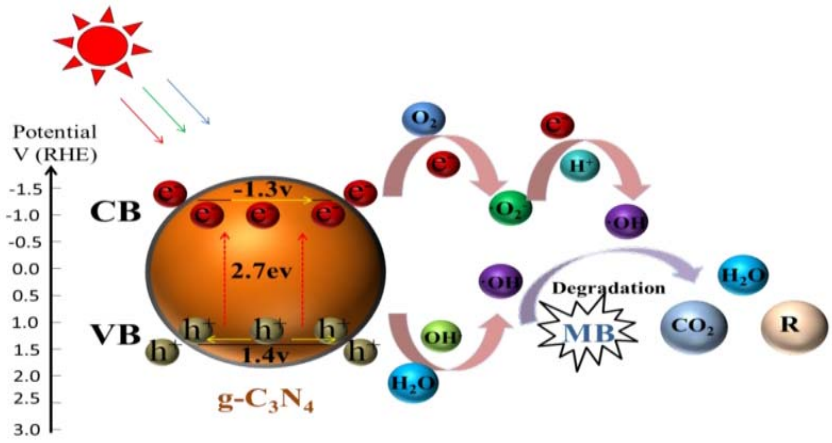

Figure 1.19 The g-C_3N_4 photocatalytic mechanism

1.3.3.2.2 Application of g-C_3N_4 in photocatalysis

1.3.3.2.2.1 Photolysis of water for hydrogen production

In 1972, it was first reported by Japanese scholars Fujishima A and Honda K that TiO_2 single crystals can photocatalyze the decomposition of water to hydrogen, thus opening the way for the research of electrolysis of hydrogen by solar photocatalysis.[137] Bulk g-C_3N_4 was prepared by using melamine as precursor, and then the rod-like g-C_3N_4 was obtained by hydrothermal treatment at 180 ^oC for 2 h.[138] Under visible light irradiation, the rod-like g-C_3N_4 was used as catalyst and triethanolamine as electron donor and Pt as co-catalyst for photodissociation of aqueous hydrogen. The experimental results showed that the relative specific surface area of rod-like g-C_3N_4 increased. Thus, more active sites are provided and the rate of hydrogen production is obviously increased.

1.3.3.2.2.2 Degradation of organic pollutants

Since g-C_3N_4 has been attracting the attention of many researchers, the catalytic degradation of organic pollutants has become the important research

direction because g-C_3N_4 can be used as a catalyst with visible light response. Using urea as precursor, calcined at 550 ºC for 3 h to obtain g-C_3N_4.[139] The obtained g-C_3N_4 was used to photodegrade acid red G. it was found that g-C_3N_4 had good photocatalytic activity under visible light.[135] The photocatalytic activity of g-C_3N_4 can be improved under acid conditions, and the addition of surfactant and inorganic salt can promote the photocatalytic degradation of acid red G.

Zhao et al., using melamine as precursor, obtained the monolithic layer g-C_3N_4 by controlling and adjusting the pyrolysis temperature.[140] The photocatalytic properties of the samples were examined by degradation of phenol and Rhodamine B in visible light. The degradation rate of Rhodamine B by g-C_3N_4 monolayer was greatly improved because of its unique electronic structure and relatively large specific surface area, which effectively promoted the separation of photogenerated electron-hole pairs. The photocatalytic activity for phenol degradation was also improved.

1.3.3.2.2.3 Catalyzing specific chemical reactions

In recent years, with the study of g-C_3N_4, the g-C_3N_4 has been widely used in catalyzing specific chemical reactions. The mesoporous graphitic carbon nitride material (mpg-C_3N_4) was prepared by using cyanide as the precursor and colloidal silica spheres as template. The structure and morphology of mpg-C_3N_4 were analyzed by XRD, TEM, FT-IR and elemental analysis. The mpg-C_3N_4 material with adjustable pore volume can be obtained by controlling the amount of template and precursor. The Knoevenagel condensation was used as a probe reaction to test the photocatalytic performance of mpg-C_3N_4. The results showed that mpg-C_3N_4 had good photocatalytic performance in the condensation reaction with benzaldehyde and propionitrile as substrate. After 5 cycles of catalysis, high photocatalytic activity was still obtained.

As a new type of material, the C_3N_4 monomer and its composites have excellent properties in many aspects, especially in the field of photocatalytic hydrolysis hydrogen production, in order to solve the problem of energy shortage. Compared with C_3N_4 monomers, the composites have better properties. In future studies, on the one hand, people are working to improve and optimize the existing C_3N_4-based composite photocatalysts; on the other hand, researchers are trying to find new materials that can be combined with C_3N_4. This will ensure an increasingly important role in the future.

1.4 Preparation and application of ruthenium nanoparticles

Particles with sizes between 1 and 100 nm are called nanoparticles. Its properties are not only different from macroscopic particles, but also different from those of individual atoms and molecules. It is located in the transition region between clusters and macroscopic objects. The small size effect, quantum size effect, surface effect, macroscopic quantum tunneling effect and dielectric limiting effect of nanocrystalline particles make them have some properties which are not possessed by conventional coarse-crystalline materials. These nano-effects give nanomaterials to have unique functions in mechanics, electricity, magnetism, heat, optics and catalysis. For example, ruthenium exhibits good catalytic activity in hydrogenation of carbon-carbon triple bond, carbon-carbon double bond and aromatic compounds, and palladium is an excellent catalyst for the reduction of pollutants and organic compounds at low temperature.[141] Nanocrystalline silver and nickel powder can be used as electrodes in chemical batteries.[36] Metal nano-oxide ZnO and CuO are popular among new semiconductor materials.[142] Its small size and range of morphologies make it an excellent medium for sensing and photoconductivity. The high specific surface area and the high proportion of surface atoms make

Ag widely used in the production and biology of antibacterial materials, tissue contrast and other biomedical fields.[143]

Therefore, in recent years, nanomaterials have attracted extensive attention in many fields reference – reviews, books etc.. As one of the most active research and development fields in the world, it is considered to be the most promising technological field for human beings in the 21st century.

Similar to platinum group elements, ruthenium has good catalytic properties, especially in hydrogenation, oxidation, isomerization and catalytic reforming have excellent catalytic performance. Ruthenium is also relatively cheap relative to platinum. Because Ru ($4d^7 5s^1$) contains more empty orbitals, ruthenium also has excellent hydrogenation catalytic ability compare to platinum-group elements. In addition, ruthenium nanoparticles not only have high selectivity, good catalytic activity, but also very stable chemical properties. They can be used as catalysts alone or co-catalyst with other catalysts. The overall catalytic activity is improved after the formation of co-catalyst. In recent years, the preparation and catalytic performance of ruthenium nanoparticles have become a hot topic.

1.4.1 Preparation of ruthenium nanoparticles

At present, the preparation of Ru NPs is mainly achieved by chemical reduction of Ru^{3+} precursors to Ru^0, $RuCl_3$, [Ru(COD)(COT)] and $Ru_3(CO)_{12}$ are common precursors. Reducing agents are generally alcohols, such as monohydric alcohol (*n*-propanol, *n*-butanol) and polyols (ethylene glycol, glycerol), etc. The reason why alcohol can be used as reducing agent is that with hydroxyl group (-OH), the hydroxyl group can reduce ruthenium precursor to Ru NPs with zero valence, while the valence of hydroxyl group is increased and oxidized to aldehydes. The reducing agent for the synthesis of Ru NPs is usually an alcohol, and alcohols can be used not only as reducing agent but also as solvent, so the

synthesis process is simple. Secondly, the reducibility of hydroxyl group is not high, the ruthenium precursor is difficult to nucleate and crystallize, so it needs a long reaction time. Therefore, the particle size of Ru NPs obtained by this alcohol reduction method is more uniform. In addition, the longer reaction time is one of the advantages, so we can add some structural guidance agents, such as halogen ions, which can cover on some crystal planes of Ru NPs, and have enough time to control the growth of Ru NPs. It is favorable for the control of size and morphology.

Due to the difference of reductivity between monohydric alcohol and polyols, it is often reported that the growth of Ru NPs is regulated by adding different kinds of alcohols, the advantages of this method are that the synthesized Ru NPs are small in size, spherical in shape and mostly less than 10 nm in size.

Sodium citrate and ascorbic acid with hydroxyl groups can also be used as reducing agents, but because of their high cost and no obvious advantage over alcohols, they are seldom used in the synthesis of Ru NPs. In addition, H_2 can also be used as reducing agent, but because H_2 is explosive, it is seldom used in laboratory synthesis, being used mostly in industrial large-scale production. In addition, both $NaBH_4$ and $N_2H_4 \cdot H_2O$ can be used as reductants to synthesize Ru NPs.[144] However, because of their strong reductivity, especially the high reduction rate of $NaBH_4$, the nucleation rate of the Ru precursor is very fast and the reaction is difficult to control. The diameter of Ru NPs obtained is below 1nm. As a result, the synthesized nanoparticles are particularly easy to aggregate.

There are also solid reducing agents, such as zinc powder, but is generally not used alone, it can be combined with an alcohol reductant, which can accelerate the reaction rate.[145] After the reaction, the excess zinc powder can be dissolved

into ionic state by hydrochloric acid to avoid the difficulty of separating zinc powder and Ru NPs during later treatment.

Since nanoparticles aggregate readily, stabilizers need to be added. Polyvinylpyrrolidone (PVP) is the common stabilizer for the synthesis of Ru NPs, but ionic liquids such as 1-butyl-3-methylimidazole lactate ionic liquid and 1-butyl-3-methyl-midazole tetrafluoroborate [(BMIM)BF_4] have also been used.[146, 147]

1.4.2 Application of ruthenium nanoparticles in catalysis

Ru NPs have important applications in many fields, such as biology, medicine and chemical industry.

1.4.2.1 Ammonia synthesis reaction ($N_2+3H_2 \rightarrow 2NH_3$)

Since the first application of iron to ammonia synthesis, people have been looking for new catalysts to obtain higher conversion rates under mild conditions for nearly a century. As the reaction needs to be carried out at high pressure, there is room for further reduction in energy consumption. Researchers have found that Ru NPs catalyst has high catalytic activity for ammonia synthesis under low temperature and low pressure, and is regarded as the second generation ammonia synthesis catalyst after iron. The catalytic activity of Ru is higher than that of other metal nanoparticles. One of the reasons is that Ru has a higher antitoxicity to CO and NH_3 than other metals, and its activity is not easily passivated.[148]

1.4.2.2 Catalytic hydrogenation

Ru NPs are excellent catalysts for the hydrogenation of unsaturated carbon carbon double bonds and carbon carbon triple bonds. During the hydrogenation

of unsaturated aldehydes and ketones, Ru NP catalysts can selectively hydrogenate C=O, thus increasing the selectivity and yield of the target products. For example, Ru NP as catalysts can catalyze the hydrogenation of benzene rings. Zhu et al. used the physical adsorption of C and the electrostatic effect of NiO, Ni as a bridge for electron transfer (Figure 1.20), which greatly increases the ability of adsorption benzene rings for Ru under the catalysis of Ru NPs. The yield of hydrogen can reach 100%.[149]

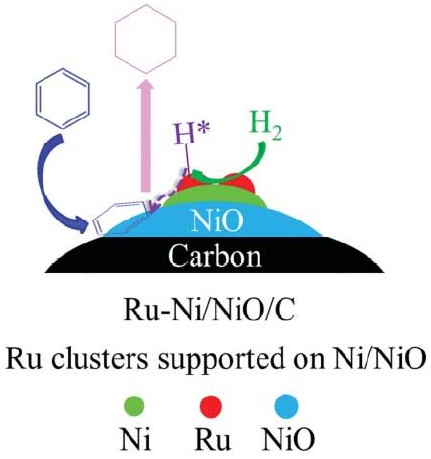

Figure 1.20 Schematic diagram of Ru–Ni/Ni O catalyzed hydrogenation of benzene ring

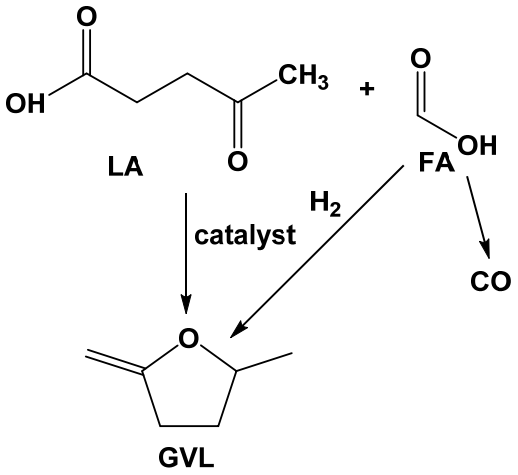

Figure 1.21 Ru NPs catalyst for hydrogenation of levulinic acid (LA) and formic acid (FA) into *γ*-valerolactone (GVL)

In addition, Using H_2 as a reducing agent, Ru NPs can catalyze the hydrogenation of lactic acid to propylene glycol and catalyze the hydrogenation of D-glucose to sorbitol with a selectivity of more than 95%.[150, 151] Besides using H_2 as a reductant, Ru NPs can also catalyze the hydrogenation of levulinic acid from formic acid (Figure 1.21).

1.4.2.3 Hydrogen production

Besides participating in hydrogenation, Ru NPs can also participate in hydrogen production.[152] H_2 is considered to be a clean energy source, but H_2 storage is still a challenge. Ammonia borane ($NH_3 \cdot BH_3$) has a very high hydrogen storage ability in solid hydrogen storage materials. It is a suitable hydrogen source. Ru NP catalysts can be used to catalyze the decomposition of aminoborane to H_2. The catalytic reaction showed high catalytic activity at room temperature and atmospheric pressure.

$$H_3NBH_3\,(aq) + 2H_2O\,(L) \xrightarrow{\text{catalyst}} NH_4^+\,(aq) + BO_2^-\,(aq) + 3H_2\,(g)$$

1.4.2.4 Water gas shift reaction ($CO+H_2O \rightarrow CO_2+H_2$)

The water gas shift reaction is a common reaction in industry. It is widely used in ammonia and methanol synthesis and hydrogen production.[153] It is the main reaction to remove CO and produce high purity H_2 in mixed gas. In fuel cells, it is often necessary to remove CO to avoid Pt electrode poisoning, while water gas shift reaction can not only remove CO, but also provide a rich hydrogen flow to avoid CO residue on Pt electrode. Therefore, it is very important to improve the conversion rate of water gas. Generally, Cr_2O_3 is used as catalyst, but the use of Cr^{3+} is strictly prohibited because of its high toxicity to human beings and organisms. The activity of Ru NPs is not easily passivated in CO

and NH_3, and it has excellent stability and low temperature catalytic activity in shift reaction, which makes Ru NPs ideal catalysts for water gas shift reaction.

1.5 References

1. L. Pauling, *J. Am. Chem. Soc.*, 1929, **51**, 2868-2880.

2. J. Keggin, *Proc. R. Soc. Lond. A*, 1934, **144**, 75-100.

3. B. Dawson, *Acta Crystallogr.*, 1953, **6**, 113-126.

4. J. S. Anderson, *Nature*, 1937, **140**, 850.

5. J. Waugh, D. P. Shoemaker and L. Pauling, *Acta Crystallogr.*, 1954, **7**, 438-441.

6. T. H. Tsay and J. Silverton, *Z. Kristallogr.-New Cryst. Struct.*, 1973, **137**, 256-279.

7. M. T. Pope, book of Heteropol and Isopoly Oxometalates. *Springer-Verlag*, 1983.

8. M. Misono, *Cat. Rev.-Sci. Eng.*, 1987, **29**, 269-321.

9. I. Kozhevnikov and K. Matveev, *Appl. Catal.*, 1983, **5**, 135-150.

10. T. Kitano, Y. Kuroda, A. Itoh, J. Li-Fen, A. Kunai and K. Sasaki, *J. Chem. Soc.*, 1990, 1991-1995.

11. I. V. Kozhevnikov, *Cat. Rev.*, 1995, **37**, 311-352.

12. M. R. Basila and T. R. Kantner, *J. Phys. Chem.*, 1967, **71**, 467-472.

13. E. Parry, *J. Catal.*, 1963, **2**, 371-379.

14. L. A. Cardoso, W. Alves Jr, A. R. Gonzaga, L. M. Aguiar and H. M. Andrade, *J. Mol. Catal. A: Chem.*, 2004, **209**, 189-197.

15. P. Vázquez, L. Pizzio, C. Cáceres, M. Blanco, H. Thomas, E. Alesso, L. Finkielsztein, B. Lantano, G. Moltrasio and J. Aguirre, *J. Mol. Catal. A: Chem.*, 2000, **161**, 223-232.

16. L. Yang, Y. Qi, X. Yuan, J. Shen and J. Kim, *J. Mol. Catal. A: Chem.*, 2005, **229**, 199-205.

17. C. Padró and C. Apesteguıa, *J. Catal.*, 2004, **226**, 308-320.

18. K. Eguchi, T. Seiyama, N. Yamazoe, S. Katsuki and H. Taketa, *J. Catal.*, 1988, **111**, 336-344.

19. U. Mioč, P. Colomban and A. Novak, *J. Mol. Struct.*, 1990, **218**, 123-128.

20. N. M. Dimitrijevic and P. V. Kamat, *Langmuir*, 1988, **4**, 782-784.

21. A. Frattini, N. Pellegri, D. Nicastro and O. De Sanctis, *Mater. Chem. Phys.*, 2005, **94**, 148-152.

22. J. Zhang, H. Wang, Y. Bao and L. Zhang, *Life Sci.*, 2004, **75**, 237-244.

23. F. Kim, J. H. Song and P. Yang, *J. Am. Chem. Soc.*, 2002, **124**, 14316-14317.

24. Y. Niidome, K. Nishioka, H. Kawasaki and S. Yamada, *Chem. Commun.*, 2003, 2376-2377.

25. Y. Zhu, Y. Qian, H. Huang and M. Zhang, *Mater. Lett.*, 1996, **28**, 119-122.

26. W. Chen, W. Cai, L. Zhang, G. Wang and L. Zhang, *J. Colloid Interf. Sci.*, 2001, **238**, 291-295.

27. X. Wang, X. Zheng, J. Lu and Y. Xie, *Ultrason. Sonochem.*, 2004, **11**, 307-310.

28. Y. Wang and I. A. Weinstock, *Chem. Soc. Rev.*, 2012, **41**, 7479-7496.

29. A. Z. Ernst, L. Sun, K. Wiaderek, A. Kolary, S. Zoladek, P. J. Kulesza and J. A. Cox, book of *Electroanalysis: An International Journal Devoted to Fundamental and Practical Aspects of Electroanalysis*, 2007, **19**, 2103-2109.

30. S. Zoladek, I. A. Rutkowska, K. Skorupska, B. Palys and P. J. Kulesza, *Electrochim. Acta*, 2011, **56**, 10744-10750.

31. K. M. Wiaderek and J. A. Cox, *Electrochim. Acta*, 2011, **56**, 3537-3542.

32. J. Yuan, Y. Chen, D. Han, Y. Zhang, Y. Shen, Z. Wang and L. Niu, *Nanotechnology*, 2006, **17**, 4689.

33. E. Papaconstantinou, *Chem. Soc. Rev.*, 1989, **18**, 1-31.

34. A. Troupis, A. Hiskia and E. Papaconstantinou, *Angew. Chem. Int. Ed.*, 2002, **41**, 1911-1914.

35. A. Troupis, E. Gkika, A. Hiskia and E. Papaconstantinou, *Comptes Rendus Chimie*, 2006, **9**, 851-857.

36. T. S. Ahmadi, Z. L. Wang, T. C. Green, A. Henglein and M. A. El-Sayed, *Science*, 1996, **272**, 1924-1925.

37. K.-S. Chou and C.-Y. Ren, *Mater. Chem. Phys.*, 2000, **64**, 241-246.

38. P. Lee and D. Meisel, *J. Phys. Chem.*, 1982, **86**, 3391-3395.

39. N. Shirtcliffe, U. Nickel and S. Schneider, *J. Colloid Interface Sci.*, 1999, **211**, 122-129.

40. I. Sondi, D. V. Goia and E. Matijević, *J. Colloid Interface Sci.*, 2003, **260**, 75-81.

41. I. A. Weinstock, *Chem. Rev.*, 1998, **98**, 113-170.

42. T. Yamase, *Chem. Rev.*, 1998, **98**, 307-326.

43. E. Gkika, A. Troupis, A. Hiskia and E. Papaconstantinou, *Appl. Catal. B: Environ.*, 2006, **62**, 28-34.

44. S. Mandal, A. Das, R. Srivastava and M. Sastry, *Langmuir*, 2005, **21**, 2408-2413.

45. A. Troupis, T. Triantis, A. Hiskia and E. Papaconstantinou, *Eur. J. Inorg. Chem.*, 2008, **36**, 5579-5586.

46. A. Gordeev and B. Ershov, *High Energ. Chem.*, 1999, **33**, 218-223.

47. S. Shanmugam, B. Viswanathan and T. Varadarajan, *Mater. Chem. Phys.*, 2006, **95**, 51-55.

48. S. Mandal, P. Selvakannan, R. Pasricha and M. Sastry, *J. Am. Chem. Soc.*, 2003, **125**, 8440-8441.

49. J. Zhang, B. Keita, L. Nadjo, I. M. Mbomekalle and T. Liu, *Langmuir*, 2008, **24**, 5277-5283.

50. N. Mizuno and M. Misono, *Chem. Rev.*, 1998, **98**, 199-218.

51. E.-b. WANG, B.-t. LI and B. Zhang, *Chem. Res. Chin. Univ.*, 1996, **12**, 322-323.

52. L. Xu, C. Hu and E. Wang, *Chin. Sci. Bull.*, 1999, **44**, 481-488.

53. N. Casan-Pastor and L. C. Baker, *J. Am. Chem. Soc.*, 1992, **114**, 10384-10394.

54. S. Borshch and B. Bigot, *Chem. Phys. Lett.*, 1993, **212**, 398-402.

55. J. M. Clemente-Juan, E. Coronado, J. R. Galán-Mascarós and C. J. Gómez-García, *Inorg. Chem.*, 1999, **38**, 55-63.

56. L. C. Baker and D. C. Glick, *Chem. Rev.*, 1998, **98**, 3-50.

57. M. Pope and A. Müller, *Angew. Chem.*, 1991, **103**, 56-70.

58. X. Chen, Z. Xu and T. Okuhara, *Appl. Catal. A: General*, 1999, **180**, 261-269.

59. D. E. Katsoulis, *Chem. Rev.*, 1998, **98**, 359-388.

60. C. Hu, Q. He, Y. Zhang, E. Wang, T. Okuhara and M. Misono, *Catal. Today*, 1996, **30**, 141-146.

61. C.-w. Hu, Q.-l. He, Y.-h. Zhang, Y.-y. Liu, Y.-f. Zhang, J.-y. Zhang and E.-b. Wang, *Chem. Commun.*, 1996, 121-122.

62. A. Griboval, P. Blanchard, E. Payen, M. Fournier and J.-L. Dubois, *Chem. Lett.*, 1997, **26**, 1259-1260.

63. M. K. Harrup, G.-S. Kim, H. Zeng, R. P. Johnson, D. VanDerveer and C. L. Hill, *Inorg. Chem.*, 1998, **37**, 5550-5556.

64. T. Yamase, H. Fujita and K. Fukushima, *Inorganica chimica acta*, 1988, **151**, 15-18.

65. X. H. Wang, H. C. Dai and J. F. Liu, *Polyhedron*, 1999, **18**, 2293-2300.

66. X.-H. Wang, J.-F. Liu, Y.-G. Chen, Q. Liu, J.-T. Liu and M. Pope, *J. Chem. Soc., Dalton Trans.*, 2000, 1139-1142.

67. X. Zhang, Q. Chen, D. C. Duncan, R. J. Lachicotte and C. L. Hill, *Inorg. Chem.*, 1997, **36**, 4381-4386.

68. K. Li, L. Chen, H. Wang, W. Lin and Z. Yan, *Appl. Catal. A: General*, 2011, **392**, 233-237.

69. S. Dong, X. Xi and M. Tian, *J. Electroanal. Chem.*, 1995, **385**, 227-233.

70. M. T. Pope and A. Müller, *Angew. Chem.*, 1991, **30**, 34-48.

71. B. Keita and L. Nadjo, *J. Electroanal. Chem. Interfac. Electrochem.*, 1987, **217**, 287-304.

72. B. Keita and L. Nadjo, *J. Electroanal. Chem. Interfac. Electrochem.*, 1988, **240**, 325-332.

73. B. Keita, L. Nadjo and J. Haeussler, *J. Electroanal. Chem. Interfac. Electrochem.*, 1988, **243**, 481-491.

74. S. Liu, Z. Shi and S. Dong, *Electroanalysis: An International Journal Devoted to Fundamental and Practical Aspects of Electroanalysis*, 1998, **10**, 891-896.

75. J. E. Toth, J. D. Melton, D. Cabelli, B. H. J. Bielski and F. C. Anson, *Inorg. Chem.*, 1990, **29**, 1952-1957.

76. M. Isobe, F. Marumo, T. Yamase and T. Ikawa, *Acta Crystallogr. Section B*, 1978, **34**, 2728-2731.

77. J. T. Rhule, C. L. Hill, D. A. Judd and R. F. Schinazi, *Chem. Rev.*, 1998, **98**, 327-358.

78. M. A. Fox, R. Cardona and E. Gaillard, *J. Am. Chem. Soc.*, 1987, **109**, 6347-6354.

79. A. Hiskia and E. Papaconstantinou, *Inorg. Chem.*, 1992, **31**, 163-167.

80. A. Mylonas, A. Hiskia and E. Papaconstantinou, *J. Mol. Catal. A: Chem.*, 1996, **114**, 191-200.

81. S. Antonaraki, E. Androulaki, D. Dimotikali, A. Hiskia and E. Papaconstantinou, *J. Photochem. Photobiol., A*, 2002, **148**, 191-197.

82. A. Hiskia, M. Ecke, A. Troupis, A. Kokorakis, H. Hennig and E. Papaconstantinou, *Environ. Sci. Technol.*, 2001, **35**, 2358-2364.

83. A. Mylonas and E. Papaconstantinou, *J. Photochem. Photobiol., A*, 1996, **94**, 77-82.

84. R. F. Renneke, M. Pasquali and C. L. Hill, *J. Am. Chem. Soc.*, 1990, **112**, 6585-6594.

85. A. Hiskia, A. Mylonas and E. Papaconstantinou, *Chem. Soc. Rev.*, 2001, **30**, 62-69.

86. A. Mylonas and E. Papaconstantinou, *J. Mol. Catal.*, 1994, **92**, 261-267.

87. H. Einaga and M. Misono, *Bull. Chem. Soc. Jpn.*, 1997, **70**, 1551-1557.

88. H. Einaga and M. Misono, *Bull. Chem. Soc. Jpn.*, 1996, **69**, 3435-3441.

89. A. Hiskia, A. Mylonas, D. Tsipi and E. Papaconstantinou, *Pestic. Sci.*, 1997, **50**, 171-174.

90. T. Yamase, B. Botar, E. Ishikawa and K. Fukaya, *Chem. Lett.*, 2001, **30**, 56-57.

91. S. Shigeta, S. Mori, E. Kodama, J. Kodama, K. Takahashi and T. Yamase, *Antiviral Res.*, 2003, **58**, 265-271.

92. I. Kozhevnikov, *Catalysts for fine chemical synthesis, catalysis by polyoxometalates*, Wiley, 2002.

93. F. H. Hurley and T. P. Wier, *J. Electrochem. Soc.*, 1951, **98**, 203-206.

94. P. A. Hunt, C. R. Ashworth and R. P. Matthews, *Chem. Soc. Rev.*, 2015, **44**, 1257-1288.

95. P. Bonhote, A.-P. Dias, N. Papageorgiou, K. Kalyanasundaram and M. Grätzel, *Inorg. Chem.*, 1996, **35**, 1168-1178.

96. R. F. de Souza, V. Rech and J. Dupont, *Adv. Synth. Catal.*, 2002, **344**, 153-155.

97. D. A. Waterkamp, M. Heiland, M. Schlüter, J. C. Sauvageau, T. Beyersdorff and J. Thöming, *Green Chem.*, 2007, **9**, 1084-1090.

98. A. K. Burrell, R. E. Del Sesto, S. N. Baker, T. M. McCleskey and G. A. Baker, *Green Chem.*, 2007, **9**, 449-454.

99. S. Peleteiro, S. Rivas, J. L. Alonso, V. Santos and J. C. Parajó, *Bioresour. Technol.*, 2016, **202**, 181-191.

100. R. Giernoth, *Angew. Chem. Int. Ed.*, 2010, **49**, 2834-2839.

101. S.-g. Lee, *Chem. Commun.*, 2006, 1049-1063.

102. O. Green, S. Grubjesic, S. Lee and M. A. Firestone, *Polym. Rev.*, 2009, **49**, 339-360.

103. D. Mecerreyes, *Prog. Polym. Sci.*, 2011, **36**, 1629-1648.

104. N. Nishimura and H. Ohno, *Polymer*, 2014, **55**, 3289-3297.

105. J. Lu, F. Yan and J. Texter, *Prog. Polym. Sci.*, 2009, **34**, 431-448.

106. J. Yuan and M. Antonietti, *Polymer*, 2011, **52**, 1469-1482.

107. P. Zhang, J. Yuan, T. P. Fellinger, M. Antonietti, H. Li and Y. Wang, *Angew. Chemie*, 2013, **125**, 6144-6148.

108. Y. Men, M. Drechsler and J. Yuan, *Macromol. Rapid Commun.*, 2013, **34**, 1721-1727.

109. J. Yuan, D. Mecerreyes and M. Antonietti, *Prog. Polym. Sci.*, 2013, **38**, 1009-1036.

110. A. Dewan, T. Sarma, U. Bora and D. K. Kakati, *Tetrahedron lett.*, 2011, **52**, 2563-2565.

111. Y. Leng, J. Liu, P. Jiang and J. Wang, *Catal. Commun.*, 2013, **40**, 84-87.

112. Y. Leng, J. Liu, P. Jiang and J. Wang, *Chem. Eng. J.*, 2014, **239**, 1-7.

113. Y. Leng, P. Jiang and J. Wang, *Catal. Commun.*, 2012, **25**, 41-44.

114. Y.-F. Song and R. Tsunashima, *Chem. Soc. Rev.*, 2012, **41**, 7384-7402.

115. Y. Leng, J. Liu, P. Jiang and J. Wang, *RSC Adv.*, 2012, **2**, 11653-11656.

116. Raisa I M, Lidia I K, Raisa I M, *Catal. Lett.*, 2011,**141**,1442-1450.

117. L. I. Kuznetsova, N. I. Kuznetsova, R. I. Maksimovskaya, G. I. Aleshina, O. S. Koscheeva and V. A. Utkin, *Catal. Lett.*, 2011, **141**, 1442.

118. G. Chen, Y. Zhou, P. Zhao, Z. Long and J. Wang, *ChemPlusChem*, 2013, **78**, 561-569.

119. J. Wu, P. Jiang, Y. Leng, Y. Ye and X. Qin, *Chinese J. Catal.*, 2013, **34**, 2236-2244.

120. A. Y. Liu and M. L. Cohen, *Science*, 1989, **245**, 841-842.

121. D. M. Teter and R. J. Hemley, *Science*, 1996, **271**, 53-55.

122. X. Wang, K. Maeda, X. Chen, K. Takanabe, K. Domen, Y. Hou, X. Fu and M. Antonietti, *J. Am. Chem. Soc.*, 2009, **131**, 1680-1681.

123. B. Molina and L. E. Sansores, *Mod. Phys. Lett. B*, 1999, **13**, 193-201.

124. Q. Guo, Q. Yang, C. Yi, L. Zhu and Y. Xie, *Carbon*, 2005, **43**, 1386-1391.

125. Q. Fu, C.-B. Cao and H.-S. Zhu, *J. Mater. Sci. Lett.*, 1999, **18**, 1485-1488.

126. Y. Wang, X. Wang, M. Antonietti and Y. Zhang, *ChemSusChem: Chem. Sustain. Energy Mater*, 2010, **3**, 435-439.

127. Q. Guo, Y. Xie, X. Wang, S. Zhang, T. Hou and S. Lv, *Chem. Commun.*, 2004, 26-27.

128. F. Goettmann, A. Fischer, M. Antonietti and A. Thomas, *Angew. Chem. Int. Ed.*, 2006, **45**, 4467-4471.

129. F. Goettmann, A. Fischer, M. Antonietti and A. Thomas, *New J. Chem.*, 2007, **31**, 1455-1460.

130. F. Goettmann, A. Fischer, M. Antonietti and A. Thomas, *Chem. Commun.*, 2006, 4530-4532.

131. X. Jin, V. V. Balasubramanian, S. T. Selvan, D. P. Sawant, M. A. Chari, G. e. Q. Lu and A. Vinu, *Angew. Chem. Int. Ed.*, 2009, **48**, 7884-7887.

132. S. N. Talapaneni, S. Anandan, G. P. Mane, C. Anand, D. S. Dhawale, S. Varghese, A. Mano, T. Mori and A. Vinu, *J. Mater. Chem.*, 2012, **22**, 9831-9840.

133. Y. Wang, J. Zhang, X. Wang, M. Antonietti and H. Li, *Angew. Chem. Int. Ed.*, 2010, **49**, 3356-3359.

134. Y. Wang, H. Li, J. Yao, X. Wang and M. Antonietti, *Chem. Sci.*, 2011, **2**, 446-450.

135. C. Zhang, N. Li, W. Lv, T. Zhang and W. Chen, *J. Zhejiang Sci-Tech Uni*, 2014, **31**, 117-121.

136. G.Dong, Cent China Normal Univ, 2015.

137. A. Fujishima and K. Honda, *nature*, 1972, **238**, 37.

138. L. Shi, D. Guo, J. Gu, R.Liang, J. Qi, L.Huang and W. Mai, *Chin. Sci. Bul.l*, 2016, 1323-1329.

139. B. Tang, J. Xu, P. Liu and Y. Li, *Chem. Bull*, 2013, **76**, 150-156.

140. H. Zhao, H. Yu, X. Quan, S. Chen, H. Zhao and H. Wang, *RSC Adv.*, 2014, **4**, 624-628.

141. J. Zhu, S. Liu, O. Palchik, Y. Koltypin and A. Gedanken, *Langmuir*, 2000, **16**, 6396-6399.

142. B. Brocklehurst and R. N. Young, *J. Phys. Chem. A*, 1999, **103**, 3809-3817.

143. X. Zhang and Y. Yang, *Pre. Met.*, 1998, **19**, 54-58.

144. J. Yang, J. Y. Lee, T. C. Deivaraj and H.-P. Too, *J. Colloid Interface Sci.*, 2004, **271**, 308-312.

145. S. Kim, E. Kim and B. M. Kim, *Chem.– Asian J.*, 2011, **6**, 1921-1925.

146. B. B. Xu, Z. C. Ma, H. Wang, X. Q. Liu, Y. L. Zhang, X. L. Zhang, R. Zhang, H. B. Jiang and H. B. Sun, *Electrophoresis*, 2011, **32**, 3378-3384.

147. B.-B. Xu, R. Zhang, X.-Q. Liu, H. Wang, Y.-L. Zhang, H.-B. Jiang, L. Wang, Z.-C. Ma, J.-F. Ku and F.-S. Xiao, *Chem. Commun.*, 2012, **48**, 1680-1682.

148. N. Saadatjou, A. Jafari and S. Sahebdelfar, *Chem. Eng. Commun.*, 2015, **202**, 420-448.

149. L. Zhu, Y. Jiang, J. Zheng, N. Zhang, C. Yu, Y. Li, C. W. Pao, J. L. Chen, C. Jin and J. F. Lee, *small*, 2015, **11**, 4385-4393.

150. S. Iqbal, S. A. Kondrat, D. R. Jones, D. C. Schoenmakers, J. K. Edwards, L. Lu, B. R. Yeo, P. P. Wells, E. K. Gibson and D. J. Morgan, *ACS Catalysis*, 2015, **5**, 5047-5059.

151. A. A. Dabbawala, D. K. Mishra and J.-S. Hwang, *Catal. Today*, 2016, **265**, 163-173.

152. M. Rakap, *Appl. Catal. A: General*, 2014, **478**, 15-20.

153. Y. Ma, B. Liu, M. Jing, R. Zhang, J. Chen, Y. Zhang and J. Li, *Chem. Eng. J.*, 2016, **287**, 155-161.

Chapter 2

Catalysis with Polyoxometalate-Stabilized Ruthenium Nanoparticles Catalysts

Chapter 2. Catalysis with polyoxometalate-stabilized ruthenium nanoparticles catalysts

2.1 Introduction

Particles in the nanometer, size range often have properties, such as surface effect and quantum tunneling effect.[1,2] Among them, surface effect which refers to nanoparticles with high surface area, multi-active centers and strong adsorption ability, makes nanomaterials have excellent performance in such aspects as catalysis, electrochemistry, magnetism and superconductivity.[3]

Metal nanoparticles are widely used in different fields, mainly because of their photochemistry, photovoltaic, photoelectron properties and catalytic activity.[2,4] The exploration of the synthesis and properties of noble metals has attracted great interest because noble metals show higher catalytic activity and selectivity compared with other metals.[5] In order to increase the efficiency of noble metals in heterogeneous catalysis, composite materials are usually prepared by combining noble metals with suitable substrates.

Polyoxometalates (POMs) are increasingly being used in catalysis because they are well-defined, molecular species with a wide variety of structures and compositions and they exhibit the ability to reversibly take up multiple electrons and protons.[6] POMs plays an important role in the preparation of metal NPs, and can act as a reducing agent and stabilizer. The preparation of metal NPs using POMs as surface capping groups is attracting much interest.

It is straight forward to synthesize metal nanomaterial using POMs. The metal ions can be reduced to metal elements in a one-step synthesis method by choosing the appropriate POMs. A variety of methods can be used to reduce POMs, such as electrochemistry, photochemistry and radiation chemistry. However, the preparation of metal nanomaterial by POMs is mainly through photochemical reduction or direct addition of reducing agent.

In this Chapter, ruthenium ions were reduced to ruthenium nanoparticles (Ru NPs) in the presence of POMs in aqueous solutions by hydrogen. POMs have an electrostatic and steric effect at the surface of the Ru NPs.[7-9] Kinetic stability is achieved between POMs and Ru NPs, and reduces the aggregation of Ru NPs. I

POMs have basically act similar to surfactants by stabilizing the nanoparticles, therefore a detailed comparison between standard surfactant stabilized nanoparticles and the present POM stabilized nanoparticles is warranted in this Chapter.

2.1.1 Hydrogenation of unsaturated compounds

The hydrogenation of unsaturated compounds is important in organic synthesis, medicine, and the chemical industry. Different unsaturated organic compounds such as olefins, diolefins, alkynes, aromatic hydrocarbons, aldehydes, ketones, imines, carboxylic acid derivatives, nitriles and carbon dioxide can be hydrogenated by homogeneous or heterogeneous catalysts. Unsaturated compounds have the characteristics of small volume, high mobility and low viscosity. The key factor to determine the rate of hydrogenation reaction is whether the reactant molecules can interact efficiently with the catalyst. Therefore, supported catalysts with high specific surface area and porous structure are usually used in the hydrogenation of unsaturated compounds. The efficiency of the hydrogenation reaction can be raised as much as possible, and the recovery and reuse of the catalyst can be easily realized.

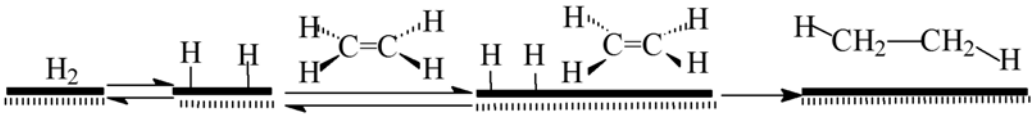

Scheme 2.1 Hydrogenation of olefin reaction mechanism

The addition reaction of olefin and hydrogen is discussed in current general textbooks of organic chemistry as follows: The mixture of olefin and hydrogen can not react at 200 ^{o}C, but in the presence of catalyst, alkanes can be formed by addition reaction with hydrogen. It is generally believed that the hydrogenation of olefins takes place on the surface of the catalyst. When the olefin and hydrogen are adsorbed on the surface of the dispersed metal, the surface of the catalyst breaks the H-H covalent bond of the hydrogen molecule and forms an active hydrogen atom (Scheme 2.1). At the same time, the π bond in olefin is also weakened, which greatly reduces the activation energy required for the hydrogenation reaction and increases the reaction rate. When hydrogen atoms combine with carbon atoms of alkenes to form alkanes, the adsorption ability of alkanes on the catalyst surface is smaller than that of alkenes, so once alkanes are formed, they are immediately liberated from the catalyst surface.

2.1.2 Fischer-Tropsch synthesis

Fischer-Tropsch (F-T) synthesis was first discovered by German scientists Frans Fischer and Hans Tropsch in 1923.[10] F-T synthesis is the production of hydrocarbons from CO/H_2 mixtures. CO / H_2 as raw materials, can produce wide distribution of carbon produced (alkanes and alkenes) under catalysts. By-products of organic oxygenated compounds such as alcohol, aldehydes, ketones, acids and esters are also formed. High-quality liquid fuels, high-grade wax and other chemicals can be obtained by further refining and processing of F-T synthetic products.[11] F-T synthesis is a process based mainly on coal and natural gas to produce gasoline, diesel and some chemicals.[12,13] Since the reserves of coal and natural gas far exceed those of petroleum, the F-T synthetic reaction can provide a certain amount of liquid fuel, represented by gasoline and diesel, for a longer period of time, and the fuel produced is characterized by low sulfur content. With the depletion of petroleum resources and the increasing of energy consumption,

the search for alternative petroleum energy becomes an important issue, and determines the national energy security. In this context, F-T synthesis technology has been more and more researched.

There are many reactions in the process of producing low molecular weight olefins by adding hydrogen to CO. The most important reaction is the hydrogenation of CO to surface bound methylene and water, as follows:

$$CO + 2H_2 = -CH_2- + H_2O$$

Methylene can form alkenes and alkanes by increasing the chain length. The total reaction formula is as follows:

$$nCO + 2nH_2 = C_nH_{2n} + nH_2O$$

$$nCO + (2n+1)H_2 = C_nH_{(2n+2)} + nH_2O$$

In this process, water-gas shift reaction, methanation reaction, carbon deposition reaction and many other side reactions will occur. The reaction formula is:

$$CO + H_2O = CO_2 + H_2$$

$$CO + 3H_2 = CH_4 + H_2O$$

$$2CO = C + CO_2$$

F-T synthesis is an exothermic reaction. Kinetic analysis show that increasing the reaction temperature is beneficial to the formation of short chain and saturated hydrocarbon products. Therefore, with the increase of reaction temperature (350 ^oC), the selectivity of methane byproduct will increase. In the temperature range of F-T synthesis, the selectivity of the obtained product is quite different. According to kinetic calculations, when the composition of syngas H_2 : CO = 1 : 1, the main products of F-T synthesis under atmospheric pressure should be CH_4, CO_2 and C, and the ratio of long chain hydrocarbon products can be neglected. However, experiments show relatively low selectivity to CH_4, and the carbon accumulation can be ignored. If the reaction pressure is raised from atmospheric pressure to 60 atmospheres, the calculated yield of heavy hydrocarbons will increase by nearly a

hundredfold, but its selectivity to methane is still very low. This is still very different from the actual F-T synthetic product data. At the same time, the ratio of alkane to olefin in the product, the hydrogenation or dehydration of alcohols all deviated greatly from the thermodynamic calculated values. Therefore, it can be concluded that the distribution of the products of F-T synthetic reaction does not correspond to the calculated values of ideal thermodynamic equilibrium.

F-T synthesis is a complex reaction process. Many scholars have studied the reaction mechanism in depth and put forward a variety of mechanism models. These mechanisms are supported by experimental facts to a certain extent, but evidence of the exact surface mechanism is still lacking, and so far there is no consensus. However, it is generally accepted that the carbide mechanism, the oxygen intermediate condensation mechanism and the CO insertion mechanism are all relevant under certain circumstance. The reason for carbides mechanism was first proposed by Fischer and Tropsch, who believed that CO and active metals will first form corresponding carbides, and then, through hydrogen reduction, an intermediate $M=CH_2$ is obtained. This intermediate undergoes polymerization to produce corresponding hydrocarbon compounds. Hydrocarbon products can be explained by this mechanism, but the production of products such as alcohols cannot be explained. The schematic diagram is shown in Figure 2.1. In the CO insertion mechanism proposed by Pichler et al., CO is hydrogenated to formyl. The formyl group is then hydrodehydrated to give carbene and methyl, respectively.[14,15] According to the homogeneous organometallic catalysis mechanism, CO can complete carbon chain growth by inserting M-H bonds or by adding H_2. The schematic diagram of this mechanism is shown in Figure 2.2. Anderson et al. proposed the condensation mechanism of oxygenates, which exist as intermediates. In this mechanism, CO and H_2 first generate HCOH, and then undergo dehydration to achieve carbon chain growth.[16,17] Finally, after polymerization, the corresponding product is obtained. The mechanism diagram is

shown in Figure 2.3. The condensation mechanism of oxygen-containing intermediates can well explain the formation of linear and branched products, but it lacks the necessary experimental basis for the intermediate HCOH.

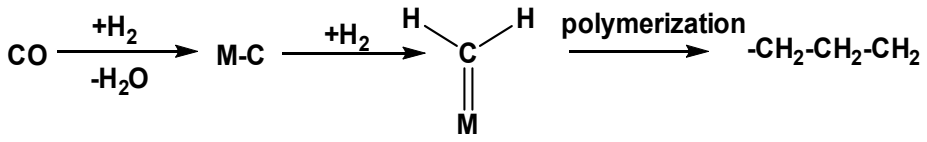

Figure 2.1 The carbide mechanism

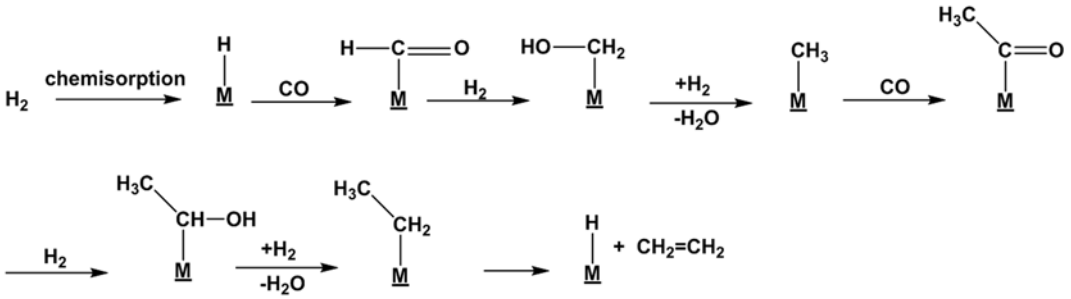

Figure 2.2 The CO insertion mechanism

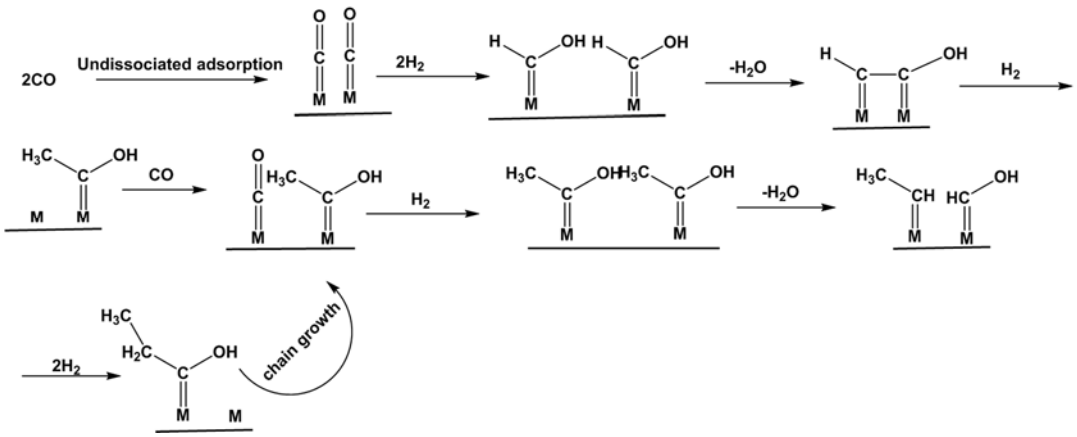

Figure 2.3 The oxygen intermediate condensation mechanism

The mechanism of F-T synthesis proposed above is more or less defective from different angles. Although the study of F-T synthesis has a history of nearly 90 years, up to now, the reaction mechanism of F-T synthesis is still a controversial issue in the field of catalysis. It can be predicted that with the progress of surface science and technology and the improvement of research methods, further

investigations will provide more details of the catalyst active site and reveal the mechanism of F-T synthesis. According to the result and discussion for the F-T synthesis experiment in this Chapter, using the CO insertion mechanism to explain the F-T synthesis result seems more reasonable.

It has now been found that almost all of elements from the groups 8, 9 and 10 have F-T synthesis catalytic activity. Previous studies have investigated the catalytic activity of the groups 8, 9 and 10 elements in the F-T reaction, resulting in the following sequence of catalytic activity: Ru > Fe > Ni > Co > Rh > Pd > Pt.[18] Among them, ruthenium is the metal with the highest catalytic activity in hydrogenation, especially for high molecular weight straight chain alkanes. Because of its high price, the possibility of industrialization is very small. However, it is of great significance to develop new process and explore reaction mechanism. Nickel-based catalysts tend to produce too much methane.[19] Cobalt and iron are most widely used in industrial F-T synthesis, while iron is cheaper; cobalt-based catalysts have higher activity and selectivity, are less easily deactivated, and are mostly used in the generation of alkanes with longer carbon chains, e.g. paraffin and diesel.[13,20,21] The development of catalysts is mainly for iron and cobalt-based catalysts, and has been implemented in industrial demonstration plants of some major oil companies around the world where they are sources of CH_4 to provide H_2.

2.1.3 Electrochemical reduction of CO_2

The increasing demand for coal, oil and natural gas not only aggravates the depletion of fossil energy, but also significantly increases the CO_2 content of the atmosphere.[22] CO_2 is the most important greenhouse gas, which is increasing at a rate of 2 ppm in the atmosphere, and is about to reach and exceed 400 ppm.[23] Global warming and ecological problems are the severe challenges of human sustainable development. Facing the worsening energy and environmental problems, governments attach great importance to emission reduction, and to the

capture and fixation of CO_2.[24-26] On the other hand, CO_2 provides a feedstock for transformation into high value-added fuel or fine chemicals.[27,28] The artificial carbon cycle will effectively recycle CO_2, and promote its transformation into new and green carbon resources, which will revolutionize human environment and energy.

Table 2.1 Methods of CO_2 conversion[30,31]

Transformation mode	Product type
electrochemical conversion method	HCOOH, CH_3OH, CO, ethylene
catalytic hydrogenation method	Hydrocarbon, CH_3OH, CH_3CH_2OH,
catalytic reforming method	$CO+H_2$
photochemical conversion method	CO, HCOOH, CH_4
biological transformation method	CH_3CH_2OH, carbohydrate, CH_3COOH
inorganic chemical absorption method	carbonate, carbaminate, etc.

CO_2 has very high chemical stability, and with existing scientific and technological means, level of CO_2 reuse is far lower than the scale and speed of its production. A new artificial carbon cycle therefore needs new methods for CO_2 activation. Highly efficient catalysts are required to activate the C-O bond, and provide the basis for the formation of new C-H or C-C bonds.[29] There have been many reports on CO_2 conversion, mainly focused on the catalytic hydrogenation of CO_2, photochemical or electrochemical conversion, or catalytic reforming with natural gas to syngas, as shown in Table 2.1. Traditional chemical conversion methods are usually carried out at high temperature and high pressure, which involve large amounts of energy and expensive reaction vessels to provide the necessary levels of safety.

The electrochemical conversion of CO_2, or electrochemical reduction of CO_2, can effectively utilize renewable electrical energy and provide an effective way for the "carbon-neutral" strategy, which has a good prospect of research and application.[32] The advantages are: (1) the electroreduction reaction can be carried out under mild conditions, with no need for high temperature and high pressure; (2) electrochemical equipment can achieve higher energy efficiency than other chemical conversion equipment; (3) the free energy of catalyst surface can be directly controlled by the electrode potential, which creates conditions for controlling reaction rate and product selectivity.[33,34] At present, research on CO_2 electroreduction mainly focuses on exploring new catalysts and the formation mechanism of corresponding products.[35,36] In addition, the conditions of reaction and the exploration of new electrochemical reactors also provide engineering verification for key materials. The electrochemical reduction theory of CO_2 began in the 19th century. In the last 30 years, the common products of electrochemical reduction of CO_2 are formate, CO and ethylene.[37,38] Methanol and methane can also be produced in 6 or 8 electron reactions.[31,39] The thermodynamic potentials for the formation of various products are given in equations (1) - (7): (pH = 7, in aqueous solution, Vs. NHE 25 ^oC, 1 atm (1atm = 101,300 Pa), 1 M solute):[40]

$$CO_2 + H^+ + 2e^- \longrightarrow HCOO^- \quad E^0 = -0.61\ V \quad (1)$$

$$CO_2 + 2H^+ + 2e^- \longrightarrow CO + H_2O \quad E^0 = -0.53\ V \quad (2)$$

$$CO_2 + 6H^+ + 6e^- \longrightarrow CH_3OH + H_2O \quad E^0 = -0.38\ V \quad (3)$$

$$CO_2 + 8H^+ + 8e^- \longrightarrow CH_4 + 2H_2O \quad E^0 = -0.24\ V \quad (4)$$

$$CO_2 + 12H^+ + 12e^- \longrightarrow C_2H_4 + 12H_2O \quad E^0 = -0.34\ V \quad (5)$$

$$2H_2O + 2e^- \longrightarrow 2OH^- + H_2 \quad E^0 = -0.41V \quad (6)$$

$$CO_2 + e^- \longrightarrow CO_2 \quad E^0 = -1.90\ V \quad (7)$$

Figure 2.4 CO_2 electrochemical reduction equation

The electrochemical reduction of CO_2 mainly includes the process of CO_2 activation and hydrogenation (Figure 2.4). It is a complex multi-step reaction occurring at the electrode interface, involving processes such as gain and loss of electrons, adsorption and proton transfer. The whole reaction is restricted by the single electron reduction reaction in the first step of CO_2 activation (the reaction formula is (7) in Figure 2.4), and usually occurs at high overpotential, therefore, reducing the step overpotential is the key to improve the energy efficiency of the whole reaction.[41] There are many factors affecting the yield and selectivity of the electrochemical reduction products of CO_2. However, the key technology is mainly through the interfacial action of the catalyst, so the existing research can be divided into two aspects: heterogeneous and homogeneous catalysts.

2.2 Results and discussion

2.2.1 Characterization of polyoxometalate-stabilized ruthenium catalyst

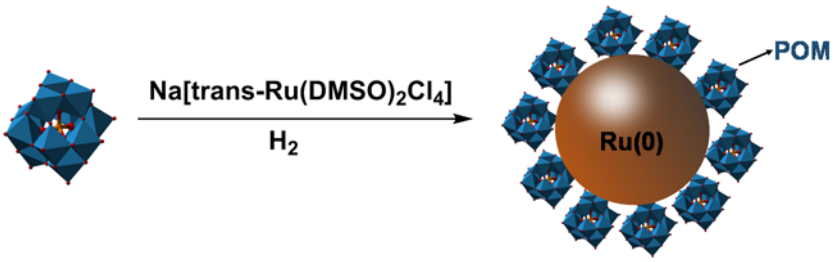

Scheme 2.2 The designed route for Ru^0@POM nanoclusters

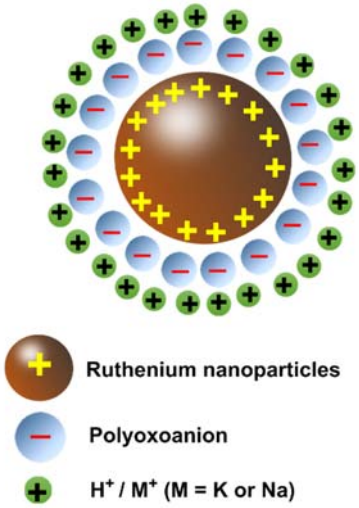

Figure 2.5 Scheme of POM stabilized Ru^0 nanoclusters

The first polyoxometalate (POM) of 12-ammonium molybdophosphate has a history of 170 years and was successfully synthesized in 1826. POM chemistry is an important field and has developed rapidly in recent years. In this Chapter, typical and well-known POMs were selected for study into: Keggin spcies $H_3PW_{12}O_{40}$, $H_3PMo_{12}O_{40}$ and $H_4SiW_{12}O_{40}$, and the lacunary derivatives $Na_7(PW_{11}O_{39})$ as well as the Wells-Dawson species $K_{10}(P_2W_{17}O_{61})$. Ru^{3+} was reduced to Ru^0 in aqueous solution by reduction with hydrogen to form ruthenium nanoparticles, which have positively charged surfaces at which the polyoxoanions are adsorbed to form stable

water-soluble nanoclusters, Ru^0@POM. The synthesis of Ru^0@POM nanoclusters and a representation of the structure is shown in Scheme 2.2 and Figure 2.5.

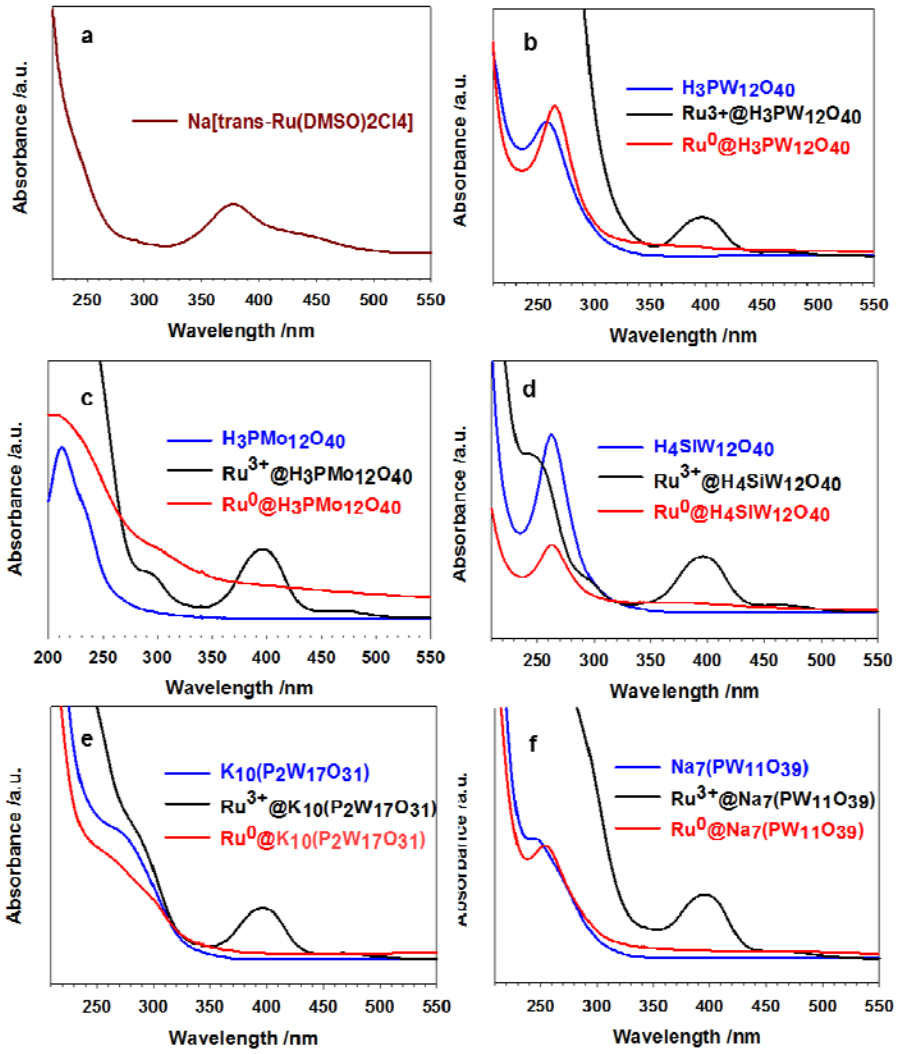

Figure 2.6 UV-Vis spectra of (a) Na[*trans*-$Ru(DMSO)_2Cl_4$], (b) $H_3PW_{12}O_{40}$, Ru^{3+}@$H_3PW_{12}O_{40}$ s and Ru^0@$H_3PW_{12}O_{40}$, (c) $H_3PMo_{12}O_{40}$, Ru^{3+}@$H_3PMo_{12}O_{40}$ and Ru^0@$H_3PMo_{12}O_{40}$, (d) $H_4SiW_{12}O_{40}$, Ru^{3+}@$H_4SiW_{12}O_{40}$ and Ru^0@$H_4SiW_{12}O_{40}$, (e) $K_{10}(P_2W_{17}O_{61})$, Ru^{3+}@$K_{10}(P_2W_{17}O_{61})$ and Ru^0@$K_{10}(P_2W_{17}O_{61})$ and (f) $Na_7(PW_{11}O_{39})$, Ru^{3+}@$Na_7(PW_{11}O_{39})$ and Ru^0@$Na_7(PW_{11}O_{39})$ in aqueous solution.

Figure 2.6 (a) shows the ultraviolet–visible (UV-Vis) spectra of Na[*trans*-$Ru(DMSO)_2Cl_4$] in water. The Ru^{3+} solution gives a strong absorption peak at 375

nm and a shoulder at 440 nm, which is characteristic of aqueous Ru^{3+}.[42] Figures 2.6 (b)-(f) show a series of spectra which illustrate the effect of addition of different POMs to Ru^{3+} (aq) and subsequent reduction. The aqueous POMs show no absorption peak in the range 350-500 nm, but $H_3PW_{12}O_{40}$, $H_3PMo_{12}O_{40}$, $H_4SiW_{12}O_{40}$, $K_{10}(P_2W_{17}O_{61})$ and $Na_7(PW_{11}O_{39})$ show absorption peaks at 258, 212, 263, 266, 245 nm respectively due to O→M charge transfer.[43] After H_2 reduction, the absorption peaks around 350-500 nm disappear indicating that Ru^{3+} is reduced to Ru^0 nanoparticles. In addition, the POM charge transfer bonds are shifted slightly to longer wavelength.

Figure 2.7 (a) shows Fourier transform infrared (FT-IR) spectroscopy of Na[*trans*-$Ru(DMSO)_2Cl_4$]: 3021 (m), 2920 (m), γ (C−H); 1427 (m), 1393 (m), 1310 (m), 1290 (m), 1015 (s), 970 (s), 940 (m), 910 (w), ρ (CH_3); 1090 (vs), 1065 (s), ν (S−O); 735 (m), 690 (m), γ (C−S); 425 (m), γ (Ru−S) is consistent with literature reports.[44] In order to confirm Figure 2.7 (b)-(f) gives the comparison spectroscopy of POM and their stabilized Ru^0 nanoparticles to illustrate the presence of POM on ruthenium nanoparticles.

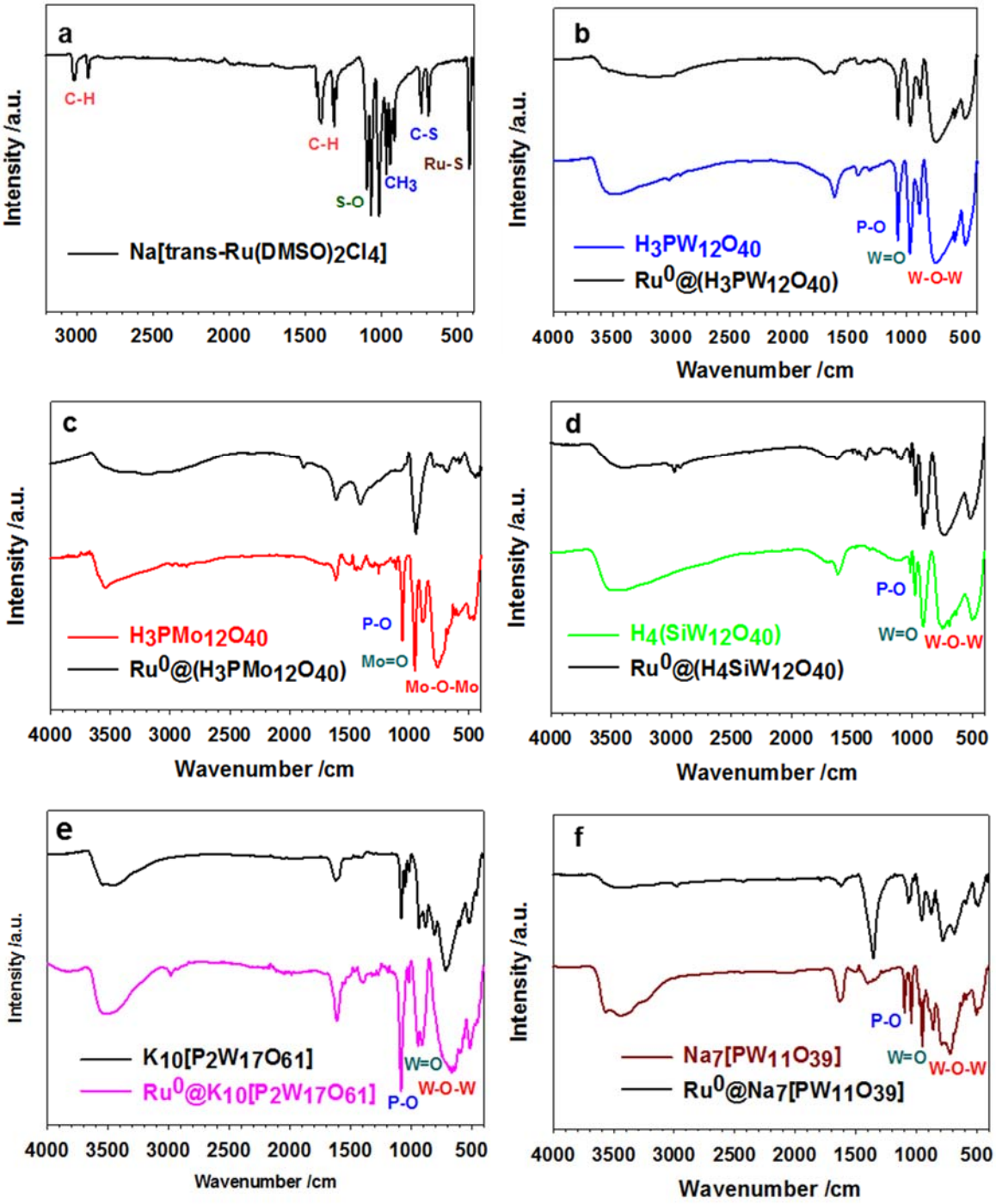

Figure 2.7 FT-IR spectra of (a) Na[*trans*-$Ru(DMSO)_2Cl_4$], (b) $H_3PW_{12}O_{40}$, Ru^0@ $H_3PW_{12}O_{40}$, (c) $H_3PMo_{12}O_{40}$, Ru^0@ $H_3PMo_{12}O_{40}$, (d) $H_4SiW_{12}O_{40}$, Ru^0@ $H_4SiW_{12}O_{40}$, (e) $K_{10}(P_2W_{17}O_{61})$, Ru^0@$K_{10}(P_2W_{17}O_{61})$ and (f) $Na_7(PW_{11}O_{39})$, Ru^0@$Na_7(PW_{11}O_{39})$.

Table 2.2 FT-IR assignments for POM and Ru^0@POM

POM	γ (P−O_a)	γ (W=O_d)	γ(W−O_b-W)	γ(W-O_c-W)	(cm^{-1})
$H_3PW_{12}O_{40}$	1081	976	891	756	
Ru^0@$H_3PW_{12}O_{40}$	1083	971	887	755	
$H_3PMo_{12}O_{40}$	1056	955	886	767	
Ru^0@$H_3PMo_{12}O_{40}$	1079	943	820	747	
$H_4SiW_{12}O_{40}$	1015	975	908	751	
$Na_7(PW_{11}O_{39})$	1039	953	868	796	
Ru^0@$Na_7(PW_{11}O_{39})$	1046	955	879	786	
Ru^0@$H_4SiW_{12}O_{40}$	1022	973	909	746	
$K_{10}(P_2W_{17}O_{61})$	1082	934	877	811	
Ru^0@$K_{10}(P_2W_{17}O_{61})$	1077	942	904	808	

Table 2.2 shows the FT-IR spectral assignments for the series of POM and their stabilized Ru^0 nanoparticles. The presence of the important peaks in the fingerprint region for the POMs ($H_3PW_{12}O_{40}$, $H_3PMo_{12}O_{40}$, $H_4SiW_{12}O_{40}$, $K_{10}(P_2W_{17}O_{61})$, $Na_7(PW_{11}O_{39})$) in the spectra of POM stabilized Ru^0 nanoparticles proves the presence of the POM anions on the Ru^0 nanoparticles.[45,46] According to comparison with the tiny shift band of stretching *γ* (P−O_a), *γ* (W=O_d), *γ*(W−O_b-W), *γ*(W-O_c-W), the analysis results also demonstrate H_2 reduction process has not transformed the basic structure of POM when they stabilized on ruthenium nanoparticles. In brief, FT-IR analysis of POM and Ru^0@POM is carried out to confirm the presence of POM on ruthenium nanoparticles and their chemical structures remain intact.

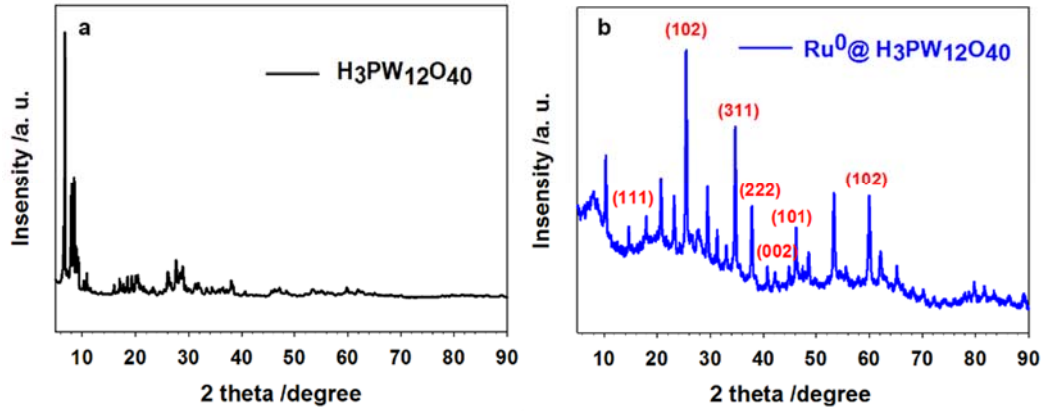

Figure 2.8 XRD spectra of (a) $H_3PW_{12}O_{40}$ and (b) $Ru^0@H_3PW_{12}O_{40}$

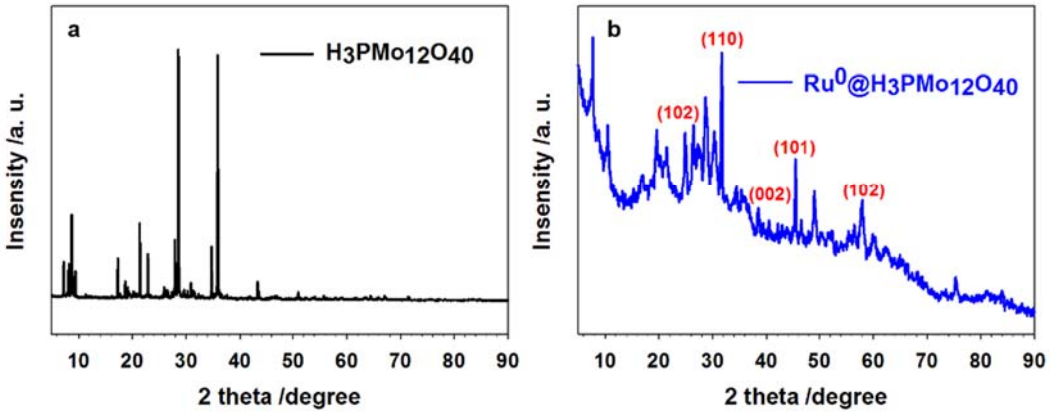

Figure 2.9 XRD spectra of (a) $H_3PMo_{12}O_{40}$ and (b) $Ru^0@H_3PMo_{12}O_{40}$

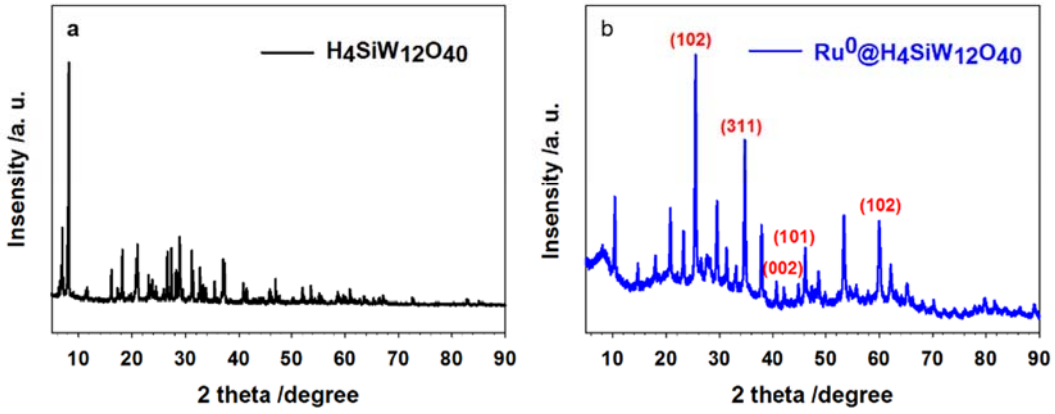

Figure 2.10 XRD spectra of (a) $H_4SiW_{12}O_{40}$ and (b) $Ru^0@H_4SiW_{12}O_{40}$

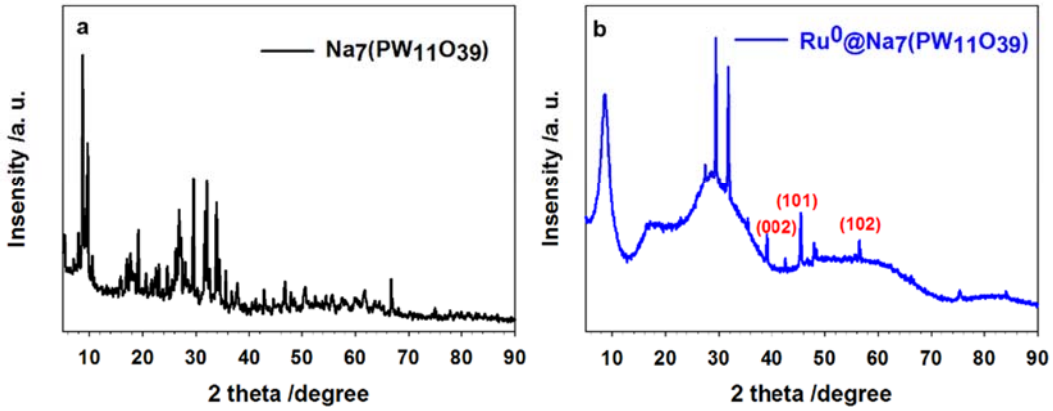

Figure 2.11 XRD spectra of (a) $Na_7(PW_{11}O_{39})$ and (b) $Ru^0@Na_7(PW_{11}O_{39})$

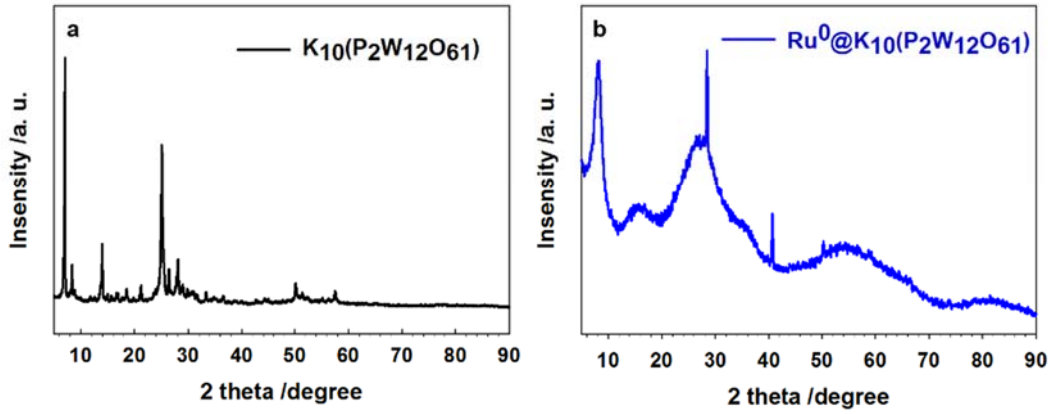

Figure 2.12 Powder XRD spectra of (a) $K_{10}(P_2W_{17}O_{61})$ and (b) $Ru^0@K_{10}(P_2W_{17}O_{61})$

Figure 2.8-2.12 shows the powder X-ray diffraction (XRD) patterns of POM and POM stabilized Ru^0 nanoparticles. The XRD patterns of the series of POM have well-defined diffraction crystalline structures and the diffraction patterns observed, which are exactly consistent with literature reports. The XRD patterns of ruthenium nanoparticles gives peaks at 18.45°, 25.93°, 35.77°, 31.42°, 42.19°, 44.04°, 58.37°representing Bragg reflections from (111), (102), (311), (222), (002), (101) and (102) crystal lattice planes of the standard Ru cubic phase.[47-49] As shown in Figure 2.8 (b), $Ru^0@H_3PW_{12}O_{40}$ complex demonstrates the presence of several peaks at 18.04°, 25.2°, 35.0°, 37.7°, 42.2°, 44.0° and 59.0° of ruthenium cubic phase.[50-52] Similarly, Figure 2.9 and Figure 2.10 shows the presence of Ru

nanoparticles on the basis of the XRD spectra. However, in Figures 2.11 and 2.12, the XRD patterns of $Ru^0@Na_7(PW_{11}O_{39})$ and $Ru^0@K_{10}(P_2W_{17}O_{61})$ show no obvious strong peaks of metallic Ru, which may be due to poor crystallinity. Therefore, the XRD of Ru nanoparticles in Figures 2.11 and 2.12 show broad and weak peaks, which indicates the size of POM stabilized Ru nanoparticles from $Ru^0@H_3PW_{12}O_{40}$, $Ru^0@H_3PMo_{12}O_{40}$, $Ru^0@H_4SiW_{12}O_{40}$, $Ru^0@Na_7(PW_{11}O_{39})$ to $Ru^0@K_{10}(P_2W_{17}O_{61})$ is gradually increasing. The the size of samples can be calculated On the basis of Scherer equation, but when the size of nanoparticles is under 15 nm, the peaks of XRD are wide, not sharp. According to the XRD patterns, the presence of Ru nanoparticles in POM was further confirmed.

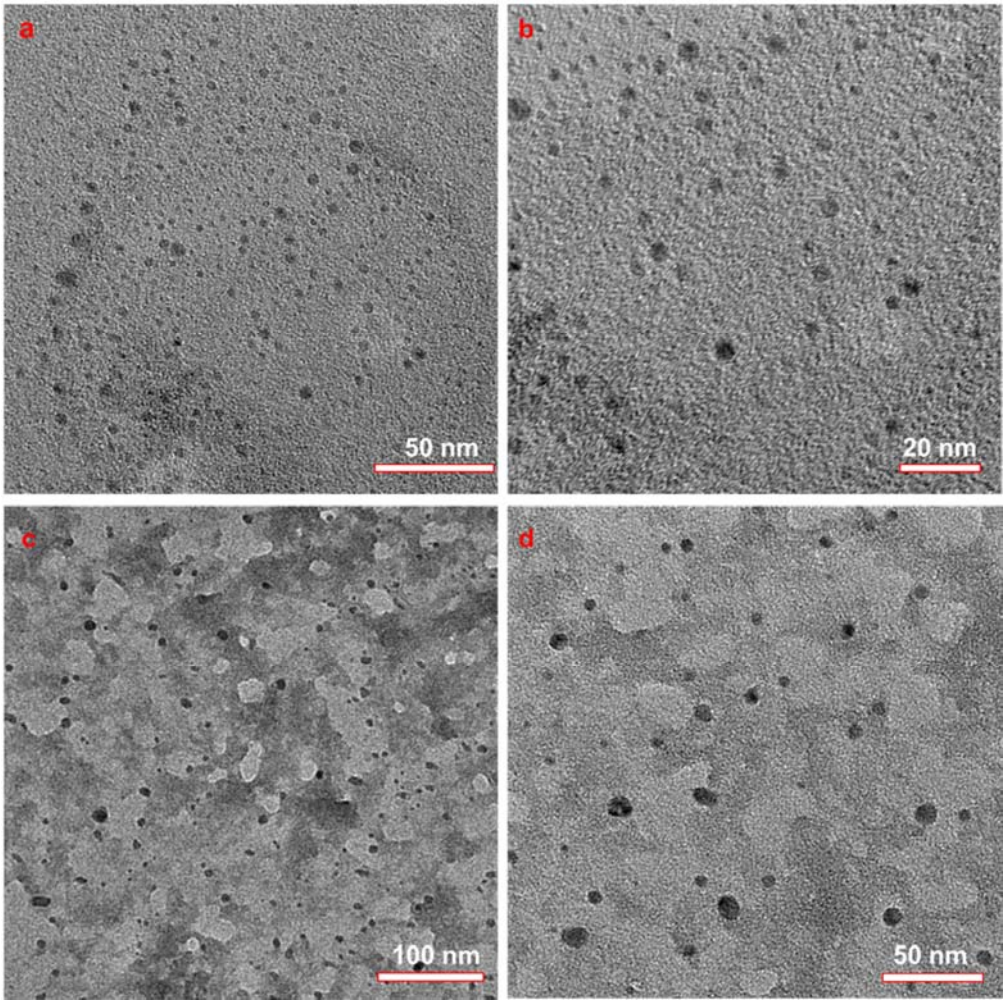

Figure 2.13 TEM images of (a), (b) $Ru^0@H_3PW_{12}O_{40}$ and (c), (d) $Ru^0@H_3PMo_{12}O_{40}$ in water solutions

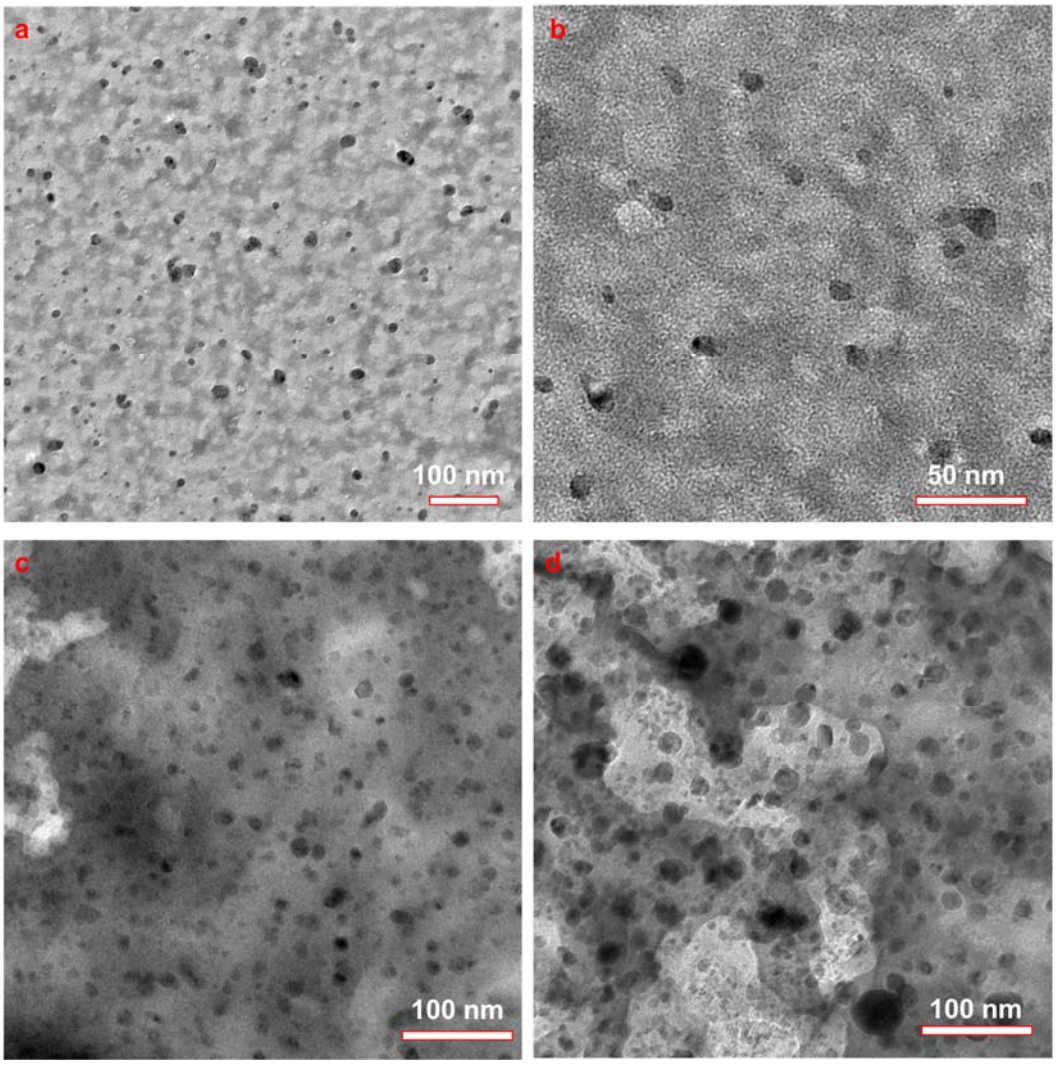

Figure 2.14 TEM images of (a), (b) $Ru^0@H_4SiW_{12}O_{40}$, (c) $Ru^0@Na_7(PW_{11}O_{39})$ and (d) $Ru^0@K_{10}(P_2W_{17}O_{61})$ in water solutions

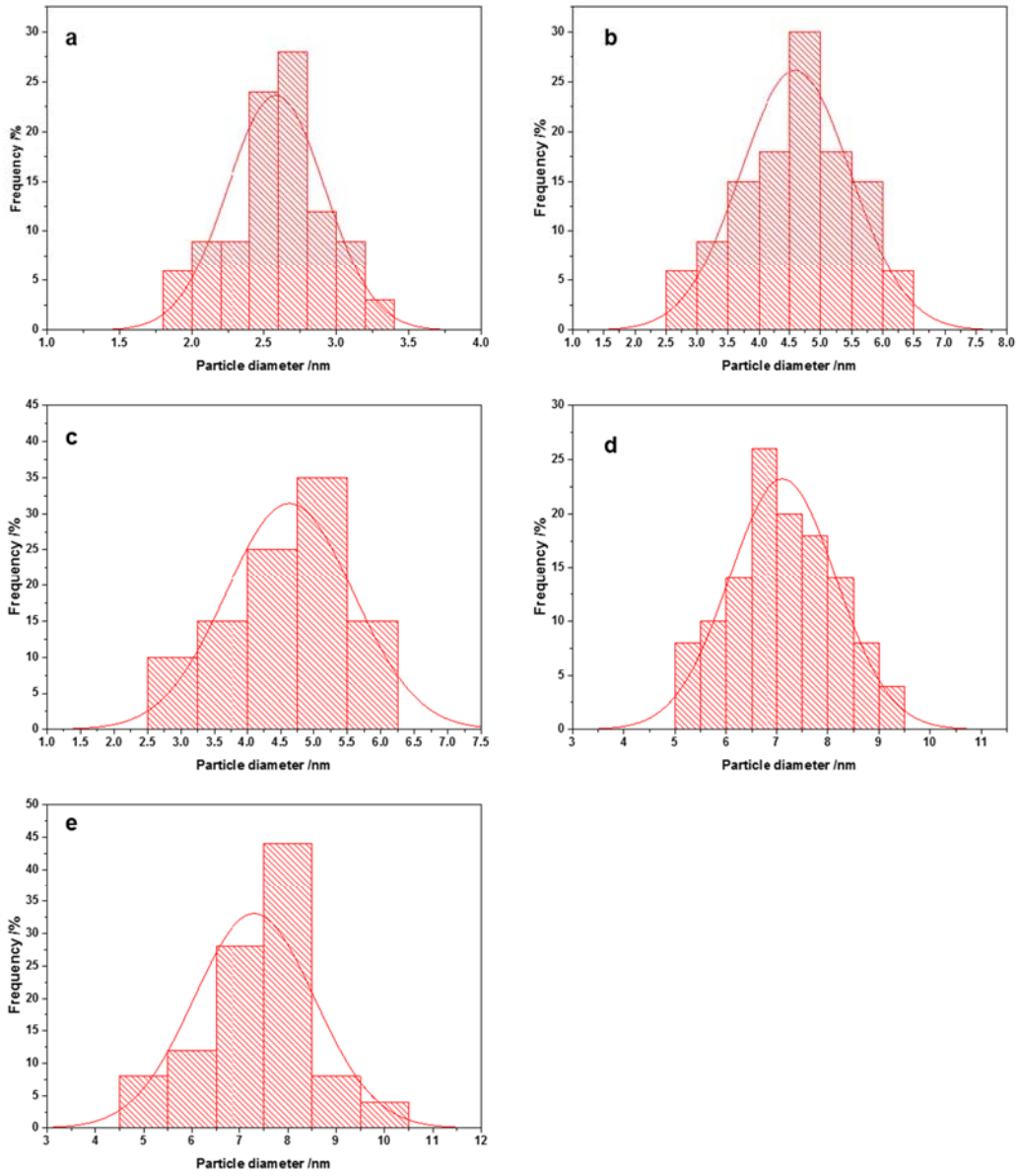

Figure 2.15 Particle size distribution of (a) $Ru^0@H_3PW_{12}O_{40}$, (b) $Ru^0@H_3PMo_{12}O_{40}$, (c) $Ru^0@H_4SiW_{12}O_{40}$, (d) $Ru^0@Na_7(PW_{11}O_{39})$ and (e) $Ru^0@K_{10}(P_2W_{17}O_{61})$

Transmission electron microscopy (TEM) images of POM stabilized ruthenium nanoparticles and their corresponding Ru^0 nanoparticles size distribution histograms were shown in Figure 2.13 to Figure 2.15. TEM images of Figure 2.13 and Figure 2.14 illustrated ruthenium nanoparticles were well distributed and stabilized by POM. Particles size for ruthenium nanoparticles were given in Figure

2.15, the average size of ruthenium nanoparticles for $Ru^0@H_3PW_{12}O_{40}$, $Ru^0@H_3PMo_{12}O_{40}$, $Ru^0@H_4SiW_{12}O_{40}$, $Ru^0@Na_7(PW_{11}O_{39})$ and $Ru^0@K_{10}(P_2W_{17}O_{61})$ were about 2.5-3 nm, 4.5-5 nm, 4-5 nm, 6.5-7.5 nm and 7-8 nm respectively. The diameter of ruthenium nanoparticles were gradually increasing from 2.5-8 nm, owing to the size of POM changed. As the size of the POM anion increased, the radius of the ruthenium nanoparticles gradually enlarged. As a consequence, it appears the size of ruthenium nanoparticles might be controlled by suitable choice of POM.

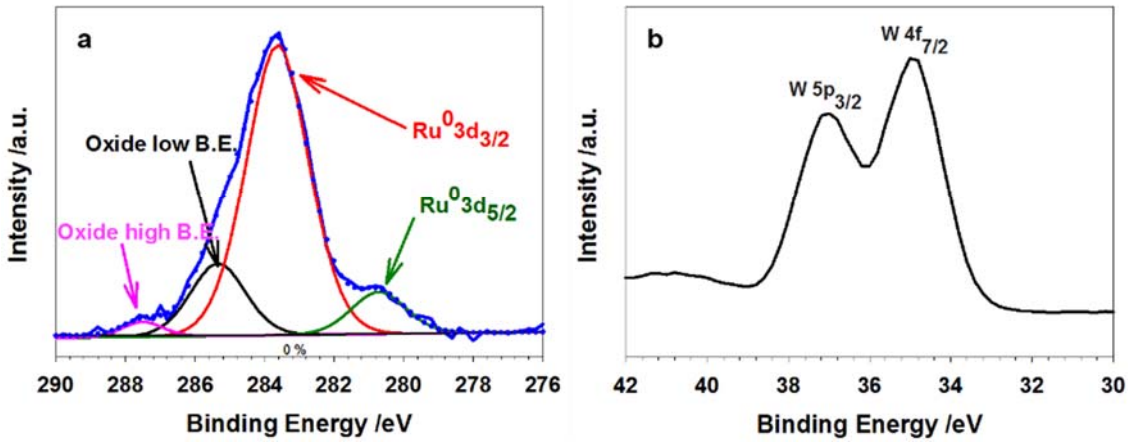

Figure 2.16 XPS spectra of (a) Ru1s and (b) W1s for $Ru^0@H_3PW_{12}O_{40}$

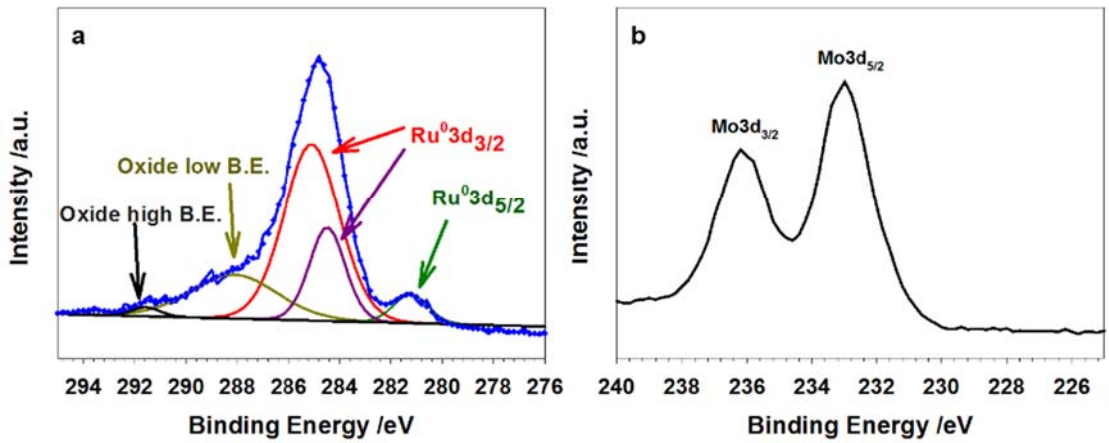

Figure 2.17 XPS spectra of (a) Ru1s and (b) Mo1s for $Ru^0@H_3PMo_{12}O_{40}$

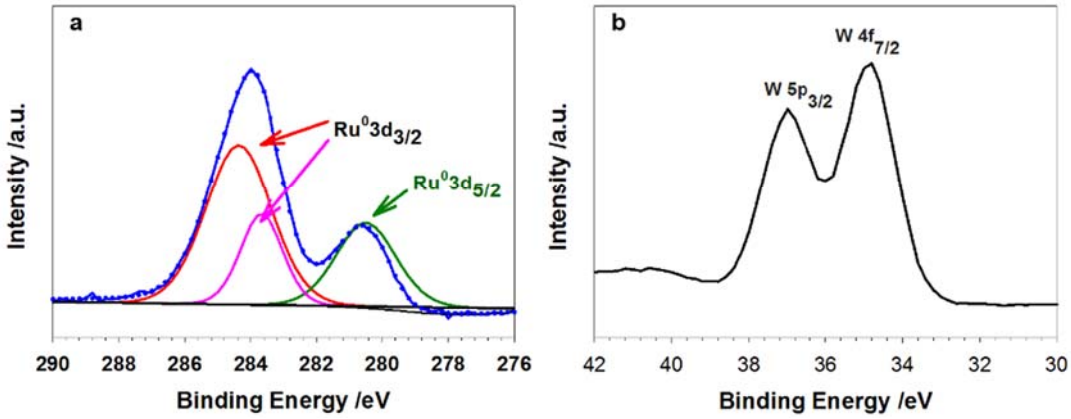

Figure 2.18 XPS spectra of (a) Ru1s and (b) W1s for Ru^0@ $H_4SiW_{12}O_{40}$

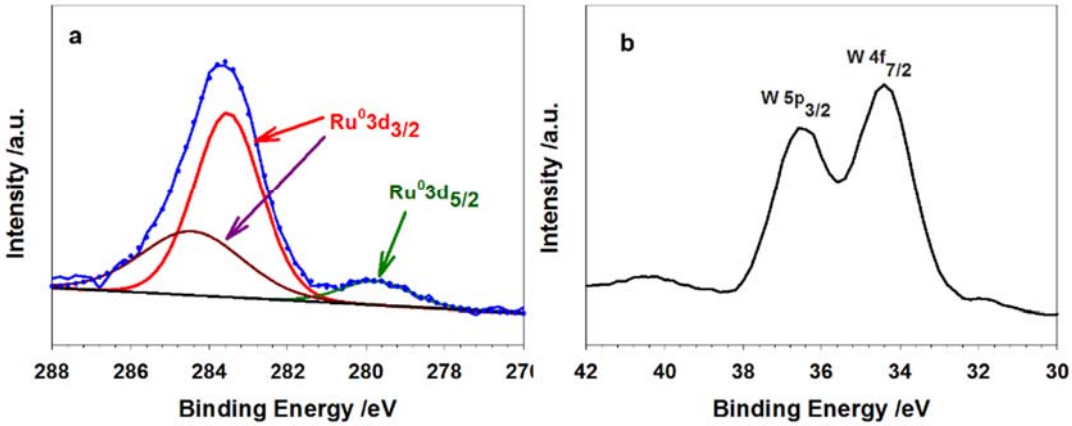

Figure 2.19 XPS spectra of (a) Ru1s and (b) W1s for Ru^0@$Na_7(PW_{11}O_{39})$

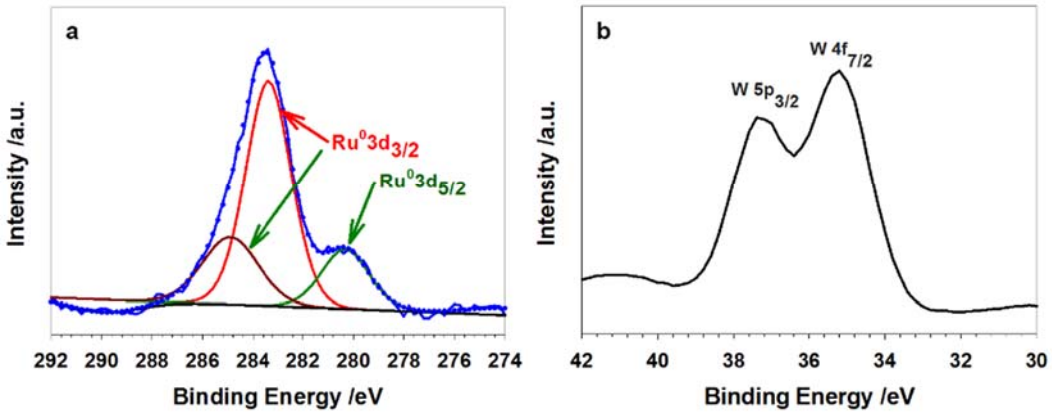

Figure 2.20 XPS spectra of (a) Ru1s and (b) W1s for Ru^0@$K_{10}(P_2W_{17}O_{61})$

Figures 2.16 to 2.20 show X-ray photoelectron spectra (XPS) for POM stabilized Ru^0 nanoparticles. The XPS spectra ($Ru3d_{5/2}$ at 280.7 eV and Ru $3d_{3/2}$ at 283.7 eV) of POM stabilized ruthenium nanoparticles verified Ru in the nanoparticles was in zero oxidation state which was consistent with the literature reports.[53-55] Moreover, XPS spectra of Ru in Figure 2.16 and Figure 2.17 (a) show peaks due to oxide at low and high B.E. at 285.4 eV and 287.6 eV, showing that proved Ru(IV) is present. Probably the surface of Ru^0 nanoparticles on samples was oxidized in air when they were prepared for analysis by XPS.[127] The presence of W (W $4f_{7/2}$ at 35 eV, W $5p_{3/2}$ at 37 eV) and Mo ($Mo3d_{5/2}$ at 233 eV, $Mo3d_{3/2}$ at 236 eV) was also demonstrated in all samples.[56-59]

The interaction between POMs and ruthenium nanoparticles is important, and XPS spectra for W or Mo compared with Ru can indicate how many POM anions are present on Ru^0 nanoparticles. Calculation of the relative amounts of W, Mo and Ru and demonstrated that on average 15 $[PW_{12}O_{40}]^{3-}$and $[PMo_{12}O_{40}]^{3-}$ anions, 16 $[SiW_{12}O_{40}[^{4-}$ anions, 23 $[PW_{11}O_{39}]^{7-}$ anions and 31 $[P_2W_{17}O_{61}]^{10-}$were absorbed on each respective Ru^0 nanoparticle.

2.2.2 Stability and redispersion of POM stabilized Ru^0 nanoparticles in aqueous solution

Freshly prepared POM stabilized Ru^0 nanoparticles in aqueous solution under nitrogen were used to examine the stability. We found that $Ru^0@H_4SiW_{12}O_{40}$ was the least stable, and it was found that there was a precipitate of ruthenium metal particles in its solution after three days, while for the other four nanocluster solutions, the solution remained homogeneous and did not produce precipitation after six months. The results showed that the $Ru^0@H_3PW_{12}O_{40}$, $Ru^0@H_3PMo_{12}O_{40}$, $Ru^0@Na_7(PW_{11}O_{39})$ and $Ru^0@K_{10}(P_2W_{17}O_{61}$ nanocluster solutions are stable but the $Ru^0@H_4SiW_{12}O_{40}$ solution precipitate after three days under nitrogen.

In order to study the redispersity of Ru^0@POM nanoclusters, we removed the water from the solutions of nanoclusters under vacuum to form dark brown powders, and then re-dispersed the powders in water under nitrogen. We found that all of the Ru^0@POM nanoclusters could be uniformly re-dispersed in aqueous solution. Hence, we can see that the Ru^0@POM nanoclusters solution can be stored in the form of powders, and when re-dispersed in water, their chemical properties remain unchanged.

2.2.3 Hydrogenation of 1-decene to decane

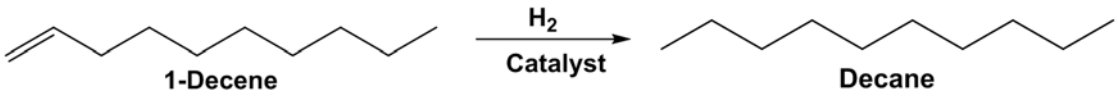

Scheme 2.3 Reaction formula of hydrogenation of 1-decene to decane

In this section, the hydrogenation of olefins in the presence of ruthenium catalyst is discussed by using the frontier orbital theory and a satisfactory explanation is given. In the study of the reaction mechanism using the molecular orbital theory, the most important orbitals are the highest energy filled orbitals (HOMO) and the lowest energy empty molecular orbital (LUMO). The electrons in the occupied molecular orbitals with the highest energy are not held tightly, with the properties of electron donators, while the empty orbitals with the lowest energy LUMOs have stronger affinity to electrons and have the properties of electron acceptors. These two kinds of orbitals play a key role in the chemical reaction process.They are called Frontier-molecular Orbital (FMO).

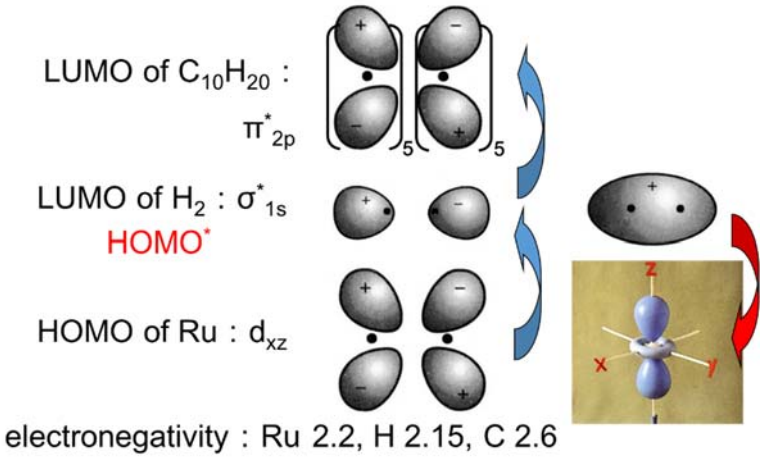

Scheme 2.4 Hydrogenation of decene with Ru catalyst mechanism

The FMO interaction of the two orbitals is analyzed by taking the hydrogenation of 1-decene as an example. It is known that when 1-decene and hydrogen in addition reaction, HOMO of 1-decene molecule and LUMO of hydrogen molecule or LUMO of ethylene molecule and HOMO of hydrogen molecule are symmetrically forbidden. Therefore, the addition of 1-decene and hydrogen can not be directly carried out under heating conditions. To make this reaction feasible, ruthenium or some other transition metal must be used as catalyst. Because the d orbital of ruthenium (HOMO) and the σ* orbital of H_2 (LUMO) have adaptive symmetry, they can react directly with hydrogen molecule, and electrons flow from the full d orbital into the empty σ* orbital of H_2. The H_2 is dissociated into two separate atoms, combined with ruthenium atoms, and then the two hydrogen atoms can be transferred to a 1-decene molecule in a synergistic manner, and these are the paths allowed by orbital symmetry (Scheme 2.4). In conclusion, alkenes can react with hydrogen to form alkanes only in the presence of ruthenium or other transition metals such as Pd and Pt, and the stereochemistry of alkenes is cis-addition.

Table 2.3 Hydrogenation of 1-decene to decane by different Ru^0@POM catalysts

Entry	Catalyst	Conversion(%)[a]	Selectivity(%)[a]
1	$Ru^0@H_3PW_{12}O_{40}$	45	＞99
2	$Ru^0@H_3PMo_{12}O_{40}$	41	＞99
3	$Ru^0@H_4SiW_{12}O_{40}$	42	＞99
4	$Ru^0@Na_7(PW_{11}O_3)$	64	＞99
5	$Ru^0@K_{10}(P_2W_{17}O_{61})$	53	＞99

Reaction conditions: 1-decene (1 mmol), H_2O (12 mL), Ru^0@POM catalyst (0.01 mmol, n_{Ru} : n_{POM}=1 :1), H_2 pressure (1MPa), temperature (20 ^oC), time (1.5 hours). [a]Determined by GC-MS, 1,3-dinitrobenzene as an internal standard.

Freshly prepared POM stabilized Ru^0 nanoparticle nanoclusters were tested for catalytic activity through hydrogenation of 1-decene to decane, thus we can compare and illustrate which kind of POM has better catalytic activity between Keggin and Wells-Dawson species. The reaction formula of hydrogenation of 1-decene to decane is shown in Scheme 2.3. After the hydrogenation reaction the solution of Ru^0@POM was homogeneous without any precipitate formed by bulk ruthenium particles, which indicated that all the solution of Ru^0@POM nanoclusters was stable after reaction.

Table 2.3 gives the results of hydrogenation of 1-decene to decane for different POM stabilized Ru^0 nanoparticles. Different conversions but the same slectivity of decane (＞99%) were observed for different species of POM after 1-decene hydrogenation, and no by-products were observed. The Keggin POM stabilized Ru^0 nanoparticles catalysts ($Ru^0@H_3PW_{12}O_{40}$, $Ru^0@H_3PMo_{12}O_{40}$, $Ru^0@H_4SiW_{12}O_{40}$) showed the similar catalytic activity, with conversion of 1-decene of 45%, 41%, 42%, respectively. Compared with the plenary (i.e. EM_{12}) structure POM catalysts, the conversion efficiency of the catalysts with lacunary structures were better, with

conversion for $Ru^0@Na_7(PW_{11}O_{39})$ and $Ru^0@K_{10}(P_2W_{17}O_{61})$ of 64% and 53% respectively. With the same amount of ruthenium in the catalysts, it seems that the natural properties of heteropoly acid will affect the catalytic activity of catalytic reaction. The catalytic activity of lacunary species catalysts are better than that of plenary species catalysts for hydrogenation of 1-decene.

2.2.4 Aqueous-phase Fischer-Tropsch synthesis

Table 2.4 Results of Fischer-Tropsch synthesis activity over different Ru based catalysts

Catalyst	CO conversion (%)	CO_2 selectivity (%)	HC distribution (%)		
			CH_4	C_2-C_4	C_5^+
$Ru^0@H_3PW_{12}O_{40}$	31.1	39.8	16.0	25.5	58.5
$Ru^0@H_3PMo_{12}O_{40}$	39.0	42.9	8.6	26.8	64.6
$Ru^0@H_4SiW_{12}O_{40}$	50.0	35.8	13.8	26.9	59.3
$Ru^0@K_{10}(P_2W_{17}O_{61})$	21.8	46.9	18.2	17.1	64.7
$Ru^0@Na_7(PW_{11}O_{39})$	25.1	46.5	12.0	11.5	76.5
Ru^0/C	16.0	62.9	5.7	6.6	87.7

Reaction conditions: 2.79×10^{-4} mol Ru catalyst， H_2 / CO = 1 : 1，P= 4 MPa，T = 150 ^oC, t = 18 hrs, H_2O = 12 mL

Traditional F-T synthesis uses heterogeneous catalyst and gas phase reaction in very large plants, liquid phase is a lower energy process and in water the hydrocarbons are easily separated and the aqueous phase catalyst re-used.

As mentioned above, most of the Ru based catalysts are supported mainly on oxides, molecular sieve or carbon. The specific effects include: (1) increasing the specific surface area and providing appropriate pore structure; (2) enhancing the

thermal conductivity of the catalyst, to avoid deactivation of catalyst due to local overheating; (3) to provide active center / acid-base center, to influence the adsorption and desorption of reactants and products, and then to influence the selectivity of reaction products; (4) to improve the mechanical strength and stability of the catalyst.

In aqueous-phase F-T synthesis, we compared a series of Ru^0@POM catalysts and Ru/C catalysts under the same reaction conditions (shown in Table 2.4). The CO conversion with Ru^0@POM catalysts was obviously better than that with Ru/C catalyst. The CO conversion of Ru/C catalyst was only 16%, and the order of CO conversion of Ru^0@POM catalyst was as follows: $Ru^0@H_4SiW_{12}O_{40}$ (50%) > $Ru^0@H_3PMo_{12}O_{40}$, (39%) > $Ru^0@H_3PW_{12}O_{40}$ (31.1%) > $Ru^0@Na_7(PW_{11}O_{39})$ (25.1%) > $Ru^0@K_{10}(P_2W_{17}O_{61})$ (21.8%). We know that the CO conversion of $Ru^0@H_4SiW_{12}O_{40}$ catalyst was 3.1 times higher than Ru/C catalyst in F-T synthesis reaction and CO conversion of $Ru^0@H_4SiW_{12}O_{40}$ catalyst was the best in the Ru^0@POM catalysts we prepared. The selectivity of catalyst to CO_2 in aqueous-phase F-T synthesis reaction was very high, for Ru^0@POM (39.8%, 42.9%, 35.8%, 46.9% and 46.5%), but these were lower than that of Ru/C (62.9%). The high selectivity for CO_2 was due to the water-gas shift reaction which produces CO_2 easily in aqueous system. The selectivity for low carbon hydrocarbons and heavy hydrocarbons of the Ru/C catalyst was 6.6% and 87.7% respectively, whereas for Ru^0@POM catalysts, the selectivity for low carbon hydrocarbons of $Ru^0@H_3PW_{12}O_{40}$, $Ru^0@H_3PMo_{12}O_{40}$, $Ru^0@H_4SiW_{12}O_{40}$, $Ru^0@Na_7(PW_{11}O_{39})$ and $Ru^0@K_{10}(P_2W_{17}O_{61})$ catalysts were 25.2%, 26.8%, 26.9%, 17.1% and 11.5% respectively. The selectivity for heavy hydrocarbons of $Ru^0@H_3PW_{12}O_{40}$, $Ru^0@H_3PMo_{12}O_{40}$, $Ru^0@H_4SiW_{12}O_{40}$, $Ru^0@Na_7(PW_{11}O_{39})$ and $Ru^0@K_{10}(P_2W_{17}O_{61})$ catalysts were 58.5%, 64.6%, 59.3%, 64.7% and 76.5% respectively. Compared with the Ru/C catalyst, the selectivity for low carbon

hydrocarbon products with Ru^0@POM catalysts increased, while the selectivity for heavy hydrocarbon products decreased. This is probably because the direct products of the F-T synthesis reaction, n-alkanes and *α*-olefin, are catalytically cleaved or isomerized by the acidic sites of the Ru^0@POM catalyst, thereby inhibiting the formation of heavy hydrocarbons. Therefore, we can use the unique nature of Ru^0@POM catalysts to improve the selectivity for low carbon hydrocarbons.

It can be seen from the CO insertion reaction mechanism that the activity and conversion of CO hydrogenation will be determined by the ease with which CO is adsorbed and dissociated in the first step. The strength of hydrogenation ability and the ability of carbon chain growth in the second and third steps are the key factors to determine the selectivity of each component in the product. In order to improve the activity of CO hydrogenation and the selectivity of low olefins, we should improve the adsorption and dissociation ability of CO. On the other hand, the hydrogenation ability in the reaction process and the carbon chain growth ability should be controlled by the acid site of the catalyst, so that the activity of CO hydrogenation and the selectivity of low carbon hydrocarbon can reach a higher value.

2.2.5 Electrochemical CO_2 reduction

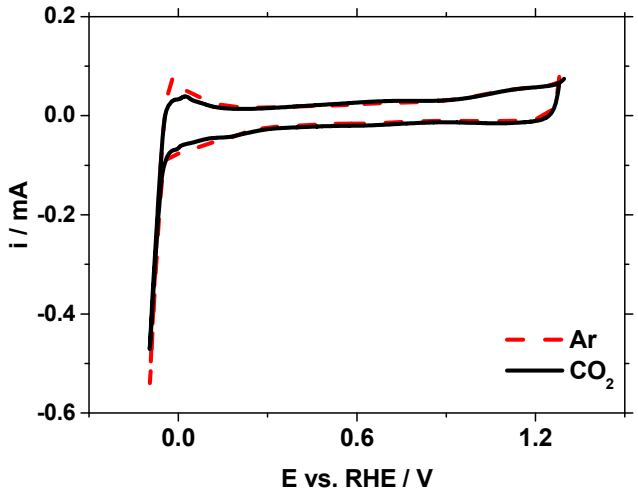

Figure 2.21 Comparison of catalytic performance (CO_2-electroreduction) of bare ruthenium nanoparticles in 0.1 M $HClO_4$ solution. Scan rate: 10 mV s^{-1}, Ru nanoparticles; 6-8 nm.

The cyclic voltammetry curve of PVP stabilized ruthenium nanopraticles modified electrode in saturated CO_2 and N_2 solution is shown in Figure 2.21. The cyclic voltammetry curves illustrate no difference between responses in the presence and absence of CO_2. Hydrogen evolution (proton discharge) dominates electroreduction. By comparison, similar experiments using electrodes modified with POM-stabilised Ru nanoparticles are described below.

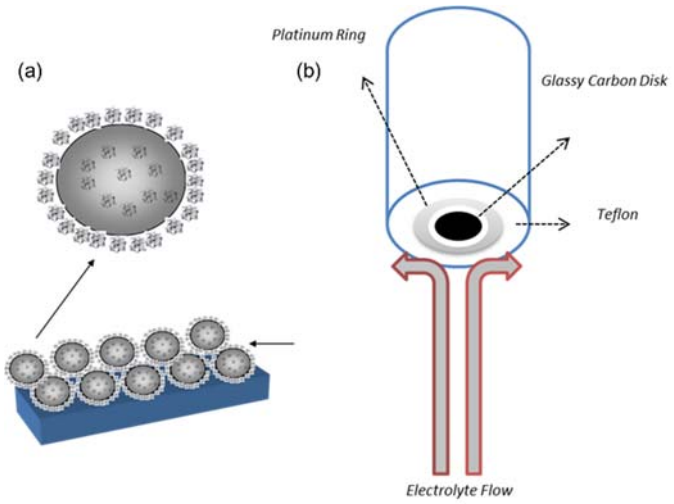

Scheme 2.5 Catalyst(Ru^0@$H_3PW_{12}O_{40}$) (a) and Rotating ring-(Pt) disk-(glassy carbon with catalyst) electrode (b)

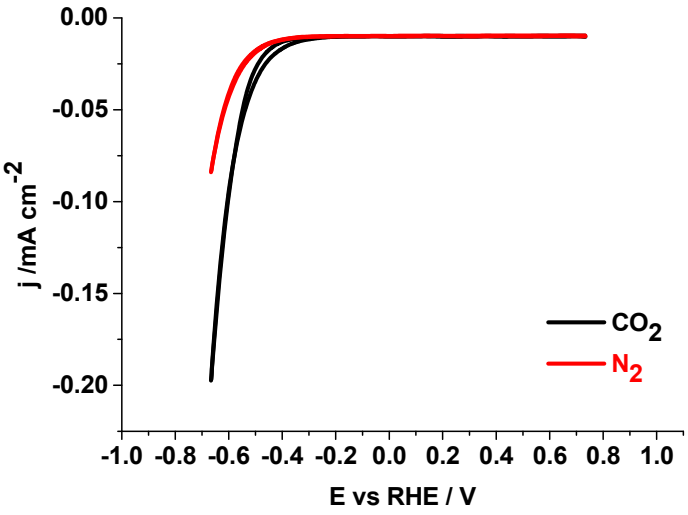

Figure 2.22 Reduction of CO_2 at Ru^0@$H_3PW_{12}O_{40}$ catalyst deposited on glassy carbon electrode in 0.1 M $HClO_4$ solution. Scan rate: 10 mV s^{-1}.

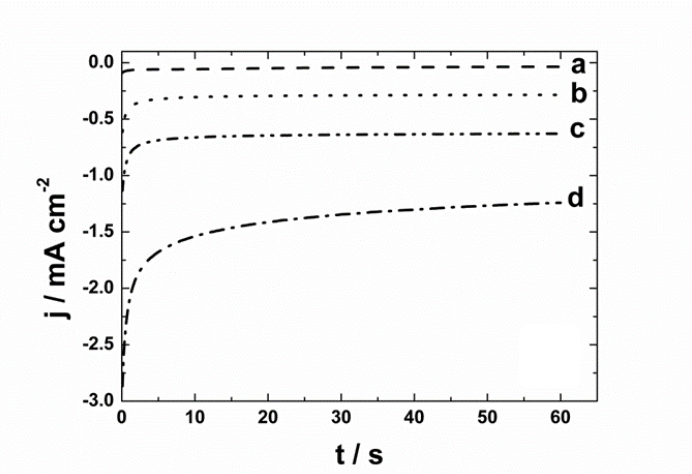

Figure 2.23 Chronoamperometric reduction of CO_2 of (a) 0, (b) -0.15, (c) -0.25 and (d) -0.30 V. at carbon disk with Ru^0@$H_3PW_{12}O_{40}$ catalyst

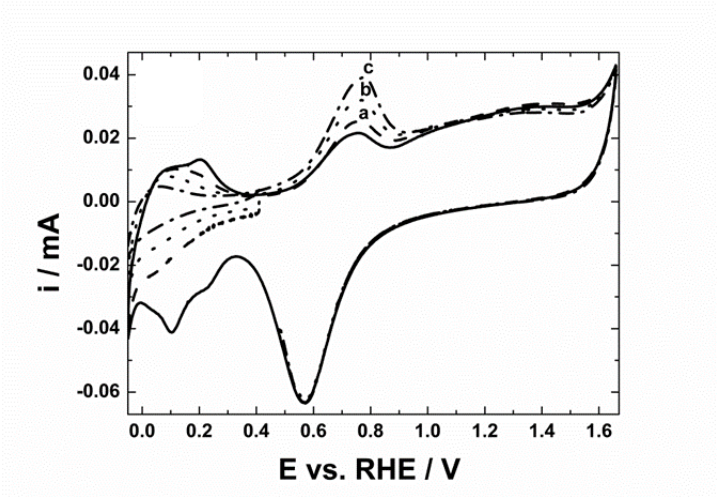

Figure 2.24 Voltammetric oxidation (stripping) of reaction products at Pt ring with $Ru^0@H_3PW_{12}O_{40}$ catalyst. Electrode 0.5 mol·dm^{-3} $HClO_4$, scan rate: 10 mV s^{-1}.

Perchloric acid was used as the model acid electrolyte was used for monitoring oxidation of the reaction products at a Pt ring generated during the CO_2 reduction at the catalytic disk electrode (Scheme 2.5). Figure 2.22 shows the voltammetric responses recorded with $Ru^0@H_3PW_{12}O_{40}$ catalyst in the absence and presence of CO_2 respectively. Under rotating disk electrode (RDE) voltammetric conditions, N_2 was saturated in the electrolyte, and the hydrogen evolution current was generated when the negative potential is scanned to -0.35 V. This shows that the catalytic disk electrode has a lower hydrogen evolution overpotential. When CO_2 was saturated in the electrolyte and the negative potential was less than -0.35 V, the reduction current began to increase, and the more negative the potential shifted, the more the reduction current increased. The potential was more negative than that observed in nitrogen (CO_2 -free) atmosphere. The increase of reduction current was ascribed to the electrochemical reduction of CO_2 and the formation of CO as an intermediate which tended to adsorb strongly and inhibit the performance of the $Ru^0@H_3PW_{12}O_{40}$ catalyst on the surface of the catalytic disk electrode. Apparently,the CO-poisoning effect was diminished due to polytungstate-Ru interactions. Furthermore, the steady state electroreduction currents (Figure 2.23)

using the rotating disk electrode with the $Ru^0@H_3PW_{12}O_{40}$ catalyst were obtained. Chronoamperograms recorded upon application of (a) -0.00, (b) -0.15, (c) -0.25 and (d) -0.30 V showed well-behaved steady-state responses. The electrode showed good stability during electrolysis, and no electrode shedding was found in the electrolyte, which indicated that the catalytic disk electrode was stable in aqueous $HClO_4$. With the increase of the RDE chronoamperometric currents, the electrolysis potential decreased.

During RDE stripping-type experiments (Figure 2.24), with more negative potentials applied to the catalytic disk electrode, the oxidation (stripping) peaks tended to increase. This result may reflect formation of individual CO_2 reduction products under different electroreduction conditions or their generation in larger amounts upon application of more negative potentials. Upon application of the minimum negative reduction potential of -0.23 V (where contribution from proton discharge and hydrogen evolution is negligible) to the catalytic disk electrode, a single stripping (oxidation) peak was observed (at Pt ring). The other stripping voltammetric peaks (developed on Pt ring at about 0.6-0.8 V) stretched (Figure 2.24 a, b, c) seemed to result from the overlapping of two or more peaks, related to the generation of adsorbates containing -CHO or -CHO groups in addition to CO.

2.3 Conclusions

A series of ruthenium nanoparticles stabilized POM nanoclusters (Ru^0@$H_3PW_{12}O_{40}$, Ru^0@$H_3PMo_{12}O_{40}$, Ru^0@$H_4SiW_{12}O_{40}$, Ru^0@$Na_7(PW_{11}O_{39})$ and Ru^0@$K_{10}(P_2W_{17}O_{61})$) were synthesized using a hydrogen reduction method. The Ru^0@POM nanoclusters have been characterization by analysis UV-Vis, FT-IR, XRD, TEM and XPS and their stability and redispersion was demonstrated.

The Ru^0@POM catalysts were active for hydrogenation of 1-decene, and it was observed that the conversion depended on which kind of POM was used. In our test, the order was $[PW_{11}O_{39}]^{7-}$ > $[P_2W_{17}O_{61}]^{10-}$ > $[PW_{12}O_{40}]^{3-}$ > $[SiW_{12}O_{40}]^{4-}$ > $[PMo_{12}O_{40}]^{3-}$, the catalytic activity of lacunary species catalysts were better than plenary species catalysts.

In aqueous-phase Fischer-Tropsch synthesis, under the conditions of reaction pressure of 4.0 MPa, reaction temperature of 150 °C and reaction time of 18 hours, the CO conversion of the new Ru^0@POM catalysts were higher than that of Ru/C catalyst. Among them, the CO conversion rate of Ru^0@$H_4SiW_{12}O_{40}$ is 3.1 times higher than that of Ru/C. The selectivity for low carbon hydrocarbons was higher than that of the Ru/C catalyst, and the low hydrocarbon selectivity of Ru^0@$H_4SiW_{12}O_{40}$ was as high as 26.9%. At the same time, the selectivity for CO_2 was increased because of the water-gas shift reaction. The results suggest that the new Ru^0@POM catalysts can effectively promote the cracking of high carbon hydrocarbons and reduce the selectivity for high carbon hydrocarbons. The improved selectivity for low carbon hydrocarbons is ascribed to the formation of acidic sites. A new bifunctional type of Ru^0@POM catalyst with acid and supported ruthenium was prepared. Our idea is to exploit the synergistic behavior of Ru nanoparticles and POMs by creating a Ru-POM interface in POM-stabilized Ru nanoparticles. In the future, by optimising the conditions, the Ru^0@POM catalysts

can be applied to some important industrial processes such as F-T synthesis, hydrodesulfurization ect.

Commercially available ruthenium nanoparticles do not exhibit significant electrocatalytic activity toward CO_2-reduction in acid medium (the reduction is dominated by hydrogen evolution or proton discharge). In acid medium, POM stabilized Ru nanoparticles ($Ru^0@H_3PW_{12}O_{40}$) produced much higher electroreduction currents in the presence of carbon dioxide than in the absence CO_2. Adsorbed polytungstates are likely to interact with metallic Ru sites, inhibit hydrogen evolution (shift proton discharge to more negative potentials) and absorb reactive hydrogen to form heteropolyblues. The polytungstate adsorbates on the Ru nanoaprticles appear to modify the electronic nature of ruthenium, and decrease CO catalyst poisoning, possibly via competition with CO for Ru catalytic sites. Consequently, the phosphotungstate modified Ru nanostructures are more active than conventional Ru nanoparticles.

2.4 Experimental

2.4.1 General Chemicals

All chemicals were purchased from commercial suppliers (Alfa Aesar, Sigma Aldrich, Fisher Scientific, Acros Organics) and used without any purification. Distilled water was used throughout all this work. All manipulations of air-sensitive materials were carried out using standard Schlenk techniques under nitrogen and a glove-box with a recirculation system.

2.4.2 Instrumentation

2.4.2.1 Fourier transform infrared spectroscopy (FT-IR)

FT-IR spectra were recorded on a Bruker Alpha spectrometer using a Platinum ATR module. Spectra were recorded for dried solid powder samples after vacuum drying for 5 hours.

2.4.2.2 Ultraviolet–visible spectroscopy (UV-Vis)

UV-Vis spectra were recording on a UV-1800 Shimadzu UV spectrometer, over the range 200~900 nm, with a resolution of 2.00 nm. The aqueous samples were measured in 1 cm quartz cuvettes.

2.4.2.3 Powder X-ray diffraction (XRD)

Powder XRD analyses were recorded on a Rigaku Ultima IV diffractometer with Cu Kα radiation, and the scanning angle range was 5~90 degrees at 40 Kv and 40 mA.

2.4.2.4 X-ray photoelectron spectroscopy (XPS)

XPS spectra were recorded on a PHI Quantum-2000 system with Al Kα X-ray source. The samples were pressed into pieces and then measured.

2.4.2.5 Transmission electron microscopy (TEM)

TEM photographs were taken using a 50 kV~300 kV high resolution transmission electron microscope (TECNAI F-30) from FEI, Holland. After ultrasonic dispersion of the samples, they were deposited onto a copper net.

2.4.2.6 Gas chromatography-mass spectrometer (GC-MS)

GC-MS ananlysis was performed on a Varian CP 3800 GC coupled to a Saturn 2200 ion trap MS instrument. The column with GC we used was the Varian FactorFour VF-5ms CP 8944 (30m x 0.25mm x 0.25um).

2.4.2.7 Gas chromatography (GC)

GC analysis used a GC 2060 instrument. The gaseous products were analysed by a gas chromatograph equipped with a thermal conductivity detector (TCD) which is connected to a TDX-01 packed column and a flame ionization detector (FID) which is using an alumina capil-lary column. The products in the liquid phase were analysed by a gas chromatograph equipped with an FID, PONA and Bond-Q capillary columns was connected to FID.

2.4.2.8 Electrochemical measurements

Electrochemical experiments were performed with CH Instruments (Austin, TX, USA) Model 750D and 920D workstations. Rotating ring disk electrode (RRDE) experiments were executed using a variable speed rotator (Pine Instruments, USA).

2.4.3 Synthesis and Catalysis

2.4.3.1 Synthesis of $[(DMSO)_2H][trans\text{-}Ru(DMSO)_2Cl_4]$[60]

In an oven-dried Schlenk flask, a mount of commercial $RuCl_3$ (0.75 g, 3.6 mmol) was partially dissolved in DMSO (4 mL), and 37% aqueous HCl (0.5 mL) added. The mixture was stirred and heated to 80 ^oC and keep this temperature in 30 min until $RuCl_3$ was totally dissolved. The resultant red solution was the heated to 100 ^oC and allowed to stir for 20 min. The color of mixture is gradually changed from deep red to bright orange. The orange transparent solution was cooled to room temperature followed by acetone (15 mL) and then stored in the fridge, big red-orange crystal was formed after 24 hours. The crystal was filtered with a Buchner funnel, vacuum dried to obtain a red- orange crystal powder, which was washed with cold acetone and diethyl ether (yield 70%).

2.4.3.2 Synthesis of $Na[trans\text{-}Ru(DMSO)_2Cl_4]$[60]

In an oven-dried Schlenk flask, a sample of ground $[(DMSO)_2H][\textit{trans}\text{-}Ru(DMSO)_2Cl_4]$ (0.69 g, 1.24 mmol) was gently dissolved in the mixture of H_2O (0.45 mL) and ethanol (30 mL). The clear red-orange solution was added NaCl (109 mg, 1.86 mmol) dissolved in H_2O (0.45 mL). The product of light orange crystal was rapidly precipitated in the solution. The crystal was filtered with a Buchner funnel, vacuum dried to obtain a light orange microcrystal powder, which was washed with cold ethanol and diethyl ether. The complex was recrystallized by addition of small amounts of acetone and diethyl ether (yield 66%).

2.4.3.3 Synthesis of $K_6[P_2W_{18}O_{62}]\cdot 19H_2O$[61]

A sample of $Na_2WO_4{\cdot}2H_2O$ (100 g, 0.38 mol) was dissolved in water (250 mL), followed by the addition of 85% orthophosphoric acid (105 mL, 1.55 mol). The solution was heated to 50 ^oC at reflux for 5 h. If any greenish coloration appeared, it was removed by several drops of bromine. The solution was cooled to room temperature followed by ammonium chloride (50 g), and allowed to stir for 10 min. The yellow-green salt was removed by filtering, dissolved in water (100 mL) and a precipitate formed immediately with ammonium chloride (25 g). The mixture was filtered before stirring 20 min, the precipitate was dissolved in 50 ^oC water (100-200 mL). After cooling to room temperature, the solution was added a quantity of potassium chloride (20 g, 0.27 mol) to formed pale green solid. The solid was filtered and redissolved in 80 ^oC water (100 mL) which was enabled white needles of $K_{14}NaP_5W_{30}O_{11}.XH_2O$ to be removed by filtration. The solution was then refluxed for hours. After cooling, the solution was added potassium chloride (10 g, 0.24 mol) to precipitate $K_6[P_2W_{18}O_{62}]\cdot 19H_2O$ (yield 92%).

2.4.3.4 Synthesis of $K_{10}[P_2W_{17}O_{61}]\cdot 20H_2O$[61]

A sample of $K_6[P_2W_{18}O_{62}]\cdot 19H_2O$ (80 g, 0.012 mol) in water (200 mL) was added a solution of potassium hydrogen carbonate (20 g, 0.2 mol) in water (200 mL) and a white precipitate was formed immedietaly. The precipitate was filtered, redissolved in 95 ^oC water (500 mL) and then cooled to room temperature, during which time the snowlike crystals formed (yield 88%). The crystals were isolated by filtration and dried under high vacuum.

2.4.3.5 Synthesis of $Na_7[PW_{11}O_{39}]\cdot 11H_2O$[61]

A beaker was charged with $Na_2HPO_4{\cdot}12H_2O$ (7.2 g, 0.02 mol), $N_2WO_4{\cdot}2H_2O$ (74.2 g, 0.225 mol) and water (150 mL). The solution was treated with nitric acid to

approximately PH = 4.8 and heated to 100 °C with rapid stirring. The solution was cooled to room temperature after the water (75 mL) was evaporated and acetone (80-100 mL) was added with continuous stirring to give two layers. The acetone layer was removed using a separatory funnel, and repeat this step a few times until no NO_3^- in removed acetone by brown ring test. The resulting aqueous layer was dried in oven to give the white product (yield 82%).

2.4.3.6 Synthesis of Ru@$H_3PW_{12}O_{40}$ nanoparticle solution

Added $H_3PW_{12}O_{40}$ (28.8 mg, 0.01mmol) and Na[*trans*-Ru(DMSO)$_2$Cl$_4$] (4.2 mg, 0.01 mmol) to reaction flask with water (12 mL), then reduced under 1.0 MPa H_2 at 50 °C for 5 hours in an 50 mL stainless steel autoclave with a stirring speed of 600 rpm. After reaction, the autoclave was cooled to room temperature, to give blue black stable and homogeneous sample solutions, and no deposits were formed.

2.4.3.7 Synthesis of Ru@$H_3PMo_{12}O_{40}$ nanoparticle solution

Added $H_3PMo_{12}O_{40}$ (18.3 mg, 0.01mmol) and Na[*trans*-Ru(DMSO)$_2$Cl$_4$] (4.2 mg, 0.01 mmol) to reaction flask with water (12 mL), then reduced under 1.0 MPa H_2 at 50 °C for 5 hours in an 50 mL stainless steel autoclave with a stirring speed of 600 rpm. After reaction, the autoclave was cooled to room temperature, to give blue black stable and homogeneous sample solutions, and no deposits were formed.

2.4.3.8 Synthesis of Ru@$H_4SiW_{12}O_{40}$ nanoparticle solution

Added $H_4SWi_{12}O_{40}$ (28.78 mg, 0.01mmol) and Na[*trans*-Ru(DMSO)$_2$Cl$_4$] (4.2 mg, 0.01 mmol) to reaction flask with water (12 mL), then reduced under 1.0 MPa H_2 at 50 °C for 5 hours in an 50 mL stainless steel autoclave with a stirring speed of 600

rpm. After reaction, the autoclave was cooled to room temperature, to give black stable and homogeneous sample solutions, and no deposits were formed.

2.4.3.9 Synthesis of Ru@$K_{10}[P_2W_{17}O_{61}]$ nanoparticle solution

Added $K_{10}[P_2W_{17}O_{61}]\cdot 20H_2O$ (52.5 mg, 0.01mmol) and Na[*trans*-$Ru(DMSO)_2Cl_4$] (4.2 mg, 0.01 mmol) to reaction flask with water (12 mL), then reduced under 1.0 MPa H_2 at 50 ^oC for 5 hours in an 50 mL stainless steel autoclave with a stirring speed of 600 rpm. After reaction, the autoclave was cooled to room temperature, to give black stable and homogeneou sample solutions, and no deposits were formed.

2.4.3.10 Synthesis of Ru@$Na_7[PW_{11}O_{39}]$ nanoparticle solution

Added $Na_7[PW_{11}O_{39}]\cdot 11H_2O$ (30.4 mg, 0.01mmol) and Na[*trans*-$Ru(DMSO)_2Cl_4$] (4.2 mg, 0.01 mmol) to reaction flask with water (12 mL), then reduced under 1.0 MPa H_2 at 50 ^oC for 5 hours in an 50 mL stainless steel autoclave with a stirring speed of 600 rpm. After reaction, the autoclave was cooled to room temperature, to give black stable and homogeneous sample solutions, and no deposits were formed.

2.4.3.11 General procedure for hydrogenation of decene to decane

Catalyst (Ru@POM, 0.01 mmol) in water solution (12 mL) and decene (1 mmol, 189 μL)) and water (12 mL) were placed in a Parr reactor and heated at 20 ^oC under different H_2 (1 MPa) before being allowed to stir for 1 hour. Upon cooling to room temperature, the reaction mixture was added diluted with diethyl ether (15 mL). The organic layer was separated, dried with magnesium sulfate, filtered and solvent removed under reduced vacuum. The resulting residue was analyzed by ^1H NMR spectroscopy to determine conversion.

2.4.3.12 General procedure for aqueous-phase Fischer-Tropsch synthesis

An aqueous solution of the freshly prepared Ru@POM (POM = $H_3PW_{12}O_{40}$, $H_3PMo_{12}O_{40}$, $H_4SWi_{12}O_{40}$, $K_{10}[P_2W_{17}O_{61}]$ and $Na_7[PW_{11}O_{39}]$) was prepared from $Na[trans\text{-}Ru(DMSO)_2Cl_4]$ (2.79 mmol) and POM (2.79 mmol) placed in a stainless steel autoclave (50 mL). The autoclave was heated to 150 ^oC with stirring 18 hours at 800 rmp in the presence of 2.0 MPa CO and 2.0 MPa H_2. After reaction, the autoclave was cooled to room temperature, the gas phase products was collected and analyzed by GC. The solution phase was added to cyclohexane (10 mL) and n-Hexadecane (10 μL), then heated to 150 ^oC with stirring 2 hours and cooled to room temperature. The organic phase products were then analyzed by GC.

2.4.3.13 General procedure for electrochemical CO_2 reduction

To the catalyst (Ru@POM, 1 mmol) in water (12 mL) was added Nafion (20% by weight) as binder and the mixture was sonicated for 20 min. The suspension (7 μL) was dropped onto the glassy carbon electrode surface including a glassy carbon disk (with geometric area of 0.247 cm^2) and a Pt ring by using a micropipette. The resulting layer was dried on the air for 30 min at room temperature. The collection efficiency (N) of the RRDE assembly, as determined from the ratio of ring and disk currents (at 1600 rpm) using the argon-saturated $K_3[Fe(CN)_6]$ (5 $mmol/dm^3$) in K_2SO_4 solution (0.1 mol/dm^3), was equal to 0.388. The inert counter electrode was a gold rod. A Hg/Hg_2SO_4 electrode was used as a reference electrode, but all potentials were reported versus the Reversible Hydrogen Electrode (RHE). The pH values of the pure and CO_2-saturated potassium bicarbonate (0.1 mol/dm^3) (electrolyte) were 8.4 and 6.8, respectively. They were considered when recalculating and expressing the potential values against RHE. During diagnostic voltammetric experiments, the electrolyte was saturated with CO_2 for at least 30

min. The voltammetric responses were recorded under conditions of gentle CO_2 - bubbling.

2.5 Referance

1. J. Z. Zhang, *Acc. Chem. Res.*, 1997, **30**, 423-429.

2. D. M. Dotzauer, J. Dai, L. Sun and M. L. Bruening, *Nano Lett.*, 2006, **6**, 2268-2272.

3. A. Haryono and W. H. Binder, *Small*, 2006, **2**, 600-611.

4. P. V. Kamat, *J. Phys. Chem. B, 2002, **106**, 7729–7744*

5. L. Zhang, Y. Shen, A. Xie, S. Li and C. Wang, *J. Mater. Chem.*, 2008, **18**, 1196-1203.

6. L. Ruhlmann, C. Costa‐Coquelard, S. Sorgues and I. Lampre, *macromol. symp.*, 2008, **270**, 117-122.

7. R. Güzel, Z. Üstündağ, H. Ekşi, S. Keskin, B. Taner, Z. G. Durgun, A. A. İ. Turan and A. O. Solak, *J. Colloid Interface Sci.*, 2010, **351**, 35-42.

8. P. Lei, C. Chen, J. Yang, W. Ma, J. Zhao and L. Zang, *Environ. Sci. Technol.*, 2005, **39**, 8466-8474.

9. C. Chen, W. Zhao, P. Lei, J. Zhao and N. Serpone, *Chem. Eur. J.*, 2004, **10**, 1956-1965.

10. F. Fischer and H. Tropsch, *Brennstoff-Chem*, 1923, **4**, 276-285.

11. Y. Wang, J. Kang and Q. Zhang, *Petrochem Technol*, 2009, **38**, 1225-1263.

12. Y. Sun, J. Chen, J. Wang, L. Jia, B. Hou, D. Li and J. Zhang, *Cuihua Xuebao/Chi. J. Catal.*, 2010, **31**, 1505–1511.

13. F. Botes, J. Niemantsverdriet and J. Van De Loosdrecht, *Catal. Today*, 2013, **215**, 112-120.

14. J. Hindermann, G. Hutchings and A. Kiennemann, *Cat. Rev. Sci. Eng.*, 1993, **35**, 1-127.

15. E. Iglesia, *Appl. Catal. A: General*, 1997, **161**, 59-78.

16. B. H. Davis, *Catal. Today*, 2009, **141**, 25-33.

17. G. P. Van Der Laan and A. Beenackers, *Cat. Rev.*, 1999, **41**, 255-318.

18. M. Vannice, *Cat. Rev. Sci. Eng.*, 1976, **14**, 153-191.

19. J. Van de Loosdrecht, A. Van der Kraan, A. Van Dillen and J. Geus, *J. Catal.*, 1997, **170**, 217-226.

20. A. Dalai and B. Davis, *Appl. Catal. A: General*, 2008, **348**, 1-15.

21. D. Schanke, A. Hilmen, E. Bergene, K. Kinnari, E. Rytter, E. Ådnanes and A. Holmen, *Catal. Lett.*, 1995, **34**, 269-284.

22. P. Nema, S. Nema and P. Roy, *Renew. Sust. Energ. Rev.*, 2012, **16**, 2329-2336.

23. E. J. Maginn, *J. Phys. Chem. Lett,* 2010, **1**, 3478-3479.

24. S. N. Riduan and Y. Zhang, *Dalton Trans.*, 2010, **39**, 3347-3357.

25. M. M. Maroto-Valer, C. Song and Y. Soong, *Environmental challenges and greenhouse gas control for fossil fuel utilization in the 21st century*, Springer Science & Business Media, 2012.

26. D. Damiani, J. T. Litynski, H. G. McIlvried, D. M. Vikara and R. D. Srivastava, *Greenhouse Gases: Sci. Technol.*, 2012, **2**, 9-16.

27. C. Song, *Catal. Today*, 2006, **115**, 2-32.

28. D. T. Whipple and P. J. Kenis, *J. Phys. Chem. Letters*, 2010, **1**, 3451-3458.

29. G. A. Olah, G. S. Prakash and A. Goeppert, *J. Am. Chem. Soc.*, 2011, **133**, 12881-12898.

30. T. Sakakura, J.-C. Choi and H. Yasuda, *Chem. Rev.*, 2007, **107**, 2365-2387.

31. M. Jitaru, D. Lowy, M. Toma, B. Toma and L. Oniciu, *J. Appl. Electrochem.*, 1997, **27**, 875-889.

32. S. Bensaid, G. Centi, E. Garrone, S. Perathoner and G. Saracco, *ChemSusChem*, 2012, **5**, 500-521.

33. C. Costentin, M. Robert and J.-M. Savéant, *Chem. Soc. Rev.*, 2013, **42**, 2423-2436.

34. N. S. Spinner, J. A. Vega and W. E. Mustain, *Sci. Technol.*, 2012, **2**, 19-28.

35. A. S. V. Gasque, I. Chorkendorff and I. Stephens, 2013.

36. H. Yin, X. Mao, D. Tang, W. Xiao, L. Xing, H. Zhu, D. Wang and D. R. Sadoway, *Energ. Environ. Sci.*, 2013, **6**, 1538-1545.

37. D. Cheng, F. R. Negreiros, E. Apra and A. Fortunelli, *ChemSusChem*, 2013, **6**, 944-965.

38. J. Wu, F. G. Risalvato, P. P. Sharma, P. J. Pellechia, F. S. Ke and X. D. Zhou, *J. Electrochem. Soc.*, 2013, **160**, 953-957.

39. E. E. Benson, C. P. Kubiak, A. J. Sathrum and J. M. Smieja, *Chem. Soc. Rev.*, 2009, **38**, 89-99.

40. B. Viswanathan, *Int. J. Photoenergy*, 2012, **11**, 1110-1120,.

41. J. Lee, Y. Kwon, R. L. Machunda and H. J. Lee, *Chemistry*, 2009, **4**, 1516-1523.

42. X. Yan, H. Liu and K. Y. Liew, *J. Mater. Chem.*, 2001, **11**, 3387-3391.

43. G. M. Varga Jr, E. Papaconstantinou and M. T. Pope, *Inorg. Chem.*, 1970, **9**, 662-667.

44. T. Rajkumar and G. R. Rao, *Chem. Sci.*, 2008, **120**, 587-594.

45. G. R. Rao and T. Rajkumar, *J. Colloid Interface Sci.*, 2008, **324**, 134-141.

46. A. Yokozeki, D. J. Kasprzak and M. B. Shiflett, *Phys. Chem*, 2007, **9**, 5018-5026.

47. S. Miao, Z. Liu, B. Han, J. Huang, Z. Sun, J. Zhang and T. Jiang, *Angew. Chem.*, 2006, **118**, 272-275.

48. S. Alayoglu, A. U. Nilekar, M. Mavrikakis and B. Eichhorn, *Nat. Mater.*, 2008, **7**, 333-338.

49. L. Li and Y. Xing, *J. Phys. Chem. C*, 2007, **111**, 2803-2808.

50. S. Fu, J. Chu, X. Chen, W. Li and Y.-F. Song, *Ind. Eng. Chem.*, 2015, **54**, 11534-11542.

51. T. Cai, Y. Liao, Z. Peng, Y. Long, Z. Wei and Q. Deng, *J. Environ. Sci*, 2009, **21**, 997-1004.

52. X. Cuixia, Y. Kedi, L. Zili, Q. Zuzeng, H. Wei, D. Qianwen, J. Zhang and F. Zhang, *Chin. J. Chem. Eng.*, 2014, **22**, 305-311.

53. Y. Y. Liu, W. Zhao, S. Zhang and Y. Fang, *Appl. Surf. Sci.*, 1992, **59**, 299-303.

54. R. Kötz, H. Lewerenz and S. Stucki, *J. Electrochem. Soc.*, 1983, **130**, 825-829.

55. K. C. Park, I. Y. Jang, W. Wongwiriyapan, S. Morimoto, Y. J. Kim, Y. C. Jung, T. Toya and M. Endo, *J. Mater. Chem.*, 2010, **20**, 5345-5354.

56. R. Liu, S. Li, X. Yu, G. Zhang, S. Zhang, J. Yao and L. Zhi, *J. Mater. Chem.*, 2012, **22**, 3319-3322.

57. P. A. Jalil, M. Faiz, N. Tabet, N. Hamdan and Z. Hussain, *J. Catal.*, 2003, **217**, 292-297.

58. A. Bielański, R. Dziembaj, A. Małecka-Lubańska, J. Poźniczek, M. Hasik and M. Drozdek, *J. Catal.*, 1999, **185**, 363-370.

59. L. Pesaresi, D. Brown, A. F. Lee, J. Montero, H. Williams and K. Wilson, *Appl. Catal. A: General*, 2009, **360**, 50-58.

60. E. Alessio, G. Balducci, M. Calligaris, G. Costa, W. M. Attia and G. Mestroni, *Inorg. Chem.*, 1991, **30**, 609-618.

61. A. P. Ginsberg, *Inorganic syntheses*, John Wiley & Sons, 1990.

Chapter 3

Polymer Immobilized Ionic Liquids Containing Polyoxometalate-Stabilized Ruthenium Nanoparticles

Chapter 3. Polymer immobilized ionic liquids containing polyoxometalate-stabilized ruthenium nanoparticles

3.1 Introduction

Ru^0 nanoparticles and POMs have been shown to act in tandem for (i) activation of H_2 and (ii) creation of strong Brønsted acidity, but these POM-stabilised Ru^0 nanoparticles are difficult to recover and recycle. The high solubility of POMs in aqueous solution has limited the application of Ru^0@POM nanoclusters in water, and this Chapter describes attempts to address this problem through the use of water-tolerant polymer-immobilised ionic liquid phase (PIILP) supports upon which to immobilize Ru^0/POM nanoparticles, to give Ru^0@POM/PIILP bifunctional catalysts.

3.1.1 Hydrogenation of 5-hydroxymethylfurfural (HMF)

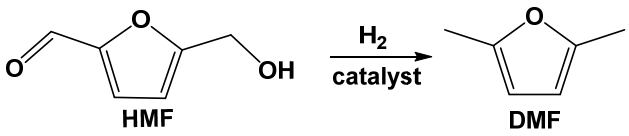

Scheme 3.1 Hydrogenation of HMF to DMF

Over time, the conflicting decrease in non-renewable petroleum resources and the increasing demand for petroleum fuel will become increasingly prominent.[1] The search for renewable resources to replace petroleum as fuel has great significance in reducing the dependence on petroleum fuels. 5-Hydroxymethylfurfural (HMF) is one of the intermediate products of cellulose degradation and it contains a carbonyl group and a hydroxyl group in the molecule.[2] Many furan chemical products can be derived from HMF, by e.g. hydrogenation, oxidative dehydrogenation, esterification and halogenation.[3-6] The catalytic hydrogenation of HMF can yield 2,5-dimethylfuran (DMF)

(Scheme 3.1), which has an energy density of 30 MJ/L, close to that of gasoline (31.6 MJ/L).[7] Moreover, DMF has a low boiling point (336.5K), is insoluble in water, and can be used to increase the octane number of gasoline. Due to its excellent combustion performance and renewable properties, DMF is considered as one of the most likely alternative fuels. Although DMF can be obtained by catalytic hydrogenation of HMF, there is no reasonable and efficient catalytic hydrogenation method for the preparation of DMF. Studies of the catalytic reduction of HMF to DMF, provide a good foundation for the preparation and application of HMF, and provide a reference for the conversion of renewable biomass resources to energy.

Catalytic systems for the preparation of DMF can be divided into three categories, which include monometallic catalysts (such as Ru, Pd and Ni), bimetallic catalysts (such as Ni-Pd, Cu-Ru) and Ni-W_2C, Ru-CoOx with transition metal additives, on supports such as activated carbon, ZrO_2, SiO_2 and CeO_2.[2,8,9] Although non-noble metal catalysts are cheaper, the conversion of DMF are poor due to its low catalytic activity. In contrast, transition metal catalyst has good catalytic activity and stability, because the transition metal contains d-orbital, it can combine with oxygen, which shows the properties of Lewis acid. Therefore, the oxygen-containing groups such as alcohol-hydroxyl and aldehyde group in HMF molecule are activated, the aldehyde group is hydrogenated to form the CH_2-OH bond under the action of metal site, and then the C-O bond is selectively broken under the action of acidic site, thus enhancing the selectivity of DMF. In this metal-acid type catalyst, the synergism of metal site and acid site is very important. In addition, the occurrence of side reactions such as hydrogenation of the furan ring due to the strong hydrogenation activity of the metal sites, and the ring opening of the furan ring due to the too strong acidity, etc.. Therefore, the prevention of side reactions is

one of the key factors to be considered in the reaction process. Summarizing the previous research results of HMF conversion to DMF, we conclude that HMF easily undergoes side reactions in aqueous systems, which leads to low selectivity to DMF. The highest selectivity to DMF was observed in the THF solution, compared with isopropanol, methanol, butanol, n-butyl alcohol, tetrahydrofuran and hexane solution.[2,9-11] Hu and Saha et al. reported that THF solvent can promote the hydrogenation of HMF into 2,5-dimethylfuran.[12,13] Zu and Nagpure et al. demonstrated that Ru/C has the best catalytic activity for hydrogenation of HMF to DMF compared to Raney Ni, Pt/C, Pd/C, Ru/C, catalysts, which is bacause Ru has superior activity in hydrogenation of polyols to alkanes.[14-18]

α,β-Unsaturated aldehydes and ketones are widely used in daily life. Their hydrogenation products are important fine chemical products, and occupy an important position in the perfume, chemical, pharmaceutical and other industries. Because of the C=O and C=C bonds in α,β-unsaturated aldehyde ketones, there are various possible products of catalytic hydrogenation. Different hydrogenation sites and degrees of hydrogenation will produce many different kinds of hydrogenation products. Excessive hydrogenation will also produce alkanes. Since the C=C bond and the C=O bond form a conjugated system, the bond energy of the C=C bond is relatively lower, so that the hydrogenation of the other unsaturated bond C=O bond becomes very difficult. The selective control of the reduction of this kind of compound is therefore important in industrial production and scientific experimental research.

3.1.2 Hydrogenation of cinnamaldehyde (CAL)

Cinnamaldehyde (CAL) is a representative *α, β*-unsaturated aldehyde. In recent years, many researchers have done a lot of research on selective hydrogenation of cinnamaldehyde. Its hydrogenation products are important

organic synthetic materials, which are widely used in the synthesis of flavours, spices, cosmetics, medicine and fungicides.[19-27] The bond energy of C=O in cinnamaldehyde structure (715 KJ/mol) is higher than that of C=C (615 KJ/mol), which makes the hydrogenation reaction more likely to occur on the C=C double bond.[28,29] But the hydrogenation products of CAL were found mostly to be a mixture of hydrocinnamic aldehyde (HCAL), cinnamyl alcohol (COL) and hydrocinnamic alcohol (HCOL) (Scheme 3.2).[30] Therefore, the design of a hydrogenation catalyst with moderate activity and high selectivity is of great significance in theoretical research and industrial application.

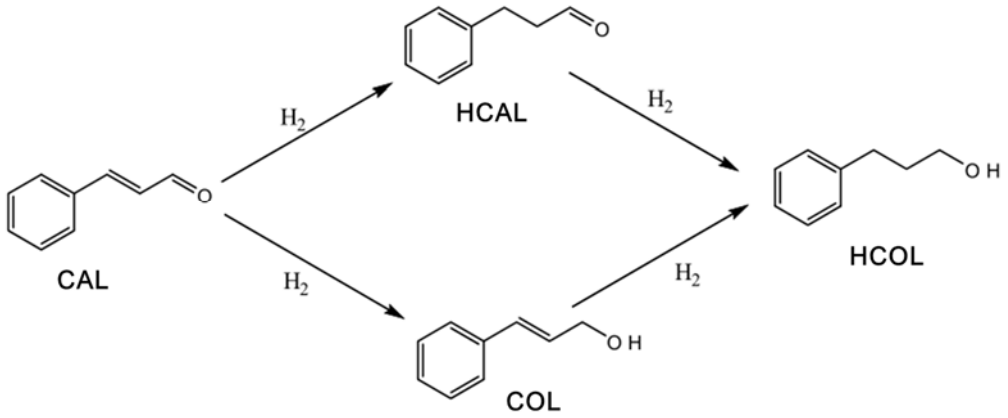

Scheme 3.2 Hydrogenation of CAL to HCAL, COL and HCOL

Cordier and Gallezot et al. reported hydrogenation of CAL using platinum group metal as catalysts as early as the 1980s.[31-33] The selectivity order of the formation of COL is Os > Ir > Pt > Ru > Rh > Pd, which is related to the width of the d band of metal.[24,34,35] The wider the d-band, the stronger the four-electron repulsion of the unsaturated aldehyde, and as a result, the harder for C=C to be adsorbed. The d-band width of Pd is the smallest, so the η^4 type conjugated adsorption is easier to perform. Since the activation energy required for C=C hydrogenation is lower than that of C=O.[31] However, the hydrogenation selectivity of Pt and Ru can be adjusted by loading or doping.[36,37] Ru is one of

the cheaper precious metals and can be used to selectively catalyze the hydrogenation of CAL to COL, and has been studied extensively. In order to suppress side reactions and increase the selectivity of target products, researchers have tried to use suitable supports and additives. In the optimized ruthenium-based catalysts, commonly used supports are C, certain oxides and molecular sieves, widely commonly used additives are Sn.

3.1.3 Hydrogenation of furfural

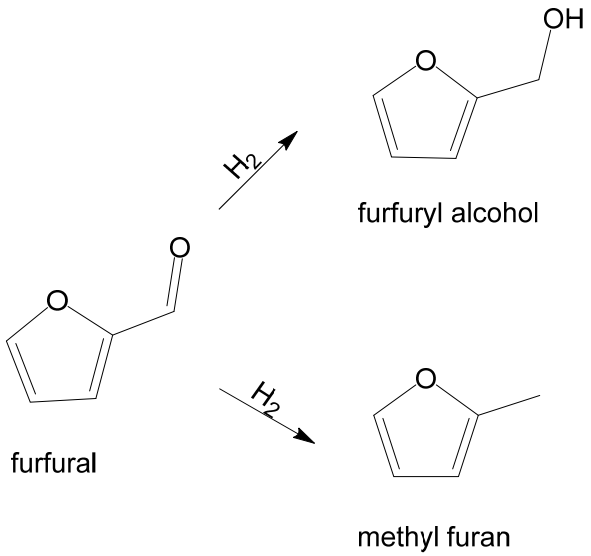

Scheme 3.3 Hydrogenation of furfural

Furfural is an important chemical raw material. It is mainly produced from renewable biomass resources such as corn cobs, rice husks and bagasse.[38-40] These biomass resources are hydrolyzed to pentose under the action of acidic catalysts, and then dehydrated and cyclized to obtain furfural. Furfural is very active chemically, result from the furan ring and the aldehyde group. The furan ring contains two double bonds and a ring ether bond, which can undergo chemical reactions such as hydrogenation, oxidation, decarburization and condensation to give many derivatives. The carbonyl group is one of the active sites of furfural, and the carbonyl carbon atom is sp^2 hybridized in which two

sp^2 hybrid orbitals and two H atoms form two σ C-H bonds. Another hybrid orbital forms an σ bond with the O atom, and an un-hybridized p-orbital and a O-atom p-orbital overlap in parallel to form a C=O double bond. Both C-H and C=O are in the same plane centered on the carbonyl C atom. This planar configuration facilitates the attack of reagents, which is one of the reasons for the higher activity of the carbonyl group. Since the electronegativity of O atom is larger than that of C atom, the bonding electrons, especially the p electron, are biased toward the O atom, so that the C=O bond has a greater polarity, the carbonyl C band is partially positively charged, and the O band is partially negatively charged. The dipole moment is 2.3-2.9 D. This is one of the reasons why carbonyls have high activity. Since the C=O bond energy is 715 KJ/mol, compared with the C=C bond energy of 615 KJ/mol, and the two are conjugated, it is difficult for the reaction to selectively hydrogenate the C=O bond without also hydrogenating the C=C bond. Therefore, a complicated reaction may occur during the hydrogenation of furfural. Moreover, the difference in hydrogenation activation energy of various functional groups is very small, which puts high requirements on the selectivity of the catalyst and the control of the reaction conditions.

Hydrogenation of furfural is a complex reaction system. Different products can be obtained by using different catalysts and reaction conditions. When a copper-based catalyst with a weaker hydrogenation ability is used, hydrogenation of the carbonyl group in the side chain occurs mainly, and this reaction mainly generates furfuryl alcohol at a relatively low temperature, and methyl furan at a higher temperatures (Scheme 3.3). In this Chapter, hydrogenation of furfural using Ru based catalyst to produce furfuryl alcohol is our aim. The reduction of furfural to furfuryl alcohol is challenging because the formation of tetrahydrofuran and polymerization products may also occur in

addition to selective reduction of furfural. Furfuryl alcohol is an important fine chemical, widely used in synthetic fiber, rubber and pesticide industries. Furfuryl alcohol can be used as rocket fuel and hydrolyzed to give levulinic acid; furfuryl alcohol also can be used to produce high temperature resistant phenolic resin binder for friction wheel, such as brake pads for automobiles, etc. Furfuryl alcohol is also an intermediates for the production of perfumes, fragrances, medicines and pesticides.

3.2 Results and discussion

3.2.1 Characterization of PIILP containing POM stabilized ruthenium nanoparticles (Ru^0@POM($H_3PW_{12}O_{40}$) /PIILP)

Imidazolium styrene based monomers were synthesized to produce both linear and cross-linked polymers to react with $H_3PW_{12}O_{40}$ stabilized ruthenium nanoparticles. The synthesis of the monomers and the cross-linked polyionic liquid is described and discussed in the following section (Figure 3.1).

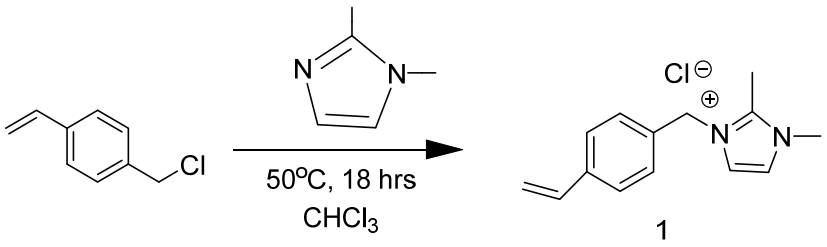

Figure 3.1 Synthesis of 2-methylated imidazolium chloride monomer

Styrene monomer **1** was synthesized as a white powder with a 90% yield in the reaction between 1,2-dimethylimidazole and 4-chloromethyl styrene. The ^1H NMR showed the characteristic peaks for the $H_aC=CH_bH_c$ of the alkene (a doublet of doublets at 6.63 ppm), the other two alkene protons at δ 5.71 and δ 5.54 ppm and methyl group (a three proton singlet at δ 2.73 ppm).

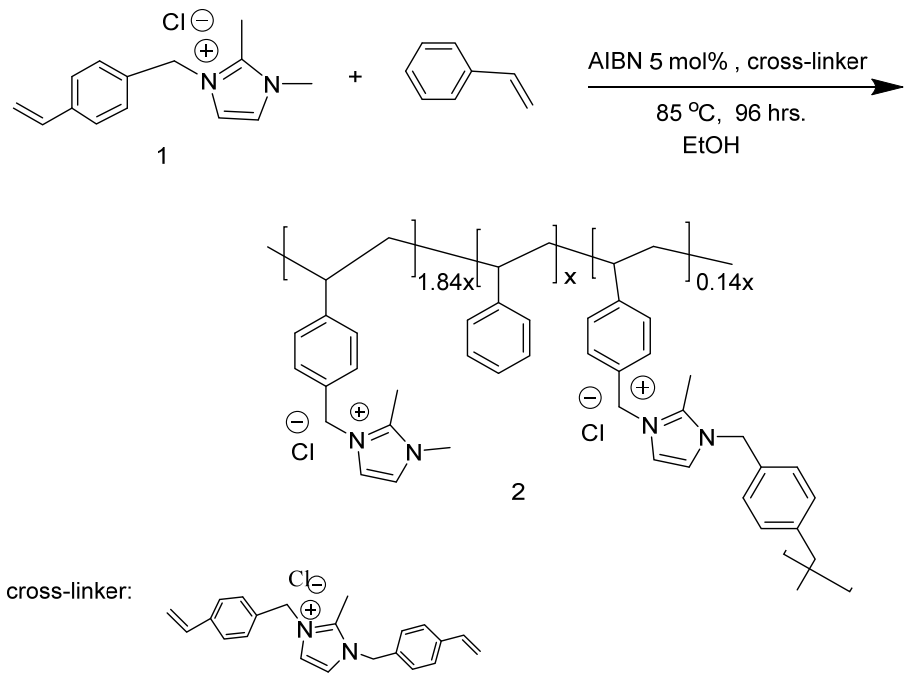

Figure 3.2 Radical polymerization of monomers

The Polymer immobilized ionic liquids (PIILP) was synthesized by the AIBN initiated radical polymerization 2-methylated imidazolium chloride monomer **1** and styrene in the presence of a cross-linker. The designed ratio of imidazolium monomer: styrene monomer cross-linker was 1.84 : 1 : 0.14 (Figure 3.2) and ^{1}H NMR data of PIILP were as expected. The extent of polymerization was confirmed by ^{1}H NMR spectroscopy which showed the presence of only a minor amount of unreacted monomer (<1%). The broadening of peaks in the spectra are indicative of a polymer; this is especially evident for polymer immobilized ionic liquids. The polymer immobilized ionic liquid was produced as a white solid in a high yield which could be easily ground to a fine powder. PIILP was characterized by solution state ^{1}H NMR spectra in methanol-d solvent (Figure 3.3) and solid state ^{13}C NMR spectra (Figure 3.4), which showed proof of the characteristic broadening.

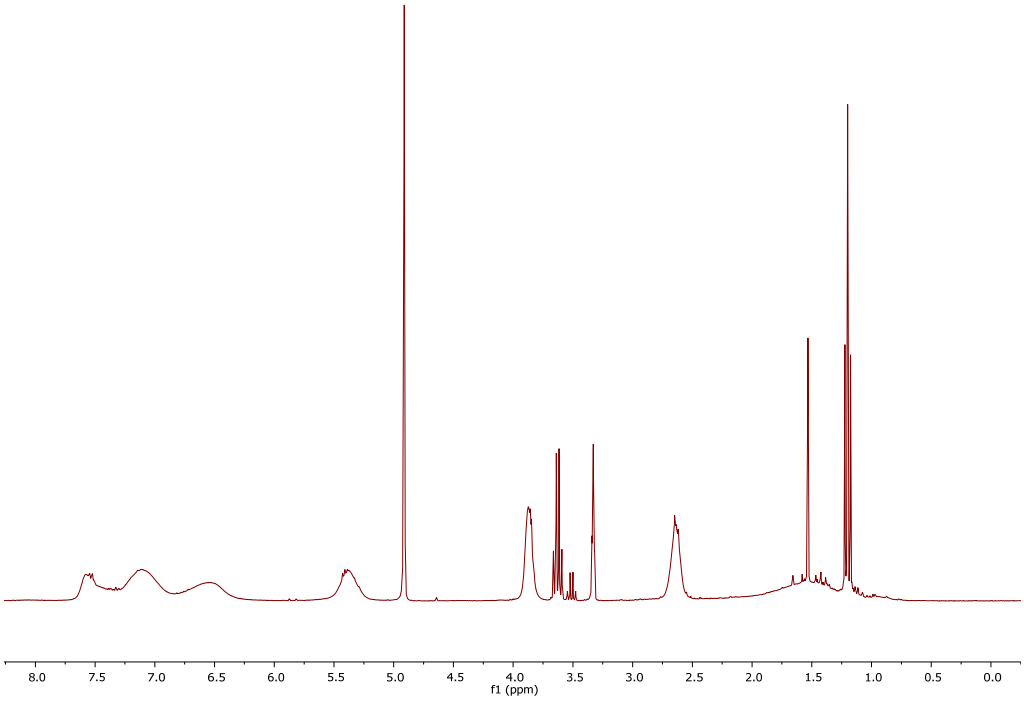

Figure 3.3 ^{1}H NMR spectrum of polymer

A solution of $H_3PW_{12}O_{40}$ stabilized ruthenium nanoparticles was prepared as described in Chapter 2 and it was allowed to react with PIILPs under nitrogen. $H_3PW_{12}O_{40}$ stabilized Ruthenium nanoparticles appeared to enter into the channels of PIILP easily. The molecular structure, surface structure and thermal stability of the prepared Ru^0/POM@PIILP (POM= $[PW_{12}O_{40}]^{3-}$) hybrid composites were examined by solid state NMR, FT-IR, XRD, SEM, EDS, TEM, TGA and XPS analysis methods.

As shown in Figure 3.4 (a), the solid state ^{13}C NMR spectrum of PIILP and Ru^0@POM/PIILP were consistent, that indicated the presence of PIILP in Ru^0@POM/PIILP. Figure 3.4 (b) shows the solid state ^{31}P NMR spectrum of POM ($H_3PW_{12}O_{40}$) which exhibited a sharp peak at -15.58 ppm and Ru^0@POM/PIILP which exhibited a broader peak at -15.73 ppm. The minor peak shift and the wide peak were owing to electrostatical interactions between

POM and PIILP. The solid state ^{31}P and ^{13}C NMR spectrum provides evidence for the successful preparation of Ru^0@POM/PIILP.

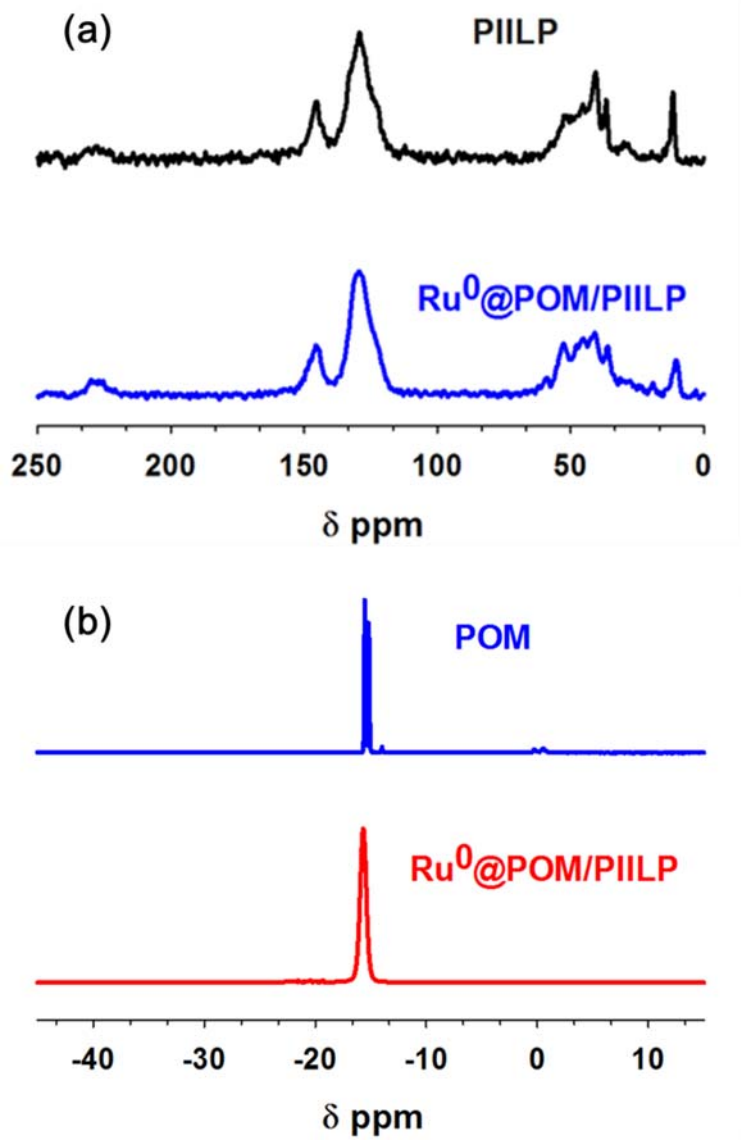

Figure 3.4 Solid state ^{13}C NMR spectrum of PIILP and Ru^0@POM/PIILP (a) and solid state ^{31}P NMR spectrum of POM ($H_3PW_{12}O_{40}$) and Ru^0@POM/PIILP (b)

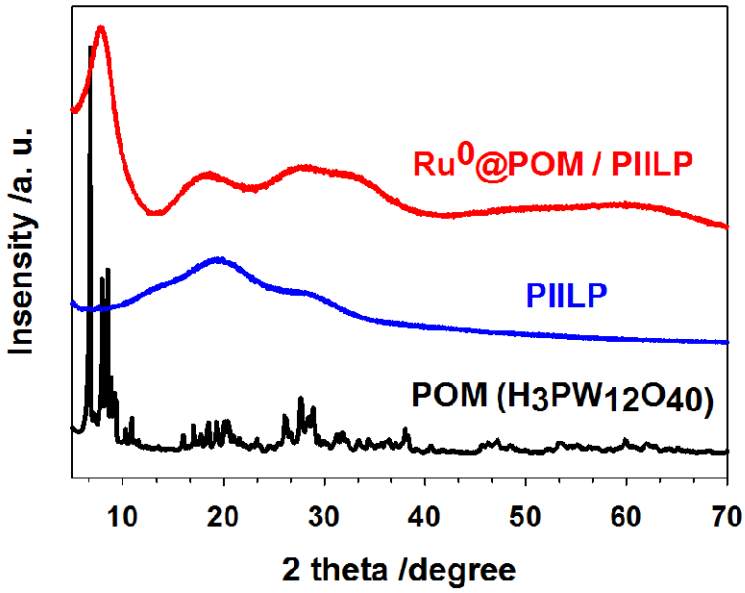

Figure 3.5 XRD spectra of POM ($H_3PW_{12}O_{40}$), PIILP and Ru^0@POM/PIILP

Figure 3.5 shows the powder X-ray diffraction (XRD) patterns of POM ($H_3PW_{12}O_{40}$), PIILP and Ru^0@POM/PIILP. The XRD pattern of $H_3PW_{12}O_{40}$ is characteristic of a crystalline structure. The XRD pattern of PIILP had two wide and weak peaks at 19 and 28 degrees respectively, indicating that the form of PIILP was amorphous. The XRD pattern of Ru^0@POM/PIILP is shown in Figure 3.5, shows a strong intensity peak at 7.8 degrees because of the presence of POM ($[PW_{12}O_{40}]^{3-}$), which indicates the $[PW_{12}O_{40}]^{3-}$ is in Ru^0@POM/PIILP, the PIILP contributed the low intensity of peaks at 19 and 28 degrees. No obvious ruthenium nanoparticles cubic phase were observed in XRD spectra of Ru^0@POM/PIILP as the results of the broadening peaks of PIILP covered up the ruthenium nanoparticles crystallite phase.

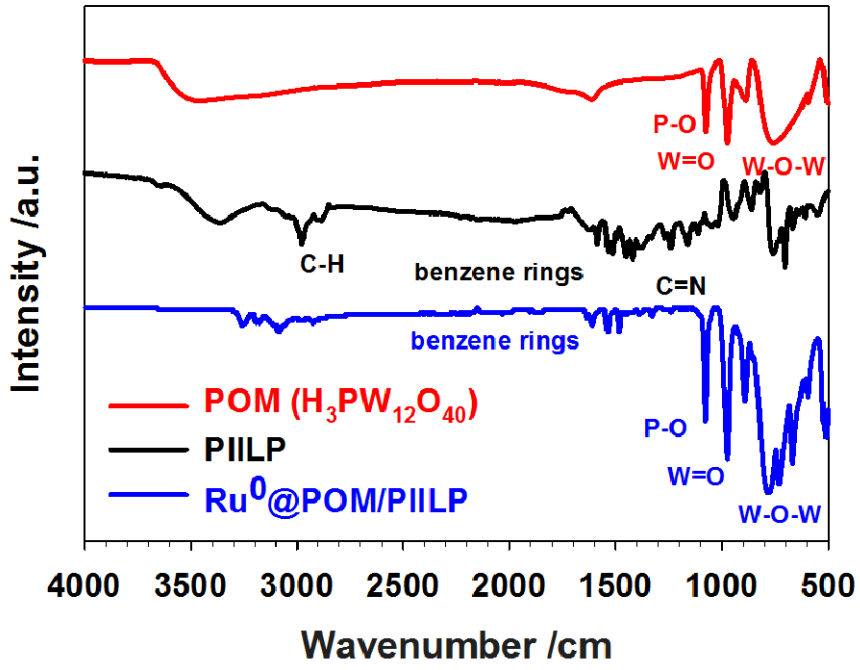

Figure 3.6 FT-IR spectra of POM ($H_3PW_{12}O_{40}$), PIILP and Ru^0@POM/PIILP

The FT-IR spectra of Keggin structure of $H_3PW_{12}O_{40}$ showed the typical peaks: *v* (P−O_a) at 1076 cm^{-1}, *v* (W=O_d) at 975 cm^{-1}, *v* (W−O_b-W) at 891 cm^{-1} and *v* (W-O_c-W) at 769 cm^{-1} in Figure 3.7.[41] The characteristic bonds of PIILP were shown in FT-IR spectra: the deformation of benzene rings at 1451-1531 cm^{-1}, C=N stretching at 1160-1240 cm^{-1} and C-H stretching at 2986 cm^{-1}. The Ru^0@POM/PIILP hybrid composites contained the absorption characteristic peaks for POM, $[PW_{12}O_{40}]^{3-}$ and PIILP, all the results confirmed that the presence of the $[PW_{12}O_{40}]^{3-}$ and PIILP in the hybrid composites.

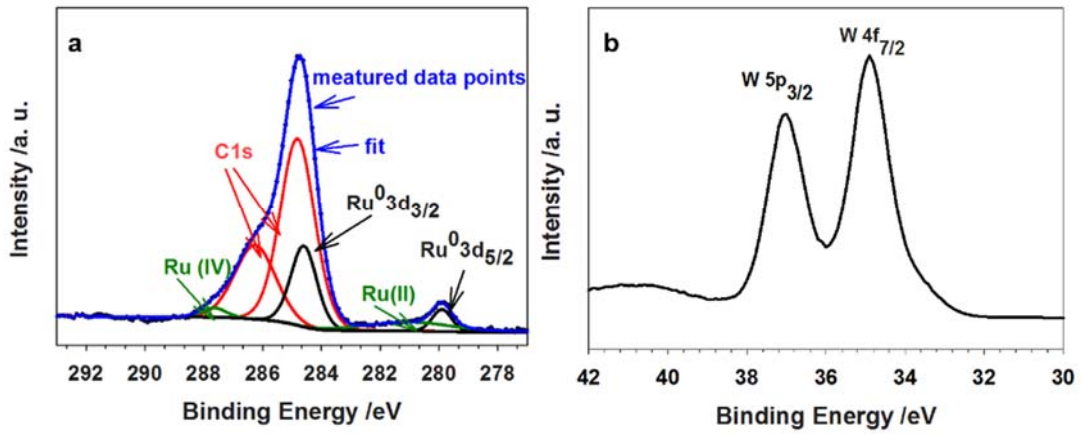

Figure 3.7 XPS spectra of Ru^0@POM/PIILP with (a) ruthenium, carbon and (b) tungsten

In order to prove the chemical composition and elemental valence of Ru^0@POM/PIILP composites, XPS analysis was carried out and results are shown in Figure 3.7. Figure 3.7 (a) gave XPS spectra (Ru $3d_{5/2}$ at 280.0 eV and Ru $3d_{3/2}$ at 284.3 eV) of ruthenium nanoparticles verified that the Ru nanoparticles in samples contained Ru in a zero oxidation state, as in previous literature reports.[42,43] Moreover, XPS spectra of Ru in Figure 3.7 (a) showed the oxide to have a low and high B.E.at 281.0 eV and 287.6 eV, that proved Ru^{2+} and Ru^{5+} atoms existed in the samples, probably Ru atoms at the surface might be oxidized by POM or the surface of Ru^0 nanoparticles on samples was oxidized in the air when they were ready for analysis by XPS.[43] Nevertheless, the binding energy was clearly presented for the valence state of Ru^0. The relative element such as W (W $4f_{7/2}$ at 34.9 eV, W $5p_{3/2}$ at 37 eV) proved the presence of $[PW_{12}O_{40}]^{3-}$ in hybrid composites.

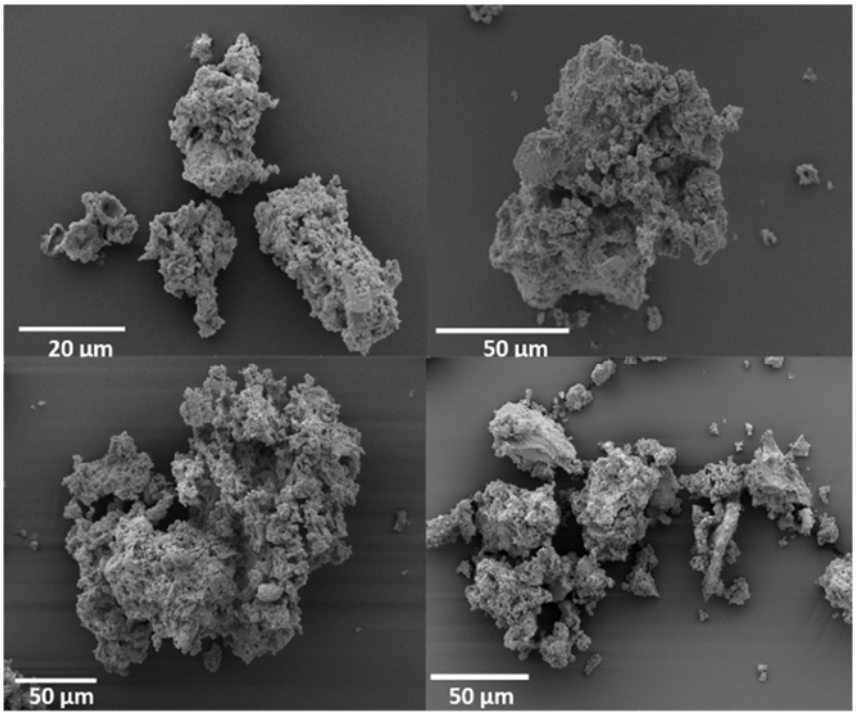

Figure 3.8 SEM images of Ru^0@POM/PIILP composites

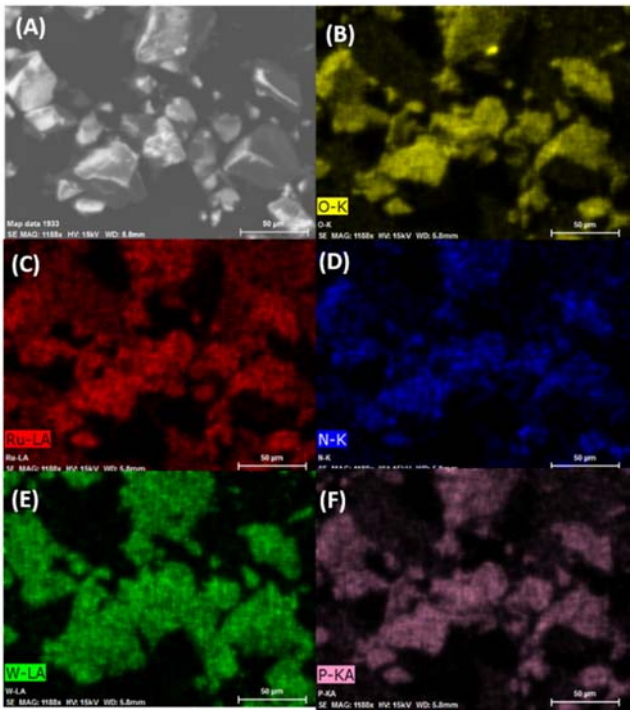

Figure 3.9 Typical images of (A) Ru^0@POM/PIILP sample and the corresponding elemental mapping images of (B) oxygen, (C) ruthenium, (D) nitrogen, (E) tungsten, (F) phosphorus

The Ru^0@POM/PIILP composites were also analysed by scanning electron microscope (SEM) analysis to examine the surface morphology. In Figure 3.8, the PIILP appeared to have a porous surface, due to the highly crosslinked nature characteristics of the PIILP. As the polymer was a porous material, Ru^0@POM was included in the pores of PIILP. As shown in Figure 3.9, the corresponding SEM elemental mapping images of oxygen, ruthenium, nitrogen, tungsten, phosphorus for Ru^0@POM/PIILP sample showed a uniform dispersion of Ru^0@POM/PIILP in the porous PIILP.

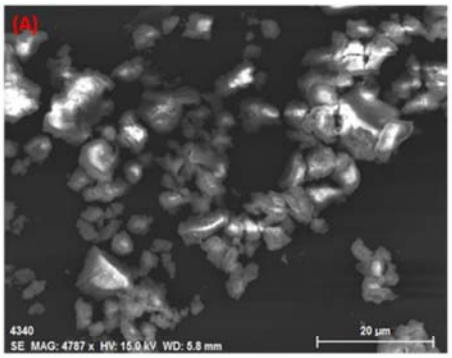

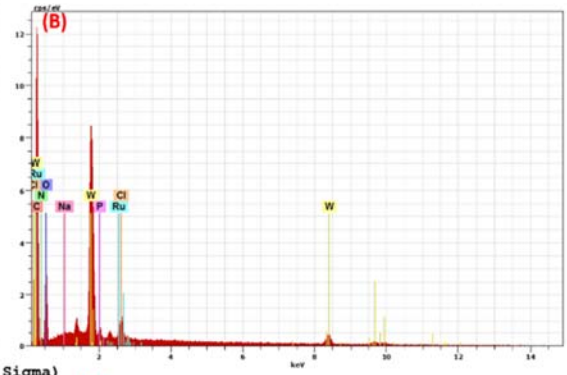

(C)

Element	Series	unn. C [wt.%]	norm. C [wt.%]	Atom. C [at.%]	(1 Sigma) [wt.%]
Carbon	K-series	51.65	51.78	74.30	6.22
Nitrogen	K-series	4.00	4.01	4.93	0.91
Oxygen	K-series	16.04	16.08	17.32	2.25
Ruthenium	L-series	0.70	0.70	0.12	0.06
Phosphorus	K-series	0.19	0.19	0.10	0.04
Tungsten	L-series	25.50	25.57	2.40	0.99
Chlorine	K-series	1.62	1.62	0.79	0.09
Sodium	K-series	0.05	0.05	0.04	0.03
	Total:	99.74	100.00	100.00	

(D)

Element	Atom%	Ratio
Ru K	0.12	1
P K	0.10	1
W M	2.47	12

Figure 3.10 SEM(A) and EDS(B) images of Ru^0@POM/PIILP sample. The contents (C) and ratio (D) of different elements in Ru^0@POM/PIILP sample

In order to verify the contents of Ru^0@POM/PIILP sample, energy dispersive spectrometer (EDS) analysis was performed in Figure 3.10. According to the result of EDS, in the presence of elements of C, N, O, Ru, P, W, Cl, Na was confirmed in the Ru^0@POM/PIILP sample. Through the calculating of the Ru, P, W elements, we can draw the following conclusion that the mole ratio of Ru

nanoparticles and $[PW_{12}O_{40}]^{3-}$ was 1:1 which was beneficial to calculate the amount of catalyst in the catalytic reaction.

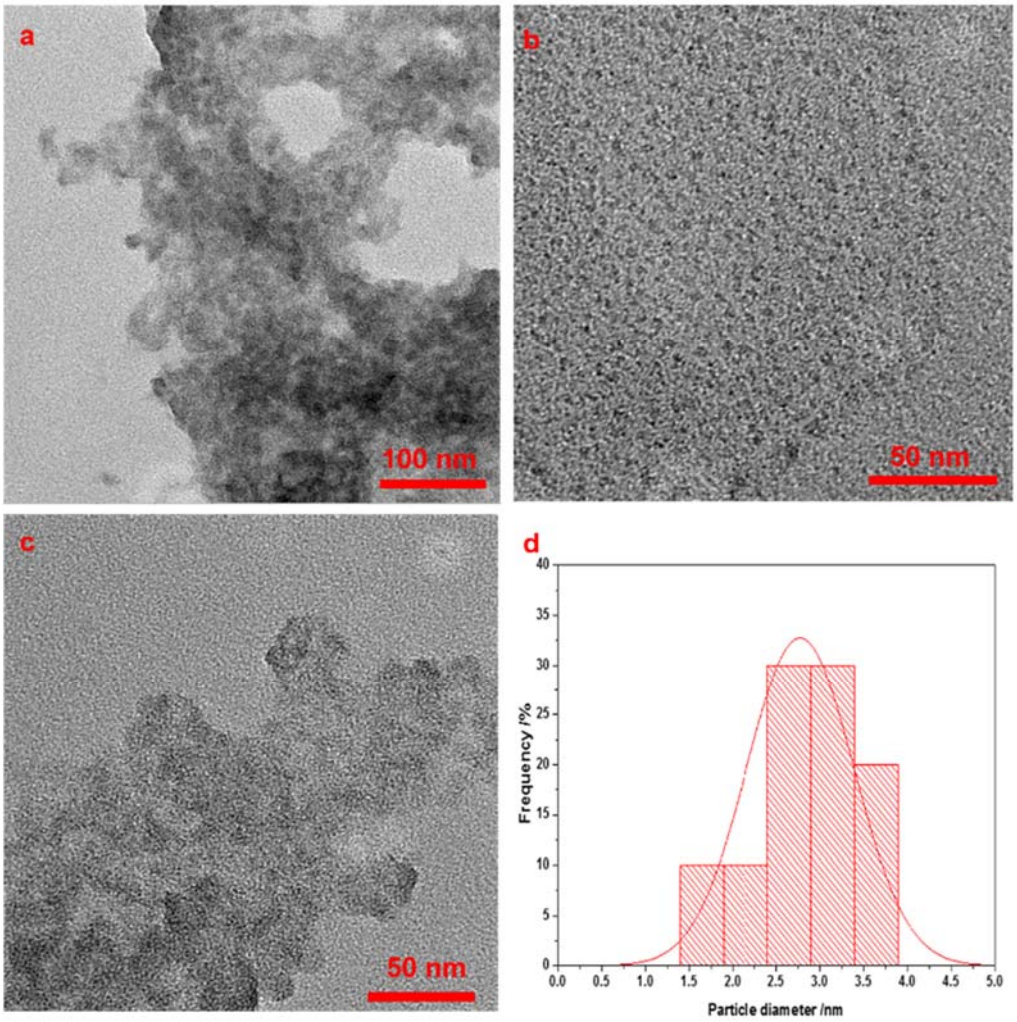

Figure 3.11 TEM images (a), (b), (c) and (d) particle size distribution of Ru^0@POM/PIILP

TEM images in Figure 3.11 clarified the morphologies of the Ru^0@POM/PIILP sample. The black spots of ruthenium nanoparticles were observed to be well distributed on the surface of PIILP. A Ru^0 nanoparticle size histogram showed a distribution ranging from 2.5-3.5 nm (Figure 3.11 (d)). The Ru^0@POM/PIILP TEM images indicated the presence of ruthenium nanoparticles in composites.

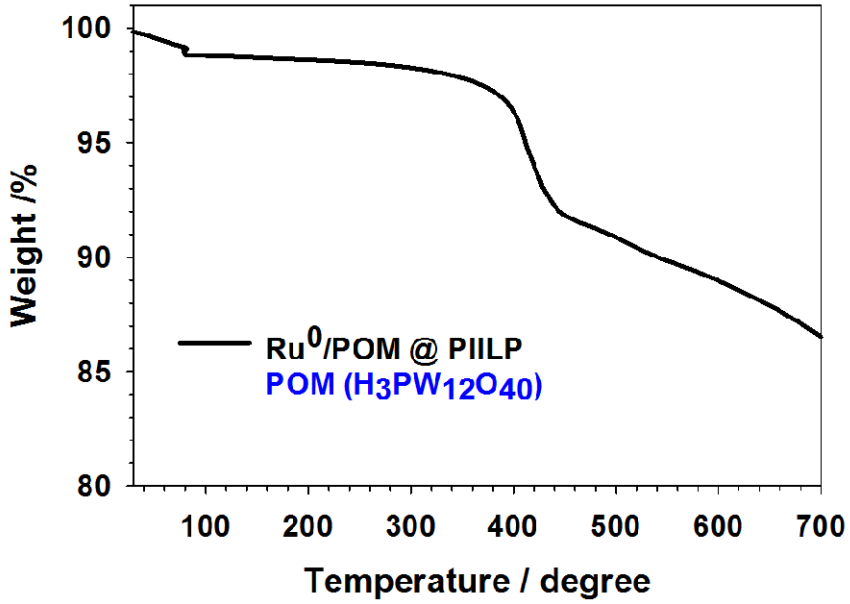

Figure 3.12 TGA pattern of Ru^0@POM/PIILP sample

Thermal gravimetric analysis (TGA) of the sythesized Ru^0@POM/PIILP composite is given in Figure 3.12. Ru^0@POM/PIILP sample before reaction in TGA curve was indicated 2.5% weight loss in the range of 25 to 100 °C was due to the weight loss of water, the primary 6% weight loss for composites was observed between 100 to 450 °C was due to the decomposition of organic PIILP. The Keggin type $H_3PW_{12}O_{40}$ has been shown to decompose at 550 °C, whereas when the $PW_{12}O_{40}^{3-}$ anion was interacted with PIILP, the decomposition of POM proceeded at a lower temperature of 450 °C. As a result, the futher weight loss occurred above 450 °C was ascribed to the decomposition of the $[PW_{12}O_{40}]^{3-}$ anion.

3.2.2 Hydrogenolysis of HMF to DMF

3.2.2.1 Reaction pathway for hydrogenolysis of HMF

Catalytic hydrogenation is usually carried out in an autoclave reactor or fixed bed reactor and usually requires higher reaction temperature and hydrogen

pressure. Unsaturated organic compounds are transferred from the solvent to the catalyst surface, where hydrogenation occurs. After the reaction, reduction products are automatically desorbed from the catalyst surface into the solvent. Therefore, hydrogenation requires the selection of catalysts for hydrogenation of compounds with functional groups containing unsaturated bonds, such as carbon-carbon double bond, carbon-oxygen double bond, carbon-nitrogen triple bond, carbon-oxygen single bond, etc.

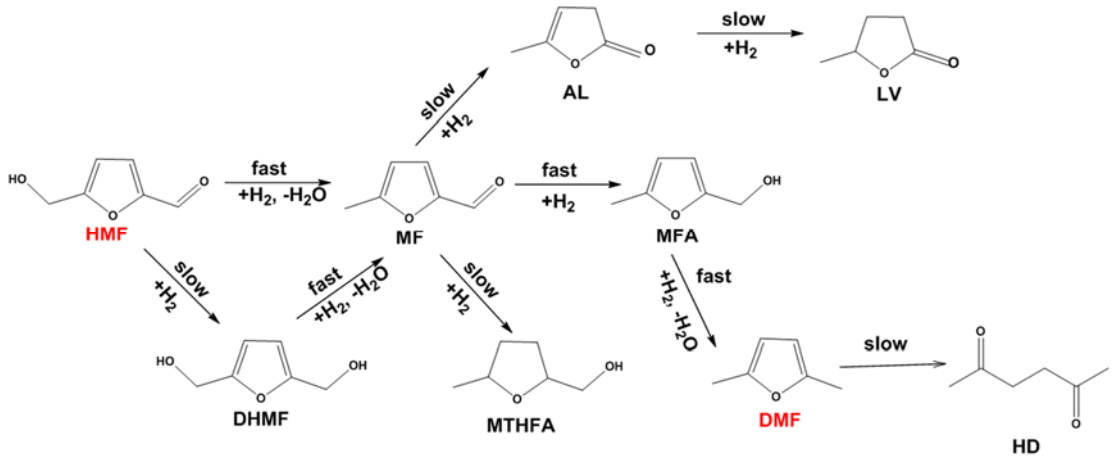

Scheme 3.4 Reaction pathways for hydrogenolysis of HMF to DMF

In recent years, scientists have developed a variety of catalytic systems for the selective hydrogenation of HMF to DMF, most of which are liquid phase hydrogenation. However, the selective hydrogenation of HMF in catalytic reaction system takes three steps (in Scheme 3.4): (1) the aldehyde and alcohol hydroxyl groups in the HMF molecule were hydrogenated to form 2,5-dihydroxymethyl furan (DHMF) and 5-methyl furfural (MF); (2) DHMF and MF were further hydrogenated to form 5-methyl furfuryl alcohol (MFA); (3) MFA was finally hydrogenated to form DMF. HMF is very active chemically because it contains simultaneously an aldehyde group, an alcohol hydroxyl group and a furan ring. In the presence of catalyst and hydrogen donor, hydrogenation occurs easily to form different products. Therefore, in the process of selective hydrogenation of HMF, in addition to the target product DMF, it will also produce

2,5-dihydroxymethyltetrahydrofuran (DHMF) and 5-methyltetrahydrofurfuryl alcohol (MTHFA) as by-products.

3.2.2.2 Conversion of HMF on different catalysts

Table 3.1 Effect of catalysts for the conversion of HMF.

Entry	Catalyst	HMF conversion (%)	DMF yield (%)
1	Ru^0@ POM/PIILP	100	87
2	Ru^0@PIILP	56	51
3	5%Ru^0/Carbon	91	75
4	None	7	0

Reaction conditions: 0.5 mmol HMF, 12mL THF, 200 ¹&, 2 MPa H_2, 5 hours. 1 mmol% Ru catalyst. Determined by GC-MS, decane was the internal standard.

The hydrogenolysis of HMF to DMF was investigated using different catalysts. The conversion of HMF and the yield of DMF under the reaction conditions (temperature = 200 ¹&, reaction time = 5 h, and H_2 pressure = 2 MPa) are shown in the Table 3.1. The HMF conversion was 7% and the yield of DMF was 0% without the catalyst under the same reaction conditions. Compared with results, using different supported Ru catalysts, Ru^0@POM/PIILP achieved good conversion of HMF (100%) and yield of DMF (87%), which was better than Ru^0@PIILP and 5% Ru^0/Carbon catalysts. When Ru^0@PIILP and 5% Ru^0/Carbon were used as catalysts, the conversion of HMF was 56% and 91% and the yield of DMF was 51% and 75% respectively. These results proved that the Ru based catalysts are selective for the conversion of HMF to DMF, which was consistent with the literature reports. Ru^0@POM/PIILP catalyst has better catalytic activity than the other two catalysts due to it being a bifuncional catalyst, the Ru metal and Brønsted acid sites associated with the POM.

Wang's group proposed that in hydrogenation using $Ru/Cs_3PW_{12}O_{40}$ catalyst, the Brønsted acid sites were generated from molecular hydrogen, by adsorption and dissociation on the Ru surface. Similar to $Ru/Cs_3PW_{12}O_{40}$, the unique generation of Brønsted acid sites from hydrogen over Ru^0@POM/PIILP catalyst can increase the deoxygenation ability and improve the yield of DMF.

3.2.2.3 Study on kinetic factors of hydrogenolysis of HMF over Ru^0@POM/PIILP

In order to further study the catalytic performance of Ru^0@POM/PIILP catalyst, the kinetic factors such as hydrogen pressure, reaction temperature and reaction time were investigated.

3.2.3.3.1 Effect of reaction temperature

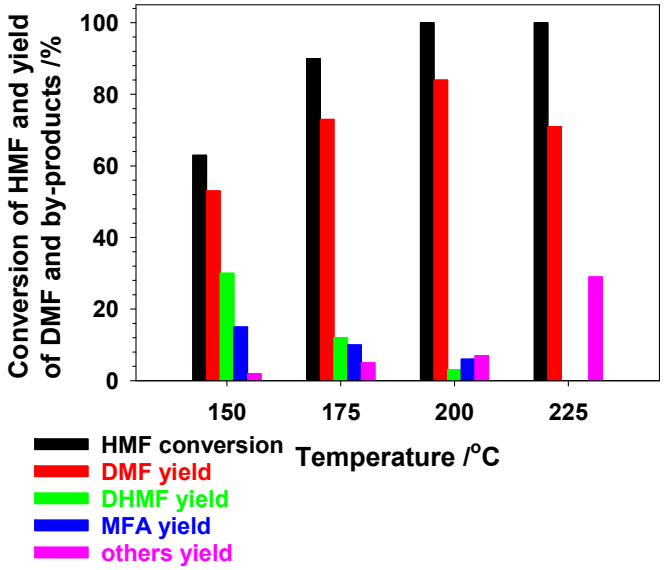

Figure 3.13 Effect of temperature on the Ru^0@POM/PIILP catalysed conversion of HMF. Reaction conditions: 0.5 mmol HMF, 1 mmol% catalyst, 12mL THF, 2 MPa H_2, 5 hours. Determined by GC-MS, decane was the internal standard.

The effect of reaction temperature on HMF conversion and DMF yield were studied (shown in Figure 3.13), when the reaction temperature was 150 °C, the conversion of HMF was 63%, but the yield of DMF was only 53%, while the yield of the intermediate products (such as DHMF and MFA) were 45% and the yield of others (such as MTHFA and DMTHF) were 2%. When the temperature was raised from 150 °C to 200 °C, the conversion rate of HMF increased from 63% to 100%, the yield of DMF increased from 53% to 84%, while by-products of the intermediates DHMF and MFA were not detected, indicating that the two intermediates were gradually converted into the target product DMF. In addition, the amount of by-products (MTHFA and DMTHF) also was lower (16%). When the temperature was 225 °C, the yield of DMF decreased to 71% and at the same time, the yield of the by-product (MTHFA and DMTHF) increased to 12.5%, so 200 °C was the best reaction temperature.

3.2.3.3.2 Effect of reaction time

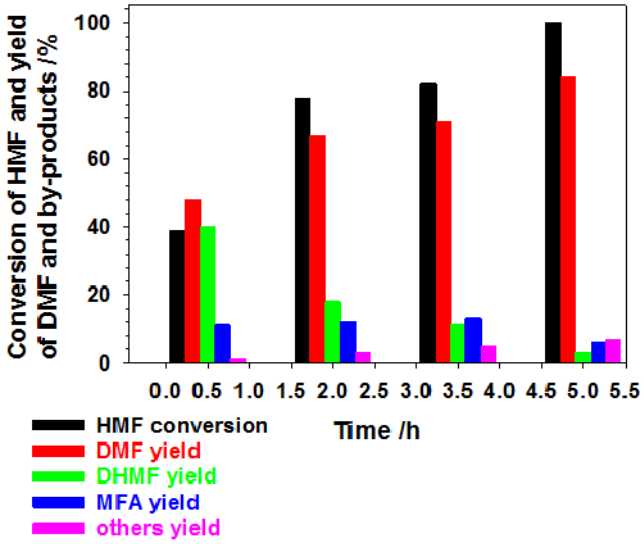

Figure 3.14 Effect of reaction time on Ru^0@POM/PIILP catalysed conversion of HMF. Reaction conditions: 0.5 mmol HMF, 1 mmol% catalyst, 12mL THF, 2 MPa H_2, 200 °C. Determined by GC-MS, decane was the internal standard.

The effect of reaction time on HMF conversion and DMF yield were studied (shown in Figure 3.14). The reaction time was 1-5 hours and the interval was 1.5 hours. The experimental results showed that when the reaction time was 1 hour, the HMF conversion was only 39%, the main products (51%) were the reaction intermediates (MTHF and MFA), the yield of DMF was only 48% and the yield of by-product was 1%. With the increase of reaction time to 3.5 hours, the conversion of HMF increased to 82%, and the yield of DMF also increased to 71%, the sum of intermediate products (MTHFA and DMTHF) yield decreased to 23%, but the by-product also increased from 1% to 5%. When the reaction time increased to 5 hours, the conversion of HMF reached 100% and the sum of intermediate products yield decreased to 9%. The yield of DMF gradually increased to 84%. With the increase of DMF yield, the by-product increased to 7%. The conversion of HMF reached 100%, if the reaction time continues, the product DMF would also undergo hydrogenation or ring opening reaction, and increase the yield of by-products. Therefore, the optimum reaction time for this reaction condition was 5 hours.

3.2.3.3.3 Effect of hydrogen pressure

The influence of H_2 pressure for HMF conversion and DMF yield were studied (shown in Figure 3.15). When the hydrogenolysis of HMF was carried out at 0.5 MPa H_2, the HMF conversion was as low as 59%, the by-products of intermediate products such as DHMF, MFA were the main product (75%), the DMF yield was 25%. The selectivity of DMF increased to 79% slowly when the pressure gradually increased to 1.5 MPa, the conversion of HMF was 87%. When the pressure continued to increase to 2 MPa, the HMF conversion was almost 100%, the DMF yield was 84%, the intermediate products of DHMF and MFA were 9%, and the by-products of MTHFA and DMTHF yield increased to

7%. Excessive H_2 can promote the hydrogenolysis and ring opening reaction of furan ring, so 2 MPa H_2 is the best reaction pressure.

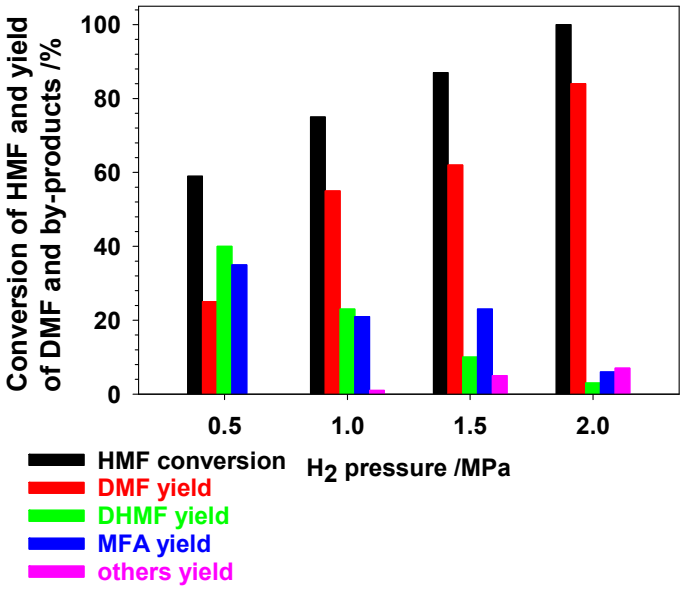

Figure 3.15 Effect of H_2 pressure on Ru^0@POM/PIILP catalysed conversion of HMF. Reaction conditions: 0.5 mmol HMF, 1 mmol% catalyst, 12mL THF, 2 MPa H_2, 5 hours, 200 ^oC. Determined by GC-MS, decane was the internal standard.

3.2.3.3.4 Study on the stability of Ru^0@POM/PIILP catalysts

In order to explore the recycling performance of the Ru^0@POM/PIILP catalyst, we used 1 mol% Ru catalyst, under the best experimental conditions (5 hours, 2 MPa H_2, 200 ^oC). After the first reaction, the catalyst and the solution was separated by centrifugation and washed with THF solvent. After washing three times, the next reaction was carried out directly. From Figure 3.16, it shows the HMF conversion of the first three cycles were all 100%, the DMF yields were decreased from 84% to 81%. After the third cycle, the HMF conversion was 95%, the selectivity of DMF gradually decreased to 77%. At the fifth cycle, the conversion of HMF was decreased to 91%, indicating the gradual inactivation of the catalyst. It has been shown in the literature that due to the gradual

formation of carbon-containing compounds (humin) during the hydrogenation reaction, these carbon-containing compounds can be deposited on the surface of the catalyst, resulting in deactivation of the catalyst.[40,44,45]

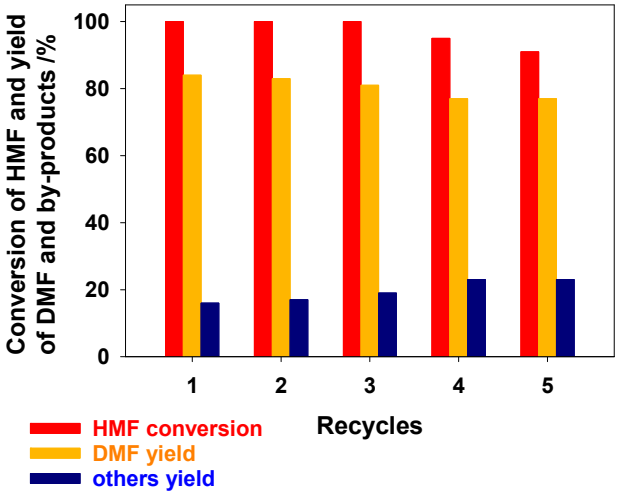

Figure 3.16 Effect of recycling the Ru^0@POM/PIILP catalyst in the conversion of HMF. Reaction conditions: 0.5 mmol HMF, 1 mmol% Ru catalyst, 12mL THF, 5 hours, 2 MPa H_2, 200 °C. Determined by GC-MS, decane was the internal standard.

3.2.3 Hydrogenation of trans-cinnamaldehyde

3.2.3.1. The pathways of hydrogenation of cinnamaldehyde (CAL)

Three types of products can arise in the hydrogenation of cinnamaldehyde (CAL): (1) the C=C double bond is hydrogenated to give a saturated aldehyde; (2) the C=O double bond is hydrogenated giving an unsaturated alcohol; (3) both C=C and C=O double bond are hydrogenated to give a saturated alcohol. The bond energy of a C=C bond is 615 kJ/mol and the bond energy of a C=O bond is 715 kJ/mol, so that C=C bond hydrogenation is easier than C=O bond hydrogenation. Competitive reduction of C=C and C=O double bonds will give the products including hydrocinnamaldehyde (HCAL), cinnamyl alcohol (COL)

and hydrocinnamyl alcohol (HCOL) (Figure 3.17). The products obtained are usually difficult to separate; and consequently the selectivity towards the desired product must be high in order for the reaction to be viable. For this, the choice of catalyst is key.

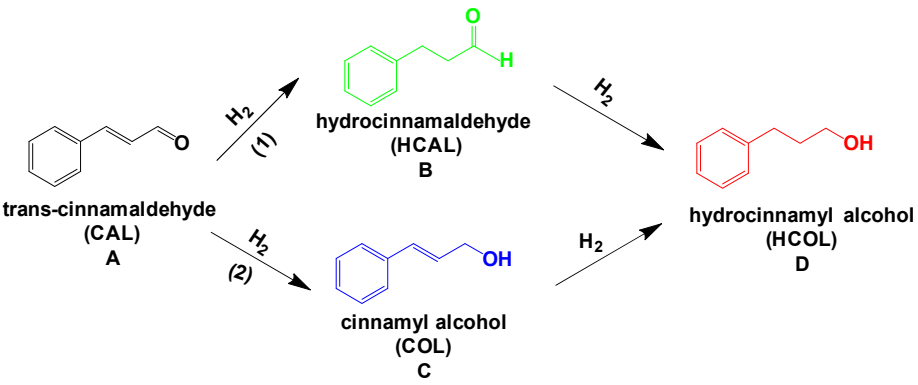

Figure 3.17 Products formed after the hydrogenation of the trans-cinnamaldehyde.

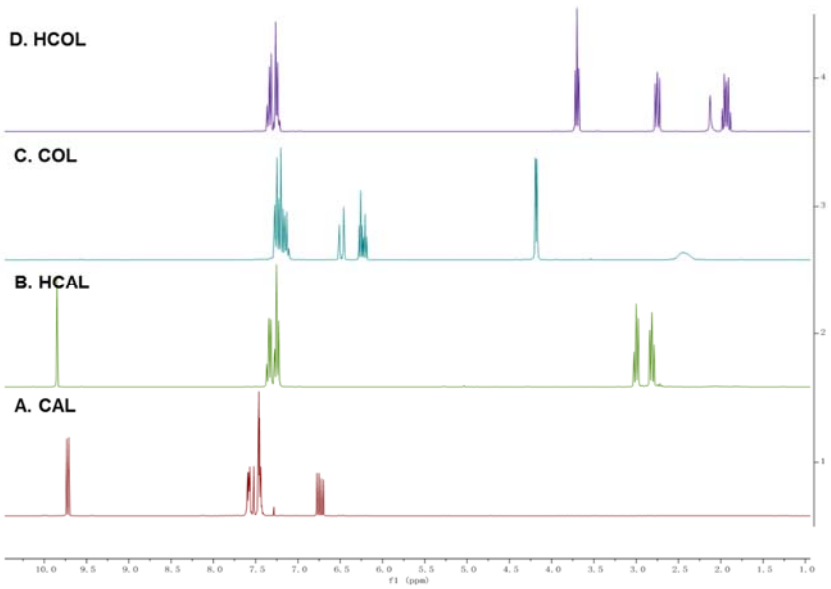

Figure 3.18 ^{1}H NMR spectra of cinnamaldehyde (CAL) (A) and all possible products: hydrocinnamaldehyde (HCAL) (B), cinnamyl alcohol (COL) (C) and hydrocinnamyl alcohol (HCOL) (D) in $CDCl_3$.

The hydrogenation reactions were conducted in a Parr bench top pressure reactor. ^{1}H NMR spectroscopy was used to analyze the reaction mixture and obtain conversion and selectivity. The amounts of each product were calculated from the integrals. Conversion was calculated using the difference between the starting material CAL (A) and all possible products (B, C, D) in the ^{1}H NMR and selectivity was calculated using the difference between the product B or C or D and all other possibilities (B+C+D) (Figure 3.19). The equations conversion% = (B+C+D)/(A+B+C+D)×100% and selectivity % = B or C or D /(B+C+D)×100% were used to calculate both conversion and selectivity. From the ^{1}H NMR spectrum, we can observe none of the COL (B). The catalyst most likely hydrogenated the alkene first. A mass balance reaction using 1,3-dinitrobenzene as an internal standard showed that no substrate was lost during the reaction.

3.2.3.2 The performance of different solvents in the hydrogenation of cinnamaldehyde

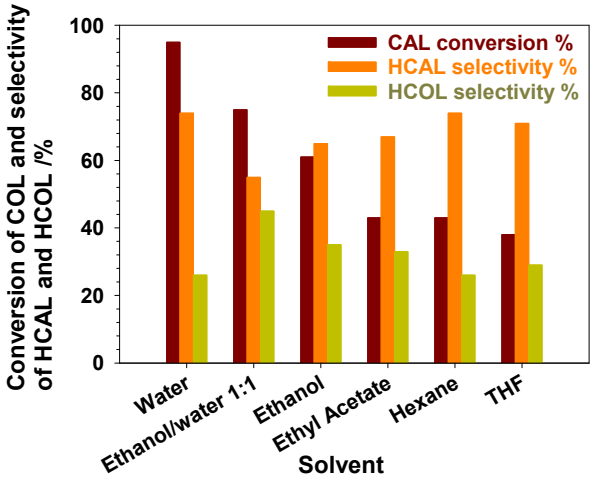

Figure 3.19 Effect of different solvents on the hydrogenation of CAL. Reaction conditions: CAL 1 mmol, solvent, 12 mL, 1 mmol% Ru^{0}@POM/PIILP catalyst, H_2, 0.7 MPa, temperature, 60 ^{o}C, time, 2 hours. Determined by ^{1}H NMR, 1,3-dinitrobenzene as an internal standard.

Figure 3.19 showed the different catalytic hydrogenation performance of the Ru^0@POM/PIILP catalyst in water, ethanol, ethanol/water 1:1, ethyl acetate, hexane and THF as solvent under the conditions of temperature 60 ^oC, hydrogen pressure 0.7 MPa and reaction time 2 hours. Solubility and dielectric constant in water are the criteria for measuring solvent polarity. Different solvents affect the solubility of hydrogen in the solvent. The higher the polarity of the solvent, the higher the hydrogen solubility, the higher the conversion of reactants. The conversion of CAL and selectivity of HCAL were 95% and 74% respectively in water. When ethanol and ethanol/water 1:1 are were used as solvents, the CAL conversion and HCAL selectivity were slightly lower, the conversion was 75% and 61%, and the selectivity of HCAL were 55% and 65%. When ethyl acetate, hexane and THF were used as solvents, the conversion and selectivity of CAL catalyzed by hydrogenation were very low. In this experiment, considering the solubility of substrate and hydrogen in solvent, although CAL can only be slightly soluble in water, the polarity of water is great. Considering the conversion and selectivity, water was chosen as solvent.

3.2.3.3 Study of the kinetic factors affecting hydrogenation of LA over Ru^0@POM/PIILP catalysts

In order to further study the catalytic performance of Ru^0@POM/PIILP catalyst, the kinetic factors such as hydrogen pressure, reaction temperature and reaction time were investigated.

3.2.3.3.1 Effect of reaction temperature

The influence of reaction temperature on the hydrogenation reaction was investigated using Ru^0@POM/PIILP catalyst (shown in Figure 3.20). The reaction conditions were as follows: hydrogen pressure 0.7MPa, hydrogenation

reaction time 2 hours, the reaction temperature changed from 20 °C to 80 °C. When the reaction temperature increased from 20 °C to 60 °C, the conversion and selectivity of CAL also increased. At 60 °C, the CAL conversion reached 95% and the HCAL selectivity reached 74%. Because the hydrogenation reaction is endothermic reaction, the conversion rate of the reaction keeps rising with the increase of temperature step by step. The selectivity of HCAL was reduced from 74% to 66% in the temperature range of 60 °C to 80 °C. It can be seen that too high temperature will lead to excessive hydrogenation of HCAL. Therefore, the effects of selectivity and conversion of CAL were considered. The optimum temperature of hydrogenation was 60 °C.

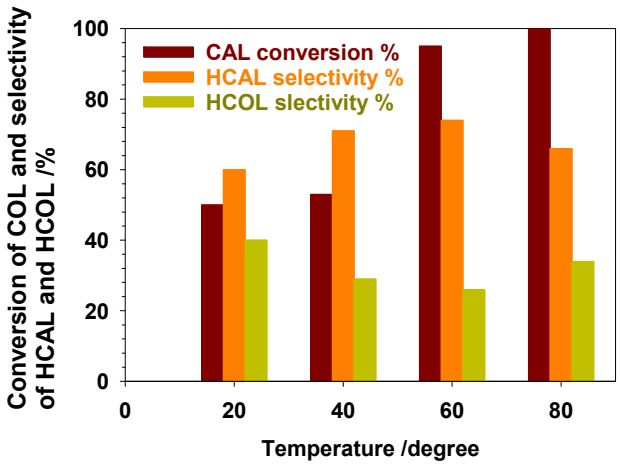

Figure 3.20 Effect of reaction temperature on the hydrogenation of CAL. Reaction conditions: CAL 1 mmol, H_2O, 12 mL, 1 mmol% Ru^0@POM/PIILP catalyst, H_2, 0.7 MPa, time, 2 hour. Determined by ^1H NMR, 1,3-dinitrobenzene as an internal standard.

The influence of reaction temperature on the hydrogenation reaction was investigated using Ru^0@POM/PIILP catalyst (shown in Figure 3.20). The reaction conditions were as follows: hydrogen pressure 0.7MPa, hydrogenation reaction time 2 hours, the reaction temperature changed from 20 °C to 80 °C. When the reaction temperature increased from 20 °C to 60 °C, the conversion

and selectivity of CAL also increased. At 60 °C, the CAL conversion reached 95% and the HCAL selectivity reached 74%. Because the hydrogenation reaction is endothermic reaction, the conversion rate of the reaction keeps rising with the increase of temperature step by step. The selectivity of HCAL was reduced from 74% to 66% in the temperature range of 60 °C to 80 °C. It can be seen that too high temperature will lead to excessive hydrogenation of HCAL. Therefore, the effects of selectivity and conversion of CAL were considered. The optimum temperature of hydrogenation was 60 °C.

3.2.3.3.2 Effect of hydrogen pressure

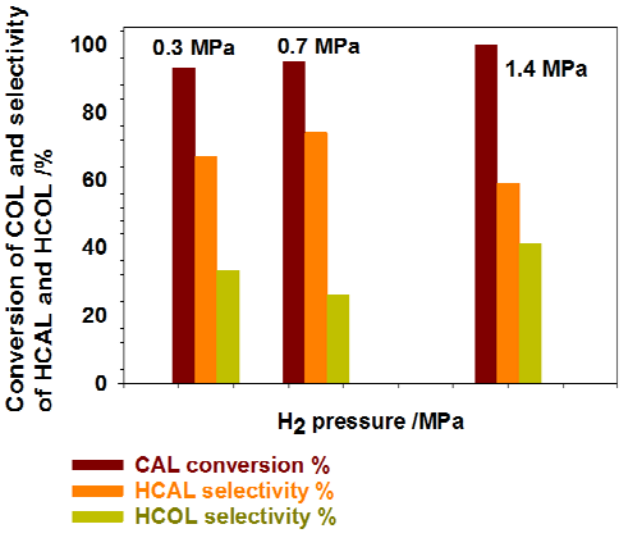

Figure 3.21 Effect of hydrogen pressure on the hydrogenation of CAL. Reaction conditions: CAL 1 mmol, H_2O, 12 mL, 1 mmol% Ru^0@POM/PIILP catalyst, temperature, 60 °C, time, 2 hours. Determined by ^1H NMR, 1,3-dinitrobenzene as an internal standard.

The effects of hydrogen pressure on the selectivity and conversion of CAL to HCAL by hydrogenation were investigated by using Ru^0@POM/PIILP catalyst at 60 °C for 2 hours. From Figure 3.21, when the hydrogen pressure in the

reactor is 0.3 MPa, the conversion of CAL was 93% and the HCAL selectivity was 67%. When the hydrogen pressure was raised from 0.3 MPa to 0.7 MPa, the conversion rate was increased to 95%, and the HCAL selectivity was increased from 67% to 74%. When the hydrogen pressure continues to increase to 1.4 MPa, the conversion rate reaches 100%, it can be seen that the conversion rate increases with the increase of reaction pressure, but the selectivity of HCAL decreased from 74% to 59% with increasing pressure to 2 MPa. If the reaction pressure is too high, the saturation of hydrogen will lead to excessive hydrogenation. In this section, 0.7 MPa was selected as the pressure for the hydrogenation of CAL.

3.2.3.3.3 Effect of reaction time

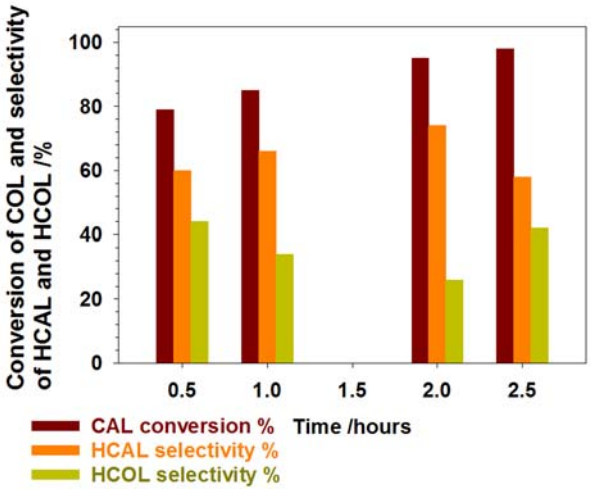

Figure 3.22 Effect of reaction time on the hydrogenation of CAL. Reaction conditions: CAL 1 mmol, H_2O, 12 mL, 1 mmol% Ru^0@POM/PIILP catalyst, H_2, 0.7 MPa, temperature, 60 ^oC. Determined by ^1H NMR, 1,3-dinitrobenzene as an internal standard.

The influence of reaction time on the selectivity and conversion of CAL by hydrogenation of C=C bond with Ru^0@POM/PIILP catalyst was investigated

under the condition of 60 °C and 0.7 MPa H_2. Several reactions were carried out to investigate reaction times between 0.5 hours and 2.5 hours. As shown in Figure 3.22, with the change of reaction time, the reaction was fast within 0.5 hour, and the conversion of the reaction increased rapidly to 79%. After 0.5 to 2 hours, the reaction conversion continued to increase to 95% and the selectivity of HCAL increased to 74%, which indicated that the catalyst has higher activity. The selectivity of HCAL of reaction reached the highest in 2 hours. With the prolongation of the reaction time, the selectivity gradually decreased, and when the reaction time was 2.5 hours, the selectivity decreased to 58%. Considering selectivity and conversion, the optimal time for hydrogenation of CAL was set to 2 hours.

3.2.3.4 Study on the stability of the Ru^0@POM/PIILP catalyst

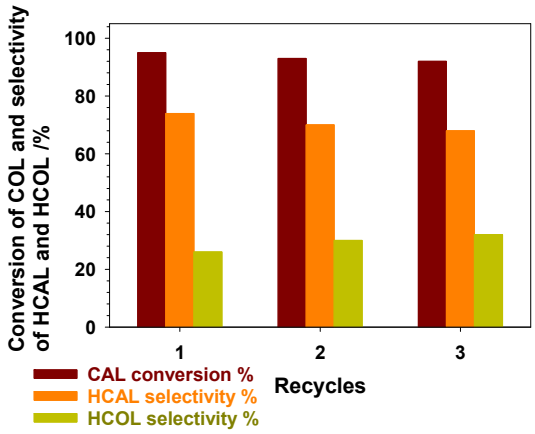

Figure 3.23 Recycles of Ru^0@POM/PIILP catalyst for the hydrogenation of CAL. Reaction conditions: CAL 1 mmol, H_2O, 12 mL, 1 mmol% Ru catalyst, H_2, 0.7 MPa, temperature, 60 °C, time, 2 hours. Determined by ^1H NMR, 1,3-dinitrobenzene as an internal standard.

Recycle experiments were carried out on the hydrogenation of CAL using Ru^0@POM/PIILP catalyst under optimum conditions (H_2O, 12 mL, H_2, 0.7 MPa,

temperature, 60 °C, time, 2 hours), to investigate the reusability of the Ru^0@POM/PIILP catalyst. In Figure 3.23, after the 3 runs, it can be seen that the selectivity of C =C bond did not decrease significantly, and the selectivity to HCAL decreases from 74% to 68%. The conversion decreased slightly from 95% to 92%. The hydrogenation conversion and selectivity can be therefore maintained at a high value. This demonstrated that the catalyst has good chemical and structural stability. To this end, XPS analysis of Ru^0@POM/PIILP catalyst after 3 runs confirmed that the ruthenium nanoparticles were stable in the catalyst.

3.2.3.5 The performance of different catalysts for hydrogenation of cinnamaldehyde

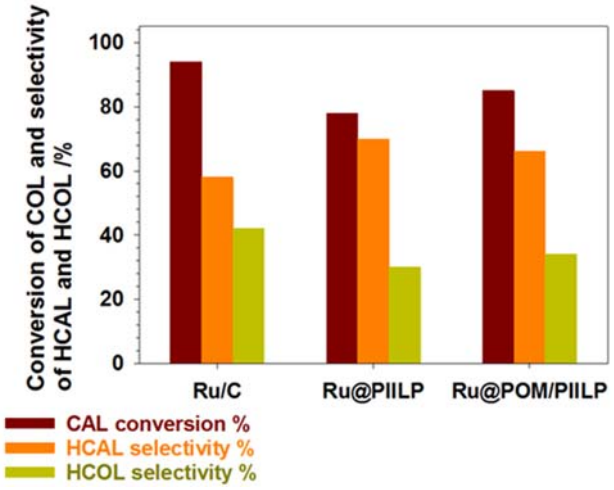

Figure 3.24 Effect of different catalysts for the conversion of CAL in aqueous solution. Reaction conditions: CAL, 1 mmol, water, 12 mL, 1mmol% Ru catalyst, H_2, 0.7 MPa, temperature, 60 °C, time, 1 hour. Determined by ^1H NMR, 1,3-dinitrobenzene as an internal standard.

In this section, Ru/C, Ru@PIILP and Ru^0@POM/PIILP catalysts are compared for the hydrogenation conversion and selectivity (Figure 3.24). When Ru/C was used as catalyst, the reaction activity was higher, the conversion of CAL was

94%, and the selectivity HCAL was low, only 58%. When Ru@PIILP was used as catalyst, the conversion was not as good as that of the Ru/C catalyst, which was 78%, but the selectivity of HCAL was higher than that of the Ru/C, which was 70%. The conversion performance of Ru^0@POM/PIILP catalyst was slightly higher than that of the Ru@PIILP, which was 85%, but the selectivity was slightly reduced to 66%. When POM was added to the catalyst, the reaction rate therefore increased, but the selectivity of HCAL decreased. We suggest that the Brønsted acid sites generated by the Ru^0@POM/PIILP catalyst in the hydrogenation reaction can improve the reaction rate, but was not conducive to the selectivity of HCAL. According to Doherty et al. report, alkaline conditions are beneficial to the selectivity of HCAL and it can reach 100%. Therefore, the selectivity of Ru^0@POM/PIILP catalyst for hydrogenation of CAL was not as good as that of Ru@PIILP because of the inhibition of HCAL selectivity by the generated Brønsted acid.

3.2.4 Hydrogenation of furfural

3.2.4.1 The pathway for hydrogenation of furfural

Hydrogenation of different functional groups of furfural (FFA) results in different products. In general, there may be four routes for the reaction. The first is the hydrogenation of furfural carbonyl to furfuryl alcohol (FA) and the subsequent hydrogenation to tetrahydrofurfuryl alcohol (THFA), followed by ring-opening hydrogenation to give pentanediol. The second is the hydrogenation of tetrahydrofurfural ring to tetrahydro-2-furancarboxaldehyde, then continued hydrogenation to tetrahydrofurfuryl alcohol, followed by ring-opening hydrogenation to give pentylene glycol. The third is furfural decarbonylation to furan, followed by hydrogenation to tetrahydrofuran (THF), and further ring

opening hydrogenation to give n-pentanol. The fourth is hydro-dehydration of furfural to methylanthran, followed by ring-opening hydrogenation to give pentanone and pentanol. These reactions are parallel competing reactions and consume raw materials furfural and hydrogen.

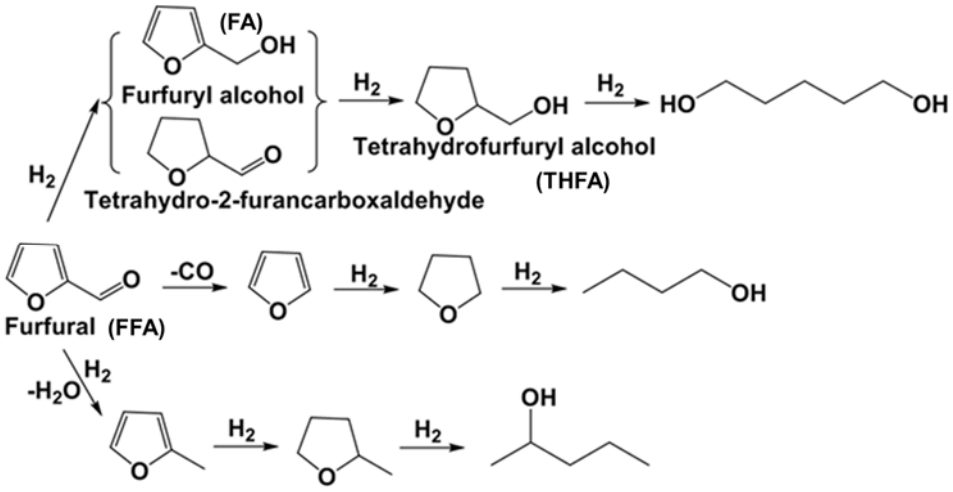

Figure 3.24 Scheme showing the possible products for hydrogenation of furfural

3.2.4.2 The performance of different catalysts for hydrogenation of furfural (FFA)

A solvent is used in most catalytic hydrogenation reactions and plays an important role in the reaction. It affects the hydrogenation rate and sometimes the reaction direction. This is mainly because the solvent changes the adsorption characteristics of the unsaturated substrate, which changes the amount of hydrogen adsorption, and also results in the change of bond energy and state of hydrogen and catalyst surface, and makes the catalyst disperse better. In general, hydrogenation takes place in a neutral medium, while hydrogenolysis takes place in acidic or alkaline medium. Polar solvents can accelerate the rate of hydrogenation. We used H_2O as the green solvent for hydrogenation of FFA.

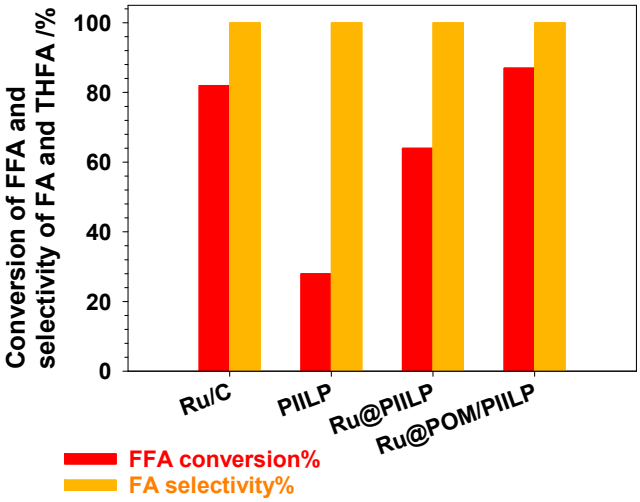

Figure 3.25 Effect of different catalysts on the conversion of furfural (FFA) in aqueous solution. Reaction conditions: FFA, 1 mmol, water, 12 mL, 1 mmol% Ru catalyst, H_2, 1 MPa, temperature, 55 ^{o}C, time, 2.5 hour. Determined by ^{1}H NMR, 1,3-dinitrobenzene as an internal standard.

Under the experimental conditions, the amount of FFA was monitored, indicating that the catalyst has a high selectivity to the target product FA (100%), and the catalytic activities of various catalysts in the FFA hydrogenation reaction are shown in Figure 3.25. It can be seen from Figure 3.25 that the catalytic activity of PIILP catalyst increased rapidly with the addition of the ruthenium nanoparticles, the FFA conversion rate increased from 28% to 64%, indicating that the ruthenium nanoparticles can increase the catalytic reaction rate. Compared with Ru/C, Ru/PIIPL catalysts, Ru@POM/PILP catalyst had the highest conversion rate of FFA, which indicated that the catalyst had the best catalytic effect. On the one hand, ruthenium as an active site was well dispersed on the carrier POM/PIILP. The presence of the carrier prevented the agglomeration of the ruthenium nanoparticles and also increased the specific surface area of the catalyst, thereby greatly increasing the activity of the

catalyst. On the other hand, due to the strong mutual electron effect between Ru, POM and PIILP, the selectivity of FFA hydrogenation product also had a great influence on the conversion of FFA, while $PW_{12}O_{40}^{3-}$ can also produce Brønsted acid to make the catalyst more strongly adsorb and polarizae C=O.

3.2.4.3 Study on kinetic factors of hydrogenation of furfural over Ru^0@POM/PIILP

In order to further study the catalytic performance of Ru^0@POM/PIILP catalyst, the kinetic factors such as hydrogen pressure, reaction temperature and reaction time were investigated.

3.2.4.3.1 Effect of hydrogen pressure

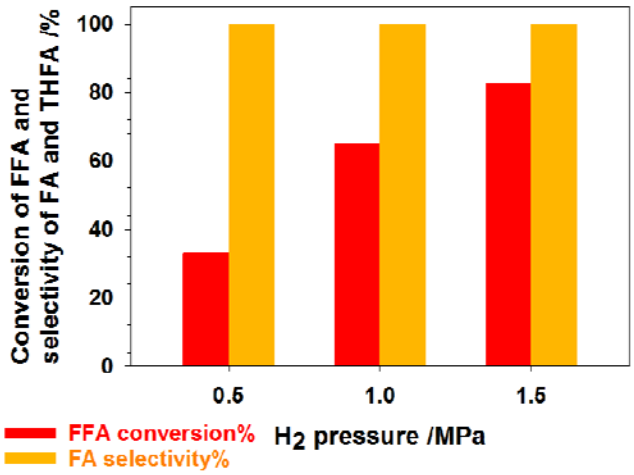

Figure 3.26 Effect of hydrogen pressure on the hydrogenation of FFA. Reaction conditions: FFA 1 mmol, H_2O, 12 mL, 1 mmol% Ru^0@POM/PIILP catalyst, temperature, 55 ^oC, time, 2 hours. Determined by ^1H NMR, 1,3-dinitrobenzene as an internal standard.

The change of conversion with hydrogen pressure is shown in Figure 3.27. It can be seen that hydrogen pressure had a great influence on the conversion of FFA. The hydrogen pressure was varied from 0.5 to 1.5 MPa and results

showed that the conversion rate of FFA was very low (33%) under the pressure of 0.5 MPa hydrogen. When the hydrogen pressure was increased to 1.0 MPa, the conversion of furfural was found to reach 65%. With the further increase of hydrogen pressure, more FFA was converted to FA (83%). This illustrated that the formation of FA required certain hydrogen pressure, and this was a powerful means to influence the hydrogenation reaction. New products can be obtained, the speed of reaction is accelerated and space resistance can be overcome. The hydrogenation of FFA to FA is a volume-reduced reaction, so increasing the pressure favors the reaction equilibrium. In addition, from the collision theory, it is known that increasing the pressure increases the chance of collisions between molecules, and from a kinetic point of view, the high pressure also favors the forward reaction.

3.2.4.3.2 Effect of reaction time

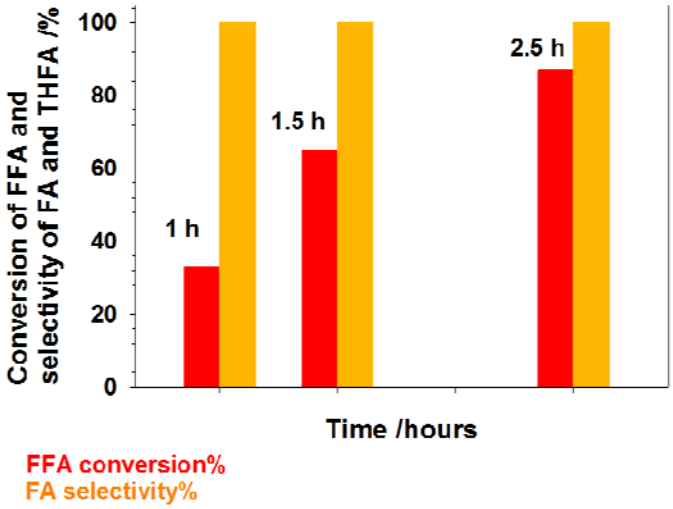

Figure 3.27 Effect of reaction time on the hydrogenation of FFA. Reaction conditions: FFA 1 mmol, H_2O, 12 mL, 1 mmol% Ru^0@POM/PIILP catalyst, temperature, 55 ^oC, H_2, 1 MPa. Determined by ^1H NMR, 1,3-dinitrobenzene as an internal standard.

Figure 3.27 shows the trend of product distribution over time using the Ru^0@POM/PIILP catalyst. The conversion of FFA gradually increased with time, with the reaction time increased from 1 hour to 1.5 hours and then to 2.5 hours, FFA conversion to FA increased from 33% to 65% to 87%. The highest yield of 87% when their reaction time was 2.5 hours.

3.2.4.3.2 Effect of reaction temperature

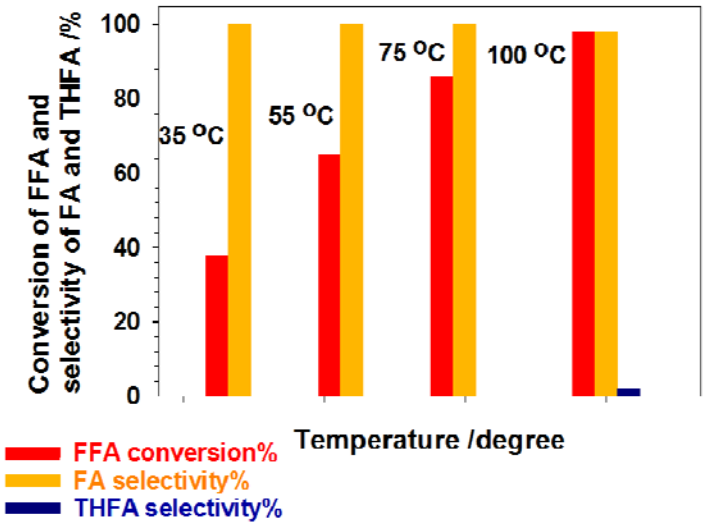

Figure 3.28 Effect of reaction temperature on the hydrogenation of FFA. Reaction conditions: FFA 1 mmol, H_2O, 12 mL, 1 mmol% Ru^0@POM/PIILP catalyst, time, 1.5 hours H_2, 1 MPa. Determined by ^1H NMR, 1,3-dinitrobenzene as an internal standard.

Figure 3.28 showed how the yield of the products varied with temperature. It can be seen that the temperature had a great influence on FFA conversion. The main product was FA produced by hydrogenation of FFA at a lower temperature of 35 °C, with a FFA conversion of 38%. With the increase of temperature, more FFA was converted to FA at 65 °C, the conversion of FFA reached 65%. When the temperature continued to rise to 75 °C, the conversion of FFA reached to

86% and the selectivity for FA was also100%. At 100 °C, the conversion rate of FFA reached 98%, but the selectivity of FA decreased to 98%, the by-products THFA had 2% yield. The hydrogenation of furfural to FA is an exothermic reaction. From the point of view of thermodynamics, too high temperature is not beneficial to the reaction in order to improve the equilibrium conversion. The thermodynamics of hydrogenation of unsaturated hydrocarbons and aromatics indicate that a favorable equilibrium can be obtained at atmospheric pressure below 200 °C, but the by-products can be produced at a high temperature.

3.2.4.4 Study on the Stability of Ru^0@POM/PIILP Catalyst for hydrogenation of FFA

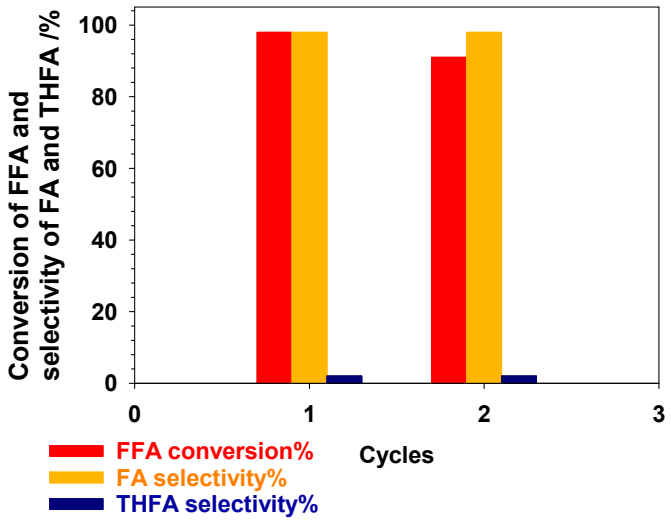

Figure 3.29 Recycles of Ru^0@POM/PIILP catalyst for the hydrogenation of FFA. Reaction conditions: FFA 1 mmol, H_2O, 12 mL, 1 mmol% Ru catalyst, H_2,1.0 MPa, temperature, 100 °C, time, 1.5 hours. Determined by ^1H NMR, 1,3-dinitrobenzene as an internal standard.

The Ru^0@POM/PIILP catalyst was used twice to investigate its stability, as shown in Figure 3.29. It can be seen from the diagram that the conversion of the two reactions was above 90%, and the conversion of FA decreases slightly from 98% to 91% in the second use, and the selectivity of FA was 98% in two runs. The decrease of FFA conversion showed that the activity of the catalyst decreased to a small extent.

3.3 Conclusions

The Ru^0@POM/PIILP composite was insoluble in water catalyst prepared. We assumed that + ve charges in PIILP will act to immobilize the – ve charged Ru@POM NPs. The morphology, structure and composition of the Ru^0@POM/PIILP catalyst were determined by various characterization methods, such as FT-IR, XRD, SEM, EDS, TEM, TGA and so on.

In the hydrogenolysis reaction of HMF to DMF, HMF contains C=C double bonds, C=O groups and OH groups. However, these active groups are likely to be reduced by catalysis in the process of hydrogenation reduction, and the interaction between the chemical groups makes it more difficult to reduce the catalytic hydrogenation to DMF, so the selection of catalyst is particularly important. By comparing the results of catalytic hydrogenolysis of HMF with Ru^0@POM/PIILP and various catalysts under the same reaction conditions, it indicated that the catalytic effect of Ru^0@POM/PIILP catalyst was the best, which was due to the fact that Ru^0@POM/PIILP was a kind of bi-functional catalyst. The synergistic effect between ruthenium nanoparticles and the POM served to generated Brønsted acid in Ru^0@POM/PIILP catalyst, making the selectivity of DMF increase in the selective catalytic reaction of hydrogenolysis. We also investigated the effect of the reaction temperature, reaction time and reaction pressure for the hydrogenolysis of HMF to DMF. It was concluded that the optimum reaction conditions for catalytic hydrogenolysis of HMF to DMF were 5 hours, 2 MPa H_2, 200 ^oC when Ru^0@POM/PIILP as catalyst, the conversion of HMF was 100% and the yield of DMF was 84%. The stability of the Ru^0@POM/PIILP catalyst was investigated by using the catalyst 5 times. When the Ru^0@POM/PIILP catalyst was repeatedly used three times, the catalyst can maintain good activity and all achieved a consistent catalytic effect on HMF conversion and DMF yield, but the conversion of HMF decreased from

100% to 91% at the fifth cycle and the DMF selectivity decreased from 84% to 77%. Although the activity of the catalyst decreased slightly at the fifth cycle, the catalytic activity remained stable.

The catalytic efficiency of CAL hydrogenation of Ru^0@POM/PIIL catalyst under different solvents was investigated, showing that water is the best reaction solvent, and the effects of different hydrogen pressure, reaction time, and reaction temperature on hydrogenation of CAL were also investigated. The optimal reaction conditions were 60 ^oC and 0.7 MPa of hydrogen, and the reaction time was 2 hours, the hydrogenation conversion of CAL was 95% and the HCAL selectivity was 74% under this conditions using Ru^0@POM/PIIL catalyst. When comparing the catalytic effects of different catalysts, it was known that the selectivity of Ru/C catalysts was poor. The conversion of Ru^0@POM/PIIL catalysts with POM was higher than that of Ru^0@PIIL, but the HCAL selectivity was slightly lower with Ru^0@POM/PIIL catalyst. This is because the generated Brønsted acid of Ru^0@POM/PIIL is not conducive to the selective hydrogenation of CAL.

In this work, the Ru^0@POM/PIIL catalyst was prepared to catalyze FFA to produce FA. The catalyst of Ru^0@POM/PIIL had the best activity and stability among different ruthenium-containing catalysts. Under different reaction temperature, time and pressure of hydrogen, the conversion of FFA and the selectivity of FA in hydrogenation catalyst were optimized, and the conversion of FFA was up to 98%. The activity of the catalyst decreased to a certain extent after two runs of use. Therefore, Ru^0@POM/PIIL is a possible catalyst for the production of FA from furfural. The catalytic performance of the catalyst was better than that of the Ru/C catalyst, mainly because of the synergetic effect of POM and the use of PIILP support for the Ru@POM nanoparticles, which improved the active surface area of the catalyst. In the hydrogenation using Ru^0@POM/PIIL catalyst, it is proposed that Brønsted acid sites are formed. A

small number of adsorption centers are beneficial to the forward reaction from a kinetic point of view. The higher selectivity is mainly due to the weak adsorption intensity of FA.

3.4 Experimental

3.4.1 General Chemicals

All chemicals were purchased from commercial suppliers (Alfa Aesar, Sigma Aldrich, Fisher Scientific, Acros Organics) and used without any purification. Distilled water was used throughout all this work. All manipulations of air-sensitive materials were carried out using standard Schlenk techniques under nitrogen and a glove-box with a recirculation system.

3.4.2 Instrumentation

3.4.2.1 Fourier transform infrared spectroscopy (FT-IR)

FT-IR spectra were analyzed on a Bruker Alpha spectrometer using a Platinum ATR module. Spectra were recorded for dried solid powder samples (vacuum drying for 5 hours).

3.4.2.2 Powder X-ray diffraction (XRD)

Powder XRD analysis was recorded on a Rigaku Ultima IV diffractometer with Cu K_α radiation, and the scanning angle range was 5~90 degrees at 40 kV and 40 mA.

3.4.2.3 X-ray photoelectron spectroscopy (XPS)

XPS characterization was recorded on a PHI Quantum-2000 system with Al K_α X-ray source. The powdered samples were pressed into sheets and then measured.

3.4.2.4 Scanning electron microscope (SEM) and energy dispersive spectrometer (EDS)

SEM images were taken using a HITACHI S-4800 instrument to check the morphology, element composition and element content of samples. The working voltage was 15 kV. In the experiment, samples were dispersed in solution and then dripped on clean silicon wafers. After drying, the silicon wafers with conductive tape on the sample stage were sent to the SEM instrument for testing.

3.4.2.5 Thermal gravimetric analysis (TGA)

TGA was performed using a SDT Q600 instrumen, at a heating rate of 10 ^{o}C/min under nitrogen, from room temperature up to 800 ^{o}C. 5-10 mg of sample was used for each measurement.

3.5.2.6 Transmission electron microscopy (TEM)

TEM photographs were taken using a 50 kV~300 kV high resolution transmission electron microscope (TECNAI F-30) from FEI, Holland. After ultrasonic dispersion of the samples, copper net is used as the observation carrier.

3.4.2.7 Nuclear magnetic resonance spectroscopy (NMR)

NMR spectra were recorded on Bruker JEOL ESC-300 and 400 instruments. Solid-state NMR spectra were recorded on a Varian VNMRS 400 instrument. Typical concentration of samples for solution NMR was 0.01 M, the mass of samples used for solid-state NMR was approxomately 10 mg.

3.4.2.8 Gas chromatography (GC)

GC results were recorded on a GC-2060 instrument. The gaseous products were analysed by a gas chromatograph equipped with a thermal conductivity detector (TCD) which was connected to a TDX-01 packed column and a flame ionization detector (FID) which used an alumina capillary column. The products in the liquid phase were analysed by a gas chromatograph equipped with an FID, PONA and Bond-Q capillary columns connected to FID.

3.4.3 Experimental

3.4.3.1 Synthesis of 1,2-dimethyl-3-(4-vinylbenzyl) imidazolium chloride

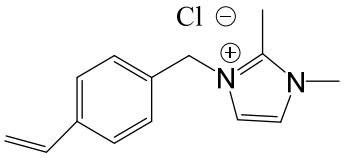

1

To an oven-dried Schlenk flask under N_2, 1,2-dimethylimidazole (5.25 g, 54.6 mmol, 1 eq.) in $CHCl_3$ (50 mL) and 4-chloromethyl styrene (10 mL, 71 mmol, 1.3 eq.) were added. The reaction mixture was stirred for 18 hours at 50 ^oC. The solvent was removed under vacuum and then washed with ethyl acetate (4 × 50 mL). The resulting fine beige powder (12.20 g，90.0 %) was dried under reduced pressure. ^1H NMR (300 MHz, chloroform-*d*) δ 7.79 – 7.69 (m, 2H), 7.39 – 7.23 (m, 3H), 6.63 (dd, *J* = 17.6, 10.9 Hz, 1H), 5.71 (dd, *J* = 17.6, 0.8 Hz, 1H), 5.54 (s, 2H), 5.25 (dd, *J* = 10.8, 0.8 Hz, 1H), 3.93 (s, 3H), 2.73 (s, 3H).^{13}C NMR (75 MHz, Chloroform-d) δ 135.76, 132.33, 128.50, 127.09, 122.85, 121.81, 115.33, 52.14, 35.85, 10.91. The ^1H NMR data is consistent with the literature (yield: 90 %).[46]

3.4.3.2 Synthesis of radical polymerisation

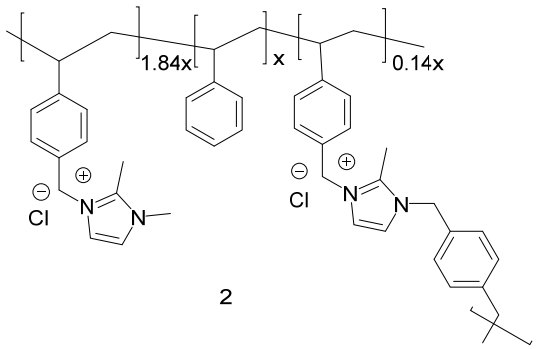

2

To an oven-dried Schlenk flask under N_2, **1** (5.00 g, 20.10 mmol, 1.84 eq), 2-methyl-1,3-bis(4-vinylbenzyl0-1H-imidazol-3-iumchloride (0.53g, 1.52 mmol, 0.14 eq), AIBN (0.25 g, 1.53 mmol, 0.14 eq.), styrene (1.45 g, 10.90 mmol, 1 eq.) were added in ethanol (100 mL). The resulting reagents were degassed using freeze-thaw method (6 cycles). After reaching room temperature, the reaction mixture was heated to 85 ^oC for 96 hours. The reaction mixture was then cooled to room temperature and an equivalent of AIBN was added followed by been degassed again (5 times) and stirring at 85 ^oC overnight. The solvent was removed under reduced pressure after cooling to room temperature. The yellow product was washed using ethanol (3 times) and dried under reduced pressure to give the polymer as a white powder (3.34 g). The sample was analysed by ^1H NMR peaks in MeOD solvent.

3.4.3.3 Synthesis of Ru/POM($H_3PW_{12}O_{40}$)@PIILP

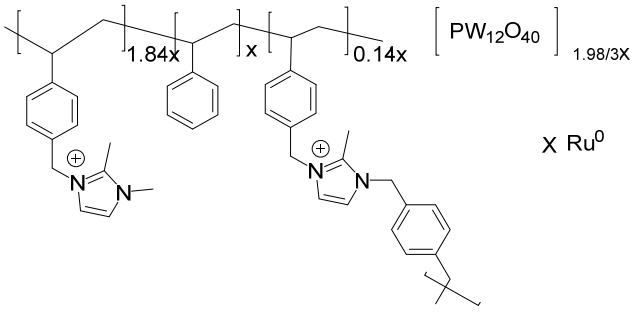

$H_3PW_{12}O_{40}$ (340 mg, 118mmol) and Na[trans-$Ru(DMSO)_2Cl_4$] (50 mg, 118 mmol) were added to reaction flask with water (12 mL), then reduced under 1.0 MPa H_2 at 50 ^oC for 5 hours in a 50 mL stainless steel autoclave with a stirring speed of 600 rpm. After reaction, the autoclave was cooled to room temperature, to obtain black stable and homogeneous solutions of $Ru@H_3PW_{12}O_{40}$. An oven-dried Schlenk flask was charged with $Ru@H_3PW_{12}O_{40}$ solution (12 mL) and polymer **2** (108 mg, 177 mmol) under nitrogen and allowed to stir at room temperature for 3 hours to form brown-black solid powder product. After reaction, the reaction mixture was centrifuged (10 min, 8000 rpm), then removed the solution and followed by washing with water (10 mL). This step was repeated 3 times, and the brown-black solid powder product was dried under reduced pressure (yield: 91 %). The sample was analysed by solid state ^1H and ^{13}C NMR.

3.4.3.4 Synthesis of Ru^0@PIILP

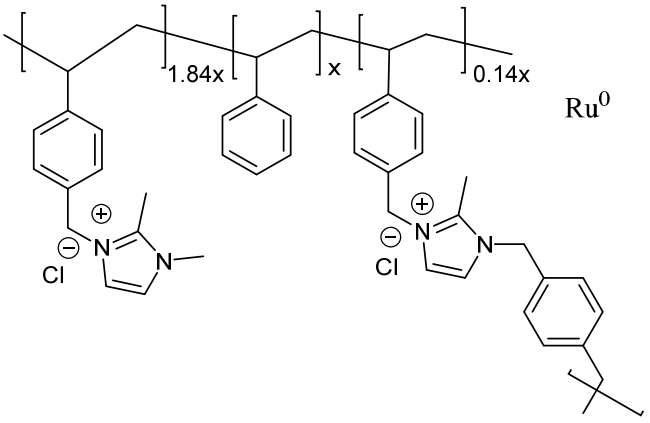

Polymer **2** (280 mg, 0.45 mmol) was dissolved in water (10 mL). The clear solution was added to Na[*trans*-$Ru(DMSO)_2Cl_4$] (127 mg, 0.3 mmol) and allowed to stir for 4 hours, the colour of the solution was changed to deep green. After reaction, the water was removed using rotary evaporator to get an amorphous solid. Diethyl ether (50 mL) was added to the solid and scratched

using spatula to obtain deep green powder [$(RuCl_4)^-$@PIILP] which was then washed with diethyl ether (3 times) and was dried under reduced pressure.

[$(RuCl_4)^-$@PIILP] (500 mg) was added to reaction flask with ethanol (12 mL), then reduced under 1.0 MPa H_2 at room temperature for 5 hours in a 50 mL stainless steel autoclave with a stirring speed of 600 rpm. After reaction, the resulting brown solid was washed with ethanol, diethyl ether and then dried overnight under reduced pressure to afford the product as an orange powder (yield: 85 %) The sample was analysed by solid state ^1H and ^{13}C NMR peaks.

3.4.3.5 Synthesis of $Cs_{1.5}H_{1.5}PW_{12}O_{40}$

In a beaker, $H_3PW_{12}O_{40}$ (8.6 g, 3.0 mmol) was dissolved in H_2O (50 mL) with stirring. In another beaker, Cs_2CO_3 was dissolved in H_2O (37.5 mL) with stirring.[47] The precipitate was obtained after the addition of the aqueous solution of Cs_2CO_3 into that of $H_3PW_{12}O_{40}$. The white precipitate was filtered and washed with H_2O and ethanol before stirring for 4 hours. After drying and calcinating the sample at 400 ^oC for 2 hours $Cs_{1.5}H_{1.5}PW_{12}O_{40}$ was obtained (yield: 88 %). The sample was analysed by solid state ^1H and ^{31}P NMR.

3.4.3.6 Synthesis of polymer supported phosphotungstate (PIILP/POM)

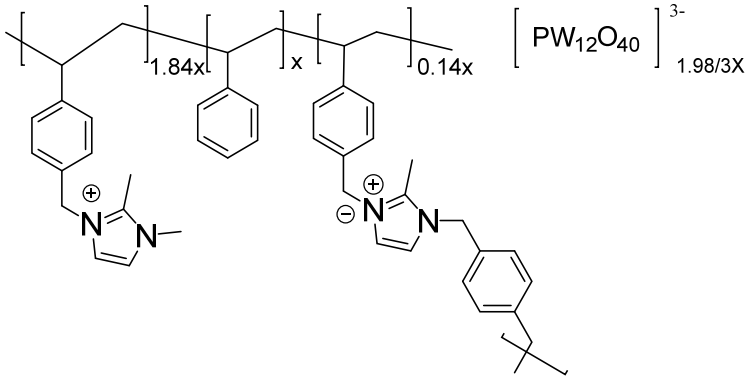

A suspension of polymer **2** (0.58 g, 0.2 mmol) and pyridine (47.46 mg, 0.6 mmol) was dissolved in ethanol (20 mL) and stirred for 40 min at room temperature, phosphotungstate acid (0.58 g, 0.2 mmol) was added and dissolved in a minimum volume of H_2O was added. The reaction mixture was stirred at room temperature for 4 hours. The white precipitate was filtered, washed with H_2O, ethanol and diethyl ether, and then dried under reduced pressure to afford the product of a white solid (yield: 93 %). The sample was analysed by solid state ^{1}H and ^{13}C NMR peaks.

3.4.3.7 General procedure for selective hydrogenation of HMF to DMF

0.1 mol% catalyst (based on Ru loading), HMF (63 mg, 0,.5 mmol) and THF (12 mL) were placed in a Parr reactor and heated at different temperatures under different H_2 pressures before being allowed to stir for the alloted time. After cooling to room temperature, the decane (27μL) was added as an internal standard substance and filtered by glass microfilter. The products solution was analyzed by GC-MS to determine conversion and selectivity.

3.4.3.8 General procedure for selective hydrogenation of trans-cinnamaldehyde

0.1 mol% catalyst (based on Ru loading), trans-cinnamaldehyde (0.125 mL, 1.0 mmol) and solvent (toluene, isopropyl alcohol, hexane or ethanol) (12 mL) were placed in a Parr reactor and heated at different temperatures under different H_2 pressures before being allowed to stir for the alloted time. After cooling to room temperature, reaction mixture was diluted with diethyl ether (15 mL). The organic layer was separated, dried with magnesium sulfate, filtered and solvent removed under vacuum. The resulting residue was analyzed by ^{1}H NMR spectroscopy to determine conversion and selectivity.

3.4.3.9 General procedure for selective hydrogenation of furfural

0.1 mol% catalyst (based on Ru loading), decene (1 mmol, 82.5 µL)) and water (12 mL) were placed in a Parr reactor and heated at different temperatures under different H_2 pressures before being allowed to stir for the alloted time. Upon cooling to room temperature, the reaction mixture was diluted with diethyl ether (15 mL). The organic layer was separated, dried with magnesium sulfate, filtered and solvent removed under reduced vacuum. The resulting residue was analyzed by ^{1}H NMR spectroscopy to determine conversion.

3.5 References

1. R. D. Cortright, R. Davda and J. A. Dumesic, in *Materials For Sustainable Energy: A Collection of Peer-Reviewed Research and Review Articles from Nature Publishing Group*, World Scientific, 2011, 289-292.

2. Y. B. Huang, M. Y. Chen, L. Yan, Q. X. Guo and Y. Fu, *ChemSusChem*, 2014, **7**, 1068-1072.

3. R. Weingarten, Y. T. Kim, G. A. Tompsett, A. Fernández, K. S. Han, E. W. Hagaman, W. C. Conner Jr, J. A. Dumesic and G. W. Huber, *J. Catal.*, 2013, **304**, 123-134.

4. I. T. Horváth, H. Mehdi, V. Fábos, L. Boda and L. T. Mika, *Green Chem.*, 2008, **10**, 238-242.

5. P. Yang, Q. Cui, Y. Zu, X. Liu, G. Lu and Y. Wang, *Catal. Commun.*, 2015, **66,** 55-59.

6. B. O. de Beeck, M. Dusselier, J. Geboers, J. Holsbeek, E. Morré, S. Oswald, L. Giebeler and B. F. Sels, *Energ. Environ. Sci.*, 2015, **8**, 230-240.

7. H. L. S. Y. L. Lu, *Progr. Chem.*, 2011, 10, 011.

8. X. Kong, R. Zheng, Y. Zhu, G. Ding, Y. Zhu and Y.-W. Li, *Green Chem.*, 2015, **17**, 2504-2514.

9. Y. Zu, P. Yang, J. Wang, X. Liu, J. Ren, G. Lu and Y. Wang, *Appl. Catal. B: Environmental*, 2014, **146**, 244-248.

10. J. Jae, W. Zheng, R. F. Lobo and D. G. Vlachos, *ChemSusChem*, 2013, **6**, 1158-1162.

11. J. Zhang, L. Lin and S. Liu, *Energy Fuels*, 2012, **26**, 4560-4567.

12. B. Saha, C. M. Bohn and M. M. Abu-Omar, *ChemSusChem*, 2014, **7**, 3095-3101.

13. L. Hu, X. Tang, J. Xu, Z. Wu, L. Lin and S. Liu, *Ind. Eng. Chem.*, 2014, **53**, 3056-3064.

14. S. Lima, D. Chadwick and K. Hellgardt, *RSC Adv.*, 2017, **7**, 31401-31407.

15. V. M. Chernyshev, O. A. Kravchenko and V. P. Ananikov, *Russian Chem. Rev.*, 2017, **86**, 357-387.

16. A. S. Nagpure, N. Lucas and S. V. Chilukuri, *ACS Sustain. Chem. Eng.*, 2015, **3**, 2909-2916.

17. Y. Yang, Q. Liu, D. Li, J. Tan, Q. Zhang, C. Wang and L. Ma, *RSC Adv.*, 2017, **7**, 16311-16318.

18. J. Requies, M. Frias, M. Cuezva, A. Iriondo, I. Agirre and N. Viar, *Ind. Eng. Chem. Res.*, 2018, **57**, 34, 11535-11546.

19. J. Hájek, N. Kumar, P. Mäki-Arvela, T. Salmi and D. Y. Murzin, *J. Mol. Catal. A: Chem.*, 2004, **217**, 145-154.

20. X. Yang, D. Chen, S. Liao, H. Song, Y. Li, Z. Fu and Y. Su, *J. Catal.*, 2012, **291**, 36-43.

21. S. Bhogeswararao and D. Srinivas, *J. Catal.*, 2012, **285**, 31-40.

22. A. M. R. Galletti, C. Antonetti, A. M. Venezia and G. Giambastiani, *Appl. Catal. A: General*, 2010, **386**, 124-131.

23. W. Lin, H. Cheng, L. He, Y. Yu and F. Zhao, *J. Catal.*, 2013, **303**, 110-116.

24. Y. Li, Z.-G. Li and R.-X. Zhou, *J. Mol. Catal. A: Chem.*, 2008, **279**, 140-146.

25. B. F. Machado, S. Morales-Torres, A. F. Pérez-Cadenas, F. J. Maldonado-Hódar, F. Carrasco-Marín, A. M. Silva, J. L. Figueiredo and J. L. Faria, *Appl. Catal. A: General*, 2012, **425**, 161-169.

26. B. Machado, S. Morales-Torres, H. Gomes, A. Pérez-Cadenas, F. Maldonado-Hódar, F. Carrasca-Marín, J. Figueiredo and J. Faria, 2008.

27. A. Plomp, D. Van Asten, A. Van der Eerden, P. Mäki-Arvela, D. Y. Murzin, K. de Jong and J. Bitter, *J. Catal.*, 2009, **263**, 146-154.

28. F. Delbecq and P. Sautet, *J. Catal.*, 1995, **152**, 217-236.

29. P. Gallezot and D. Richard, *Cat. Rev.*, 1998, **40**, 81-126.

30. A. Da Silva, E. Jordao, M. Mendes and P. Fouilloux, *Appl. Catal. A: General*, 1997, **148**, 253-264.

31. G. Cordier, Y. Colleuille, P. Fouilloux and B. In Imelik, *Editions du CNRS, Paris*, **1984**, 349.

32. A. Giroir-Fendler, D. Richard and P. Gallezot, in *Studies in Surface Science and catalysis*, Elsevier, 1988, **41**, 171-178.

33. D. Richard, J. Ockelford, A. Giroir-Fendler and P. Gallezot, *Catal. Lett.*, 1989, **3**, 53-58.

34. H. Ma, L. Wang, L. Chen, C. Dong, W. Yu, T. Huang and Y. Qian, *Catal. Commun.*, 2007, **8**, 452-456.

35. E. Ramos-Fernández, A. Ferreira, A. Sepúlveda-Escribano, F. Kapteijn and F. Rodríguez-Reinoso, *J. Catal.*, 2008, **258**, 52-60.

36. K. M. Bratlie, H. Lee, K. Komvopoulos, P. Yang, G. A. Somorjai *Nano letters*. 2007, ***7***, 3097-3101.

37. C. Milone, C. Crisafulli, R. Ingoglia, L. Schipilliti and S. Galvagno, *Catal. Today*, 2007, **122**, 341-351.

38. C. M. Cai, T. Zhang, R. Kumar and C. E. Wyman, *J. Chem. Technol. Biotechnol.*, 2014, **89**, 2-10.

39. R. Kumar, S. Singh and O. V. Singh, *J. Ind. Microbiol. Biotechnol.*, 2008, **35**, 377-391.

40. J. N. Chheda, Y. Román-Leshkov and J. A. Dumesic, *Green Chem.*, 2007, **9**, 342-350.

41. A. Bielański, J. Datka, B. Gil, A. Małecka-Lubańska and A. Micek-Ilnicka, *Catal. Lett.*, 1999, **57**, 61-64.

42. E. A. Paoli, F. Masini, R. Frydendal, D. Deiana, C. Schlaup, M. Malizia, T. W. Hansen, S. Horch, I. E. Stephens and I. Chorkendorff, *Chem. Sci.*, 2015, **6**, 190-196.

43. K. C. Park, I. Y. Jang, W. Wongwiriyapan, S. Morimoto, Y. J. Kim, Y. C. Jung, T. Toya and M. Endo, *J. Mater. Chem.*, 2010, **20**, 5345-5354.

44. Y. Yue, L. Qiying, C. Chiliu, T. Jin, W. Tiejun and M. Longlong, Prog. Chem., 2016, **28**, 363-374.

45. Z. Zhang, Q. Wang, H. Xie, W. Liu and Z. Zhao, *ChemSusChem*, 2011, **4**, 131-138.

46. W. Chen, Y. Zhang, L. Zhu, J. Lan, R. Xie and J. You, *J. Amer. Chem. Soc.*, 2007, **129**, 13879-13886.

47. M. Liu, W. Deng, Q. Zhang, Y. Wang and Y. Wang, *Chem. Commun.*, 2011, **47**, 9717-9719.

Chapter 4

Polyoxometalates Stabilized Ruthenium Nanoparticles Adsorbed Onto Carbon Nitride

Chapter 4. Polyoxometalate-stabilized ruthenium nanoparticles adsorbed onto carbon nitride

4.1 Introduction

The material g-C_3N_4 is a new type of non-metallic semiconductor photocatalyst with a band gap of about 2.7 eV.[1,2] When irradiated by sunlight, valence band electrons are excited to form electron-hole pairs and produce active particles that catalyze the decomposition of pollutants, hydrolysis and oxygen reduction.[3-6] In addition, it can also catalyze the synthesis of organic compounds. The preparation of g-C_3N_4 by conventional polycondensation has many disadvantages, such as low photocatalytic activity, small specific surface area, facile recombination of the photogenerated electrons and holes, large band gap, slow transport of photogenerated carriers, and unsatisfactory photocatalytic activity.[7-9] Using a hydrothermal method, a series of $Ru^0@H_3PW_{12}O_{40}/C_3N_4$ hybrid composites were synthesized, in which the modification of g-C_3N_4 by $Ru^0@H_3PW_{12}O_{40}$ not only solved the solubility problem of $Ru^0@H_3PW_{12}O_{40}$, but also overcame the disadvantages of the small specific surface area of C_3N_4, the high exciton binding energy and fast photo-carrier recombination, and thereby promotes the photocatalytic reaction.

4.1.1 Water splitting

Energy shortage and environmental pollution are the most important issues for humans to solve in the 21st century. In 1972, Japanese scientists Fujishima and Honda discovered that TiO_2 single crystal electrodes can be used to photolytically to decompose water to give hydrogen.[10]

Photocatalytic water splitting for hydrogen production has attracted great interest by scientists all over the world. The photocatalytic conversion of low-density solar energy to high-density chemical energy is one of the simplest hydrogen energy production technologies, and it can be used to solve energy shortage and environmental pollution.[11] Novel photocatalysts with high quantum efficiency, high visible light utilization, high stability and low cost have been designed and developed.[12,13] In the past 40 years, inorganic compounds have been developed as the main photocatalysts, including metal oxides, sulfides and nitrides.[14-16] The unique structure of g-C_3N_4 also shows good photocatalytic performance for water splitting.[3] In practice, in order to further improve the photocatalytic effect of g-C_3N_4, researchers have developed a variety of improved methods, such as physical modification, chemical doping and microstructure adjustment.[17,18] The Keggin type heteropolyacid $H_3PW_{12}O_{40}$ combined with TiO_2 can enhance the photocatalytic effect because the unoccupied W_{5d} orbital of $PW_{12}O_{40}^{3-}$ might trap photogenerated electrons.[19] The g-C_3N_4 was modified by adsorbing $Ru^0@H_3PW_{12}O_{40}$ nanoclusters using the hydrothermal method described in this Chapter, which was used to inhibit the combination of photogenerated electrons and holes, increase the absorption of visible light and improving the photocatalytic activity. The effect of g-C_3N_4 prepared with different amounts of $Ru^0@H_3PW_{12}O_{40}$ on photocatalytic hydrogen production was studied systematically. The catalytic performance of the resulting $Ru^0@H_3PW_{12}O_{40}/C_3N_4$ hybrid composites were compared with g-C_3N_4, and the photocatalytic mechanism of $Ru^0@H_3PW_{12}O_{40}/C_3N_4$ is described in this Chapter.

4.1.2 Hydrogenation of cellobiose to sorbitol

Sorbitol is an important raw material in medicine, the chemical industry, light industry and the food industry.[20,21] It can be used as a softener, a humidity regulator and in other houselold chemicals such as toothpaste and mouthwash.[21] Sorbitol is also widely used in the leather, tobacco and metallurgy industries, and can also be used as an energy platform molecule through further catalytic conversion.[22] At present, the preparation of sorbitol by heterogeneous catalytic hydrogenation mainly uses glucose, sucrose, starch and other edible sugars as raw materials.[23,24] The production cost is therefore high and does not meet sustainability requirements. If the hydrogenation of cellulose to sorbitol can be realized by designing and developing high performance catalysts, it will not only effectively reduce the production cost of sorbitol, but also play an important role in ensuring food security and social sustainable development. However, the catalytic conversion of cellulose is still a very difficult challenge primarily because of its stable crystal structure and poor solubility in water and other solvents.[25] Although some progress was been made in the development of catalysts for the hydrogenation of cellulose to sorbitol, the yield is still low, and the complexity of cellulose is not conducive to basic research. Therefore, cellobiose is used as a model for cellulose (Scheme 4.1), and was chosen as the research object in this Chapter.[26] At present, Ni and Ru based catalysts are mainly used for hydrogenation of glucose to sorbitol. Ni is used in industry, but because the active components are easily lost and the surface adsorption of by-products poisons the catalyst, the system has the disadvantages of short catalyst life and the product needs to be purified.[27-30] Compared with this, ruthenium supported catalysts have become important for the hydrogenation of glucose because the low content of Ru in the catalyst shows the same activity as the high content Ni based catalyst and its performance is stable.[30-32] The

properties of different catalysts for hydrogenation of cellobiose to sorbitol are described in this Chapter, including details of reaction mechanism and factors affecting the kinetics of hydrogenation of cellobiose using $Ru^0@H_3PW_{12}O_{40}/C_3N_4$ hybrid catalysts. $Ru^0@H_3PW_{12}O_{40}/C_3N_4$ catalysts showed good catalytic performance in the hydrogenation of cellobiose due to the unique generation of Brønsted acid sites from hydrogen over $Ru^0@H_3PW_{12}O_{40}/C_3N_4$ catalysts (Scheme 4.2). This work provides the foundation for the hydrogenation of cellulose based on the model study with cellobiose.

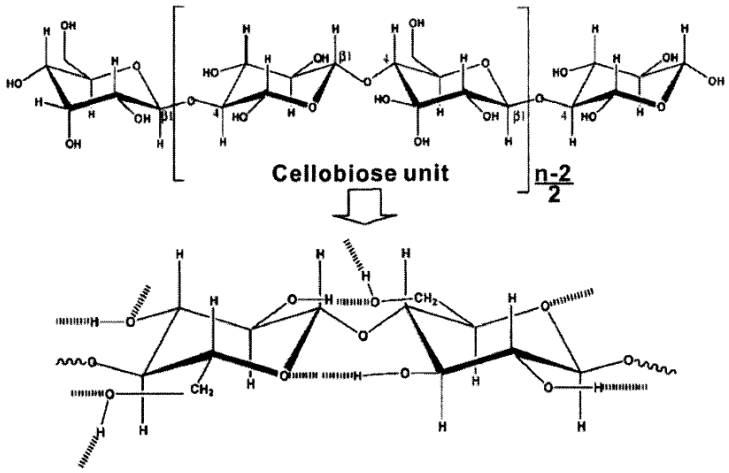

Scheme 4.1 Chemical structure of cellulose and cellobiose unit

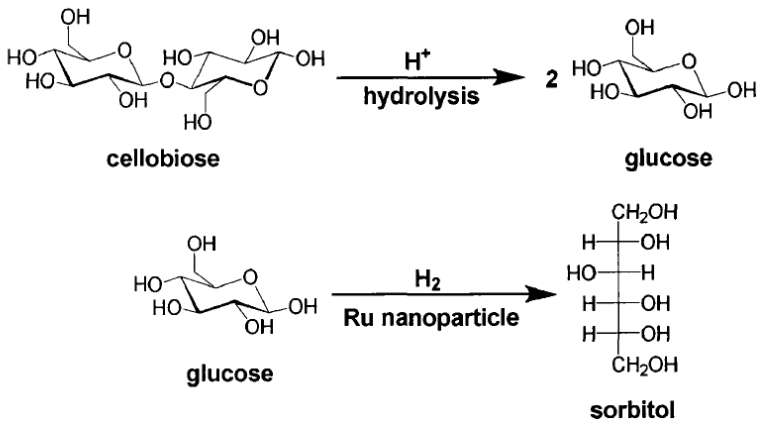

Scheme 4.2 Reaction mechanism of cellobiose under acidic conditions

4.1.3 Hydrogenation of levulinic acid (LA)

With the decreasing availability of fossil fuels and global warming, finding renewable resources to replace fossil fuels is an important way to solve the energy crisis and realize renewable energy. Biomass is a major source of renewable fuels and chemicals due to its low cost and sustainability.[33] Among the various biomass-derived compound, levulinic acid (LA) is an important platform molecule, which can be obtained by hydrolysis of lignocellulose and waste biomass.[34] Many add-value products can be obtained by LA hydrogenation, of which γ-valerolactone (GVL) is main intermediate, because of its non-toxic, stable properties, large storage and biodegradability. It is widely used in liquid fuels, food additives or solvents, so LA hydrogenation to GVL is a very important reaction.[35,36] In recent years, a growing number of catalyst supportes have been used in the hydrogenation of LA to produce GVL, including silicon dioxide (SiO_2), alumina (Al_2O_3), activated carbon (AC), ordered mesoporous carbon (OMC) and carbon nanotubes (CNTs) with supported Cu, Ni, Ir, Au, Pd, Pt, Ru, Co catalysts.[37-55] The supported Ru catalyst has the highest catalytic activity, and results showed that the pore structure (specific surface area, pore volume and pore size distribution) not only affects the dispersion of the active components but also affects the mass transfer rate during the reaction.[56-58] Therefore, the activity, selectivity and stability of the supported catalysts are closely related to the properties of the support.

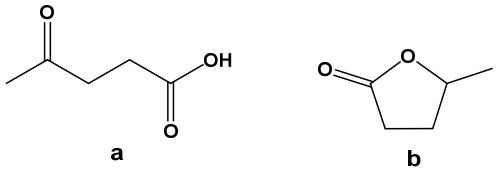

Scheme 4.3 Chemical structure of (a) LA) and (b) GVL

4.2 Results and discussion

4.2.1 Characterization of POM stabilized ruthenium nanoparticles adsorbed onto carbon nitride ($Ru^0@H_3PW_{12}O_{40}/C_3N_4$) composites

The synthesis of $Ru^0@H_3PW_{12}O_{40}/C_3N_4$ composites is shown in Scheme 4.4. POM stabilized ruthenium nanoparticles were prepared by the H_2 reduction of mixture of $H_3PW_{12}O_{40}$ and Na[*trans*-$Ru(DMSO)_2Cl_4$]. Dicyandiamide was used to synthesize g-C_3N_4, and elemental analysis showed 1.65 wt% for H, 35.10 wt % for C and 61.98 wt% for N, so the C/N mole ratio was 0.66, as previous reported. $Ru^0@H_3PW_{12}O_{40}/C_3N_4$ was synthesized from POM stabilized ruthenium nanoparticles and g-C_3N_4 using hydrothermal treatment as described in Chapter 2. The OH groups were replaced by NH_2 groups on the surface of g-C_3N_4 during hydrothermal method, and in the acidic solution of $Ru^0@H_3PW_{12}O_{40}$, the NH_2 groups of C_3N_4 are protonated by $H_3PW_{12}O_{40}$, The resulting NH_3^+ groups on the surface of g-C_3N_4 will cause adsorption of $Ru^0@H_3PW_{12}O_{40}$ by electrostatic attraction to form $Ru^0@H_3PW_{12}O_{40}/C_3N_4$.

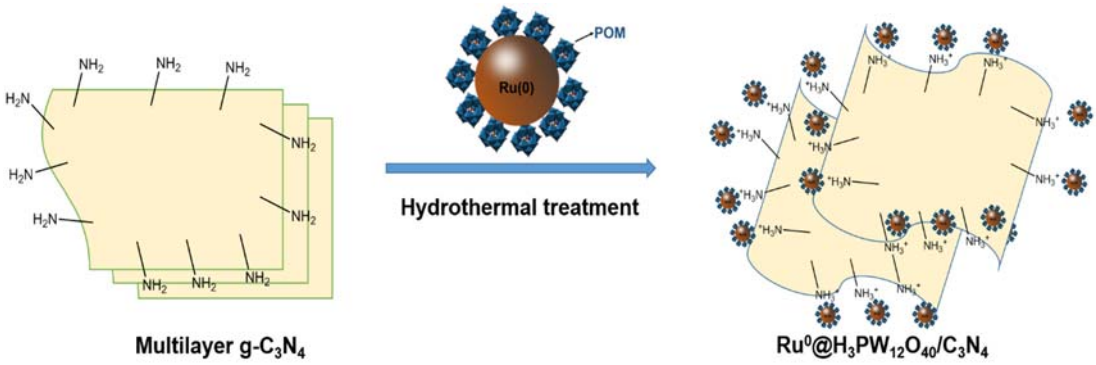

Scheme 4.4 The designed route for $Ru^0@H_3PW_{12}O_{40}/C_3N_4$ hybrid composites

The solid state ^{13}C NMR spectra of g-C_3N_4 and $Ru^0@H_3PW_{12}O_{40}/C_3N_4$ are shown in Figure 4.1 (a). The ^{13}C NMR peaks of g-C_3N_4 at 156 and 164 ppm, and the ^{13}C NMR peaks of $Ru^0@H_3PW_{12}O_{40}/C_3N$ were also at 156 and 164

ppm. The location of the ^{13}C NMR peaks of g-C_3N_4 were consistent with that of $Ru^0@H_3PW_{12}O_{40}/C_3N_4$. These indicated the presence of g-C_3N_4 in $Ru^0@H_3PW_{12}O_{40}/C_3N_4$. Figure 4.1 (b) showed the solid state ^{31}P NMR spectra of $H_3PW_{12}O_{40}$ and $Ru^0@H_3PW_{12}O_{40}/C_3N_4$, they all exhibited a sharp peak at -15.6 ppm, the ^{31}P NMR peak position of $Ru^0@H_3PW_{12}O_{40}/C_3N_4$ was consistent with $H_3PW_{12}O_{40}$ and the band width was broadened. The broadening of the signs has been attributed to electrostatic interactions between $H_3PW_{12}O_{40}$ and g-C_3N_4. The solid state ^{31}P and ^{13}C NMR spectra indicated the successful preparation of $Ru^0@H_3PW_{12}O_{40}/C_3N_4$.

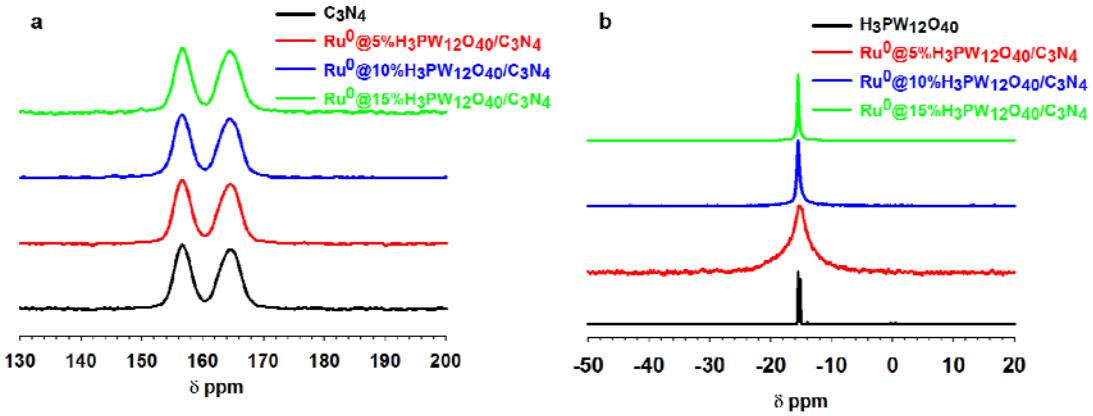

Figure 4.1 Solid state ^{13}C NMR spectra (a) and solid state ^{31}P NMR spectra (b) for samples

The g-C_3N_4, $H_3PW_{12}O_{40}$, $Ru^0@5\%H_3PW_{12}O_{40}/C_3N_4$, $Ru^0@10\%H_3PW_{12}O_{40}/C_3N_4$ and $Ru^0@15\%H_3PW_{12}O_{40}/C_3N_4$ composites were also characterized by powder X-ray diffraction (XRD) and results are shown in Figure 4.2. The g-C_3N_4 was a typical lamellar graphite phase structure, and there are two obvious XRD characteristic peaks at 13.0 ° (d = 0.618 nm) and 27.4 ° (d = 0.326 nm), which belonged to the stacked diffraction peaks of the heptazine heterocyclic units and the graphite-like layers in the crystal planes of (100) and (002).[5,59,60] The diffraction pattern of $H_3PW_{12}O_{40}$ was consistent with a monoclinic structure. For $Ru^0@H_3PW_{12}O_{40}/C_3N_4$, the co-occurrence of $[PW_{12}O_{40}]^{3-}$, ruthenium and g-C_3N_4 were exposed in XRD patterns, the

$[PW_{12}O_{40}]^{3-}$ peak intensities increased gradually with the content of $[PW_{12}O_{40}]^{3-}$ in composites from 5% to 15%, this was due to the strong diffraction peak of $H_3PW_{12}O_{40}$ covering g-C_3N_4 diffraction peak.

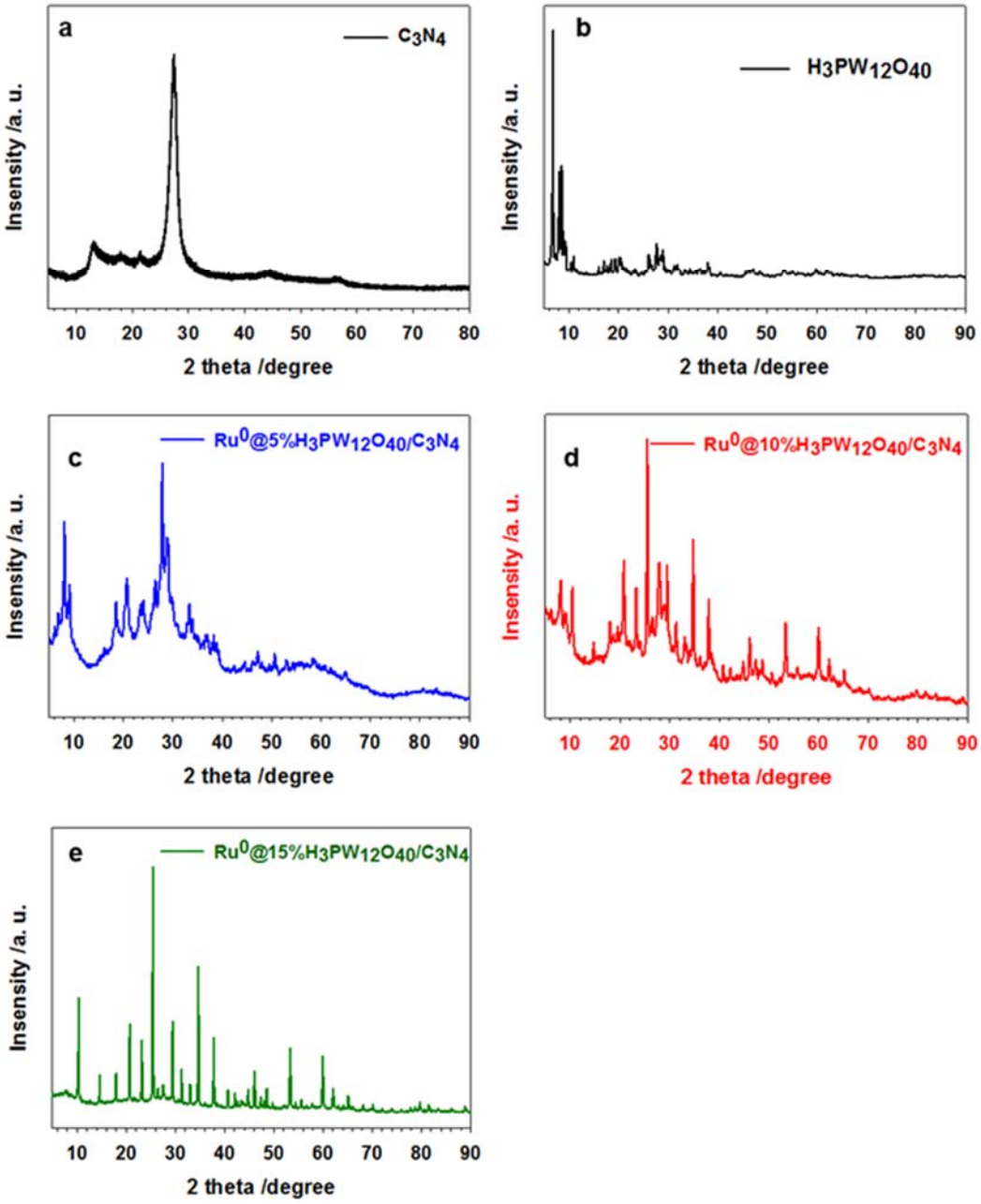

Figure 4.2 XRD patterns of (a) g-C_3N_4, (b) $H_3PW_{12}O_{40}$, (c) Ru^0@5%$H_3PW_{12}O_{40}/C_3N_4$, (d) Ru^0@10%$H_3PW_{12}O_{40}/C_3N_4$ and (e) Ru^0@15%$H_3PW_{12}O_{40}/C_3N_4$ samples

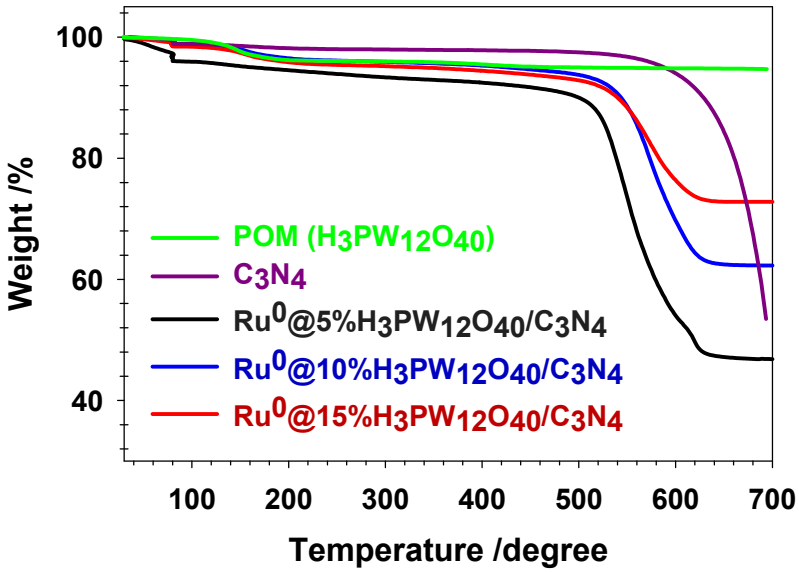

Figure 4.3 TGA curves of $H_3PW_{12}O_{40}$, g-C_3N_4, Ru^0@5%$H_3PW_{12}O_{40}/C_3N_4$, Ru^0@10%$H_3PW_{12}O_{40}/C_3N_4$ and Ru^0@15%$H_3PW_{12}O_{40}/C_3N_4$ samples

Thermal gravimetric analysis (TGA) profiles are shown in Figure 4.3. The 4% weight loss for the $H_3PW_{12}O_{40}$ between 100 to 200 °C was due to moisture volatilization. After calculation, we can make sure the x for $H_3PW_{12}O_{40}\cdot xH_2O$ is 6.6. Then the weight of $H_3PW_{12}O_{40}$ did not change with the temperature increase to 700 °C, which illustrated $H_3PW_{12}O_{40}$ was stable until 700 °C. The combustion of pure g-C_3N_4 occurred in the range of 580 to 700 °C. Rapid decomposition region was observed from 505 to 625 °C for Ru^0@5%$H_3PW_{12}O_{40}/C_3N_4$, Ru^0@10%$H_3PW_{12}O_{40}/C_3N_4$ and Ru^0@15%$H_3PW_{12}O_{40}/C_3N_4$ samples, at lower temperature than g-C_3N_4 and showed 52.5%, 36.5%, 27.5% weight losses respectively, which was attributed to the decomposition of C_3N_4. At higher temperatures, the Ru^0@$H_3PW_{12}O_{40}/C_3N_4$ samples showed no decomposition between 625 and 700 °C.

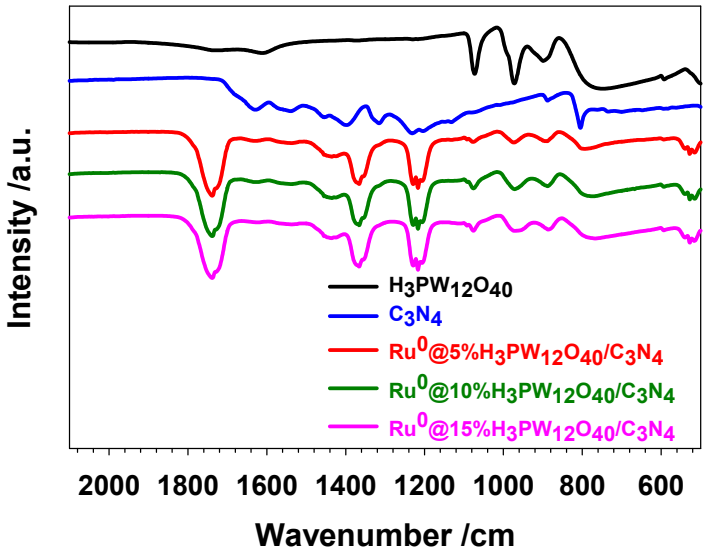

Figure 4.4 FT-IR spectra of $H_3PW_{12}O_{40}$, g-C_3N_4, Ru^0@5%$H_3PW_{12}O_{40}$/C_3N_4, Ru^0@10%$H_3PW_{12}O_{40}$/C_3N_4 and Ru^0@15%$H_3PW_{12}O_{40}$/C_3N_4 samples

Figure 4.4 shows the Fourier transform infrared (FT-IR) spectra of g-C_3N_4, $H_3PW_{12}O_{40}$ and the series of Ru^0@$H_3PW_{12}O_{40}$/C_3N_4 composites. For $H_3PW_{12}O_{40}$, the peaks at 1079, 976, 889, 765 cm^{-1} were attributable to stretching vibration of (P−O_a), (W=O_d), (W−O_b-W) and (W-O_c-W).[61,62] For g-C_3N_4, a series of bonds were contained in the range 1200-1650 cm^{-1} because of CN (C-N and C=N) heterocycles, a characteristic peak at 808 cm^{-1} was assigned to stretching vibration of the triazine units.[63] Moreover, in the case of Ru^0@$H_3PW_{12}O_{40}$/C_3N_4 composites, FT-IR modes of $[PW_{12}O_{40}]^{3-}$ were shifted to 1089, 977, 894, 755 cm^{-1}, indicating that $[PW_{12}O_{40}]^{3-}$ interacted with g-C_3N_4 upon hydrothermal treatment. The g-C_3N_4 related FT-IR mode at 808 cm^{-1} cannot be observed in the Ru^0@$H_3PW_{12}O_{40}$/C_3N_4 composites due to overlap with bonds $[PW_{12}O_{40}]^{3-}$.

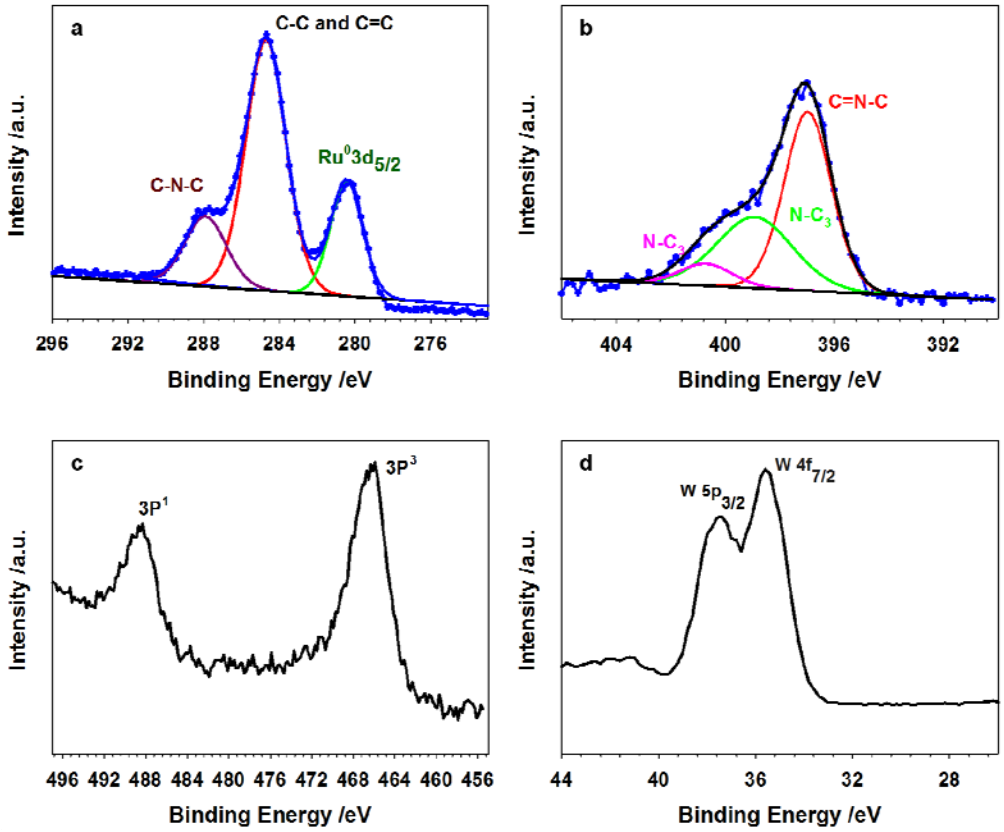

Figure 4.5 XPS spectra of Ru^0@5%$H_3PW_{12}O_{40}/C_3N_4$ sample, (a) C1s peak, (b) N1s peak, (c) Ru1s peak and (d) W1s peak

Interactions between g-C_3N_4 and Ru^0@$H_3PW_{12}O_{40}$ can be confirmed by X-ray photoelectron spectroscopy (XPS) as shown in Figures 4.5-4.7. The XPS spectra of Ru^0 (Ru^0 $3d_{5/2}$ at 280.5 eV, Ru^0 $3p^3$ at 466.2 eV, Ru^0 $3p^1$ at 488.5 eV), ndicates the existence of Ru^0 nanoparticles in the serial composites. The C1s bonding energy values for g-C_3N_4 and Ru^0@$H_3PW_{12}O_{40}$ showed a peak at 284.7 eV assigned to C-C and C=C, which was associated with adventitious carbon on the surface of Ru^0@$H_3PW_{12}O_{40}/C_3N_4$ samples, while the peak at 288 eV was attributed to sp^2 C atoms of C-N-C.[64] The W1s spectra in Figures 4.5-4.7 (d), show bonding energy values of 35.5 eV and 37.3 eV which can be assigned to W $4f_{7/2}$ and W $5p_{3/2}$ respectively, similar to the XPS results for WO_3 (35.8 eV and 37.0 eV) reported in the literature.[65,66] The minor shift of peaks

may be due to the interaction between g-C_3N_4 and Ru^0@$H_3PW_{12}O_{40}$. The N1s peaks are shown in Figures 4.5-4.7 (b), and the bonding energy peak at 397.0 eV was assigned to C=N-C (sp^2 hybrizied nitrogen), which established the presence of graphitic carbon nitride. N-C_3 groups can be confirmed from the presence of two peaks at 399.0 eV and 400.5 eV.[67]

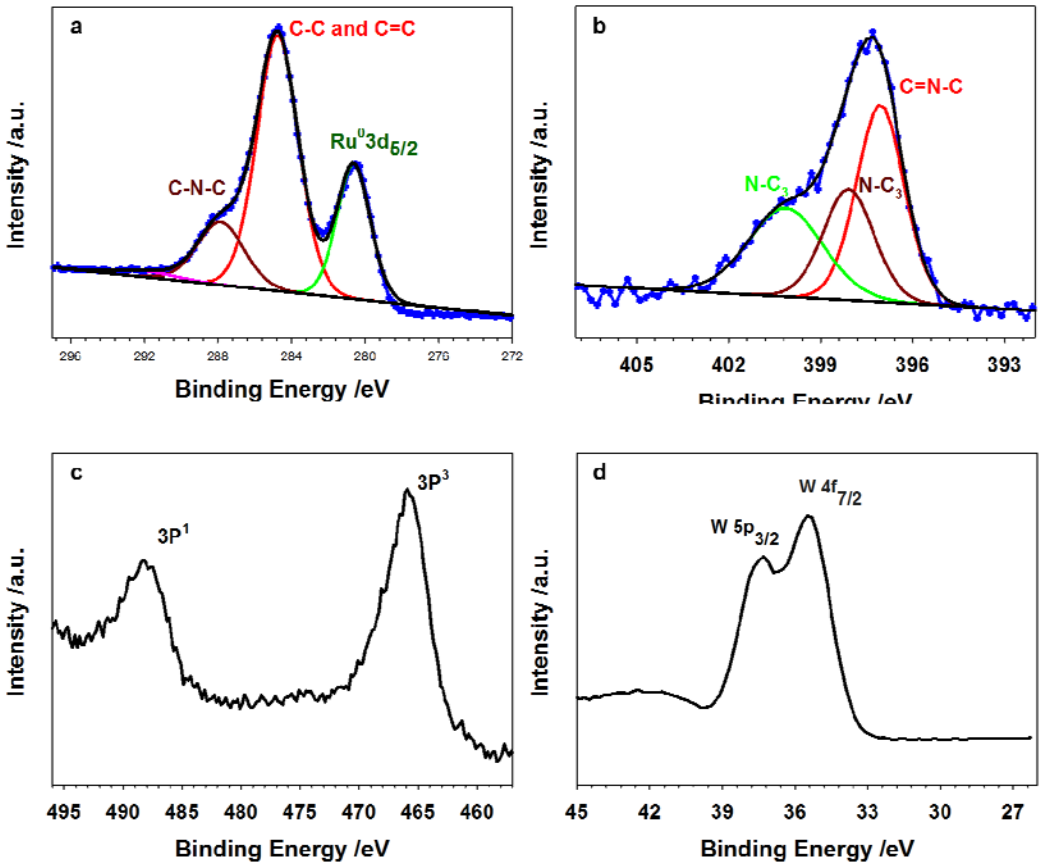

Figure 4.6 XPS spectra of Ru^0@10%$H_3PW_{12}O_{40}$/C_3N_4 sample, (a) C1s peak, (b) N1s peak, (c) Ru1s peak and (d) W1s peak

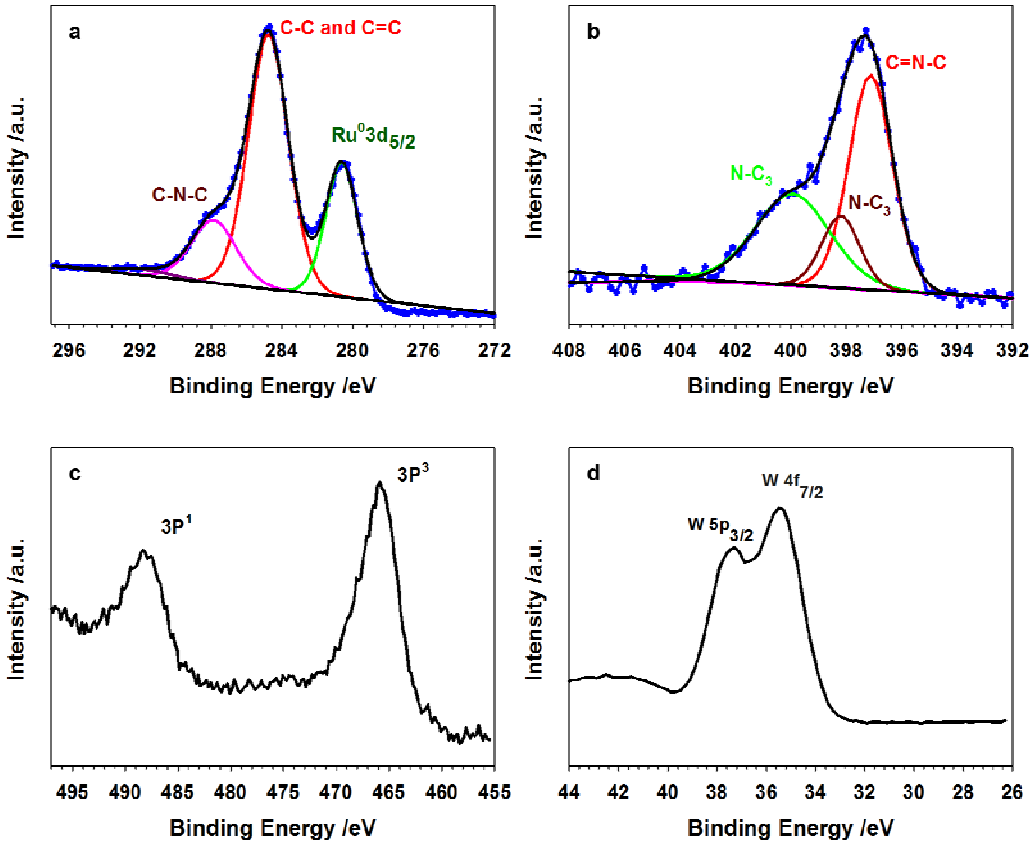

Figure 4.7 XPS spectra of Ru^0@15%$H_3PW_{12}O_{40}/C_3N_4$ sample, (a) C1s peak, (b) N1s peak, (c) Ru1s peak and (d) W1s peak

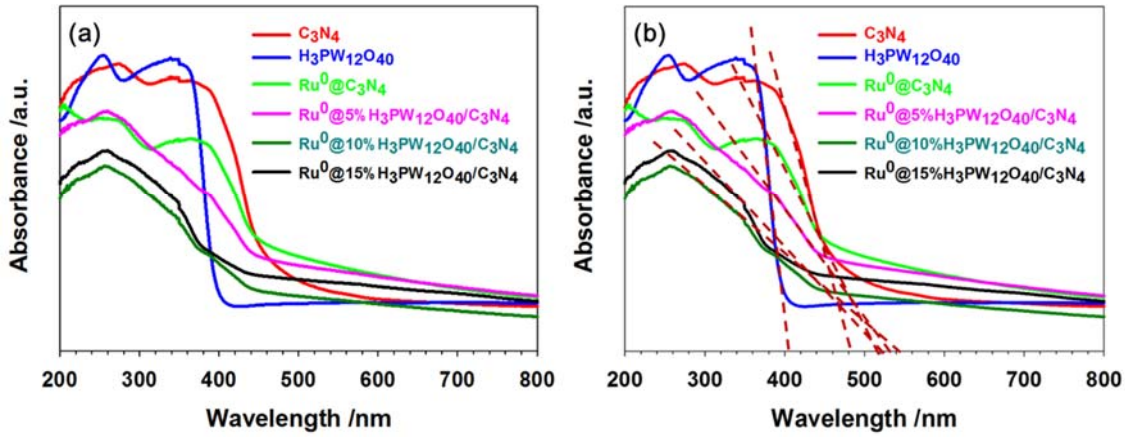

Figure 4.8 UV-DRS spectra of samples

Ultraviolet–visible diffuse reflectance spectroscopy (UV-DRS) was used to investigate the optical properties of each of the composites (Figure 4.8). The

absorption edge of g-C_3N_4 sample was at 480 nm, which can be associated with the semiconductor band gap of 2.6 eV and is consistent with the literature report.[68] The absorption edge for $H_3PW_{12}O_{40}$ at 404 nm was assigned to charge transfer from O2p orbitals to W5d orbitals, the band gap energy was about 3.0 eV. Compared with g-C_3N_4 and $H_3PW_{12}O_{40}$, the absorption edge of $Ru^0@C_3N_4$, $Ru^0@5\%H_3PW_{12}O_{40}/C_3N_4$, $Ru^0@10\%H_3PW_{12}O_{40}/C_3N_4$ and $Ru^0@15\%H_3PW_{12}O_{40}/C_3N_4$ samples moved to longer wavelengths, with values of about 514 nm (2.4 eV), 532 nm (2.33 eV), 539 nm (2.30 eV) and 553 nm (2.24 eV) respectively. The red shift of the absorption edge was attributed to the interaction between g-C_3N_4 and $H_3PW_{12}O_{40}$ (Ru) in the composites, which indicated the composites can absorb more light and create more electron hole pairs. It was suggested that the introduction of $H_3PW_{12}O_{40}$ indirectly causes at change in the electronic structure of g-C_3N_4 in the composites of $Ru^0@H_3PW_{12}O_{40}/C_3N_4$ by NH_3^+…OW coordination bond. The absorption of $Ru^0@H_3PW_{12}O_{40}/C_3N_4$ in the visible region increased with the amount of $H_3PW_{12}O_{40}$, especially in the range 500~560 nm. Therefore, the composite catalyst not only broadened absorption into the visible region, but also improves the light absorption ability of g-C_3N_4. This would improve the light utilization efficiency of these materials in photocatalytic reactions.

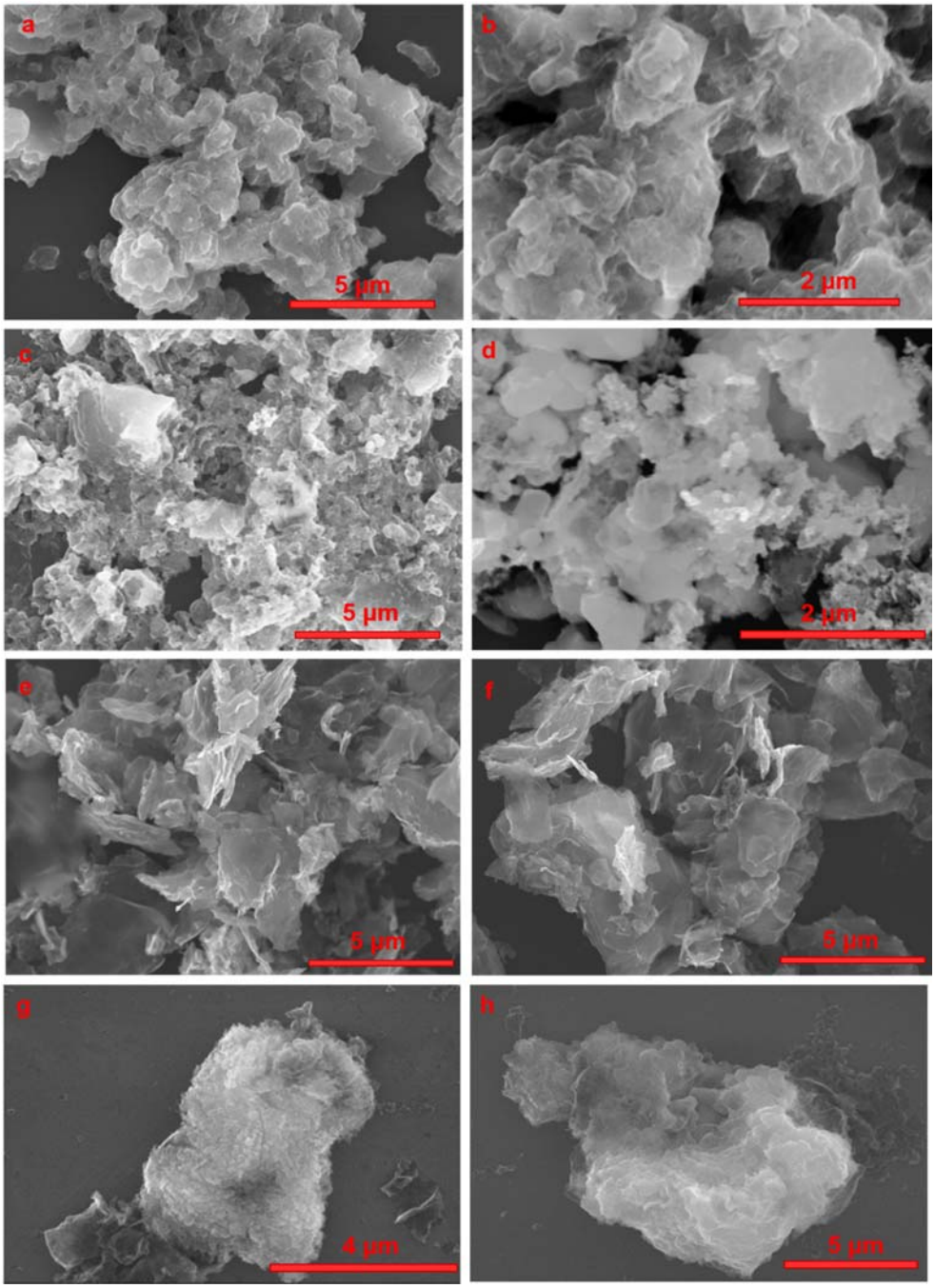

Figure 4.9 SEM images of (a), (b) Ru^0@5%$H_3PW_{12}O_{40}/C_3N_4$, (c), (d) Ru^0@10%$H_3PW_{12}O_{40}/C_3N_4$, (e), (f) Ru^0@15%$H_3PW_{12}O_{40}/C_3N_4$ and (g), (h) g-C_3N_4 samples

The morphologies and structure of Ru^0@$H_3PW_{12}O_{40}/C_3N_4$ composite materials were studied by scanning electron microscopy (SEM) and the results are shown in Figure 4.9. Typical g-C_3N_4 structure is shown in Figure.4.9 (g) and (h), the

morphology of -C_3N_4 was irregular and stacked together. After hydrothermal treatment with $Ru^0@H_3PW_{12}O_{40}$, the $Ru^0@H_3PW_{12}O_{40}/C_3N_4$ composites seemed to form nanosheets with sharp edges (Figure 4.9 (a) to (f)), and the $Ru^0@H_3PW_{12}O_{40}/C_3N_4$ were new intercalation compounds, which might be attributed to $Ru^0@H_3PW_{12}O_{40}$ inserted between layers of g-C_3N_4, this result clearly indicated that $Ru^0@H_3PW_{12}O_{40}$ impacted the microstructure.

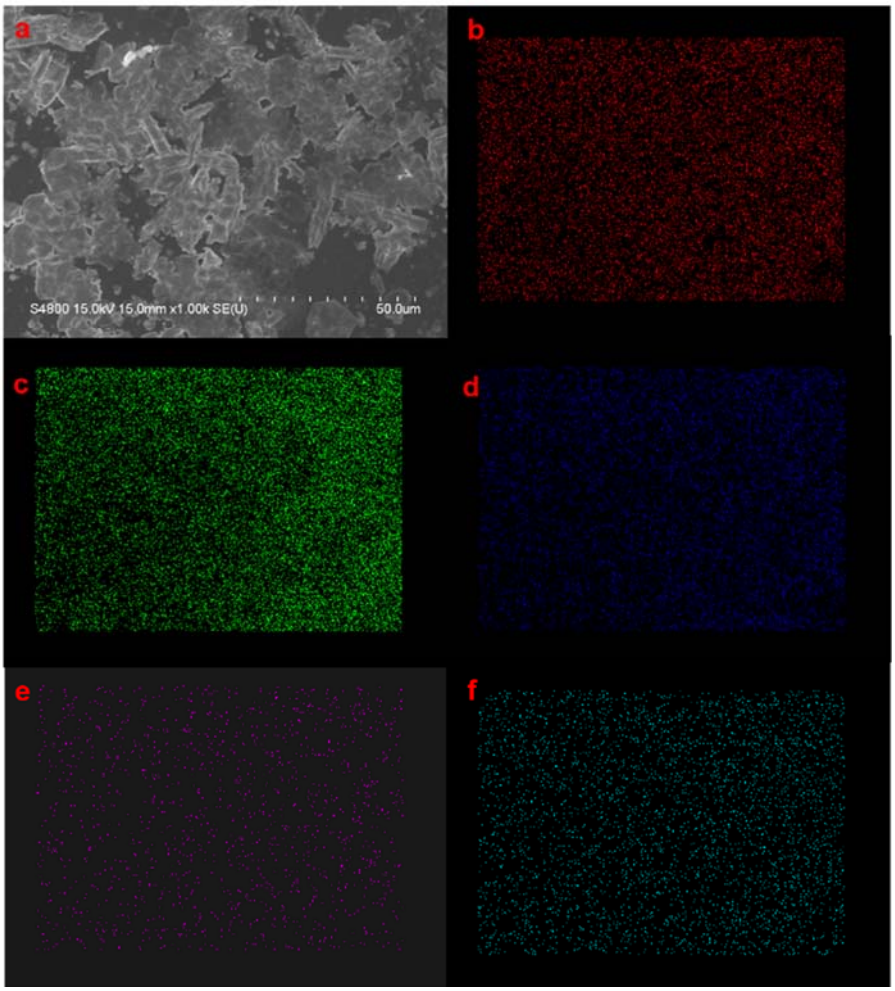

Figure 4.10 Typical images of (a) $Ru^0@5\%H_3PW_{12}O_{40}/C_3N_4$ sample and the corresponding elemental mapping images of (b) carbon, (c) tungsten, (d) phosphorus (e) nitrogen and (f) ruthenium

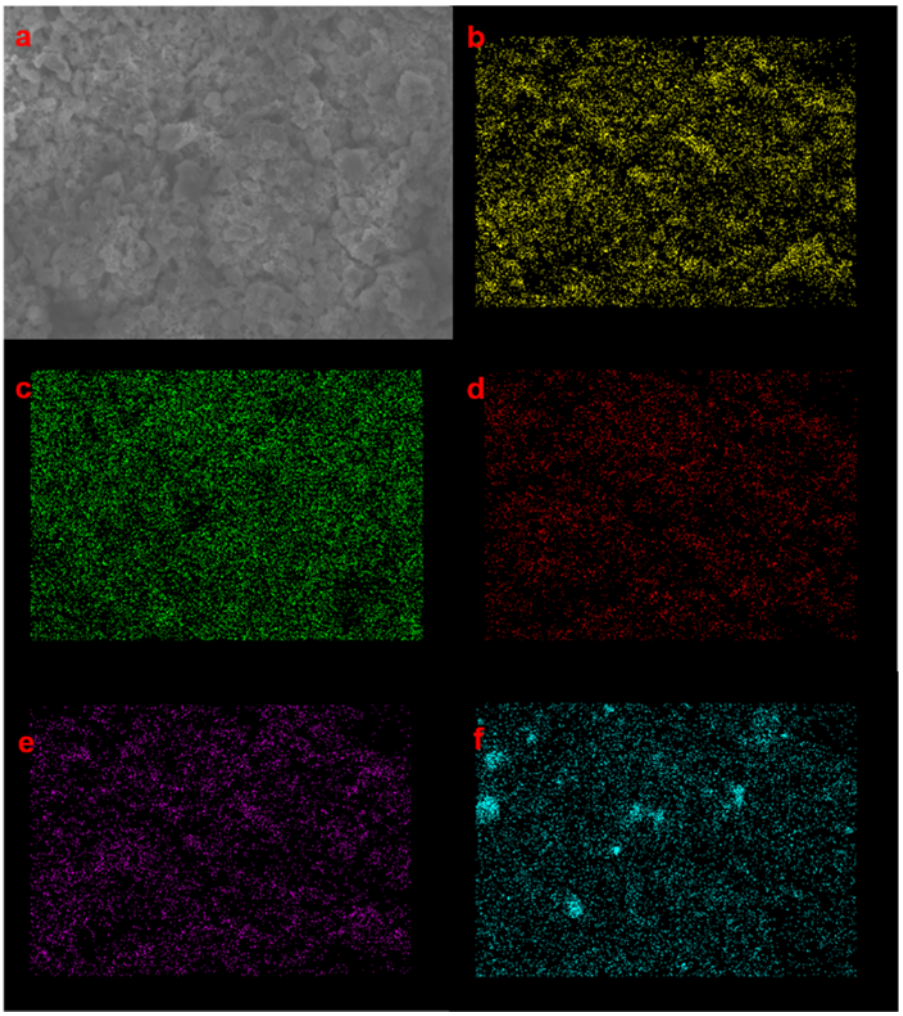

Figure 4.11 Typical images of (a) Ru^0@10%$H_3PW_{12}O_{40}/C_3N_4$ sample and the corresponding elemental mapping images of (b) carbon, (c) tungsten, (d) phosphorus, (d) nitrogen and (f) ruthenium

The energy dispersive spectroscopy (EDS) elemental mapping images of carbon, ruthenium, nitrogen, tungsten, phosphorus for Ru^0@$H_3PW_{12}O_{40}/C_3N_4$ samples indicated a uniform distribution of Ru^0@$H_3PW_{12}O_{40}$ over the g-C_3N_4 surface on the microscale.

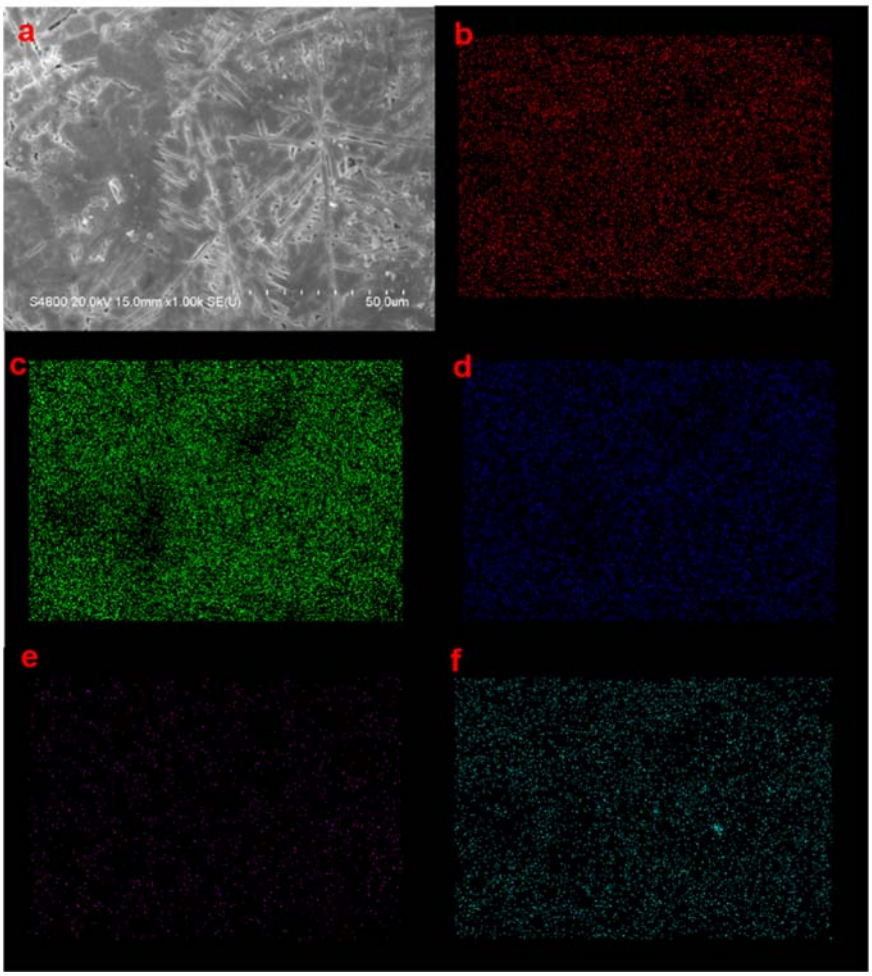

Figure 4.12 Typical images of (a) Ru^0@15%$H_3PW_{12}O_{40}/C_3N_4$ sample and the corresponding elemental mapping images of (b) carbon, (c) tungsten, (d) phosphorus, (d) nitrogen and (f) ruthenium

Table 4.1 BET results of g-C_3N_4 and Ru^0@$H_3PW_{12}O_{40}/C_3N_4$ composites

Entry	Catalyst	Surface area (m^2/g)	Pore volume (cm^3/g)	Pore size (nm)
1	g-C_3N_4	11.085	0.094	17.576
2	Ru^0@5%$H_3PW_{12}O_{40}/C_3N_4$	30.424	0.143	21.066
3	Ru^0@10%$H_3PW_{12}O_{40}/C_3N_4$	40.965	0.155	23.012
4	Ru^0@15%$H_3PW_{12}O_{40}/C_3N_4$	36.532	0.150	22.236

The BET surface area of the catalyst is another key factor affecting the catalytic activity and a large specific surface area is favorable for the adsorption and transport of the reactants. We tested the samples by N_2 adsorption isotherms and Table 4.1 lists the BET surface area, pore volume and pore size data of g-C_3N_4 and $Ru^0@H_3PW_{12}O_{40}/C_3N_4$. The BET surface areas of g-C_3N_4, $Ru^0@5\%H_3PW_{12}O_{40}/C_3N_4$, $Ru^0@10\%H_3PW_{12}O_{40}/C_3N_4$ and $Ru^0@15\%H_3PW_{12}O_{40}/C_3N_4$ were 11.085, 30.424, 40.965 and 36.532 m^2/g respectively, indicating that with the increase of $H_3PW_{12}O_{40}$ content, the BET surface areas of the series of $Ru^0@H_3PW_{12}O_{40}/C_3N_4$ composites also increased. We proposed that this is due adsorption of $Ru^0@H_3PW_{12}O_{40}$ on the g-C_3N_4 layer and electrostatic attraction causing expansion of the interlayer spacing of g-C_3N_4, and formation of intercalation compounds, which increases the BET surface areas of $Ru^0@H_3PW_{12}O_{40}/C_3N_4$. The $Ru^0@10\%H_3PW_{12}O_{40}/C_3N_4$ had the largest specific surface area, but when the content of $H_3PW_{12}O_{40}$ was increased to 15%, the value of BET surface area decreased. According to literature reports the BET surface areas of $H_3PW_{12}O_{40}$ was 8.5 m^2/g.[69] When the interlayer spacing of g-C_3N_4 increases to a certain point, the BET surface area of $Ru^0@15\%H_3PW_{12}O_{40}/C_3N_4$ decreased due to the increase of $H_3PW_{12}O_{40}$ content. From the pore size data, it can be concluded that the composites can be classified as mesoporous materials (pore diameter between 2-50 nm).

4.2.2 Efficient photocatalyst for water splitting

4.2.2.1 The performance and stability of catalysts for photocatalytic hydrogen production

The photocatalytic performance of the catalyst for hydrogen production was evaluated under visible light. Under these experimental conditions, no gas was

detected in the reaction system in the absence of catalyst. Therefore, the effect of the sacrificial agent (triethanolamie) on the activity evaluation of the catalyst could be ignored in the photochemical reaction. Under the dark reaction condition with catalyst, no gas generation was detected in the reaction system, which indicated that the gas tightness of the photocatalytic reaction system was good.

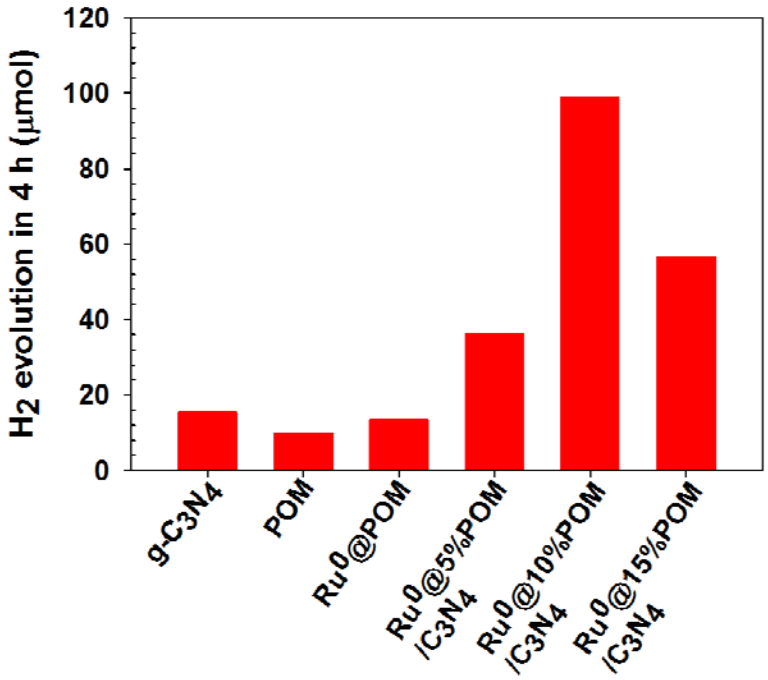

Figure 4.13 Photocatalytic hydrogen evolution as a function of catalysts

The photocatalytic performance for water splitting was investigated in the presence of triethanolamine (TEOA) as the electron sacrificial agent. Figure 4.13 shows the photocatalytic hydrogen production for g-C_3N_4, $H_3PW_{12}O_{40}$, Ru^0@$H_3PW_{12}O_{40}$, Ru^0@5%$H_3PW_{12}O_{40}$/C_3N_4, Ru^0@10%$H_3PW_{12}O_{40}$/C_3N_4 and Ru^0@15%$H_3PW_{12}O_{40}$/C_3N_4 samples irradiated for 4 hours under visible light (> 420 nm). Figure 4.13 clearly shows that the series of Ru^0@ $H_3PW_{12}O_{40}$/C_3N_4 samples were significantly more active than that of g-C_3N_4 $H_3PW_{12}O_{40}$ and Ru^0@ $H_3PW_{12}O_{40}$. The H_2 production with g-C_3N_4 was only 15.39 μmol (513

μmol g^{-1} h^{-1}) for 4 hour under visible light, which indicated that the photocatalytic activity of g-C_3N_4 was low because of its low photoelectron generation and hole separation efficiency, which is unfavorable for proton reduction on its surface. Hydrogen production with $H_3PW_{12}O_{40}$ and Ru^0@ $H_3PW_{12}O_{40}$ catalysts was only 9.9 μmol (330 μmol g^{-1} h^{-1}) and 13.52 μmol (451 μmol g^{-1} h^{-1}) in 4 hours respectively, while for Ru^0@ $H_3PW_{12}O_{40}/C_3N_4$ catalysts it was 36.34 μmol l (1211 μmol g^{-1} h^{-1}), 99.10 μmol (3303 μmol g^{-1} h^{-1}) and.56.70 μmol (1890 μmol g^{-1} h^{-1}) over the same time, respectively. The hydrogen-producing activity of the Ru^0@ $H_3PW_{12}O_{40}/C_3N_4$ series catalysts were 3.67, 6.44 and 3.68 times higher than g-C_3N_4 catalyst, respectively. With the further increase of $H_3PW_{12}O_{40}$ content, the activity for hydrogen production decreased, which might be due to excess $H_3PW_{12}O_{40}$ covering the surface active sites of g-C_3N_4 and inhibiting the activity of hydrogen production. According to UV-DRS analysis and the photocatalytic activity, the Ru^0@$H_3PW_{12}O_{40}/C_3N_4$ catalysts showed longer photoelectron lifetimes and better electron conductivities than bulk g-C_3N_4.

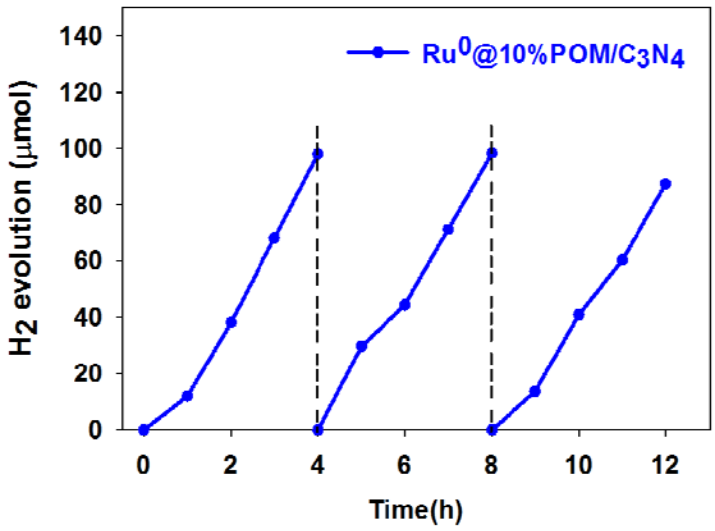

Figure 4.14 Photocatalytic stability of Ru^0@10%$H_3PW_{12}O_{40}/C_3N_4$ catalyst

The stability of Ru^0@10%$H_3PW_{12}O_{40}/C_3N_4$ catalyst was investigated by water splitting experiments under the same conditions after recycling 3 times (12 hours). Figure 4.14 shows that Ru^0@10%$H_3PW_{12}O_{40}/C_3N_4$ exhibited good photocatalytic hydrogen production stability. The hydrogen production of Ru^0@10%$H_3PW_{12}O_{40}/C_3N_4$ increased linearly with the increase of irradiation time, which indicated that it had the capability of continuous hydrogen production. In the first cycle, hydrogen production was 97.99 μmol and the second cycle, produced 98.30 μmol. After the third cycle, the hydrogen production decreased slightly (87.40 μmol), which may be due to the decrease of the interaction force between g-C_3N_4 and Ru^0@10%$H_3PW_{12}O_{40}$ under the conditions of light activation, and an increase in effective distance of photocharge transport. However, after 12 hours of continuous light reaction, the catalyst still maintained a good hydrogen production rate, indicating that the catalyst had good long termstability.

4.2.2.2 Analysis of photocatalytic hydrogen production mechanism of Ru^0@$H_3PW_{12}O_{40}/C_3N_4$ composites

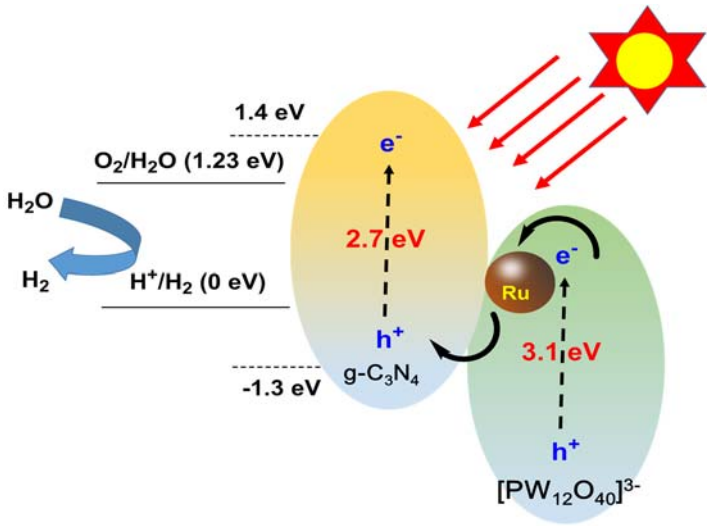

Figure 4.15 Mechanism of water splitting in Ru^0@$H_3PW_{12}O_{40}/C_3N_4$ Z-Scheme system

Among the solar energy conversion into the chemical system, the photosynthesis of green plants in nature is the most representative. The photosystem I and the photosystem II in the chloroplast membrane absorb photons as energy, and electrons are obtained from the decomposition process of water molecules and continuously transmitted to form a Z-like system (Z-Scheme).[70] Inspired by the electron transfer mechanism of photosynthesis, a Z-Scheme system had been designed for water splitting.[71] The system combines hydrogen production and oxygen generating catalyst through an electron transmitter, the electron conduction band of the oxygen-producing catalyst is transferred to the valence band of the hydrogen-producing catalyst through the electron transmitter, and are combined with the valence band holes of the hydrogen-producing catalyst, thereby realizing the overall electron hole separation. At the same time, conduction band electron of hydrogen production catalyst involved in the reduction for hydrogen production, while valence band hole of oxygen production catalyst involved in oxidation for oxygen production. According to the type of electron transmitter, the Z-Scheme system can be divided into ion-pair electron transfer Z-Scheme system (using IO^{3-}/IO^{-} and Fe^{3+}/Fe^{2+} etc, ion pair as electron transmitter), solid state electron transport Z-Scheme system (using Au, Ru, Ag, etc. as electron transmitter) and Z-Scheme system without electron transmitter.[72-78]

Compared with the traditional photocatalytic ammonia production system, the Z-scheme system has lower requirements on the catalyst band gap and could make more efficient use of visible light. At the same time, the electron hole between the oxidation catalyst and the reduction catalyst can separate the electron hole of the whole system, and effectively enhance the photocatalytic efficiency. Ru as a common solid electron transfer, is used to prepare $Ru^0@H_3PW_{12}O_{40}/C_3N_4$ catalysts containing Z-Scheme system. It is important

to increase the electron transfer path in the catalyst and enhance the efficiency of photocatalytic hydrogen production.

Under visible light irradiation, electrons and holes were generated in $PW_{12}O_{40}^{3-}$ and g-C_3N_4, respectively. Meanwhile, the conduction band potential (-4.80 eV) of $PW_{12}O_{40}^{3-}$ was more negative than that of Ru (0.69 eV), which results in Schottky barrier and leads to the transition of the conduction band electrons to Ru easily.[79] On the other hand, because the Fermi level (0.69 eV) of Ru is more negative than the valence band potential of g-C_3N_4 (1.4 eV), the electrons on Ru were rapidly transferred to the valence band of g-C_3N_4 and recombined with the valence band hole of g-C_3N_4 to form a Z-Scheme system (Figure 4.15).[80] The formation of the system hindered the combination of electron-hole pairs in the whole catalyst and enhanced the photocatalytic activity of the catalyst.

4.2.3 Conversion of cellobiose to sorbitol

4.2.3.1 Reaction pathway of cellobiose to sorbitol

Previous work by Wang's group (Scheme 4.6) has indicated that the reaction pathway of the catalytic hydrogenation of cellobiose on the solid acid supported ruthenium catalyst Ru/$Cs_3PW_{12}O_{40}$ under low temperature conditions included the following two transformation processes: (1) the C-O bond of glucose in cellobiose was first hydrogenated to produce the intermediate 3-β-D-glucopyranosyl-glucitol (glucitol), and then the glucitol intermediate was hydrolyzed to produce glucose and sorbitol.[81] The glucose will then be further hydrogenated to produce sorbitol. In scheme 4.5 (a); (b) the β-glycosidic bond in the cellobiose was first broken into glucose by the solid acid catalyst which was subsequently reduced to sorbitol over Ru catalyst (Scheme 4.5 (b)).

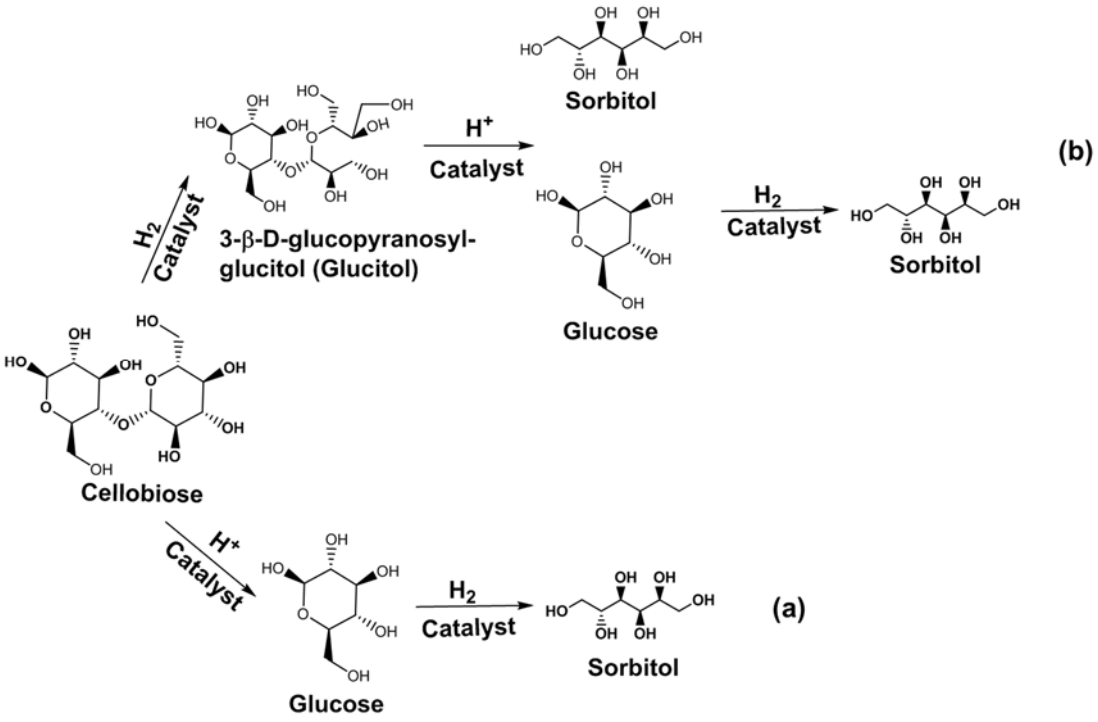

Scheme 4.5 Reaction scheme for the conversion cellobiose to sorbitol on Ru supported solid acids catalysts

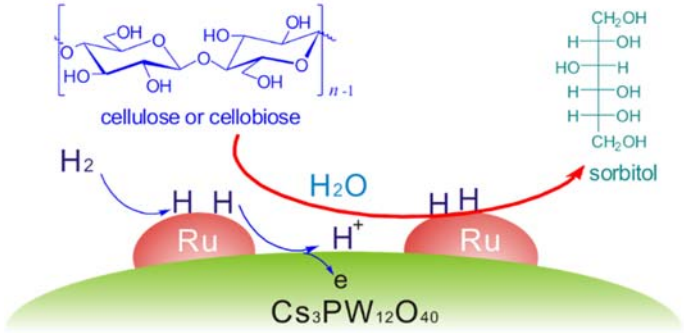

Scheme 4.6 Reaction scheme for the conversion cellobiose to sorbitol on $Ru/Cs_3PW_{12}O_{40}$ catalyst

4.2.3.2 Conversion of cellobiose on the supported ruthenium catalysts in nitrogen

The results of cellobiose hydrolysis on ruthenium catalysts are shown in Figure 4.16. The main product was glucose. Figure 4.16 shows that catalytic performance of ruthenium supported on different catalysts at 160 ^{o}C under nitrogen (in the absence of hydrogen). The conversion of cellobiose on Ru/C,

Ru/C_3N_4, Ru^0@5%$H_3PW_{12}O_{40}/C_3N_4$, Ru^0@10%$H_3PW_{12}O_{40}/C_3N_4$ and Ru^0@15%$H_3PW_{12}O_{40}/C_3N_4$ composites catalysts was about 20%, where Ru^0@$H_3PW_{12}O_{40}$ gave 75% conversion of cellobiose, which was ascribe to the acidic properties of the Ru^0@$H_3PW_{12}O_{40}$ catalyst.

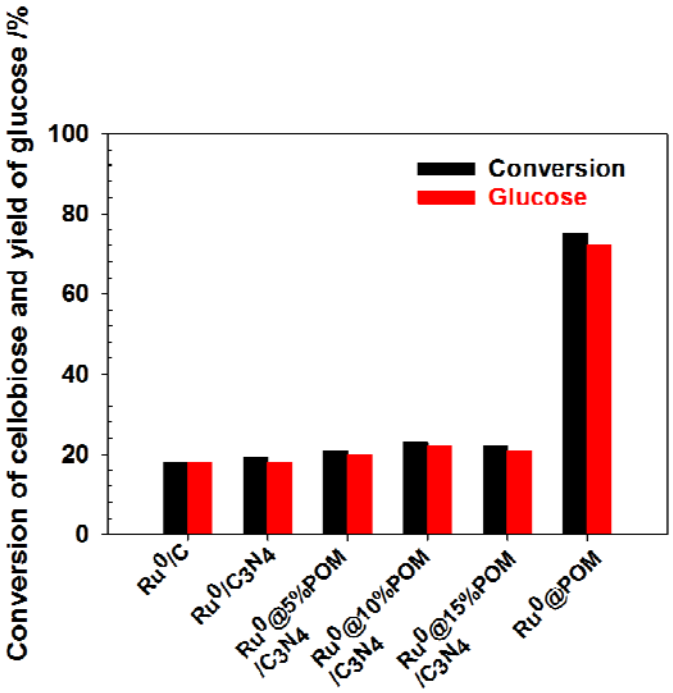

Figure 4.16 Effect of Ru catalysts for the conversion of cellobiose in water (pH = 7) under nitrogen. Reaction conditions: cellobiose (0.1 g); water (15 mL); 1% Ru catalyst; N_2, 3 MPa; temperature, 160 ^oC; time, 6 hours. Products were determined by HPLC.

4.2.3.3 Hydrogenation of cellobiose on the supported ruthenium catalysts

Using the same reaction conditions, the catalytic conversion of cellobiose on the supported ruthenium catalysts was studied under hydrogen instead of nitrogen and Figure 4.17 shows that the conversion of cellobiose was almost 100%. The main product obtained from Ru/C, Ru/C_3N_4 catalysts was 3-β-D-glucopyranosyl-glucitol (glucitol) formed by hydrogenolysis of a C-O bond of cellobiose. The main products with Ru^0@5%$H_3PW_{12}O_{40}/C_3N_4$,

Ru^0@10%$H_3PW_{12}O_{40}/C_3N_4$ and Ru^0@15%$H_3PW_{12}O_{40}/C_3N_4$ catalysts was sorbitol in 76%, 85% and 81% yields, respectively. The by-products of the reaction were mannitol and other degradation products such as erythritol and glycerin (Scheme 4.7), were due to the C-C bond cleavage of sorbitol in the hydrogenation process. The requirements for preparation of sorbitol were, on the one hand, the catalytic hydrogenation at Ru to break the unsaturated C-O bond in cellobiose and on the other hand, the effect of acid to cleave the β-glycosidic bond in cellobiose. Ru^0@5%$H_3PW_{12}O_{40}/C_3N_4$, Ru^0@10%$H_3PW_{12}O_{40}/C_3N_4$ and Ru^0@15%$H_3PW_{12}O_{40}/C_3N_4$ composites gave a high yield of sorbitol in hydrogen, which suggests that the catalysts could produce acid in hydrogen. Wang proposed that Brønsted acid sites were generated from hydrogen and played an important role in the conversion of cellobiose over Ru/$Cs_3PW_{12}O_{40}$, and analysed the catalyst by monitoring the adsorption of pyridine by FT-IR spectroscopy, in the presence of H_2, the FT-IR spectrum showed a bond at 1540 cm^{-1} which was assigned to Brønsted acid sites associated with pyridine. It appears that in a similar fashion to Ru/$Cs_3PW_{12}O_{40}$, Brønsted acid sites are generated from hydrogen over Ru^0@$H_3PW_{12}O_{40}/C_3N_4$ catalysts and promoted the conversion to sorbitol. The performance of Ru^0@10%$H_3PW_{12}O_{40}/C_3N_4$ was slightly better than Ru^0@5%$H_3PW_{12}O_{40}/C_3N_4$ and Ru^0@15%$H_3PW_{12}O_{40}/C_3N_4$ catalysts for conversion of cellobiose to sorbital. While,Ru^0@15%$H_3PW_{12}O_{40}/C_3N_4$ could generate more Brønsted acid sites than Ru^0@10%$H_3PW_{12}O_{40}/C_3N_4$ due to the higher $[PW_{12}O_{40}]^{3-}$ content, the lower performance of Ru^0@15%$H_3PW_{12}O_{40}/C_3N_4$ than Ru^0@10%$H_3PW_{12}O_{40}/C_3N_4$ may be due to the smaller surface and pore volume of Ru^0@15%$H_3PW_{12}O_{40}/C_3N_4$ showed by BET analysis, as this may well hinder access to the active sites.

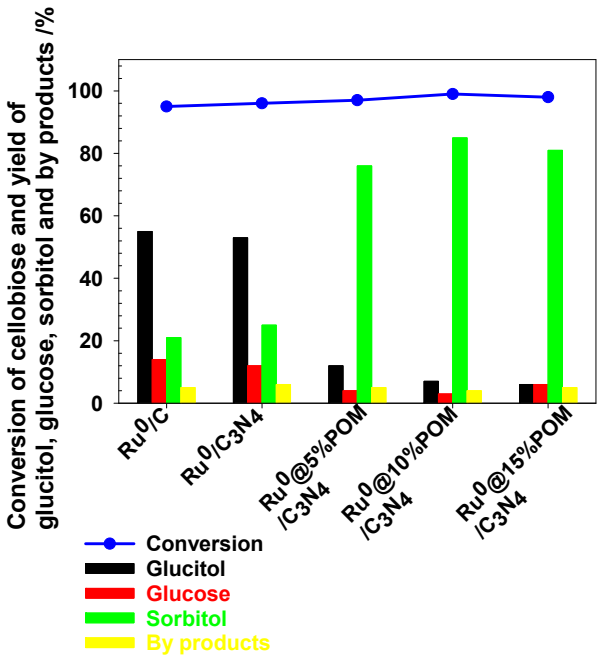

Figure 4.17 Effect of Ru catalysts for the conversion of cellobiose in water (pH=7) under hydrogen. Reaction conditions: cellobiose, 0.1 g; water, 15 mL; 1% Ru catalyst; H_2, 3MPa; temperature, 160 °C; time, 6 hours. Determined by HPLC.

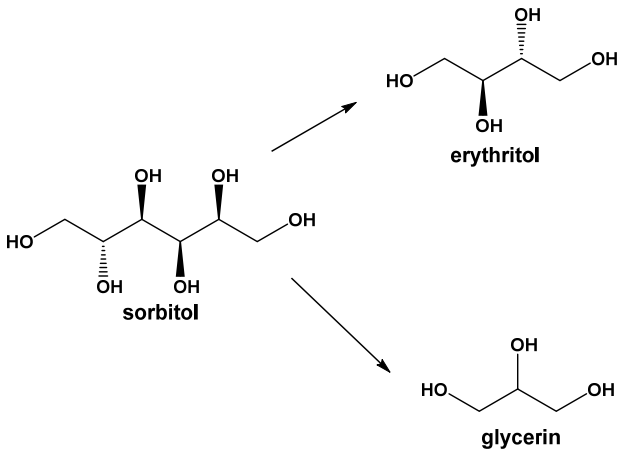

Scheme 4.7 Reaction scheme for by-products

4.2.3.3.1 Effect of surface area of catalyst on catalytic reaction performance

The surface of the catalyst is the place where the catalytic reaction takes place. In general, the larger the surface area, the higher the activity of the catalyst, but the relationship is not absolute. In this work, catalysts with different surface areas were prepared by changing the experimental conditions and their catalytic properties were investigated (Table 4.1). The specific surface area of the Ru^0@5%$H_3PW_{12}O_{40}/C_3N_4$ catalyst is 30.42 m^2/g, lower than Ru^0@10%$H_3PW_{12}O_{40}/C_3$ (40.95 m^2/g) catalyst and the catalytic activity of Ru^0@5%$H_3PW_{12}O_{40}/C_3N_4$ is similarly lower than Ru^0@10%$H_3PW_{12}O_{40}/C_3N_4$, with yields of sorbitol of 76% and 85% respectively. Moreover, the specific surface area of 36.53 m^2/g for Ru^0@15%$H_3PW_{12}O_{40}/C_3N_4$ was associated with a sorbitol yield of 81% which appears to correlate with the surface area-activity relationship described above. It can be seen that the specific surface area of the catalyst also has a certain effect on the catalytic performance.

4.2.3.4 Study of factors effecting Kinetics of hydrogenation of cellobiose over Ru^0@10%$H_3PW_{12}O_{40}/C_3N$

In order to further study the catalytic performance of Ru^0@10%$H_3PW_{12}O_{40}/C_3N_4$ catalyst, factors such as hydrogen pressure, reaction temperature and reaction time were investigated.

4.2.3.4.1 Effect of hydrogen pressure

The effect of hydrogen pressure on the catalytic hydrogenation of cellobiose is shown in Figure 4.18. When only N_2 was added to the reactor, the conversion of cellobiose was low and the main product was glucose in a yield of only 20%. With an increase in the hydrogen pressure, the conversion of cellobiose and the yield of sorbitol increased. The yield of glucose increased when hydrogen pressure was introduced and then glucose was hydrolyzed to sorbitol by an

acid-catalyzed process. The increase in yield of glucose indicated that acid was formed on the surface of Ru^0@10%$H_3PW_{12}O_{40}/C_3N_4$ catalyst, which might be derived by H atom by H_2 activation at Ru followed by H transfer to $[PW_{12}O_{40}]^{3-}$ on the surface of the Ru^0@10%$H_3PW_{12}O_{40}/C_3N_4$. When the hydrogen pressure was greater than 2 MPa, the cellobiose was almost completely transformed and the yield of sorbitol was 86%. At this point, the hydrogen dissolved in water might reach saturation and future increase no longer affects the catalytic reaction.

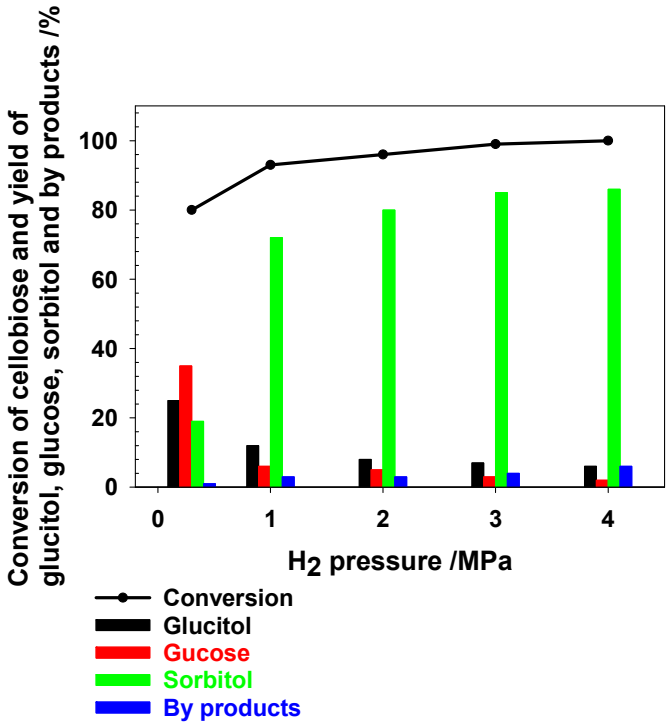

Figure 4.18 Effect of Ru^0@10%$H_3PW_{12}O_{40}/C_3N_4$ catalyst for the conversion of cellobiose in water (PH = 7) under hydrogen. Reaction conditions: cellobiose (0.1 g); water (15 mL); 1% Ru catalyst; temperature, 160 ^oC; time, 6 hours. Determined by HPLC.

4.2.3.4.2 Effect of reaction temperature

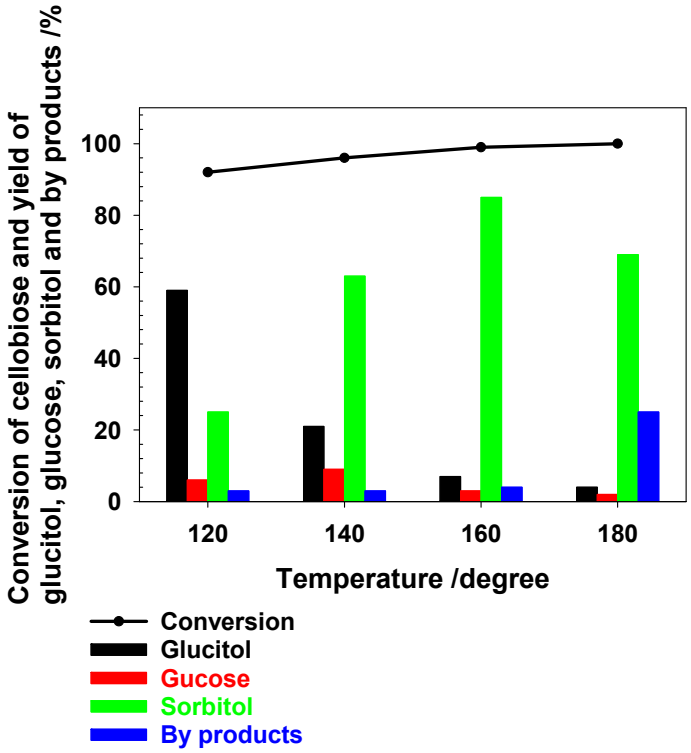

Figure 4.19 Effect of temperature on conversion of cellobiose catalyzed by Ru^0@10%$H_3PW_{12}O_{40}/C_3N_4$ in water (pH = 7) under hydrogen. Reaction conditions: cellobiose (0.1 g); water, (15 mL); 1% Ru catalyst; H_2, 3MPa; time, 6 hours. Determined by HPLC.

Figure 4.19 shows the influence of temperature on the conversion of cellobiose catalyzed by Ru^0@10%$H_3PW_{12}O_{40}/C_3N_4$ over a temperature range of 120~180 ^oC showing that the conversion of cellobiose reached 100% at 80 ^oC. At the lower temperatures, glucitol was the main product, but increasing temperature, glucitol gradually transformed to sorbitol, and the intermediate underwent breaking of the β-glycosidic bond in the presence of acid catalyst. This indicated that the increase of temperature was beneficial to the hydrolysis of cellobiose. The highest yield of sorbitol was 85% when the reaction temperature reached 160 ^oC. However, at higher temperatures, the yield of sorbitol began to

decrease, mainly due to the formation of by-products resulting from isomerization and degradation of sorbitol.

4.2.3.4.3 Effect of reaction time

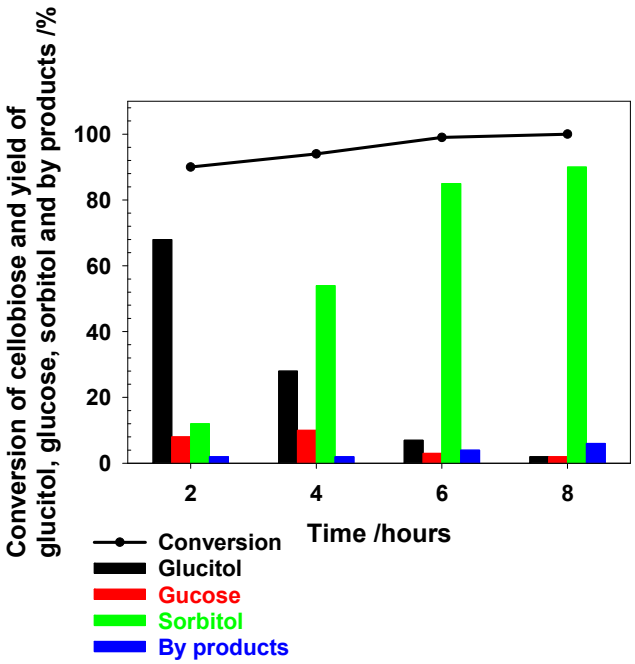

Figure 4.20 Effect of time on conversion of cellobiose catalyzed by Ru^0@10%$H_3PW_{12}O_{40}/C_3N_4$ in water (pH = 7) under hydrogen. Reaction conditions: cellobiose (0.1 g); water (15 mL); 1% Ru catalyst; H_2, 3MPa; temperature, 160 °C. Determined by HPLC.

Figure 4.20 shows that the products distribution varied with time using Ru^0@10%$H_3PW_{12}O_{40}/C_3N_4$ as catalyst. With the prolongation of reaction time, the cellobiose was transformed completely, and the main product was sorbitol. The experimental results indicated that the reaction mechanism of cellobiose conversion catalyzed by Ru^0@10%$H_3PW_{12}O_{40}/C_3N_4$ was that Ru first catalyzes cellobiose production of glucitol, when the reaction time was 2 hours, the highest yield of glucitol was 68%, the yield of glucose and sorbitol only 8% and 12%. Then an acid catalyzed process produced sorbitol and glucose from

glucitol. Meanwhile, hydrogenation of glucose to sorbitol. Between the reaction time of 2 and 6 hours, the yield of sorbitol increased from 12% to 85%, the yield of by-products was only 4%. When the reaction time was increased to 8 hours, the yield of sorbitol reached 90%, but the by-products also increased to 6%. Therefore, the yield of sorbitol increases with the increasing of reaction time.

4.2.3.5 Study on the stability of Ru^0@10%$H_3PW_{12}O_{40}/C_3N_4$ catalysts

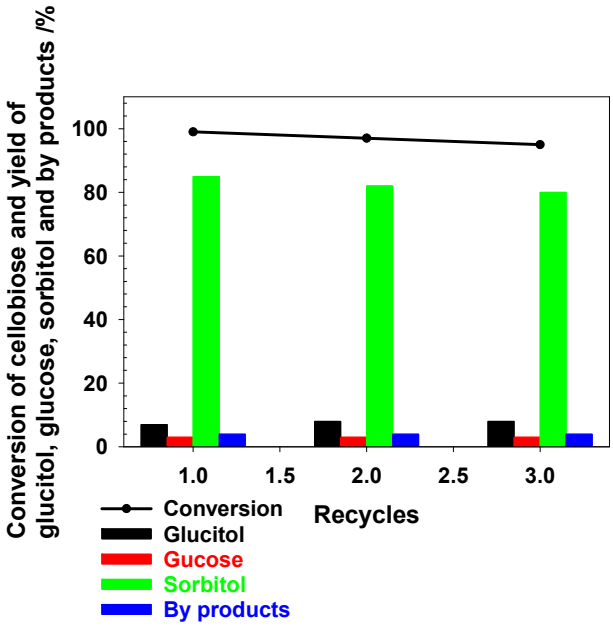

Figure 4.21 Recyclability of Ru^0@10%$H_3PW_{12}O_{40}/C_3N_4$ catalyst for the conversion of cellobiose in water (PH = 7) under hydrogen. Reaction conditions: cellobiose (0.1 g); water (15 mL); 1% Ru catalyst; H_2, 3MPa; temperature, 160 ^oC; time, 6 hours. Determined by HPLC.

As Ru^0@10%$H_3PW_{12}O_{40}/C_3N_4$ showed excellent catalytic performance for the hydrogenation of cellobiose to sorbitol, recycle studies were undertaken in order to investigate the stability, the results of which are shown in Figure 4.21. The Ru^0@10%$H_3PW_{12}O_{40}/C_3N_4$ catalyst had good catalytic stability after 3 cycles, although the yield of sorbitol reduced slightly from 85% to 80%, and the conversion of cellobiose was a little lower than in first cycle.

4.2.4 Selective hydrogenation of levulinic acid

4.2.4.1. Mechanism of hydroreduction of LA to GVL

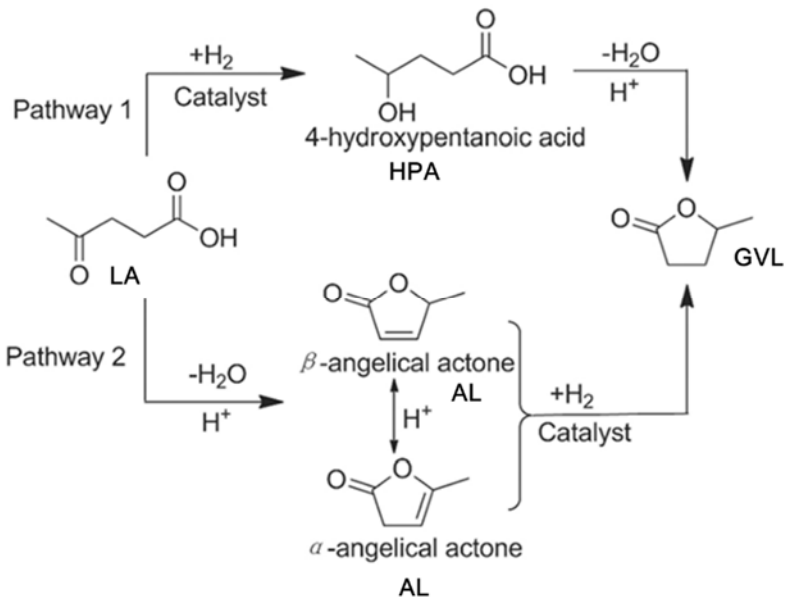

Scheme 4.8 Possible hydroren reduction pathways (1, 2) of LA to GVL

In recent years, GVL has been attracting increasing attention and catalytic studies on the reduction of LA to GVL have been investigated. The reaction can occur via different two step processes: (1) the carbonyl group in LA molecule is reduced under the effect of catalyst to form 4-hydroxypentanioc acid (HPA) and then after esterification, a molecule of water is removed and the ring closes to form GVL under acidic condition (Scheme 4.8 pathway 1). When the reaction is carried out in acidic condition, the reaction pathway (2) is slightly different. Firstly, the carbonyl group in LA can undergo enolation and α-angelica lactone (AL) is formed by dehydration of the enolate via intramolecular ring formation. The α-angelica lactone is isomerized to *β*-angelica lactone under acidic condition, and both are reduced to GVL under the action of catalyst (Scheme 4.8 pathway 2).

4.2.4.2. The performance of different catalysts for hydrogenation of LA

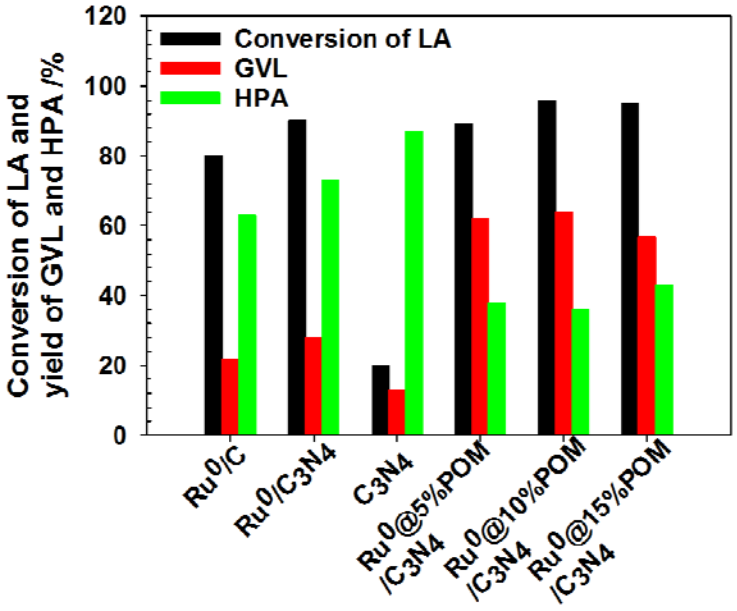

Figure 4.22 Effect of catalysts for the conversion of LA in aqueous solution (PH = 7). Reaction conditions: LA, 1 mmol; H_2O, 15 mL; 1 mmol% Ru catalyst; H_2, 1 MPa; temperature, 50 °C; time, 3 hours. Determined by ^1H NMR, decane as an internal standard.

Under the reaction conditions, the activity of Ru/C, Ru^0/C_3N_4, g-C_3N_4 and $Ru^0@H_3PW_{12}O_{40}/C_3N_4$ were investigated in aqueous solution (Figure 4.22). In the absence of Ru^0, the conversion of LA was low, showing that ruthenium had good catalytic activity for LA. Ruthenium has good hydrogen adsorption strength and hydrogenation activity for aliphatic carbonyl compounds. Under mild reaction conditions, ruthenium can rapidly achieve high conversion and selectivity, and is an ideal catalyst for hydrogenation. Figure 4.22 shows that the conversion of LA was 80% and 90% over Ru/C and Ru^0/C_3N_4 catalysts, with selectivity to GVL of 22% and 28%. However, with $Ru^0@H_3PW_{12}O_{40}/C_3N_4$ catalysts both the conversion of LA and the selectivity to GVL were higher. This

could be due to several factors. Firstly, the surface of $Ru^0@H_3PW_{12}O_{40}/C_3N_4$ has hydrophilic oxygen-containing functional groups, which might favor for the adsorption of polar LA for reaction. Secondly, mesoporous $Ru^0@H_3PW_{12}O_{40}/C_3N_4$ has uniform pore size and large specific surface area, greatly improving the speed of mass transfer. Thirdly, for $Ru^0@H_3PW_{12}O_{40}/C_3N_4$ catalysts, H_2 adsorbed and dissociated on the Ru surface, and H species were formed, which could transfer to $[PW_{12}O_{40}]^{3-}$ and generate Brønsted acid. This Brønsted acid is beneficial for fomation of GVL in LA conversion. The $Ru^0@10\%H_3PW_{12}O_{40}/C_3N_4$ catalyst had a better catalytic effect than $Ru^0@5\%H_3PW_{12}O_{40}/C_3N_4$ and $Ru^0@15\%H_3PW_{12}O_{40}/C_3N_4$ catalysts, due to its larger specific surface area and pore size than the other two catalysts. At this stage, we firmly believe that the hydrogenation of LA occurs via reduction of the carbonyl to form 4-hydroxypentanioc acid (HPA) which further reacted to give GVL as there was no evidence for the formation ofα -angelica lactoneate (AL).

4.2.4.3 Study of factors affecting the kinetics of LA hydrogenation over $Ru^0@10\%H_3PW_{12}O_{40}/C_3N$

In order to further study the catalytic performance of $Ru^0@10\%H_3PW_{12}O_{40}/C_3N_4$, the factors such as hydrogen pressure, reaction temperature and reaction time were investigated.

4.2.4.3.1 Effect of reaction temperature

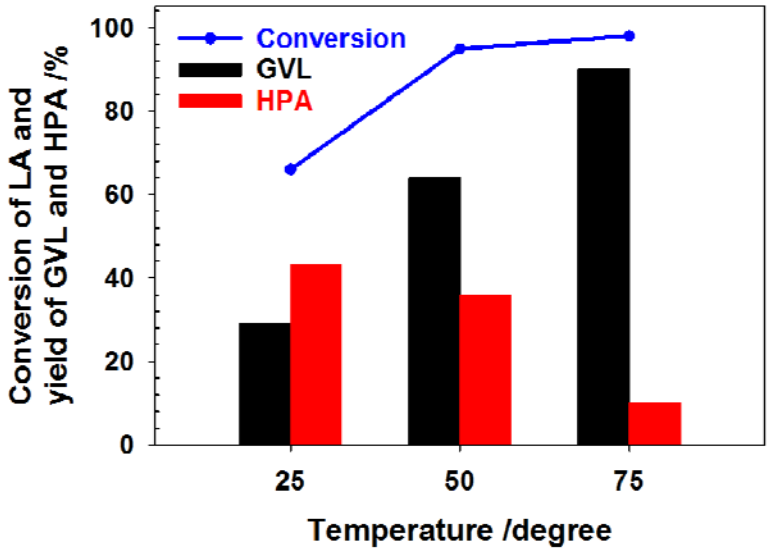

Figure 4.23 Effect of reaction temperature for the conversion of LA in aqueous solution (pH=7). Reaction conditions: LA, 1 mmol; water, 15 mL; 1 mmol % Ru catalyst; H_2, 1MPa; time, 3 hours. Determined by ^1H NMR, decane as an internal standard.

The hydrogenation of LA was carried out with Ru^0@10%$H_3PW_{12}O_{40}/C_3N_4$ as catalyst and the effect of different temperatures is shown in Figure 4.23. It can be seen that temperature had a significant effect on the reaction with an increase in temperature from 25 °C to 75 °C, resulting in an improvement in conversion of LA from 66%-98% and a dramatic increase in selectivity for GVL from 29% to 90%. We propose that this is because an increase in temperature can increase hydrogen diffusion in the liquid phase and rapidly regenerate active sites, which can increase the rate of LA reaction. However, the hydrogenation reaction is a reversible exothermic reaction. Raising the temperature can accelerate the reaction, but it is unfavorable to the equilibrium of the reaction. When the temperature increases to a certain extent, it caused

the decrease of selectivity of GVL and the increase of by-products. The optimum reaction temperature was therefore found to be 75 °C.

4.2.4.3.2 Effect of hydrogen pressure

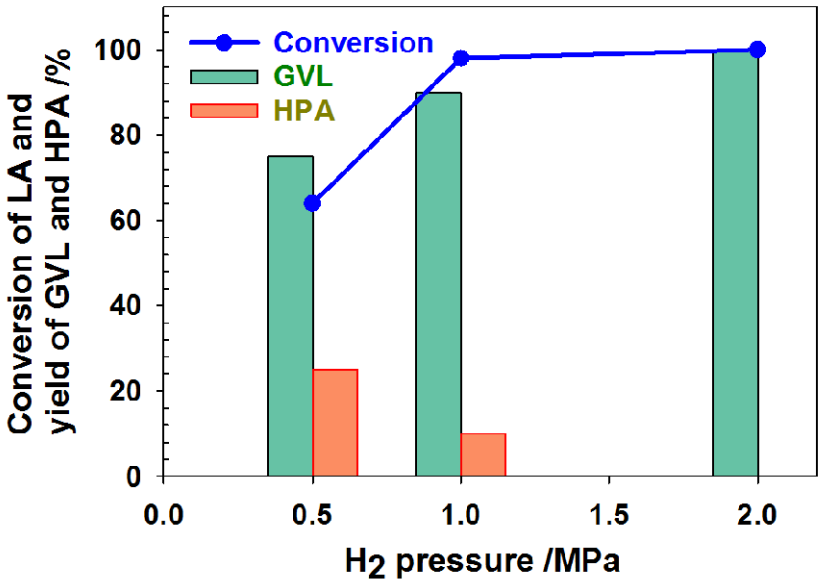

Figure 4.24 Effect of hydrogen pressure on the conversion of LA in aqueous solution (pH = 7). Reaction conditions: LA, 1 mmol; water, 15 mL; 1 mmol % Ru catalyst; temperature, 75 °C; time, 3 hours. Determined by ^{1}H NMR, decane as an internal standard.

The effect of different pressures on the hydrogenation of LA was investigated by using Ru^{0}@10%$H_3PW_{12}O_{40}/C_3N_4$ as catalyst and results are shown in Figure 4.24. The conversion of LA clearly and the selectivity of GV increased with increasing pressure. The lower reaction pressure of 0.5 MPa was unfavorable for the conversion of LA, but when the reaction pressure was increased from 0.5 MPa to 2.0 MPa, the conversion of LA increased from 64% to 100%, and the selectivity of GVL increased from 75% to 100%. We propose the reaction pressure had a great effect on the reaction rate. From Figure 4.24,

the rate of hydrogenation appears to increase with an increase in pressure. In the hydrogenation system, the adsorption rate of H_2 at the catalyst is higher than LA, so at the beginning of the reaction, there were a lot of active sites on the surface of the catalyst and with the increase of the pressure. The greater solubility of hydrogen could increase the adsorption of H_2 on the surface of the catalyst. The collision probability between hydrogen molecules and reactants on catalyst surface can be increased, as a result, reaction rate can be increased.

4.2.3.4.3 Effect of reaction time

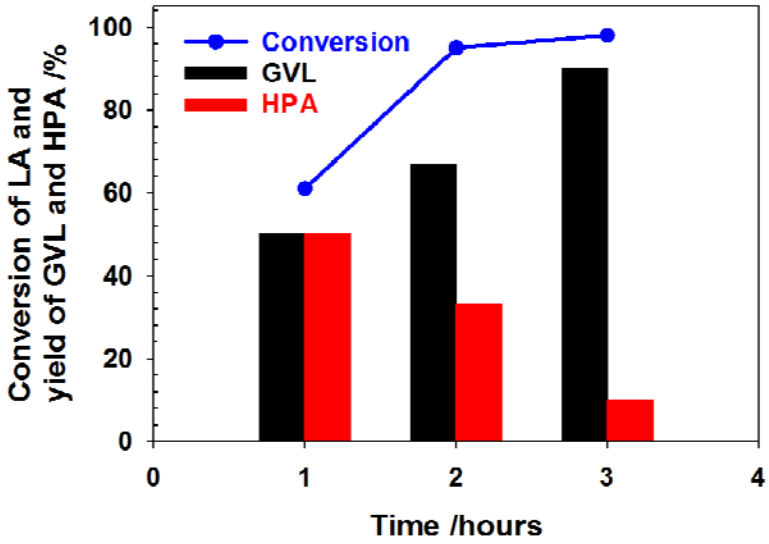

Figure 4.25 Effect of reaction time for the conversion of LA in aqueous solution (pH = 7). Reaction conditions: LA, 1 mmol; water, 15 mL; 1 mmol % Ru catalyst; H_2, 1MPa; temperature, 75 ^oC. Determined by ^1H NMR, decane as an internal standard.

The effect of different reaction times on the hydrogenation of LA was investigated with Ru^0@10%$H_3PW_{12}O_{40}/C_3N_4$ catalyst the details of which are shown in Figure 4.25. At the beginning of the reaction, the conversion of LA was 60% and the selectivity of HPA and GVL were similar. After 3 hours, the

conversion of LA was 90% and the yield of GVL was 90%, so 3 hours was the optimum reaction time.

4.2.4.3.4 Study on the Stability of Ru^0@10%$H_3PW_{12}O_{40}/C_3N_4$ Catalysts

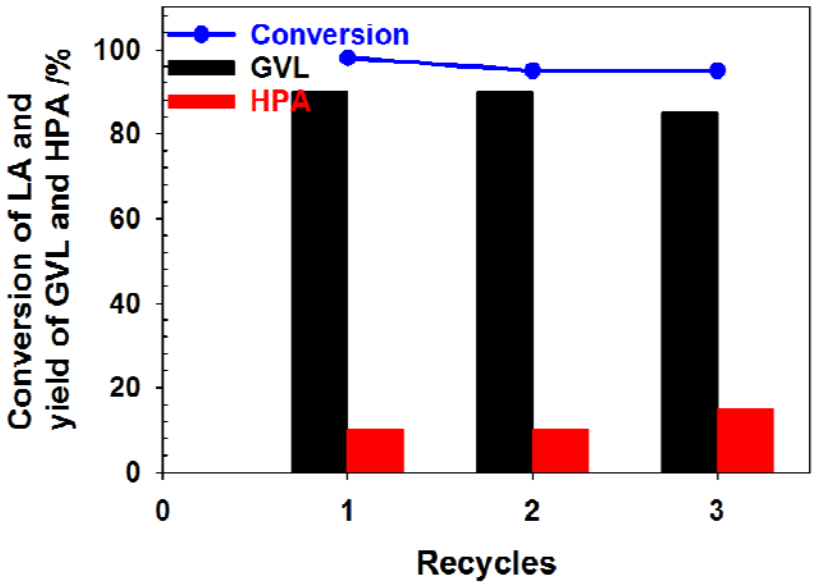

Figure 4.26 Recycles of Ru^0@10%$H_3PW_{12}O_{40}/C_3N_4$ catalyst for the conversion of LA in aqueous solution (pH = 7). Reaction conditions: LA, 1 mmol, water, 15 mL, 1 mmol % Ru catalyst, H_2, 1 MPa, temperature, 75 ^oC, time, 3 hours. Determined by ^1H NMR spectroscope using decane as an internal standard.

In order to investigate the stability of Ru^0@10%$H_3PW_{12}O_{40}/C_3N_4$ recycle experiment were conducted and the results shown in Figure 4.26 reveal that the catalyst had good stability. In the process of reusing the catalyst, levulinic acid was almost completely transformed, and the selectivity of GVL decreases only slightly. After 3 times cycles, the catalyst still had high catalytic activity as the conversion of LA was 95% with a selectivity to GVL of 85%.

4.3 Conclusions

A series of $Ru^0@H_3PW_{12}O_{40}/C_3N_4$ catalysts were prepared. The morphology of the catalyst was characterized by several techniques including XRD solid state NMR, FT-IR, TGA, XPS, SEM, EDS, UV-DRS. The UV-DRS showed that the visible light absorption ability of $Ru^0@H_3PW_{12}O_{40}/C_3N_4$ composites were greatly enhanced.

The H_2 production efficiency of $Ru^0@10\%H_3PW_{12}O_{40}/C_3N_4$ was 6.44 times higher than that of g-C_3N_4. This was mainly due to the synergism between Ru, $[PW_{12}O_{40}]^{3-}$ and g-C_3N_4, which accelerates the formation of electron hole pairs and inhibits recombination of the electron hole in the catalyst. At this stage we tentatively propose that, $[PW_{12}O_{40}]^{3-}$ produces electrons and holes under visible light irradiation, the electrons of $[PW_{12}O_{40}]^{3-}$ are then transferred to Ru and subsequently to the valence band of g-C_3N_4, which combines with the valence band holes of g-C_3N_4, and the electronhole separation of the catalyst was performed. The separated electrons are involved in the reduction of H_2O to produce hydrogen. The existence of this electron transfer path improved the separation efficiency of electrons and holes in the catalyst, and hindered the recombination of electrons and holes, this in turn increases the rate of hydrogen production in photocatalysis.

It was found that $Ru^0@10\%H_3PW_{12}O_{40}/C_3N_4$ is an efficient catalyst for the hydrogenation of cellobiose giving 85% yield of sorbitol at 160 ^oC, moreover, the catalyst had good stability and could be recycled with yields in excess of 80% over three runs. The effect of several parameters (reaction temperature, reaction time, hydrogen pressure, etc.) were studied for the catalytic conversion of cellobiose over $Ru^0@10\%H_3PW_{12}O_{40}/C_3N_4$. The results demonstrated that the highest yield of sorbitol were obtained under the following conditions: *w* (cellobiose) = 0.1 g, *V* = 15 ml, *P* (H_2) = 3 MPa, *T* = 160 ^oC, *t* = 6 h over

Ru^0@10%$H_3PW_{12}O_{40}/C_3N_4$ catalyst. The kinetic study also showed that cellobiose was first hydrogenated by Ru^0@10%$H_3PW_{12}O_{40}/C_3N_4$ to form sorbitol. It was found that in nitrogen the activity of catalysts were low for the hydrolysis of cellobiose, and the yield of glucose was only 20% at 160 ^oC. However, the catalytic performance of Ru^0@10%$H_3PW_{12}O_{40}/C_3N_4$ in hydrogenation of cellobiose was significantly improved (85% yield of sorbitol). This suggests that there was acid formation on the surface of Ru^0@$H_3PW_{12}O_{40}/C_3N_4$ catalysts in hydrogen because of the presence of $[PW_{12}O_{40}]^{3-}$.

When Ru^0@$H_3PW_{12}O_{40}/C_3N_4$ was applied to the hydrogenation of levulinic acid, the conversion of LA and the selectivity for GVL were both higher than those of Ru/C, Ru^0/C_3N_4 and g-C_3N_4 and in this regard it appears to be an ideal catalyst for the hydrogenation of LA to GVL. The factors affecting the hydrogenation of LA catalyzed by Ru^0@10%$H_3PW_{12}O_{40}/C_3N_4$, such as the reaction time, the pressure and the temperature of the reaction were studied. The optimum reaction conditions were identified as a temperature of 75 ^oC and a H_2 pressure of 2 MPa. The catalysis was conducted in aqueous solution and which eliminate the use of organic solvents and due to the synergetic effect of Ru^0 and $[PW_{12}O_{40}]^{3-}$ to generate acid sites, avoids addition of acid to the reaction to improve the effect of hydrogenation of LA. Under these conditions, the conversion of LA reached 100% and the selectivity of GVL was almost 100%. Presently, GVL is mainly obtained by hydrogenation of LA, which is usually obtained from hydrolysis of biomass (lignocellulose, cellulose, glucose, fructose, etc.) and the process of separation and purification of raw material and products is complicated. In the future, it may be possible to produce GVL directly from biomass by a combination of dehydration and hydrogenation using Ru^0@$H_3PW_{12}O_{40}/C_3N_4$ which would greatly reduce the production cost of GVL.

4.4 Experimental

4.4.1 General Chemicals

All chemicals were purchased from commercial suppliers (Alfa Aesar, Sigma Aldrich, Fisher Scientific, Acros Organics) and used without any purification. Distilled water was used throughout all this work. All manipulations of air-sensitive materials were carried out using standard Schlenk techniques under nitrogen and a glove-box with a recirculation system.

4.4.2 Instrumentation

4.4.2.1 Fourier transform infrared spectroscopy (FT-IR)

FT-IR spectra was analyzed on a Bruker Alpha spectrometer using a Platinum ATR module. Spectra were recorded for dried solid powder samples (vacuum drying for 5 hours).

4.4.2.2 Ultraviolet–visible spectroscopy (UV-Vis)

UV-Vis spectra were recorded on a UV-1800 Shimadzu UV spectrometer. The scanning range is 200~900 nm, and the scanning slit is 2.00 nm. The water solution samples were measured in 1 cm quartz cuvette.

4.4.2.3 X-ray diffraction (XRD)

XRD analysis wwas recorded on a Rigaku Ultima IV diffractometer with Cu K_α radiation, and the scanning angle range was 5~90 degrees at 40 Kv and 40 mA.

4.4.2.4 X-ray photoelectron spectroscopy (XPS)

XPS characterization was recorded on a PHI Quantum-2000 system with Al K_α X-ray source. The powdered samples pressed into sheets and then measured.

4.4.2.5 Scanning electron microscope (SEM) and energy dispersive spectrometer (EDS)

SEM images were taken using HITACHI S-4800 to check the morphology, element composition and element content of samples, the working voltage is 15 kV. In the experiment, samples were dispersed in solution and then dripped on clean silicon wafers. After drying, the silicon wafers with conductive tape on the sample stage were sent to the SEM instrument for testing.

4.4.2.6 UV diffuse reflectance spectrum (UV-DRS)

UV-DRS spectra were recorded on a Varian Cary 5000 spectrometer equipped with a diffuse reflectance attachment with an integrating sphere. The dried samples were mixed with analytical grade KBr and measured.

4.4.2.7 Thermal gravimetric analysis (TGA)

TGA was performed using a SDT Q600 at a heating rate of 10 ^{o}C/min under nitrogen, from room temperature increased to 800 ^{o}C. 5-10 mg of sample was used for easc measurement.

4.4.2.8 BET surface area analysis (BET)

BET surface area were recorded on a Tristar II 3020 instrument, the samples were put in glass tubes and allowed to dry for 3 hours and then to be tested.

4.4.2.9 Nuclear magnetic resonance spectroscopy (NMR)

NMR spectra were recorded on Bruker JEOL ESC-300 and 400 instruments. Solid-state NMR were recorded on a Varian VNMRS 400 instrument. Typical concentration of samples for solution NMR was 0.01M, the mass of samples used for solid-state NMR was approxomately 10 mg.

4.4.2.10 Gas chromatography (GC)

GC results were recorded on a GC-2060 instrument. The gaseous products were analysed by a gas chromatograph equipped with a thermal conductivity detector (TCD) which was connected to a TDX-01 packed column and a flame ionization detector (FID) which used an alumina capillary column. The products in the liquid phase were analysed by a gas chromatograph equipped with an FID, PONA and Bond-Q capillary columns was connected to FID.

4.4.2.11 High performance liquid chromatography (HPLC)

HPLC spectra were recorded on a Shimazu LC-20A instrument equipped with a RI detector and a CHO-620 10 μm, 6.5×300 nm column. The injection volume of samples was 2.5 μL. When passing the detector, the sample concentration is converted into an electrical signal and sent to the recorder. The data is printed out as a map.

4.4.3 Experimental

4.4.3.1 Synthesis of g-C_3N_4

In a typical procedure, dicyandiamide (4.0 g) was placed in a porcelain boat and calcined at 550 ^oC for 4 hours, and then cooled to room temperature in air to form the bulk g-C_3N_4.[82] The resultant yellow solid of bulk g-C_3N_4 was ground

in a agate mortar and transferred to a porcelain boat, then annealed at 400 °C for 2 hours in air. The ground, light yellow g-C_3N_4 powder was obtained in 20% yield, 80% of dicyandiamide produced carbon monoxide and nitrogen.

4.4.3.2 Synthesis of Ru^0@POM($H_3PW_{12}O_{40}$)/g-C_3N_4

4.4.3.2.1 Synthesis of Ru^0@POM(5%$H_3PW_{12}O_{40}$)/g-C_3N_4

$H_3PW_{12}O_{40}$ (28.8 mg, 1 mmol) and Na[*trans*-$Ru(DMSO)_2Cl_4$] (4.2 mg, 1 mmol) were added to a reaction flask with water (12 mL), then reduced under 1.0 MPa H_2 at 50 °C for 5 hours in a 50 mL stainless steel autoclave with a stirring speed of 600 rpm. After reaction, the autoclave was cooled to room temperature, to give a blue black stable and homogeneous sample solution of Ru^0@POM($H_3PW_{12}O_{40}$). The g-C_3N_4 (1.84 g, 20 mmol) was added to Ru^0@POM($H_3PW_{12}O_{40}$) solution and allowed to stir at 110 °C for 24 hours under nitrogen in the 50 mL stainless steel autoclave. After the reaction, the resulting light brown solid was cooled to room temperature and isolated by filtration, washed with water and dried under high vacuum to give Ru^0@POM(5%$H_3PW_{12}O_{40}$)/g-C_3N_4

4.4.3.2.2 Synthesis of Ru^0@POM(10%$H_3PW_{12}O_{40}$)/g-C_3N_4

$H_3PW_{12}O_{40}$ (28.8 mg, 1 mmol) and Na[*trans*-$Ru(DMSO)_2Cl_4$] (4.2 mg, 1 mmol) were added to a reaction flask with water (12 mL), then reduced under 1.0 MPa H_2 at 50 °C for 5 hours in a 50 mL stainless steel autoclave with a stirring speed of 600 rpm. After reaction, the autoclave was cooled to room temperature, to give a blue black stable and homogeneous solution of Ru^0@POM($H_3PW_{12}O_{40}$). The g-C_3N_4 (0.92 g, 10 mmol) was added to Ru^0@POM($H_3PW_{12}O_{40}$) solution and allowed to stir at 110 °C for 24 hours under nitrogen in the 50 mL stainless

steel autoclave. After the reaction, the resulting light brown solid was cooled to room temperature and isolated by filtration, washed with water and dried under high vacuum to give Ru^0@POM(10%$H_3PW_{12}O_{40}$)/g-C_3N_4

4.4.3.2.3 Synthesis of Ru^0@POM(15%$H_3PW_{12}O_{40}$)/g-C_3N_4

$H_3PW_{12}O_{40}$ (28.8 mg, 1 mmol) and Na[trans-$Ru(DMSO)_2Cl_4$] (4.2 mg, 1 mmol) were added to a reaction flask with water (15 mL), then reduced under 1.0 MPa H_2 at 50 ^oC for 5 hours in a 50 mL stainless steel autoclave with a stirring speed of 600 rpm. After reaction, the autoclave was cooled to room temperature, to give a blue black stable and homogeneous sample solution of Ru^0@POM($H_3PW_{12}O_{40}$). The g-C_3N_4 (0.61 g, 6.6 mmol) was added to Ru^0@POM($H_3PW_{12}O_{40}$) solution and allowed to stir at 110 ^oC for 24 hours under nitrogen in the 50 mL stainless steel autoclave. After the reaction, the resulting light brown solid was cooled to room temperature and isolated by filtration, washed with water and dried under high vacuum to give Ru^0@POM(15%$H_3PW_{12}O_{40}$)/g-C_3N_4

4.4.3.3 General procedure for selective hydrogenolysis of cellobiose to sorbitol

Catalyst (40 mg), cellobiose (100 mg) and water (15 mL) were placed in a Teflon-lined stainless steel reactor and heated at different temperatures under different H_2 pressures before being allowed to stir for the alloted time. Upon cooling to room temperature, the liquid products was separated by glass microfilter and analyzed by a HPLC to determine conversion and selectivity.

4.4.3.4 General procedure for selective hydrogenation of levulinic acid

1 mmol% catalyst (based on repeat unit, assuming complete Ru loading), and levulinic acid (1 mmol, 102 μL) and water (15 mL) were placed in a Parr reactor and heated at different temperatures under different H_2 pressures before being allowed to stir for the allotted time. Upon cooling to room temperature, the reaction mixture was diluted with diethyl ether (15 mL). The organic layer was separated, dried with magnesium sulfate, filtered and the solvent removed under vacuum. The resulting residue was analyzed by ^{1}H NMR spectroscopy, decane as the internal standard used to determine and ensure mass balance.

4.4.3.5 General procedure for efficient photocatalyst for water splitting

The water splitting reactions of the composite photocatalyst were performed in a Pyrex photoreactor with top irradiation, connected to a glass closed circulation system. The photoreactor was charged with photocatalyst (40 mg), H_2O (80 mL), triethanolamine (20 mL) and the suspension was stirred (600 rpm) to ensure homogeneity and eliminate sedimentation, and was degassed to remove air under vacuum. Then the suspension was irradiated with a 300W Xenon lamp (PLS-SXE 300) with 320 nm filter. A flow of cooling water was used to control the reaction under room temperature. The H_2 evolved was analyzed by an online SP-6890 gas chromatograph (GC) equipped with a TCD detector and a 5 A˚ molecular sieve column and N_2 carrier.

4.5 References

1. S. Cao and J. Yu, *J. Phys. Chem. Lett.*, 2014, **5**, 2101-2107.

2. J. Xu and M. Shalom, *ACS Appl. Mater. interfaces*, 2016, **8**, 13058-13063.

3. X. Wang, K. Maeda, A. Thomas, K. Takanabe, G. Xin, J. M. Carlsson, K. Domen and M. Antonietti, *Nat. Mater.*, 2009, **8**, 76-80.

4. X. Wang, S. Blechert and M. Antonietti, *Acs Catalysis*, 2012, **2**, 1596-1606.

5. X. Chen, Y.-S. Jun, K. Takanabe, K. Maeda, K. Domen, X. Fu, M. Antonietti and X. Wang, *Chem. Mater.*, 2009, **21**, 4093-4095.

6. X. Hao, Z. Jin, S. Min and G. Lu, *RSC Adv.*, 2016, **6**, 23709-23717.

7. S. Yan, Z. Li and Z. Zou, *Langmuir*, 2010, **26**, 3894-3901.

8. F. Raziq, Y. Qu, X. Zhang, M. Humayun, J. Wu, A. Zada, H. Yu, X. Sun and L. Jing, *J. Phys. Chem.*, 2015, **120**, 98-107.

9. W. Wu, J. Zhang, W. Fan, Z. Li, L. Wang, X. Li, Y. Wang, R. Wang, J. Zheng and M. Wu, *ACS Catal.*, 2016, **6**, 3365-3371.

10. A. Fujishima and K. Honda, *Nature*, 1972, **238**, 37-38.

11. B. G. Oliver and J. H. Carey, in *Homogeneous and heterogeneous photocatalysis*, Springer, 1986, pp. 629-650.

12. J. Lv, T. Kako, Z. Li, Z. Zou and J. Ye, *J. Phys. Chem.*, 2010, **114**, 6157-6162.

13. H. Wang, J. Gao, T. Guo, R. Wang, L. Guo, Y. Liu and J. Li, *Chem. Commun.*, 2012, **48**, 275-277.

14. W. Cui, W. An, L. Liu, J. Hu and Y. Liang, *J. Hazard. Mater.*, 2014, **280**, 417-427.

15. F. X. Xiao, J. Miao, H. B. Tao, S. F. Hung, H. Y. Wang, H. B. Yang, J. Chen, R. Chen and B. Liu, *Small*, 2015, **11**, 2115-2131.

16. L. Liu, L. Ding, Y. Liu, W. An, S. Lin, Y. Liang and W. Cui, *Appl. Surf. Sci.*, 2016, **364**, 505-515.

17. Y. Wang, X. Wang and M. Antonietti, *Angew. Chem. Int. Ed.*, 2012, **51**, 68-89.

18. A. Thomas, A. Fischer, F. Goettmann, M. Antonietti, J. O. Müller, R. Schlögl and J. M. Carlsson, *J. Mater. Chem.*, 2008, **18**, 4893-4908.

19. D. E. Katsoulis, *Chem. Rev.*, 1998, **98**, 359-388.

20. G. W. Huber, J. N. Chheda, C. J. Barrett and J. A. Dumesic, *Science*, 2005, **308**, 1446-1450.

21. Y. Ning, Z. Chen, G. Weijia and K. Yuan, *Chin. J. Catal.*, 2006, **27**, 1159-1163.

22. G. W. Huber, S. Iborra and A. Corma, *Chem. Rev.*, 2006, **106**, 4044-4098.

23. P. Mäki-Arvela, B. Holmbom, T. Salmi and D. Y. Murzin, *Cat. Rev.*, 2007, **49**, 197-340.

24. P. L. Dhepe and A. Fukuoka, *ChemSusChem: Chem. Sustain. Energy Mater.*, 2008, **1**, 969-975.

25. K. Fleming, D. G. Gray and S. Matthews, *Chem. Eur. J.*, 2001, **7**, 1831-1836.

26. J. Chen, S. Wang, J. Huang, L. Chen, L. Ma and X. Huang, *ChemSusChem*, 2013, **6**, 1545-1555.

27. H. Li, H. Li and M. Wang, *Appl. Catal., A*, 2001, **207**, 129-137.

28. H. Li, W. Wang and J. F. Deng, *J. Catal.*, 2000, **191**, 257-260.

29. H. Li, H. Li, W. Wang and J.-F. Deng, *Chem. Lett.*, 1999, **28**, 629-630.

30. B. Hoffer, E. Crezee, P. Mooijman, A. Van Langeveld, F. Kapteijn and J. Moulijn, *Catal. Today*, 2003, **79**, 35-41.

31. P. Betancourt, A. Rives, R. Hubaut, C. Scott and J. Goldwasser, *Appl. Catal., A*, 1998, **170**, 307-314.

32. H. Guo, H. Li, Y. Xu and M. Wang, *Mater. Lett.*, 2002, **57**, 392-398.

33. J. R. Regalbuto, *Science*, 2009, **325**, 822-824.

34. J. J. Bozell, L. Moens, D. Elliott, Y. Wang, G. Neuenscwander, S. Fitzpatrick, R. Bilski and J. Jarnefeld, *Resources, conservation and recycling*, 2000, **28**, 227-239.

35. J. Thomas and R. Barile, *Biomass Wastes*, 1985, **8**, 1461-1494.

36. R. H. Leonard, *Journal*, 1957.

37. M. Selva, M. Gottardo and A. Perosa, *ACS Sustain. Chem. Eng.*, 2012, **1**, 180-189.

38. S. Cao, J. R. Monnier, C. T. Williams, W. Diao and J. R. Regalbuto, *J. Catal.*, 2015, **326**, 69-81.

39. W. Luo, U. Deka, A. M. Beale, E. R. van Eck, P. C. Bruijnincx and B. M. Weckhuysen, *J. Catal.*, 2013, **301**, 175-186.

40. V. S. Jaya, M. Sudhakar, S. N. Kumar and A. Venugopal, *RSC Adv.*, 2015, **5**, 9044-9049.

41. K. Yan, T. Lafleur, G. Wu, J. Liao, C. Ceng and X. Xie, *Appl. Catal., A*, 2013, **468**, 52-58.

42. K. Yan, T. Lafleur and J. Liao, *J. Nanopart. Res.*, 2013, **15**, 1906.

43. K. Yan, T. Lafleur, C. Jarvis and G. Wu, *J. Clean Prod.*, 2014, **72**, 230-232.

44. F. Ye, D. Zhang, T. Xue, Y. Wang and Y. Guan, *Green Chem.*, 2014, **16**, 3951-3957.

45. Y. Kuwahara, W. Kaburagi and T. Fujitani, *Bull. Chem. Soc. Jpn.*, 2014, **87**, 1252-1254.

46. X. L. Du, Q. Y. Bi, Y. M. Liu, Y. Cao and K. N. Fan, *ChemSusChem*, 2011, **4**, 1838-1843.

47. X. L. Du, L. He, S. Zhao, Y. M. Liu, Y. Cao, H. Y. He and K. N. Fan, *Angew. Chem.*, 2011, **123**, 7961-7965.

48. D. Xianlong, L. Yongmei, W. Jianqiang, C. Yong and F. Kangnian, *Chin. J. Catal.*, 2013, **34**, 993-1001.

49. P. Sun, G. Gao, Z. Zhao, C. Xia and F. Li, *ACS Catal.*, 2014, **4**, 4136-4142.

50. V. Molinari, M. Antonietti and D. Esposito, *Sci. Technol.*, 2014, **4**, 3626-3630.

51. Z. Rong, Z. Sun, L. Wang, J. Lv, Y. Wang and Y. Wang, *Catal. Lett.*, 2014, **144**, 1766-1771.

52. I. Obregón, E. Corro, U. Izquierdo, J. Requies and P. L. Arias, *Chin. J. Catal.*, 2014, **35**, 656-662.

53. K. Yan and A. Chen, *Fuel*, 2014, **115**, 101-108.

54. A. M. Hengne and C. V. Rode, *Green Chem.*, 2012, **14**, 1064-1072.

55. J. Yuan, S.-S. Li, L. Yu, Y.-M. Liu, Y. Cao, H.-Y. He and K.-N. Fan, *Energ. Environ. Sci.*, 2013, **6**, 3308-3313.

56. Z.-p. Yan, L. Lin and S. Liu, *Energy Fuels*, 2009, **23**, 3853-3858.

57. D. J. Braden, C. A. Henao, J. Heltzel, C. C. Maravelias and J. A. Dumesic, *Green Chem.*, 2011, **13**, 1755-1765.

58. A. M. R. Galletti, C. Antonetti, E. Ribechini, M. P. Colombini, N. N. o Di Nasso and E. Bonari, *Appl. energ.*, 2013, **102**, 157-162.

59. J. Liu, T. Zhang, Z. Wang, G. Dawson and W. Chen, *J. Mater. Chem.*, 2011, **21**, 14398-14401.

60. K. Schwinghammer, M. B. Mesch, V. Duppel, C. Ziegler, J. r. Senker and B. V. Lotsch, *J. Am. Chem. Soc*, 2014, **136**, 1730-1733.

61. W. Yang, J. Billy, Y. B. Taarit, J. Vedrine and N. Essayem, *Catal. Today*, 2002, **73**, 153-165.

62. J. A. Dias, E. Caliman, S. I. C. Dias, M. Paulo and A. T. C. de Souza, *Catal. Today*, 2003, **85**, 39-48.

63. M. J. Bojdys, J. O. Müller, M. Antonietti and A. Thomas, *Chem. Eur. J.*, 2008, **14**, 8177-8182.

64. D. Dontsova, S. Pronkin, M. Wehle, Z. Chen, C. Fettkenhauer, G. Clavel and M. Antonietti, *Chem. Mater.*, 2015, **27**, 5170-5179.

65. Z. Obalı and T. Doğu, *Chem. Eng. J.*, 2008, **138**, 548-555.

66. D. Mucha, L. Matachowski, T. Machej, J. Gurgul and R. P. Socha, *Solid State Sci.*, 2011, **13**, 1276-1284.

67. J. Liu, Y. Liu, N. Liu, Y. Han, X. Zhang, H. Huang, Y. Lifshitz, S.-T. Lee, J. Zhong and Z. Kang, *Science*, 2015, **347**, 970-974.

68. G. Dong and L. Zhang, *J. Mater. Chem.*, 2012, **22**, 1160-1166.

69. E. Rafiee and S. Shahebrahimi, *Chin. J. Catal.*, 2012, **33**, 1326-1333.

70. Q. Wang, T. Hisatomi, S. S. K. Ma, Y. Li and K. Domen, *Chem. Mater.*, 2014, **26**, 4144-4150.

71. J. Yan, H. Wu, H. Chen, Y. Zhang, F. Zhang and S. F. Liu, *Appl. Catal. B: Environ.*, 2016, **191**, 130-137.

72. Y. Miseki, S. Fujiyoshi, T. Gunji and K. Sayama, *Sci. Technol.*, 2013, **3**, 1750-1756.

73. K. Maeda, D. Lu and K. Domen, *ACS Catal.*, 2013, **3**, 1026-1033.

74. L. Ding, H. Zhou, S. Lou, J. Ding, D. Zhang, H. Zhu and T. Fan, *Int. J. Hydrogen Energy*, 2013, **38**, 8244-8253.

75. Q. Jia, A. Iwase and A. Kudo, *Chem. Sci.*, 2014, **5**, 1513-1519.

76. Y. Yang, W. Guo, Y. Guo, Y. Zhao, X. Yuan and Y. Guo, *J. Hazard. Mater.*, 2014, **271**, 150-159.

77. S. Chen, Y. Hu, L. Ji, X. Jiang and X. Fu, *Appl. Surf. Sci.*, 2014, **292**, 357-366.

78. S. S. K. Ma, K. Maeda, T. Hisatomi, M. Tabata, A. Kudo and K. Domen, *Chem. Eur. J.*, 2013, **19**, 7480-7486.

79. A. Hiskia, A. Mylonas and E. Papaconstantinou, *Chem. Soc. Rev.*, 2001, **30**, 62-69.

80. Z. Jin, N. Murakami, T. Tsubota and T. Ohno, *Appl. Catal., B: Environ.*, 2014, **150**, 479-485.

81. M. Liu, W. Deng, Q. Zhang, Y. Wang and Y. Wang, *Chem. Commun.*, 2011, **47**, 9717-9719.

82. X. Chen, L. Zhang, B. Zhang, X. Guo and X. Mu, *Sci. R*, 2016, **6**, 28571.